Hydrodynamic Modelling of the Electronic Response of Carbon Nanotubes

by

Duncan J. Mowbray

A thesis
presented to the University of Waterloo
in fulfilment of the
thesis requirement for the degree of
Doctor of Philosophy
in
Applied Mathematics

Waterloo, Ontario, Canada, February 2007

I hereby declare that I am the sole author of this thesis. This is a true copy of the thesis, including any required final revisions, as accepted by my examiners.

I understand that my thesis may be made electronically available to the public.

Abstract

The discovery of carbon nanotubes by Iijima in 1991 has created a torrent of new research activities. Research on carbon nanotubes ranges from studying their fundamental properties, such as their electron band structure and plasma frequencies, to developing new applications, such as self-assembled nano-circuits and field emission displays. Robust models are now needed to enable a better understanding of the electronic response of carbon nanotubes. We use time-dependent density functional theory to derive a two-fluid two-dimensional (2D) hydrodynamic model describing the collective response of a multiwalled carbon nanotube with dielectric media embedded inside or surrounding the nanotube.

We study plasmon hybridization of the nanotube system in the UV range, the stopping force for ion channelling, the dynamical image potential for fast ions, channelled diclusters and point dipoles, and the energy loss for ions with oblique trajectories. Comparisons are made of results obtained from the 2D hydrodynamic model with those obtained from an extension of the 3D Kitagawa model to cylindrical geometries.

Acknowledgements

I acknowledge the aid of my supervisors Dr. Z. L. Mišković and Dr. F. O. Goodman in the development of this thesis. I also acknowledge the contributions of J. Zuloaga and S. Chung to the research which is contained herein, and L.-J. Hou for his many supportive comments.

Dedication

To the memory of my father, John V. Mowbray

Contents

List of Figures

List of Tables

Chapter 1

Introduction

In 1991, it was Sumio Iijima who first interpreted the electron microscopy images shown in Fig. 1.1 as being "helical microtubules of graphitic carbon", now known as carbon nanotubes (CNTs) [1]. Although evidence for CNTs has since been found in microscopy images dating back to the 1950's, it would take more than thirty years for these images to be properly understood. Since the discovery of CNTs, this stable nanoscale material has been the subject of intensive research efforts throughout the world. Potential applications include single wall CNT transistors [2, 3], self assembled circuits [4], field emission displays [2, 5], particle detectors (SO_2, NO, NO_2) [6], nano-beam extractors [7, 8], and light-bulb filaments [9]. The interest in CNTs is motivated by their many interesting electronic properties. CNTs may be either semi-conducting or metallic depending on the graphitic folding method of their construction, also called the CNT's chirality, shown in Fig. 1.1. It may even be possible to change a nanotube from a semiconductor to a metal by applying a sufficiently high external magnetic field, based on the Aharonov-Bohm effect, as discussed by Ajiki and Ando [10]. Ando also showed that metallic nanotubes may behave as near ballistic conductors, even at room temperature [11], with an absence of back-scattering [12]. It has also been shown that ion irradiation changes the structure of CNTs, with "straightening" of nanotubes observed by Jung *et al.* [13] and induced defects observed by Nordlund *et al.* [14, 15].

The electronic properties of single-walled carbon nanotubes (SWNTs) have been probed by Pichler *et al.* [16] via electron energy loss spectroscopy (EELS) and measurements of the plasmon energies as shown in Fig. 1.2. Single-electron excitations occur at energies of a few electron volts, while collective excitations of the electron "fluid" occur for energies on the order of tens

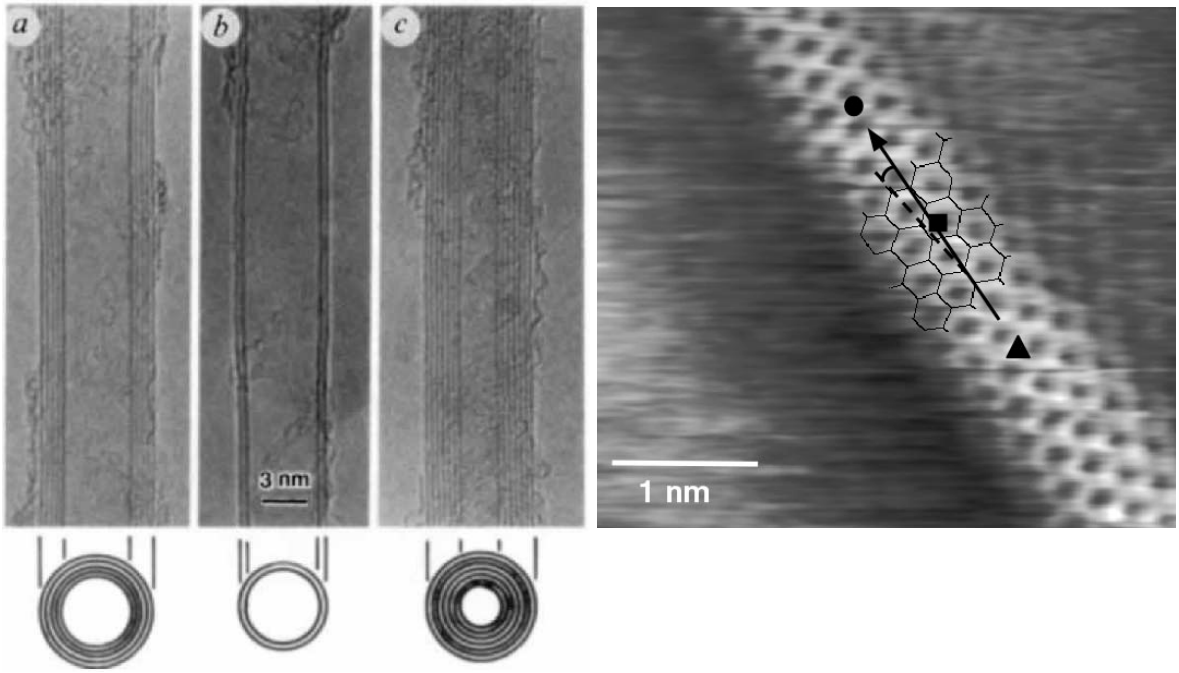

Figure 1.1: Electron micrographs of (*a*) five-wall CNT with outer radius $R_5 = 33.5$ Å, (*b*) double-wall CNT with outer radius $R_2 = 27.5$ Å, (*c*) seven-wall CNT with outer radius $R_7 = 32.5$ Å and inner radius $R_1 = 11$ Å [1, 2]. Scanning tunneling microscopy image of a SWNT on the surface of a rope, showing a nanotube's chirality [2, 17, 18].

of electron volts. To understand these collective plasmon excitations, a robust model for the electronic properties of CNTs is needed.

The many interesting properties of CNTs (high tensile strength, ballistic conduction, semiconductivity, etc.) [2] have also motivated researchers to attempt to functionalize nanotubes in various different materials. For example, silicon dioxide is often used as a substrate for nanotube experiments, as well as an embedding matrix for the formation of nano-composites [19, 20, 21]. On the other hand, although amorphous carbon is often created as a byproduct during nanotube formation, Nishino *et al.* have also observed nanotubes surrounded by amorphous carbon "walls", a structure which they have named an amorphous carbon nanotube (α-CNT) [22]. Also, SWNTs are typically formed in "bundle" or "rope" structures, as shown in Fig. 1.1, which may be approximated by external amorphous carbon layers.

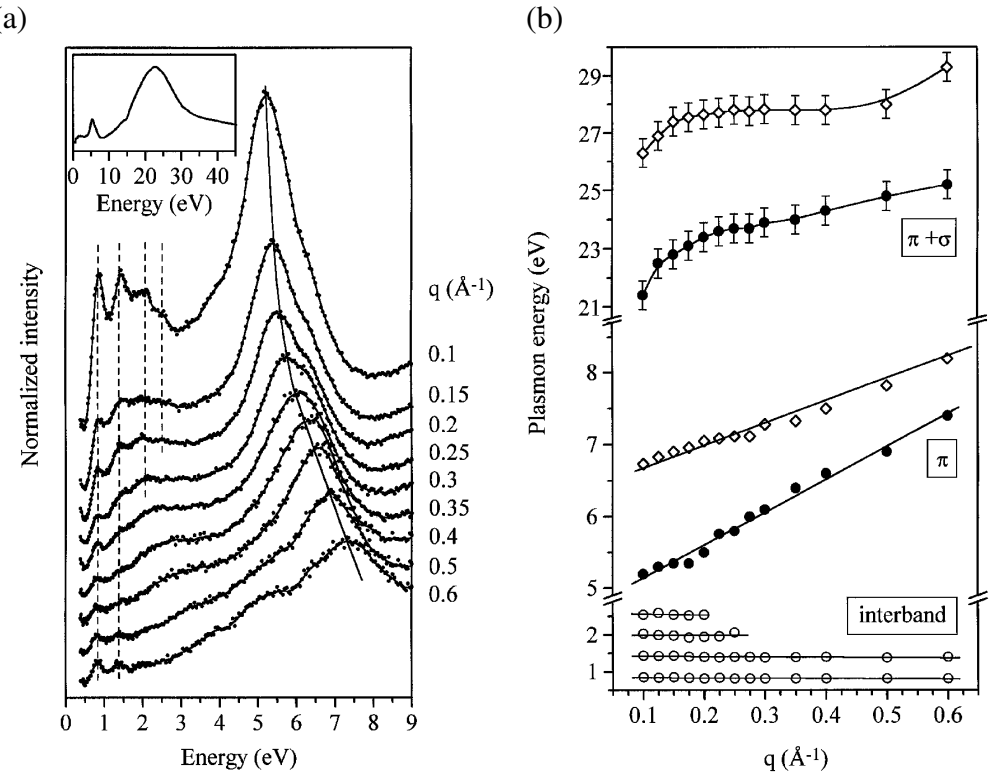

Figure 1.2: (a) Electron energy loss spectroscopy experimental results for CNTs [16]. (b) Plasmon energy experimental results for $\pi + \sigma$ and π bands of CNTs ($\bullet$) and graphite sheets ($\diamond$), with interband plasmon energies for CNTs ($\circ$) [16].

The use of nanotubes as templates for the formation of nano-wires, both inside and surrounding the nanotube, has been realized by experimentalists for many different metals, as described by Guerret-Piécourt *et al.* [23]. They were able to produce nickel "nanowire" coatings of nanotubes more than 1 μm in length. They suggest that the tendency of nickel to form long consistent coatings is due to the metal's morphology, and ability to bond with carbon. Considering the encapsulating nickel to be a solid channel is justified by the work of Chen *et al.* [24] on nano-composites, Zhang *et al.* [25] on nickel coatings of SWNTs, and Ninomiya *et al.* [26] on nickel nano-channels. This differs from aluminum, which although of theoretical interest due to its simple dielectric function, is found to "clump" into nano-ring type structures, as discussed by Bagci *et al.* [27]. Nickel has also been intercalated inside CNTs to form wires of nickel carbide

by Bao *et al.* [28] and pure nickel by Liang *et al.* [29]

Some of the most intriguing applications of CNTs are expected in the area of biomedical research where they can be used, for example, for targeted drug delivery, or as artificial ion channels in cell membranes. In that context, there has been a recent increase of interest in the interactions of CNTs with aqueous environments, especially addressing the hydrophobic properties of CNTs and how this affects the transport of water through and around CNTs. A number of molecular dynamic (MD) simulations of the interactions between water and CNTs have been conducted in recent years [30, 31]. Several interesting effects of water on SWNTs have been studied experimentally in various contexts, such as CNT probes [32], their electrical conductivity [33], CNT transistors [34], functionalization of CNTs with aqueous solutions [35], CNT synthesis in water [36], flexibility of CNTs [37] and their alignment in aqueous solution [38].

Studying hybridization among the resonant excitation modes in the components of complex nanostructures is a continuing project aimed at engineering the optical properties of matter at the nanoscale [39, 40, 41]. In particular, understanding of the dielectric response of nanotubes with various materials may be applied in the UV region to model interactions with fast charged particles. Such interactions occur both in EELS [16, 42, 43] and the emerging field of ion transport through nano-capillaries in solids [44, 45, 46]. Moreover, recent theoretical investigations of the feasibility of ion channelling through CNTs, at both high [47, 48] and low energies [49], are concerned with the practicality of "holding" a straight nanotube, or nanotube rope, effectively using, e.g., metal "clamps". In this context, we explore here how the stopping and dynamical image forces on ions channelled through CNTs [50] will be affected by the presence of a polarizable medium outside the nanotube. On the other hand, the recently discovered toroidal electron image states around CNTs [51, 52] pose interesting questions regarding the existence of such states when, e.g., a metallic nanowire is embedded in the nanotube, which we also briefly address here.

1.1 Modelling the Electronic Response of CNTs

Given the typically large size of complex nano-structures, *ab initio* methods such as time dependent density functional theory (TDDFT) [40, 41, 53] are of limited use for describing the dielectric response of carbon nanostructures. As a result, various versions of the hydrodynamic

model of the dielectric response of carbon valence electrons are becoming increasingly used to study plasmon excitations in such structures [42, 54, 55, 56, 57, 58]. It has been recently shown that such two-dimensional (2D) hydrodynamic models give a good account of both the energy loss due to collective electron excitations and the dynamic image interaction for fast point charges moving perpendicular [42] or parallel to the axes of CNTs [55]. In particular, the hydrodynamic model was found to give results in good agreement with those obtained from random-phase-approximation (RPA) models [55, 56]. It should be noted that both the hydrodynamic [58] and RPA models [59, 60, 61, 62, 63] for nanotubes have been formulated to include encapsulated and surrounding dielectric media. However, only constant dielectric functions were used in these calculations [58, 59, 60, 61, 62, 63].

The two-fluid version of the 2D hydrodynamic model was originally developed by Cazaux to model σ and π plasmons in graphene [64, 65], and has since been used to model plasmon hybridization in C_{60}, C_{70} [66], and SWNTs [67, 68]. In these materials, the four carbon valence electrons are sp^2 hybridized, with three electrons per atom in planar σ hybridized orbitals, and one electron per atom in out-of-plane $2p_z$ hybridized π orbitals. As discussed by Weissbluth pp. 597–598 [69], the $2p_z$ orbital is antisymmetric with respect to the molecular plane, while the in-plane σ sp^2 hybridized orbitals are symmetric with respect to the molecular plane, since they are linear combinations of the $2s$, $2p_x$, and $2p_y$ orbitals. Since the Hamiltonian $\widehat{\mathcal{H}}$ is invariant under reflection in the molecular plane, $\langle 2p_z|\widehat{\mathcal{H}}|sp^2\rangle$ must vanish. This means that all single electron quantum mechanical internal interactions occur only between electrons in the same sp^2 hybridized orbital, so that electrons in σ orbitals mainly interact electrostatically with electrons in π orbitals. This behaviour is modelled in the two-fluid formalism by two different electron fluids, called the σ and π fluids, consisting of $3/4$ and $1/4$ of the carbon valence electrons, respectively. When the two electron fluids spatially coincide, they differ from a single electron fluid only in the lack of internal interaction between electrons in different fluids. These interactions are typically modelled by fitting free parameters to experimental data for graphene [66, 67]. In our approach, these internal interactions are modelled by a separate treatment of the Thomas-Fermi kinetic energy of each electron fluid. This approach gives rise to a hybridization of the collective oscillations in each fluid, yielding a low energy π plasmon [68] and a high energy $\sigma+\pi$ plasmon, in qualitative agreement with experiment [16, 43]. When internal interactions are neglected, the low energy π plasmon collapses to zero, while the high energy $\sigma + \pi$ plasmon reduces to the

single-fluid plasmon result.

Hydrodynamic models are most useful when describing the collective behaviour of an electron gas, while disregarding low energy single-electron excitations [70]. In the UV range, collective oscillations dominate the electric response of both fullerenes and CNTs, so that the two-fluid hydrodynamic model has been found to describe the EELS rather well [16, 43, 66, 67, 68, 71]. Collective oscillations also dominate the response for ion channelling trajectories, since the ions are steered away from the nanotube walls at distances typically larger than the π orbital size, and undergo only distant collisions with the nanotube electrons. Also, channelled ions typically have speeds well above those at which single-particle excitations and band structure effects dominate [61, 72]. As well, the quantities of interest for ion channelling, namely the ion stopping force and image potential, are well suited to calculation using hydrodynamic models [70], but are impractical for calculation using *ab initio* type methods [73]. Perhaps just as importantly, the hydrodynamic model is based on a clear physical intuition, which aids in the construction of physical explanations of its predictions.

Similar semi-classical methods have been developed by Stöcli, Bonard, Stadelmann and Châtelain [42, 74, 75], Yannouleas, Bogacheck, and Landman [58, 76], and Que and Kornyushin [77, 78] for the calculation of plasmon excitations in CNTs. Semi-classical methods have also been applied to CNTs by Slepyan *et al.* [79, 80, 81], to study their electromagnetic response, by Granger, Král, Sadeghpour, Shapiro, and Segal [51, 82, 83, 84], and Thumm, Richard *et al.* [52, 85] to study electron image states around CNTs, by Krčmar, Saslow, and Zangwill [86] to calculate their capacitance and polarizability, and by Dedkov and Karamurzov [87, 88, 89] to study ion channelling through CNTs.

One of the most often used methods for describing the electronic response of CNTs is the random phase approximation. In this method, electrons are assumed to respond to only the total electric potential, which is the sum of the external perturbing potential and a screening potential. The external perturbing potential is assumed to oscillate at a single frequency ω, so that the model yields via a self-consistent field (SCF) method [90] a dynamic dielectric function $\varepsilon_{\mathrm{RPA}}(\mathbf{k}, \omega)$. The contribution to the dielectric function from the total electric potential is assumed to "average out", so that only the potential at wave vector $\mathbf{k}$ contributes. This is what is meant by the random phase approximation. The resulting dielectric function, also called the Lindhard dielectric function [91, 92], correctly predicts a number of properties of the electron

gas, including plasmons. A detailed derivation of the RPA dielectric function is given by Mahan pp. 430–440 [93]. RPA has been used on CNTs by M. F. Lin *et al.* [94, 95, 96, 97, 98], Vasvári [99], Tanatar [100], Longe and Bose [56] to model plasmons and plasma oscillations, Kobayashi *et al.* [101] to model plasmons and the dielectric function, Gumbs *et al.* [60, 61, 62, 63, 102] to model plasmons, stopping force, and image potential, Benedict, Louie, and Cohen [103] to model polarizabilities, Que [104] to model the Littinger parameter g, and Woods and Mahan [105] to model electron-phonon effects.

Another method often used to model the electronic response of carbon nanotubes is the pseudopotential and transfer-matrix technique. This method uses a pseudopotential to model the potential barrier to electron transmission through CNTs. The pseudopotential V^{pseudo}, as discussed by Ashcroft and Mermin pp. 208–210 [92] and Kittel pp. 252–254 [106], models the effective potential that valence electrons will feel from the screened ion cores. It is assumed to be sufficiently small to justify a nearly-free-electron calculation of the valence electron wave functions. In the transfer-matrix method, the transfer-matrix transforms and mixes the modes (or wave functions) in different regions to describe the rate of electron transmission [107]. The transfer-matrix method has been used to model field emission from both metallic and semi-conducting CNTs by Mayer *et al.* [108, 109, 110, 111, 112, 113], Nardelli [114], Han and Ihm [115].

The tight-binding model is often used to describe the equilibrium state of CNTs. In this model, it is assumed that the full Hamiltonian of the system may be approximated by the Hamiltonian of an isolated atom centred at each lattice point. The atomic orbitals, which are eigenfunctions of the single atom Hamiltonian, are assumed to be of very small amplitude at distances exceeding the lattice constant. This is what is meant by tight-binding. It is further assumed that any corrections to the atomic potential which are required to obtain the full Hamiltonian of the system are appreciable only when the atomic orbitals are small. The solution to the time-independent single electron Schrödinger equation is then assumed to be a linear combination of atomic orbitals. This leads to a matrix equation for the electronic problem in equilibrium. A detailed derivation and discussion of the tight-binding model is given by Ashcroft and Mermin pp. 176–210 [92]. Since the tight-binding approach requires the Schrödinger equation to be solved simultaneously for each atom in the unit cell, the case of chiral nanotubes, which may have thousands of atoms in the unit cell, is particularly unsuited to a direct tight-binding approach. For example, an (11,9) SWNT has 1204 atoms in its unit cell. However, various methods of simplifi-

cation, such as the use of a nanotube's screw symmetry, may greatly reduce the number of atoms which must be considered [116].

Tight-binding models have been applied to CNTs predominantly for the calculation of electronic band structure and energy gaps, by Hamada *et al.* [117], Ogloblya *et al.* [118], Popov [116], Lieber *et al.* [18], Saito, Dresselhaus *et al.* [119, 2], Kane and Mele *et al.* [120]. To calculate the dynamic response of CNTs, wave functions obtained from tight-binding Hamiltonians are often used in the random phase approximation dielectric function $\varepsilon_{\mathrm{RPA}}(\mathbf{k},\omega)$, as done by Lin [121]. In this manner, the resonance Raman profile of the radial-breathing mode and optical transition energies for CNTs have been calculated by Henrard, Meunier and Lambin *et al.* [122, 123, 124], the polarization by Amovilli and March [125], and the screened potential and induced charge density by Léonard and Tersoff [126].

Density-functional theory (DFT), in the form of the Kohn-Sham (KS) equations using a local-density approximation (LDA), is also often used to calculate the equilibrium state of CNTs. This method involves iteratively solving the KS equations until self-consistency is reached. The KS equations involve an effective potential $v_{\mathrm{eff}}(\mathbf{r})$ which is the sum of the external potential $V_{\mathrm{ext}}(\mathbf{r})$, the Coulomb potential $\iiint d^3\mathbf{r}' \, \frac{n(\mathbf{r}')}{\|\mathbf{r}-\mathbf{r}'\|}$ and an exchange and correlation potential $v_{xc}(\mathbf{r})$, a set of N orthonormal wave functions $\psi_i(\mathbf{r},s)$ which are solutions to the Schrödinger equation for N noninteracting electrons moving in the effective potential $v_{\mathrm{eff}}(\mathbf{r})$, and the electron density $n(\mathbf{r})$ which is a sum of the squared amplitudes of the wave functions $\psi_i(\mathbf{r},s)$. However, an explicit form for the exchange and correlation potential $v_{xc}(\mathbf{r})$ is needed to close the KS system of equations.

In LDA, the electron exchange and correlation potential $v_{\mathrm{eff}}^{\mathrm{LDA}}(\mathbf{r})$ is assumed to depend only "locally", that is at the position $\mathbf{r}$, on the exchange and correlation energy per particle. The exchange and correlation potential may thus be written in terms of a uniform electron gas model, involving the Dirac exchange energy and one of several empirical models for the correlation energy. A detailed derivation of the KS equations and discussion of the LDA method is given by Parr and Yang pp. 142–200 [127].

DFT-LDA models have been applied to CNTs by Mintmire *et al.* [128], Santucci, Delley *et al.* [129], Ajayan *et al.* [130], Benedict, Louie *et al.* [131], D. Tománek *et al.* [59], Lou, Nordlander, and Smalley [132], to calculate the electron structure, electrostatic potential, charge density profile, and band gap in the static regime. By assuming that when time dependence is

introduced into the electron density the KS equations are still satisfied, we may use the DFT-LDA model to solve for the dynamic response of CNTs. TDDFT has also been used by A. Rubio, V. Olevano, *et al.* [53, 133, 134] to model the structural properties, elasticity, vibrational properties, optical absorption and energy loss spectra of CNTs. The interaction forces obtained from DFT have also been employed in MD simulations of CNTs by Zhang *et al.* [135], by Moura and Amaral [136], and by Udomvech, Kerdcharoen and Osotchan [137] to study ion channelling and absorption.

The effective mass approximation (EMA) is also used to model the electronic properties of CNTs. In this model, electrons in the periodic lattice potential are accelerated relative to the nanotube lattice as if the electron mass were equal to its "effective mass", which is determined from the energy-wave vector relation. A detailed discussion of EMA is provided by Kittel pp. 209–214 [106]. EMA has been applied to CNTs by Mele, Král, and Tománek [138] to calculate electronic excitations and band structure, by Ajiki and Ando [139] to calculate band structure and band gaps, and by Margulis *et al.* [140, 141, 142] to calculate optical properties.

1.2 Thesis Outline

Using a density-functional approach, we derive from first principles the 2D hydrodynamic model for an N-walled CNT [55, 68, 143, 144, 145, 146, 147, 148, 149] with dielectric media inside and outside the nanotube. We accomplish this by modelling the walls of a CNT as a series of electron fluids confined to infinitely thin (2D) cylinders, with internal interaction energies given by DFT calculations on a 2D cylinder. Assuming the electron fluids are perturbed only slightly from equilibrium, we linearize the continuity and momentum-balance equations for each electron fluid. We include dielectric media inside and outside the nanotube by solving for the polarization charge on each dielectric boundary, following the methodology described by Doerr and Yu [150].

While we model the dielectric response of silicon dioxide using a dielectric constant $\epsilon_{\mathrm{SiO_2}} \approx 3.9$, [151] all other materials considered are modelled using frequency-dependent, optical dielectric functions in the UV part of their respective spectra. For example, the dielectric function of amorphous carbon is modelled by a sum of two Drude-type optical dielectric functions, [152] using fitting parameters to experimental data [153]. Furthermore, we model the dielectric response of aluminum as a single Drude-type dielectric function, with plasma frequency

$\omega_p \approx 15.0$ eV, as given by Abril *et al.* [153] This allows us to model the plasma energy of a combined aluminum–nanotube system, generalizing the approach by Arista *et al.* to metal nanowires and nano-channels [44, 45, 154]. Finally, following the early models of nickel by sums of Drude-type dielectric functions [155, 156, 157], we employ a sum of ten Drude-type dielectric functions with the fitting parameters of Kwei *et al.* [158], which reproduce well the optical data for nickel of Moravec *et al.* [159].

Our use of optical dielectric functions for nearby dielectric media, neglecting their momentum dependence, is reasonable for both ion stopping force and image potential calculations, due to the ion channelling condition of large separation between the ion and the nanotube wall. Furthermore, it has recently been shown in a flat geometry that the momentum dependence of the surface dielectric function has little effect on plasmon hybridization for sufficient separation between a 2D electron fluid and the dielectric surface [73]. On the other hand, models of the momentum dependence of the surface dielectric function in curved geometries have not yet been developed in a manner that generalizes the specular reflection model [160].

Ion channelling through single-wall carbon nanotubes (SWNTs), double-wall carbon nanotubes (DWNTs), and multiwalled carbon nanotubes (MWNTs) is modelled using the external potential for an ion moving parallel to the nanotube axis with constant speed v. The plasma hybridization process in single [56, 68], double [145], and multiwalled [148] CNTs is discussed in detail, with particular emphasis on the effect of dielectric media inside or outside the nanotube [147]. In this vein, we calculate the induced electron density and total electric potential using the one [144] and two-fluid [68] hydrodynamic models, paying particular attention to wake effects. The plasma hybridization results are then used to explain our stopping force (or stopping power) calculations for single [68], double [145], and multiwalled [148] CNTs with dielectric media inside or outside the nanotube [147]. Calculations of the self-energy (or image potential) are then compared for single [144], double [145], and multiwalled [148] CNTs with dielectric media inside or outside the nanotube [147], noting the nanotube's screening ability.

We then extend the 3D Kitagawa model [161] to cylindrical geometries, using Thomas-Fermi [162], Thomas-Fermi-Dirac [163], Molière [164, 165], and Cruz [166, 167] models for a radially dependent equilibrium electron density $n_0(r)$ [168]. Comparisons are made between the stopping force for ion channelling obtained from the 2D hydrodynamic model and from the 3D Kitagawa model, showing qualitative agreement for sufficiently high ion speeds and distances from the

nanotube wall [168].

Channelling of diclusters and dipoles is then considered. The 2D hydrodynamic model is used to model the total energy for a system of channelled ions using either a Doyle-Turner or Molière model for the atomic potential of the nanotube. Calculations are made for the total energy of diclusters with centre of mass on the nanotube axis and diclusters aligned with the nanotube axis. The nanotube is shown to provide efficient screening between the ions. The self-energy (or image potential) and stopping force are calculated for a point dipole, showing position, speed, and direction dependence.

Ions with trajectories at oblique angles to the axes of CNTs are then studied, and expressions for both the energy loss and deflection angle are given. Calculations of the plasmon excitation probability $\mathcal{P}(\omega)$ associated with undergoing energy loss ω, and the speed dependence of the energy loss, are made.

Finally, we conclude with a discussion of our results, and potential extensions of the hydrodynamic model to three dimensions. We perform all numerical integrations using the adaptive Gaussian-Lobatto quadrature code provided with Matlab, which is discussed by Abramowitz and Stegun pp. 888–890 [169]. Unless stated otherwise, cylindrical coordinates $\mathbf{r} = \{r, \varphi, z\}$ and atomic units are to be assumed, with $\hbar = e_p = m_e = a_0 = 1$, where $2\pi\hbar$ is Planck's constant, e_p is the charge of a proton, m_e is the mass of an electron, and a_0 is Bohr's radius. We note that, in atomic units, the speed of light $c \approx 137.03599$. All equations are in Gaussian units, so that $4\pi\epsilon_0 = 1$.

Chapter 2

2D Hydrodynamic Model

In his 1933 paper [170], Bloch first introduced a method for deriving hydrodynamical equations for a nonuniform electron gas using Thomas-Fermi theory. His approach was to use the Thomas-Fermi kinetic energy to model the ground state energy of a hydrodynamic fluid. Using this simple hydrodynamic model, Fetter found plasma oscillations and screening for electron layers [171] and in periodic arrays [172]. However, the applicability of the hydrodynamic model to non-classical systems was in doubt.

After the development of density functional theory (DFT), as discussed by Harbola and Banerjee [173], Argaman and Makov [174], Parr and Yang [127], and Lundqvist and March [175], the hydrodynamic model was further developed by Ying *et al.* [176, 177, 178, 179] to use the full energy functional $F[n]$ from DFT to approximate the ground state energy of the fluid.

2.1 Density Functional Theory

A fully quantum mechanical calculation of the ground state energy of a system of N electrons would involve solving the Schrödinger equation for the many electron wave function $\Psi(\mathbf{r}_1, s_1, \mathbf{r}_2, s_2, \ldots, \mathbf{r}_N, s_N)$. This is a function of both the N electron positions and the N electron spins, making an exact solution intractable for many electron systems.

DFT allows us to reduce the problem of finding the ground state energy E_0 from a many electron problem to a problem in terms of the electron number density $n(\mathbf{r})$, sometimes called the one electron density. This simplification is justified by the Hohenberg-Kohn theorems, as

discussed by Parr and Yang pp. 51–56 [127], which form the foundation of DFT. We will use the following variation of the Hohenberg-Kohn theorem for a ground state system, as developed by Levy [180, 181] and discussed in Appendix A.1.

Theorem 2.1 (Hohenberg-Kohn) *A system with number density $n(\mathbf{r})$ such that $n(\mathbf{r}) \geq 0$, $\iiint d^3\mathbf{r}\; n(\mathbf{r}) = N$, and $\iiint d^3\mathbf{r}\; \|\vec{\nabla}\sqrt{n(\mathbf{r})}\|^2 < \infty$, will have energy*

$$E = F[n] + \iiint d^3\mathbf{r}\; n(\mathbf{r}) V_{\text{ext}}(\mathbf{r}) \tag{2.1}$$

where $V_{\text{ext}}(\mathbf{r})$ is the potential energy per electron in the external fields and $F[n]$ is a unique functional of the electron density.

We may write the functional $F[n]$ in terms of the kinetic energy operator $\widehat{T}$ and electron-electron interaction potential operator $\widehat{V}_{ee}$ as

$$F[n] = \min_{\Psi \to n} \iiint d^3\mathbf{r}\; \Psi(\mathbf{r})(\widehat{T} + \widehat{V}_{ee})\Psi^*(\mathbf{r}) = T[n] + V_{ee}[n], \tag{2.2}$$

where the minimization is performed over all wave functions Ψ which yield density n.

The aim of DFT is to find an approximation to the unknown functionals $T[n]$ and $V_{ee}[n]$. We will begin by finding an expression for the ground state energy E, using the Hartree-Fock approximation.

Hartree-Fock Approximation

We begin by writing the Schrödinger equation for the ground state energy of a system of N electrons as

$$\widehat{\mathcal{H}}\Psi(\mathbf{r}_1, s_1, \ldots, \mathbf{r}_N, s_N) = E\Psi(\mathbf{r}_1, s_1, \ldots, \mathbf{r}_N, s_N) \tag{2.3}$$

where $\widehat{\mathcal{H}}$ is the Hamiltonian operator defined in terms of an external potential $V_{\text{ext}}(\mathbf{r}_i)$ as

$$\widehat{\mathcal{H}} = \sum_i -\frac{1}{2}\nabla^2_{\mathbf{r}_i} + V_{\text{ext}}(\mathbf{r}_i) + \sum_{j<i} \frac{1}{\|\mathbf{r}_i - \mathbf{r}_j\|}, \tag{2.4}$$

and $\Psi(\mathbf{r}_1, s_1, \ldots, \mathbf{r}_N, s_N)$, or more compactly $\Psi(\mathbf{r}^N, s^N)$, is the N-electron wave function, where $\mathbf{r}_i$ is the position and s_i is the spin of the ith electron.

By specifying that the wavefunctions are normalized, so that $\sum_{s^N}\iiint\cdots\iiint d^3\mathbf{r}^N\ \Psi^*\Psi = 1$, we obtain the integral equation for the ground state energy

$$E = \sum_{s^N}\iiint\cdots\iiint d^3\mathbf{r}^N\ \Psi^*(\mathbf{r}^N, s^N)\widehat{\mathcal{H}}\Psi(\mathbf{r}^N, s^N). \tag{2.5}$$

We now apply the Hartree-Fock approximation to the wave function $\Psi(\mathbf{r}^N, s^N)$, to obtain $\Psi_{\rm HF}$. This is done by assuming the wave function may be written as a Slater determinant, as discussed by Parr and Yang pp. 7–10 [127]. Thus $\Psi_{\rm HF}$ is an antisymmetrized product of the N orthonormal single electron wave functions $\psi_i(\mathbf{r}, s)$ which are separable into the spatial wave functions $\phi_i(\mathbf{r})$ and the spin functions $\sigma_i(s)$, so that

$$\Psi_{\rm HF} = \frac{1}{\sqrt{N!}}\begin{vmatrix} \phi_1(\mathbf{r}_1)\sigma_1(s_1) & \phi_2(\mathbf{r}_1)\sigma_2(s_1) & \cdots & \phi_N(\mathbf{r}_1)\sigma_N(s_1) \\ \phi_1(\mathbf{r}_2)\sigma_1(s_2) & \phi_2(\mathbf{r}_2)\sigma_2(s_2) & \cdots & \phi_N(\mathbf{r}_2)\sigma_N(s_2) \\ \vdots & \vdots & & \vdots \\ \phi_1(\mathbf{r}_N)\sigma_1(s_N) & \phi_2(\mathbf{r}_N)\sigma_2(s_N) & \cdots & \phi_N(\mathbf{r}_N)\sigma_N(s_N) \end{vmatrix} \tag{2.6}$$

$$= \frac{1}{\sqrt{N!}}\det[\psi_1\psi_2\cdots\psi_N]. \tag{2.7}$$

We now substitute Eqn. (2.7) for $\Psi_{\rm HF}$ into the integral equation for the Hartree-Fock ground state energy to obtain

$$E_{\rm HF} = \sum_{s^N}\iiint\cdots\iiint d^3\mathbf{r}^N\ \Psi^*_{\rm HF}(\mathbf{r}^N, s^N)\widehat{\mathcal{H}}\Psi_{\rm HF}(\mathbf{r}^N, s^N) \tag{2.8}$$

$$= T + V_{\rm ext} + K \tag{2.9}$$

$$\begin{aligned} = &\sum_i\sum_s\iiint d^3\mathbf{r}\ \psi_i^*(\mathbf{r}, s)\left[-\frac{1}{2}\nabla^2_{\mathbf{r}} + V_{\rm ext}(\mathbf{r})\right]\psi_i(\mathbf{r}, s) \\ &+\frac{1}{2}\sum_{i,j}\sum_{s,s'}\iiint d^3\mathbf{r}\iiint d^3\mathbf{r}'\ \frac{\psi_i(\mathbf{r}, s)\psi_i^*(\mathbf{r}, s)\psi_j^*(\mathbf{r}', s')\psi_j(\mathbf{r}', s')}{\|\mathbf{r}-\mathbf{r}'\|} \\ &-\frac{1}{2}\sum_{i,j}\sum_{s,s'}\iiint d^3\mathbf{r}\iiint d^3\mathbf{r}'\ \frac{\psi_i^*(\mathbf{r}, s)\psi_j(\mathbf{r}, s)\psi_i(\mathbf{r}', s')\psi_j^*(\mathbf{r}', s')}{\|\mathbf{r}-\mathbf{r}'\|}. \end{aligned} \tag{2.10}$$

If we now define the spin density matrix $\gamma(\mathbf{r}, s; \mathbf{r}', s')$ as

$$\gamma(\mathbf{r}, s; \mathbf{r}', s') = \sum_{i=1}^{N} \psi_i^*(\mathbf{r}', s')\psi_i(\mathbf{r}, s), \tag{2.11}$$

$$\gamma(\mathbf{r}, s) = \gamma(\mathbf{r}, s; \mathbf{r}, s), \tag{2.12}$$

we obtain in terms of $\gamma(\mathbf{r}, s; \mathbf{r}', s')$

$$\begin{aligned} E_{\mathrm{HF}}[\gamma] = &-\frac{1}{2}\sum_s \iiint d^3\mathbf{r}\ \nabla_{\mathbf{r}}^2 \gamma(\mathbf{r}', s; \mathbf{r}, s)\big|_{\mathbf{r}'=\mathbf{r}} + \sum_s \iiint d^3\mathbf{r}\ V_{\mathrm{ext}}(\mathbf{r})\gamma(\mathbf{r}, s) \\ &+\frac{1}{2}\sum_{s,s'} \iiint d^3\mathbf{r} \iiint d^3\mathbf{r}'\ \frac{\gamma(\mathbf{r}, s)\gamma(\mathbf{r}', s')}{\|\mathbf{r} - \mathbf{r}'\|} \\ &-\frac{1}{2}\sum_{s,s'} \iiint d^3\mathbf{r} \iiint d^3\mathbf{r}'\ \frac{\gamma(\mathbf{r}, s; \mathbf{r}', s')\gamma(\mathbf{r}', s'; \mathbf{r}, s)}{\|\mathbf{r} - \mathbf{r}'\|}. \end{aligned} \tag{2.13}$$

We now introduce the spinless density matrix, $\rho(\mathbf{r}, \mathbf{r}')$, which satisfies

$$\rho(\mathbf{r}', \mathbf{r}) = \sum_s \gamma(\mathbf{r}', s; \mathbf{r}, s), \tag{2.14}$$

$$\rho(\mathbf{r}, \mathbf{r}) = n(\mathbf{r}), \tag{2.15}$$

where $n(\mathbf{r})$ is the electron number density. We thus obtain

$$\begin{aligned} E_{\mathrm{HF}} = &-\frac{1}{2}\iiint d^3\mathbf{r}\ \nabla_{\mathbf{r}}^2 \rho(\mathbf{r}', \mathbf{r})\big|_{\mathbf{r}'=\mathbf{r}} + \iiint d^3\mathbf{r}\ V_{\mathrm{ext}}(\mathbf{r})n(\mathbf{r}) + \frac{1}{2}\iiint d^3\mathbf{r} \iiint d^3\mathbf{r}'\ \frac{n(\mathbf{r})n(\mathbf{r}')}{\|\mathbf{r} - \mathbf{r}'\|} \\ &-\frac{1}{2}\sum_{s,s'} \iiint d^3\mathbf{r} \iiint d^3\mathbf{r}'\ \frac{\gamma(\mathbf{r}, s; \mathbf{r}', s')\gamma(\mathbf{r}', s'; \mathbf{r}, s)}{\|\mathbf{r} - \mathbf{r}'\|}. \end{aligned} \tag{2.16}$$

If we now assume there is an even number of electrons so each atomic orbital is doubly occupied, we have a nondegenerate closed-shell ground state, and we obtain

$$\begin{aligned} E_{\mathrm{HF}}[\rho] = &-\frac{1}{2}\iiint d^3\mathbf{r}\ \nabla_{\mathbf{r}}^2 \rho(\mathbf{r}', \mathbf{r})\big|_{\mathbf{r}'=\mathbf{r}} + \iiint d^3\mathbf{r}\ V_{\mathrm{ext}}(\mathbf{r})n(\mathbf{r}) \\ &+\frac{1}{2}\iiint d^3\mathbf{r} \iiint d^3\mathbf{r}'\ \frac{n(\mathbf{r}')n(\mathbf{r})}{\|\mathbf{r} - \mathbf{r}'\|} - \frac{1}{4}\iiint d^3\mathbf{r} \iiint d^3\mathbf{r}'\ \frac{\|\rho(\mathbf{r}', \mathbf{r})\|^2}{\|\mathbf{r} - \mathbf{r}'\|}, \end{aligned} \tag{2.17}$$

where

$$\rho(\mathbf{r}', \mathbf{r}) = 2\sum_{i=1}^{N/2} \phi_i^*(\mathbf{r}')\phi_i(\mathbf{r}), \tag{2.18}$$

with ϕ_i being the doubly occupied spatial wave functions.

We must now write the Thomas-Fermi kinetic energy, $T_{\mathrm{TF}}[\rho]$, and the Hartree-Fock exchange energy, $K[\rho]$, given from Eqn. (2.17) as

$$T_{\mathrm{TF}}[\rho] = -\frac{1}{2}\iiint d^3\mathbf{r}\ \ \nabla^2_{\mathbf{r}}\rho(\mathbf{r}, \mathbf{r}')\big|_{\mathbf{r}'=\mathbf{r}} \tag{2.19}$$

$$K[\rho] = \frac{1}{4}\iiint d^3\mathbf{r} \iiint d^3\mathbf{r}'\ \frac{\|\rho(\mathbf{r}, \mathbf{r}')\|^2}{\|\mathbf{r} - \mathbf{r}'\|} \tag{2.20}$$

in terms of the electron number density n.

Density Functional Theory on a Cylinder

We begin by considering a uniform electron gas confined to a cylinder of radius R, with coordinates on the 2D cylindrical surface of $\mathbf{r}_R = \{r = R; \varphi, z\}$. Thus our wave functions will be approximated by the single electron solution to the Schrödinger equation for an infinite potential well of length L confining the electron to the cylinder. L represents the periodicity of the cylindrical lattice along its length. The wavefunction solution is then

$$\psi_\ell(k; \varphi, z) = \frac{e^{i\ell\varphi}e^{ikz}}{\sqrt{2\pi RL}}, \tag{2.21}$$

where $\ell = n_\varphi, k = \frac{2\pi}{L}n_z; n_\varphi, n_z \in \{0, \pm 1, \ldots\}$. The energy is then given by the Schrödinger equation as

$$E_\ell(k) = \frac{1}{2}\left(\frac{\ell^2}{R^2} + k^2\right). \tag{2.22}$$

We consider the system to have all electron levels doubly occupied up to the Fermi energy, E_F. Thus we may introduce the maximum occupied ℓ value for a given Fermi energy, E_F, as

$$\ell_F = R\sqrt{2E_F}. \tag{2.23}$$

The maximum occupied reciprocal wave vector k for a given Fermi energy, E_F may then be written as a function of ℓ as

$$k_F(\ell) = \sqrt{2E_F - \frac{\ell^2}{R^2}}. \tag{2.24}$$

We may now write the density matrix $\rho(\mathbf{r}_R, \mathbf{r}'_R)$ in terms of the wave functions $\psi_\ell(k; \varphi, z)$ as

$$\rho(\mathbf{r}'_R, \mathbf{r}_R) = \sum_{\ell=-\lfloor \ell_F \rfloor}^{\lfloor \ell_F \rfloor} \int_{-k_F(\ell)}^{k_F(\ell)} \frac{e^{i\ell\Delta\varphi} e^{ik\Delta z}}{2\pi^2 R} dk \tag{2.25}$$

where $\Delta\varphi = \varphi - \varphi'$, $\Delta z = z - z'$, $\lfloor \ell_F \rfloor$ is the largest integer less than ℓ_F, and we have approximated the summation over occupied wave functions by an integration over wave vectors. Evaluating $\rho(\mathbf{r}_R, \mathbf{r}'_R)$, we obtain

$$\rho(\mathbf{r}_R, \mathbf{r}'_R) = \frac{1}{\pi^2 R} \sum_{\ell=-\lfloor \ell_F \rfloor}^{\lfloor \ell_F \rfloor} e^{i\ell\Delta\varphi} \left(\frac{e^{ik_F(\ell)\Delta z} - e^{-ik_F(\ell)\Delta z}}{2i\Delta z} \right) \tag{2.26}$$

$$= \frac{1}{\pi^2 R} \sum_{\ell=-\lfloor \ell_F \rfloor}^{\lfloor \ell_F \rfloor} e^{i\ell\Delta\varphi} \frac{\sin(k_F(\ell)\Delta z)}{\Delta z}. \tag{2.27}$$

The density $n(\mathbf{r}_R) = \rho(\mathbf{r}_R, \mathbf{r}_R)$ is calculated in Appendix A.3 from Eqn. (2.25) to be

$$n = \frac{\ell_F^2}{2\pi R^2} + \mathcal{O}\left(\ell_F^{-3/2}\right) \approx n_{\text{plane}}, \tag{2.28}$$

where n_{plane} is the planar density with relative error $\varepsilon^n_{\text{plane}} \approx 0.302\ell_F^{-3/2}$ as discussed in Appendix A.2. Thus we are justified in using the planar density, n_{plane}, so long as $\ell_F \gg 0.45$. For a typical nanotube of radius $R = 7$ Å ≈ 13.23, the Fermi energy $E_F = v_F^2/2 = \pi n_{\text{atomic}} Z_{\text{C}} \approx 9.15 Z_{\text{C}}$ eV, where v_F is the Fermi velocity, $n_{\text{atomic}} \approx 0.107$ is the equilibrium atomic density on a nanotube, and Z_{C} is the number of conduction electrons per carbon atom [56]. Considering there to be one conduction electron per atom, this calculation of the Fermi energy gives good agreement with the density functional theory calculation of Mintmire *et al.* of $E_F \approx 9.6$ eV [128]. We then find from Eqn. (2.23) that $\ell_F \approx 11 \gg 0.45$ so that $n(\mathbf{r}_R)$ can be approximated by n_{plane}.

Thomas-Fermi Kinetic Energy

We may now use Eqn. (2.27) to calculate the Thomas-Fermi kinetic energy term. The Thomas-Fermi kinetic energy term, $T_{\rm TF}[\rho]$, can be written as

$$T_{\rm TF}[\rho] = -\frac{1}{2}\iint d^2\mathbf{r}_R \;\nabla^2_{\mathbf{r}_R}\rho(\mathbf{r}_R,\mathbf{r}'_R)\big|_{\mathbf{r}_R=\mathbf{r}'_R}. \tag{2.29}$$

The diagonal elements of the Laplacian of the density matrix, $-\nabla^2_{\mathbf{r}_R}\rho(\mathbf{r}_R,\mathbf{r}'_R)|_{\mathbf{r}'_R=\mathbf{r}_R}$, are calculated in Appendix A.4 to be

$$-\nabla^2_{\mathbf{r}_R}\rho(\mathbf{r}_R,\mathbf{r}'_R)|_{\mathbf{r}'_R=\mathbf{r}_R} = -\frac{1}{4}\nabla^2_{\mathbf{r}_R}n(\mathbf{r}_R) + \frac{\ell_F^4}{\pi R^4} + \mathcal{O}(\ell_F^{-3/2}) \tag{2.30}$$

$$\approx -\frac{1}{4}\nabla^2_{\mathbf{r}_R}n(\mathbf{r}_R) + \pi n^2_{\rm plane}(\mathbf{r}_\infty), \tag{2.31}$$

where $\mathbf{r}_\infty = \lim_{R\to\infty}\{r=R;\varphi,z\}$ are planar coordinates, and $n_{\rm plane}(\mathbf{r}_\infty)$ is the planar density, with relative error $\varepsilon^{\nabla^2\rho}_{\rm plane} \approx 0.3303\ell_F^{-3/2}$.

Thus we may use the planar density relation so long as $\ell_F \gg 0.478$. For a typical nanotube of radius $R = 7$ Å ≈ 13.23 and Fermi energy $E_F \approx 9.6$ eV [128], we find from Eqn. (2.23) that $\ell_F \approx 11 \gg 0.478$.

Assuming the density is well behaved so that $\iint d^2\mathbf{r}_R\;\nabla^2_{\mathbf{r}_R}n(\mathbf{r}_R) = 0$, the Thomas-Fermi kinetic energy on a cylinder is then

$$T_{\rm TF}[n] = \frac{\pi}{2}\iint d^2\mathbf{r}_R\, n^2(\mathbf{r}_R). \tag{2.32}$$

Exchange Energy Correction

The exchange energy correction $K[\rho]$, from Eqn. (2.20), is given by

$$K[\rho] = \frac{1}{4}\iint d^2\mathbf{r}_R\int d(\Delta z)\int d(\Delta\varphi)R\frac{\rho^2(\mathbf{r}_R,\mathbf{r}'_R)}{\sqrt{2R^2(1-\cos\Delta\varphi)+\Delta z^2}}, \tag{2.33}$$

for an electron gas confined to a 2D cylinder.

Here we will show how this correction may be calculated for the case of electrons confined to a plane, since $n \approx n_{\rm plane}$. The planar density matrix $\rho(\mathbf{r}_\infty,\Delta r)$, discussed in Appendix A.2, is given by

$$\rho(\mathbf{r}_\infty,\Delta r) = \frac{\sqrt{2\pi n_{\rm plane}}}{\Delta r\pi}J_1\left(\sqrt{2\pi n_{\rm plane}}\Delta r\right), \tag{2.34}$$

where $J_1(z)$ is the first order Bessel function of the first kind. We obtain after dropping subscripts and substituting Eqn. (2.34) into Eqn. (2.20),

$$K[n] = \frac{1}{4}\iint d^2\mathbf{r}_\infty \int d(\Delta r)\int d(\Delta\theta)\frac{2\pi n(\mathbf{r}_\infty)}{\pi^2\Delta r^2}J_1^2\left(\sqrt{2\pi n(\mathbf{r}_\infty)}\Delta r\right) \tag{2.35}$$

$$= \frac{4}{3}\sqrt{\frac{2}{\pi}}\iint d^2\mathbf{r}_\infty\, n^{3/2}(\mathbf{r}_\infty) \tag{2.36}$$

as used by Zaremba [182] and discussed in Appendix A.5.

Although in theory the inclusion of the exchange energy correction should provide some improvement over a Thomas-Fermi model, it has often been found that a simple Thomas-Fermi model often gives better qualitative agreement with experiment than more complicated models. This is because the exchange energy correction *lowers* the ground state energy, while more complicated electron correlation terms *raise* the ground state energy, providing a partial cancellation of these contributions. Also, for our calculations of the plasmon energies for CNTs, we found better agreement with the experimental results of Pichler *et al.* [16], shown in Fig. 1.2(b), was obtained by neglecting the exchange energy correction. For these reasons, we neglect the exchange term in our 2D hydrodynamic formulation, restricting ourselves to the Thomas-Fermi model.

Gradient Corrections

To provide a better approximation of the kinetic energy functional $T[n]$, von Weizsäcker introduced in his 1935 paper [183] a gradient correction term, $T_W[n]$. This was obtained by considering modified plane waves of the form $(1 + \mathbf{a}\cdot\mathbf{r})e^{i\mathbf{k}\cdot\mathbf{r}}$, where $\mathbf{a}$ is a constant vector and $\mathbf{k}$ is the local wave vector, as discussed by Parr and Yang pp. 127–128 [127]. This gives the von Weizsäcker correction to the Thomas-Fermi kinetic energy

$$T_W[n] = \frac{1}{8}\iint d^2\mathbf{r}_R\,\frac{\|\vec{\nabla}n(\mathbf{r}_R)\|^2}{n(\mathbf{r}_R)}. \tag{2.37}$$

The von Weizsäcker term may also be derived directly from the kinetic energy functional as done in Appendix A.6 [184]. The kinetic energy functional for the Thomas-Fermi model with the von Weizsäcker correction, $T_{\mathrm{TFvW}}[n]$ is then

$$T_{\mathrm{TFvW}}[n] = T_{\mathrm{TF}}[n] + \lambda_W T_W[n], \tag{2.38}$$

where λ_W is a parameter. In the original work by von Weizsäcker, $\lambda_W = 1$, and this is the value we use in our model. However using a gradient-expansion approach as described by Parr and Yang pp. 128–132 [127], one obtains $\lambda_W = 1/9$ in 3D, $\lambda_W = 0$ in 2D and $\lambda_W = -1/3$ in 1-D as discussed by Holas *et al.* [185]. Empirical values for λ_W have also been used, including $\lambda_W = 1/5$ by Yonei and Tomishima [186], $\lambda_W = 0.186$ by Lieb [187], and $\lambda_W = 1.4/9$ by Brack [188].

However, Kryachko and Ludeña [184] suggest that the von Weizsäcker term represents the "local" contribution to the kinetic energy, so that $\lambda_W = 1$. Acharya *et al.* [189] found experimentally that the contribution from the Thomas-Fermi term should instead be scaled as $1 - C/N^{1/3}$, where $C = 1.332 \pm 0.053$ for ions, $C = 1.412 \pm 0.033$ for neutral atoms, and N is the number of electrons in the fluid. The neutral atom relation has also been derived by Gázquez and Robles [190], and is discussed briefly by Parr and Yang pp. 138–139 [127] and Acharya [191]. For our purposes, $N \to \infty$, suggesting that the Thomas-Fermi term need not be scaled for the 2D hydrodynamic model.

The von Weizsäcker correction is important in that it invalidates the Teller non-binding theorem [192]. This theorem states that in Thomas-Fermi theory, there are no stable molecular systems, since binding cannot occur. This is remedied by the addition of the von Weizsäcker correction, which allows molecular binding to occur.

Thus the energy functional we obtain for the ground state energy of an electron gas confined to a 2D cylinder is

$$F[n] = \iint d^2\mathbf{r}_R \left(\frac{\pi}{2} n^2(\mathbf{r}_R) + \frac{1}{8} \frac{\|\vec{\nabla} n(\mathbf{r}_R)\|^2}{n(\mathbf{r}_R)} + \frac{1}{2} \iint d^2\mathbf{r}'_R \, \frac{n(\mathbf{r}_R) n(\mathbf{r}'_R)}{\|\mathbf{r}_R - \mathbf{r}'_R\|} \right), \tag{2.39}$$

from DFT.

2.2 Hamiltonian Dynamics

The key assumption made by Ying [178], as described by Deb and Ghosh [193], is the equation for the density functional $F[n]$, Eqn. (2.39), continues to hold when the density becomes time dependent. This prescription has been justified by Runge and Gross [194], for certain general types of densities, so that we may now let the electron density be time-dependent $n(\mathbf{r}_R, t)$.

Following the method described by Lundqvist [175], we consider our electron gas to be a classical charged fluid with internal energy given by the energy functional from DFT. We may now write the Hamiltonian for our electron fluid as the following function of the electron density $n(\mathbf{r}_R, t)$, the velocity field $\mathbf{v}(\mathbf{r}_R, t)$. and the time dependent energy functional $F[n(\mathbf{r}_R, t)]$ as

$$H[n, \mathbf{v}] = F[n(\mathbf{r}_R, t)] + \iint d^2\mathbf{r}_R \, \frac{1}{2}\|\mathbf{v}(\mathbf{r}_R, t)\|^2 n(\mathbf{r}_R, t) + \iint d^2\mathbf{r}_R \, V_{\text{ext}}(\mathbf{r}_R, t) n(\mathbf{r}_R, t). \quad (2.40)$$

Since our electron fluid is assumed to be confined to a 2D cylinder, the velocity field $\mathbf{v}(\mathbf{r}_R, t)$ must also be confined so that the radial component of the velocity field is identically zero.

Before applying the canonical equations to our Hamiltonian as described in Goldstein [195], Broer [196], and Lurie [197], we must first cast our Hamiltonian in terms of conjugate variables which satisfy the Legendre transformation. To do this, we introduce a scalar $\phi(\mathbf{r}_R, t)$ which is conjugate to the electron density $n(\mathbf{r}_R, t)$. This requires that we may express the velocity field as a functional of the conjugate variable ϕ, so that

$$H[n, \phi] = F[n(\mathbf{r}_R, t)] + \iint d^2\mathbf{r}_R \, \frac{1}{2}\|\mathbf{v}[\phi(\mathbf{r}_R, t)]\|^2 n(\mathbf{r}_R, t) + \iint d^2\mathbf{r}_R \, V_{\text{ext}}(\mathbf{r}_R, t) n(\mathbf{r}_R, t). \quad (2.41)$$

Choosing $n(\mathbf{r}_R, t)$ to be the generalized momenta gives the Legendre transformation for the Lagrangian

$$L = \iint d^2\mathbf{r}_R \, n(\mathbf{r}_R, t) \frac{\partial \phi}{\partial t} - H[n, \phi], \quad (2.42)$$

so that n satisfies the generalized momenta definition

$$n(\mathbf{r}_R, t) = \frac{\delta L}{\delta \dot{\phi}} = \frac{\partial \mathscr{L}}{\partial \dot{\phi}} \quad (2.43)$$

where we use "δ" to denote functional derivative, "$\dot{}$" to denote partial derivative with respect to time t, and $\mathscr{L}$ to denote the integrand of the Lagrangian L, also called the Lagrangian density, as discussed by Lurie [197].

Using $\mathscr{H}$ to denote the integrand of the Hamiltonian H, also called the Hamiltonian density, we may now write the canonical equation in functional derivative form for $\dot{n}$ as

$$\frac{\partial n}{\partial t} = -\frac{\delta H}{\delta \phi} \quad (2.44)$$

$$= -\frac{\partial \mathscr{H}}{\partial \mathbf{v}[\phi]} \frac{\delta \mathbf{v}[\phi]}{\delta \phi} = -n(\mathbf{r}_R, t) \mathbf{v}(\mathbf{r}_R, t) \frac{\delta \mathbf{v}[\phi]}{\delta \phi}. \quad (2.45)$$

We now notice that by choosing ϕ such that it is the scalar potential of the transverse part of the velocity field $\mathbf{v}$, ie.

$$\mathbf{v}[\phi] = -\vec{\nabla}\phi(\mathbf{r}_R, t) + \mathbf{v}_{\rm rot}(\mathbf{r}_R, t) \tag{2.46}$$

where $\mathbf{v}_{\rm rot}(\mathbf{r}_R, t)$ is the rotational part of the velocity field, and substituting Eqn. (2.46) for $\mathbf{v}$ into the Hamiltonian given in Eqn. (2.41), the canonical equation for $\dot{n}$ yields

$$\frac{\partial n}{\partial t} = -\vec{\nabla} \cdot [n(\mathbf{r}_R, t)\mathbf{v}(\mathbf{r}_R, t)] \tag{2.47}$$

the continuity equation. Here we have performed an integration by parts of the integrand as described by Lurie [197]. Since the electron fluid is confined to the 2D cylinder, we note that the radial components of both the velocity field $\mathbf{v}$, and hence the rotational part of the velocity field $\mathbf{v}_{\rm rot}$ are identically zero from Eqn. (2.46). Further, since both Eqns. (2.46) and (2.47) are evaluated on the 2D cylinder, the gradient operators in both these equations effectively act tangentially to the 2D cylindrical surface.

The second canonical equation for ϕ, as described in Goldstein [195] and Lurie [197] gives

$$\begin{aligned}\frac{\partial \phi}{\partial t} &= \frac{\delta H}{\delta n} = \frac{\partial \mathscr{H}}{\partial n} - \vec{\nabla} \cdot \frac{\partial \mathscr{H}}{\partial \vec{\nabla} n} \\ &= \frac{1}{2}\|\mathbf{v}\|^2 + V_{\rm ext}(\mathbf{r}_R, t) + \pi n(\mathbf{r}_R, t) + \iint d^2\mathbf{r}'_R \, \frac{n(\mathbf{r}'_R, t)}{\|\mathbf{r}_R - \mathbf{r}'_R\|} + \frac{1}{8}\frac{\|\vec{\nabla} n\|^2}{n^2} - \frac{1}{4}\frac{\nabla^2 n}{n}. \end{aligned} \tag{2.48}$$

Substituting Eqn. (2.46) for $\vec{\nabla}\phi$ into the canonical Eqn. (2.48) yields the momentum-balance equation from Eguiluz [198] on the cylinder

$$\begin{aligned}\frac{\partial \mathbf{v}}{\partial t} + (\mathbf{v} \cdot \vec{\nabla})\mathbf{v} = &-\pi\vec{\nabla} n(\mathbf{r}_R, t) - \vec{\nabla} V_{\rm ext}(\mathbf{r}_R, t) + \vec{\nabla}\left[\frac{1}{4}\frac{\nabla^2 n}{n} - \frac{1}{8}\frac{\|\vec{\nabla} n\|^2}{n^2}\right] \\ &-\vec{\nabla}\iint d^2\mathbf{r}'_R \, \frac{n(\mathbf{r}'_R, t)}{\|\mathbf{r}_R - \mathbf{r}'_R\|} + \frac{\partial \mathbf{v}_{\rm rot}}{\partial t} - \mathbf{v} \times (\vec{\nabla} \times \mathbf{v}_{\rm rot}), \end{aligned} \tag{2.49}$$

where we have used the identity

$$\frac{1}{2}\vec{\nabla}(\mathbf{v} \cdot \mathbf{v}) = (\mathbf{v} \cdot \vec{\nabla})\mathbf{v} + \mathbf{v} \times (\vec{\nabla} \times \mathbf{v}). \tag{2.50}$$

By now setting the rotational part of the velocity field, $\mathbf{v}_{\rm rot}(\mathbf{r}_R,t)$, equal to $\frac{1}{c}\mathbf{A}(\mathbf{r}_R,t)$ where $\mathbf{A}(\mathbf{r}_R,t)$ is the vector potential, as done by Eguiluz [198], we obtain the electric field $\mathbf{E}$ and magnetic field $\mathbf{B}$ in Eqn. (2.49), so that

$$\frac{d\mathbf{v}}{dt} = -\vec{\nabla}V_{\rm ext}(\mathbf{r}_R,t) - \left(\mathbf{E} + \frac{1}{c}\mathbf{v}\times\mathbf{B}\right) - \pi\vec{\nabla}n(\mathbf{r}_R,t) + \vec{\nabla}\left[\frac{1}{4}\frac{\nabla^2 n}{n} - \frac{1}{8}\frac{\|\vec{\nabla}n\|^2}{n^2}\right], \quad (2.51)$$

In terms of the density functional $F[n]$ we have

$$\frac{d\mathbf{v}}{dt} = -\vec{\nabla}V_{\rm ext}(\mathbf{r}_R,t) - \vec{\nabla}\frac{\delta F[n]}{\delta n} + \frac{1}{c}\frac{\partial\mathbf{A}}{\partial t} - \frac{1}{c}\mathbf{v}\times\mathbf{B}. \quad (2.52)$$

2.3 Perturbative Expansions

The external potential $V_{\rm ext}$ is the potential energy per electron in fields *external to the electron gas*. As such, it is the sum of the confining potential $-\Phi_{\rm at}(\mathbf{r})$, arising from the positive background, and the electric potential $-\Phi_{\rm ext}(\mathbf{r},t)$ *external to the system*. The time-independent confining potential $\Phi_{\rm at}(\mathbf{r})$ puts the system in equilibrium, while the time-dependent potential $\Phi_{\rm ext}(\mathbf{r},t)$ perturbs the system away from equilibrium, so long as on the cylinder $r=R$, $|\Phi_{\rm ext}| \ll |\Phi_{\rm at}|$. This is indeed the case when $\Phi_{\rm ext}(\mathbf{r},t)$ is the Coulomb potential of an external channelled ion, for example.

We now introduce a "bookkeeping parameter" λ, which we use to denote terms of the same "order" as the perturbing potential $\Phi_{\rm ext}(\mathbf{r},t)$ external to the system. The external potential is then $V_{\rm ext}(\mathbf{r},t) = -\Phi_{\rm at}(\mathbf{r}) - \lambda\Phi_{\rm ext}(\mathbf{r},t)$, and we now assume that $\lambda\|\Phi_{\rm ext}(\mathbf{r}_R,t)\|_\infty \ll \|\Phi_{\rm at}(\mathbf{r}_R)\|_\infty$ at $r=R$ so that we may perform a regular perturbation theory expansion of the surface number density and velocity field in terms of the time-dependent perturbing potential $\lambda\Phi_{\rm ext}(\mathbf{r}_R,t)$, (or effectively λ), around the equilibrium number density per unit area $n_0(\mathbf{r}_R)$ and the equilibrium velocity $\mathbf{v}_0 = 0$, respectively. We thus obtain for the surface number density and velocity field

$$n(\mathbf{r}_R,t) = n_0(\mathbf{r}_R) + \lambda n_1(\mathbf{r}_R,t) + \lambda^2 n_2(\mathbf{r}_R,t) + \cdots, \quad (2.53)$$

$$\mathbf{v}(\mathbf{r}_R,t) = 0 + \lambda\mathbf{v}_1(\mathbf{r}_R,t) + \lambda^2\mathbf{v}_2(\mathbf{r}_R,t) + \cdots, \quad (2.54)$$

respectively. Here we have assumed that in equilibrium the electron gas has no velocity. We would need to have some equilibrium velocity, as done by Eguiluz [198], or a constant external

magnetic field $\mathbf{B}_0$, in order for there to be a linear order magnetic field contribution. We similarly expand the density functional derivative as

$$\frac{\delta F[n]}{\delta n} = \left[\frac{\delta F[n]}{\delta n}\right]_0 + \lambda \left[\frac{\delta F[n]}{\delta n}\right]_1 + \lambda^2 \left[\frac{\delta F[n]}{\delta n}\right]_2 + \cdots , \tag{2.55}$$

where we have used $\left[\frac{\delta F[n]}{\delta n}\right]_N$ to denote the $\mathcal{O}(\lambda^N)$ coefficient of the density functional derivative. We will denote the $\mathcal{O}(\lambda^N)$ coefficient of the electron charge density per unit volume by $\rho_N(\mathbf{r}, t)$, which is related to the surface number density by $\rho_N(\mathbf{r}, t) = -n_N(\mathbf{r}_R, t)\delta(r - R)$.

Equilibrium Equation

In the 2D hydrodynamic model, we employ the jellium approximation, so that the equilibrium density n_0 is assumed to be constant along the length and around the nanotube. We further consider the nanotube electrons to be confined to a thin cylindrical shell, so that the equilibrium charge density per unit volume has the form $\rho_0(\mathbf{r}) = -n_0\delta(r - R)$, where R is the nanotube radius and n_0 is a constant. The equilibrium surface density n_0 is then obtained from the $\mathcal{O}(1)$ equation

$$0 = \vec{\nabla}\left(\left[\frac{\delta F[n]}{\delta n}\right]_0 - \Phi_{\rm at}\right). \tag{2.56}$$

Taking the gradient on the cylinder of the functional derivative of Eqn. (2.39) for the 2D density functional $F[n]$, we find from Poisson's equation,

$$\vec{\nabla}\left[\frac{\delta F[n]}{\delta n}\right]_0 = n_0\vec{\nabla}\iint \frac{d^2\mathbf{r}'_R}{\|\mathbf{r}_R - \mathbf{r}'_R\|}. \tag{2.57}$$

We now model the confining potential $\Phi_{\rm at}$ using the jellium approximation, so that the positive ionic background charge is confined to the same thin cylindrical shell and has atomic density $\sigma_a \approx 0.107$ and $Z_{\rm C}$ valence electrons per carbon atom. Poisson's equation for the confining potential then yields throughout the volume

$$\nabla^2\Phi_{\rm at}(\mathbf{r}) = -4\pi Z_{\rm C}\sigma_a\delta(r - R), \tag{2.58}$$

$$\vec{\nabla}\Phi_{\rm at}(\mathbf{r}_R) = Z_{\rm C}\sigma_a\vec{\nabla}\iint \frac{d^2\mathbf{r}'_R}{\|\mathbf{r}_R - \mathbf{r}'_R\|}. \tag{2.59}$$

Substituting Eqns. (2.57) and (2.59) into the $\mathcal{O}(1)$ equation, we find that the equilibrium charge density per unit volume is $\rho_0(r) = -Z_{\mathrm{C}}\sigma_a\delta(r-R)$, where Z_{C} is the number of valence electrons per atom in the electron gas.

Linear Equations

We are interested in studying the electronic response to the perturbing potential, and the linear order corrections to the number density n_1 and velocity $\mathbf{v}_1$. These are the solutions to the $\mathcal{O}(\lambda)$ equations

$$\frac{\partial^2 n_1}{\partial t^2} = \vec{\nabla}\cdot\left[n_0\vec{\nabla}\left(\left[\frac{\delta F[n]}{\delta n}\right]_1 - \Phi_{\mathrm{ext}}\right)\right], \tag{2.60}$$

$$\frac{\partial \mathbf{v}_1}{\partial t} = -\vec{\nabla}\left(\left[\frac{\delta F[n]}{\delta n}\right]_1 - \Phi_{\mathrm{ext}}\right). \tag{2.61}$$

Taking the functional derivative of Eqn. (2.39) for the 2D density functional $F[n]$ to $\mathcal{O}(\lambda)$, we find

$$\left[\frac{\delta F[n]}{\delta n}\right]_1 = \pi n_1 - \frac{1}{4}\frac{\nabla^2 n_1}{n_0} + \iint d^2\mathbf{r}'_R\,\frac{n_1(\mathbf{r}'_R,t)}{\|\mathbf{r}_R-\mathbf{r}'_R\|}. \tag{2.62}$$

Letting $\Phi(\mathbf{r},t)$ be the total electric potential, we find that

$$\Phi(\mathbf{r},t) = \Phi_{\mathrm{ext}}(\mathbf{r},t) + \iiint d^3\mathbf{r}'\,\frac{\rho_1(\mathbf{r}',t)}{\|\mathbf{r}-\mathbf{r}'\|}, \tag{2.63}$$

where $\rho_1(\mathbf{r},t) = -n_1(\mathbf{r}_R,t)\delta(r-R)$ is the linear order correction to the electron charge density per unit volume. The $\mathcal{O}(\lambda)$ equations then become

$$\frac{\partial^2 n_1}{\partial t^2} = -n_0\nabla^2\Phi(\mathbf{r}_R,t) + \pi n_0\nabla^2 n_1(\mathbf{r}_R,t) - \frac{1}{4}\nabla^2\nabla^2 n_1(\mathbf{r}_R,t) \tag{2.64}$$

$$\frac{\partial \mathbf{v}_1}{\partial t} = \vec{\nabla}\Phi(\mathbf{r}_R,t) - \pi\vec{\nabla}n_1(\mathbf{r}_R,t) + \frac{1}{4}\frac{\vec{\nabla}\nabla^2 n_1(\mathbf{r}_R,t)}{n_0} \tag{2.65}$$

$$\nabla^2\Phi(\mathbf{r},t) = -4\pi\rho_{\mathrm{ext}}(\mathbf{r},t) - 4\pi\rho_1(\mathbf{r},t), \tag{2.66}$$

where ρ_{ext} is the charge density external to the electron gas.

We now introduce into the momen-tum-balance equation (2.49) a frictional force $-\gamma\mathbf{v}_1$, to model scattering on the positive-charge background. Empirical values for the friction coefficient

γ are often quite significant, but for carbon nanotubes values for the friction coefficient are not readily available. For this reason we let the friction coefficient $\gamma \to 0^+$ numerically in order to facilitate the numerical integrations used to solve for $n_1(\mathbf{r}_R)$.

The coefficient of the Thomas-Fermi term $\alpha \equiv \pi n_0 = v_F^2/2$ is the square of the speed of propagation of density disturbances in the fluid, while we define the coefficient of the von Weizsäcker term as $\beta \equiv 1/4$. The $\mathcal{O}(\lambda)$ equations then simplify to

$$\frac{\partial^2 n_1}{\partial t^2} + \gamma \frac{\partial n_1}{\partial t} = -n_0 \nabla^2 \Phi(\mathbf{r}_R, t) + \alpha \nabla^2 n_1(\mathbf{r}_R, t) - \beta \nabla^2 \nabla^2 n_1(\mathbf{r}_R, t), \tag{2.67}$$

$$\frac{\partial \mathbf{v}_1}{\partial t} + \gamma \mathbf{v}_1 = \vec{\nabla} \Phi(\mathbf{r}_R, t) - \frac{\alpha}{n_0} \vec{\nabla} n_1(\mathbf{r}_R, t) + \beta \frac{\vec{\nabla} \nabla^2 n_1(\mathbf{r}_R, t)}{n_0}, \tag{2.68}$$

$$\nabla^2 \Phi(\mathbf{r}, t) = -4\pi \rho_{\text{ext}}(\mathbf{r}, t) - 4\pi \rho_1(\mathbf{r}, t). \tag{2.69}$$

Non-linear Equations

The generalized Nth order corrections to the number density n_N and velocity $\mathbf{v}_N$ for $N \geq 2$ are the solutions to the $\mathcal{O}(\lambda^N)$ equations

$$\frac{\partial^2 n_N}{\partial t^2} + \gamma \frac{\partial n_N}{\partial t} = \vec{\nabla} \cdot \left(n_0 \vec{\nabla} \left[\frac{\delta F[n]}{\delta n} \right]_N + \sum_{\ell=1}^{N-1} (\mathbf{v}_\ell \cdot \vec{\nabla}) \mathbf{v}_{N-\ell} - \sum_{\ell=1}^{N-1} \frac{\partial}{\partial t} n_\ell \mathbf{v}_{N-\ell} \right), \tag{2.70}$$

$$\frac{\partial \mathbf{v}_N}{\partial t} + \gamma \mathbf{v}_N = -\vec{\nabla} \left[\frac{\delta F[n]}{\delta n} \right]_N - \sum_{\ell=1}^{N-1} (\mathbf{v}_\ell \cdot \vec{\nabla}) \mathbf{v}_{N-\ell}. \tag{2.71}$$

We have thus written the number density and velocity field to arbitrary order in terms of the external potential $V_{\text{ext}} = -\Phi_{\text{at}} - \lambda \Phi_{\text{ext}}$ and the density functional $F[n]$. In the following chapter, we will solve the $\mathcal{O}(\lambda)$ equations for the linear order correction to the number density n_1 induced by an external potential, for a multiwalled carbon nanotube with dielectric media inside and outside.

Chapter 3

Electronic Response of Nanotubes

In Chapter 2, we obtained Eqns. (2.67) and (2.69) for the induced charge density per unit volume $\rho_1(\mathbf{r}, t)$ of an electron fluid confined to a 2D cylindrical shell. From the induced density, we may calculate all quantities relevant to the electron fluid's electronic response. These include the induced electric potential $\Phi_{\rm ind}(\mathbf{r}, t)$ due to an external charge perturbation $\rho_{\rm ext}(\mathbf{r}, t)$, the stopping force on the external charge, and the image potential (or self-energy) of the external charge. To solve Eqns. (2.67) and (2.69) for the induced density, we use the Fourier-Bessel transform.

3.1 Fourier-Bessel Transform

The solution to Poisson's equation, Eqn. (2.69), for the total electric potential $\Phi(\mathbf{r}, t)$, may be written in terms of the charge density $\rho_{\rm ext}(\mathbf{r}, t)$ *external to the electron gas*, the electron charge density per unit volume $\rho_1(\mathbf{r}, t)$ *induced on the electron gas*, and the Coulomb potential $\frac{1}{\|\mathbf{r}-\mathbf{r}'\|}$, as

$$\Phi(\mathbf{r}, t) = \iiint d^3\mathbf{r}' \, \frac{\rho_{\rm ext}(\mathbf{r}', t) + \rho_1(\mathbf{r}', t)}{\|\mathbf{r} - \mathbf{r}'\|}. \tag{3.1}$$

Since we are concerned only with the linear response of the electron density on a "thin" cylindrical shell of radius R_j, we introduce the induced electron number density per unit area on the jth cylindrical shell, $n_j(\varphi, z, t)$. We may express the electron charge density per unit volume induced on the electron gas, $\rho_1(\mathbf{r}, t)$, in terms of the electron density per unit area induced on the

jth cylindrical shell, $n_j(\varphi, z, t)$, as

$$\rho_1(\mathbf{r}, t) = -\delta(r - R_j) n_j(\varphi, z, t). \tag{3.2}$$

Using the method of Green's functions discussed by Jackson pp. 125–127 [199] and shown in detail in Appendix B, we find that the Coulomb potential may be written as a Fourier-Bessel transform,

$$\frac{1}{\|\mathbf{r} - \mathbf{r}'\|} = \sum_{m=-\infty}^{\infty} \int_{-\infty}^{\infty} \frac{dk}{(2\pi)^2} e^{im(\varphi - \varphi')} e^{ik(z-z')} g(r, r'; m, k) \tag{3.3}$$

where $g(r, r'; m, k)$ is the radial Green's function defined by

$$g(r, r'; m, k) \equiv 4\pi I_m(|k| r_<) K_m(|k| r_>), \tag{3.4}$$

with $r_> \equiv \max(r, r')$ and $r_< \equiv \min(r, r')$. We define the Fourier-Bessel (FB) transform $\widetilde{A}(r; m, k, \omega)$ of an arbitrary function $A(r, \varphi, z, t)$, by

$$A(r, \varphi, z, t) = \sum_{m=\infty}^{\infty} \int_{-\infty}^{\infty} \int_{-\infty}^{\infty} \frac{dk d\omega}{(2\pi)^3} e^{im\varphi + ikz - i\omega t} \widetilde{A}(r; m, k, \omega). \tag{3.5}$$

With these facts as motivation, we now take the FB transform of Eqn. (2.67) on the nanotube surface $r = R_j$, and obtain the constitutive algebraic equation

$$\omega^2 \widetilde{n}_j + i\gamma\omega \widetilde{n}_j = -n_j^0 \left(k^2 + \frac{m^2}{R_j^2} \right) \widetilde{\Phi} + \alpha_j \left(k^2 + \frac{m^2}{R_j^2} \right) \widetilde{n}_j + \beta \left(k^2 + \frac{m^2}{R_j^2} \right)^2 \widetilde{n}_j \tag{3.6}$$

for the FB transform of the induced electron density $\widetilde{n}_j$ and the total potential $\widetilde{\Phi}$, where $\alpha_j \equiv \pi n_j^0$ and n_j^0 is the equilibrium electron number density per unit area of the jth fluid. Taking the FB transform of Eqn. (3.1), we obtain for $\widetilde{\Phi}$

$$\widetilde{\Phi}(r; m, k, \omega) = \int_0^{\infty} g(r, r'; m, k) [r' \widetilde{\rho}_{\text{ext}}(r'; m, k, \omega) - \delta(r' - R_j) R_j \widetilde{n}_j(m, k, \omega)] dr'. \tag{3.7}$$

However, before Eqn. (3.6) may be solved for the induced electron density $\widetilde{n}_j$ on a cylinder of radius R_j, we must first solve for the FB transform of the charge density *external to the electron gas* $\widetilde{\rho}_{\text{ext}}$. This includes any perturbing charge density, the charge density induced by polarization of any dielectric media, and the charge density induced on other electron fluids in the system.

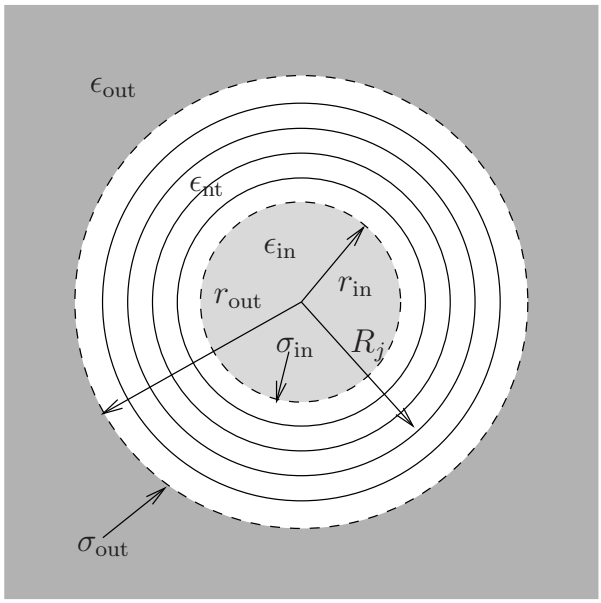

Figure 3.1: A MWNT with radii R_j and dielectric functions inside $r_{\rm in}$ of $\epsilon_{\rm in}(\omega)$, in the nanotube region between $r_{\rm in}$ and $r_{\rm out}$ of $\epsilon_{\rm nt}(\omega)$, and outside $r_{\rm out}$ of $\epsilon_{\rm out}(\omega)$. The polarization charges on the inner and outer dielectric boundaries are denoted by $\sigma_{\rm in}$ and $\sigma_{\rm out}$ respectively.

3.2 Incorporation of Dielectric Media

As shown in Fig. 3.1, our MWNT model consists of N cylindrical shells of radii R_j embedded in a medium with dielectric function $\epsilon_{\rm nt}(\omega)$ encompassing the region $r_{\rm in} \leq r \leq r_{\rm out}$. The inner region has dielectric function $\epsilon_{\rm in}(\omega)$ for $r < r_{\rm in}$, while the outer region has dielectric function $\epsilon_{\rm out}(\omega)$ for $r > r_{\rm out}$. Consequently, our system has two dielectric boundaries at $r_{\rm in}$ and $r_{\rm out}$ with surface polarization charge densities $\sigma_{\rm in}$ and $\sigma_{\rm out}$, respectively. We first consider the situation at the inner boundary.

Considering the case of no free charges on either boundary, and integrating Gauss' Law for the electric field, $\vec{\nabla} \cdot \mathbf{E} = 4\pi\rho$, the total electric potential $\Phi(\mathbf{r}, \omega)$ satisfies

$$\left.\frac{\partial \Phi}{\partial r}\right|_{r_{\rm in}^+} - \left.\frac{\partial \Phi}{\partial r}\right|_{r_{\rm in}^-} = -4\pi\sigma_{\rm in}, \tag{3.8}$$

where $\rho = \sigma_{\rm in}(\varphi, z, \omega)\delta(r - r_{\rm in})$ is the total charge density on the inner boundary. Similarly, we may integrate Gauss' Law for the electric displacement field, $\vec{\nabla} \cdot \mathbf{D} = 4\pi\rho_f$, where $\mathbf{D} \equiv \epsilon(\mathbf{r}, \omega)\mathbf{E}$

and $\rho_f = 0$ is the total *free* charge density on the inner boundary, to obtain

$$\epsilon_{\rm nt}(\omega)\left.\frac{\partial\Phi}{\partial r}\right|_{r_{\rm in}^+} - \epsilon_{\rm in}(\omega)\left.\frac{\partial\Phi}{\partial r}\right|_{r_{\rm in}^-} = 0. \tag{3.9}$$

The total electric potential is the work done to move a test charge at infinity to a position $\mathbf{r}$. For this reason, we require that the total electric potential be continuous across the inner boundary,

$$\Phi(r_{\rm in}^-, \varphi, z, \omega) = \Phi(r_{\rm in}^+, \varphi, z, \omega). \tag{3.10}$$

Following the method of Doerr and Yu [150], we now decompose the total electric potential into the sum of the screened external perturbing potential $\Phi_{\rm sc}$ (as defined in Sect. 4.3), the induced potential from the nanotube $\Phi_{\rm nt}$, the potential due to the polarization charge on the inner boundary $\Phi_{\rm in}$, and the potential due to the polarization charge on the outer boundary $\Phi_{\rm out}$, so that

$$\Phi = \Phi_{\rm sc} + \Phi_{\rm nt} + \Phi_{\rm in} + \Phi_{\rm out}. \tag{3.11}$$

Since each potential is uniquely defined only in a region for which it is a solution to Poisson's Equation, we choose each component of the total potential to be continuous across the boundaries, so that the continuity condition (3.10) is satisfied by construction. Further, defining $\Phi_{\rm in}$ to satisfy (3.8)

$$\left.\frac{\partial\Phi_{\rm in}}{\partial r}\right|_{r_{\rm in}^+} - \left.\frac{\partial\Phi_{\rm in}}{\partial r}\right|_{r_{\rm in}^-} = -4\pi\sigma_{\rm in}, \tag{3.12}$$

and Poisson's Equation $\nabla^2\Phi_{\rm in} = -4\pi\sigma_{\rm in}(\varphi, z, \omega)\delta(r - r_{\rm in})$, we may write the potential due to the polarization charge on the inner boundary as

$$\Phi_{\rm in}(\mathbf{r}, \omega) = \int dr' \int d\varphi' \int dz' \frac{r'\sigma_{\rm in}(\varphi', z', \omega)\delta(r' - r_{\rm in})}{\|\mathbf{r} - \mathbf{r}'\|}. \tag{3.13}$$

This choice of $\Phi_{\rm in}$ ensures that the total electric potential satisfies Eqn. (3.8). By applying Eqn. (3.9), we may now find an expression for $\sigma_{\rm in}$ (and hence $\Phi_{\rm in}$), in terms of the remaining potentials. Working with the Fourier-Bessel (FB) transform of the Green's function in cylindrical coordinates given in Eqn. (3.3), the FB transform of $\Phi_{\rm in}(\mathbf{r}, \omega)$ is

$$\widetilde{\Phi}_{\rm in} = r_{\rm in} g(r, r_{\rm in}; m, k)\widetilde{\sigma}_{\rm in}(m, k, \omega), \tag{3.14}$$

where $\widetilde{\sigma}_{\rm in}$ is the FB transform of the polarization charge on the inner boundary.

Substituting (3.14) via (3.11) into (3.9) we obtain for the FB transform of the polarization charge

$$\widetilde{\sigma}_{\rm in} = \mathcal{R}_{\rm in}\frac{\partial}{\partial r}\left[\widetilde{\Phi}_{\rm sc} + \widetilde{\Phi}_{\rm nt} + \widetilde{\Phi}_{\rm out}\right]_{r_{\rm in}}, \tag{3.15}$$

where

$$\mathcal{R}_{\rm in} \equiv \frac{\epsilon_{\rm nt} - \epsilon_{\rm in}}{4\pi[\epsilon_{\rm nt} - (\epsilon_{\rm nt} - \epsilon_{\rm in})\kappa_{\rm in} I'_m(|\kappa_{\rm in}|)K_m(|\kappa_{\rm in}|)]} \tag{3.16}$$

is defined to be the response function of the polarization charge due to the external electric field in the radial direction on the inner boundary, and $\kappa_{\rm in} \equiv kr_{\rm in}$.

Applying an analogous procedure on the outer boundary yields for the FB transform of the polarization charge on that boundary

$$\widetilde{\sigma}_{\rm out} = \mathcal{R}_{\rm out}\frac{\partial}{\partial r}\left[\widetilde{\Phi}_{\rm sc} + \widetilde{\Phi}_{\rm nt} + \widetilde{\Phi}_{\rm in}\right]_{r_{\rm out}}, \tag{3.17}$$

where

$$\mathcal{R}_{\rm out} \equiv \frac{\epsilon_{\rm out} - \epsilon_{\rm nt}}{4\pi[\epsilon_{\rm nt} + (\epsilon_{\rm nt} - \epsilon_{\rm out})\kappa_{\rm out} I_m(|\kappa_{\rm out}|)K'_m(|\kappa_{\rm out}|)]}, \tag{3.18}$$

and $\kappa_{\rm out} \equiv kr_{\rm out}$.

Let us denote the induced electron number density per unit area on the jth cylindrical shell of radius R_j of a MWNT by $n_j(\varphi, z, \omega)$, so that the electric potential due to the nanotube satisfies Poisson's Equation $\nabla^2\Phi_{\rm nt} = 4\pi\sum_j n_j(\varphi, z, \omega)\delta(r - R_j)$. Integrating Gauss' Law for the electric displacement field, $\vec{\nabla}\cdot\mathbf{D} = 4\pi\rho_f$, at R_j yields the boundary condition

$$\epsilon_{\rm nt}(\omega)\frac{\partial\Phi_{\rm nt}}{\partial r}\bigg|_{R_j^+} - \epsilon_{\rm nt}(\omega)\frac{\partial\Phi_{\rm nt}}{\partial r}\bigg|_{R_j^-} = 4\pi n_j. \tag{3.19}$$

The FB transform of $\Phi_{\rm nt}(\mathbf{r}, \omega)$ may now be written as

$$\widetilde{\Phi}_{\rm nt} = -\frac{1}{\epsilon_{\rm nt}(\omega)}\sum_j R_j g(r, R_j; m, k)\widetilde{n}_j(m, k, \omega), \tag{3.20}$$

where $\widetilde{n}_j$ is the FB transform of the induced electron number density n_j.

Solving the coupled equations (3.15) and (3.17) in terms of $\widetilde{n}_j$ using (3.20) and $\dfrac{\partial\widetilde{\Phi}_{\rm sc}}{\partial r}$, we obtain

$$\widetilde{\sigma}_{\rm in} = \widetilde{\sigma}^{\rm sc}_{\rm in} - \sum_\ell \frac{\widetilde{n}_\ell}{\varepsilon^\ell_{\rm in}}, \quad \text{and} \quad \widetilde{\sigma}_{\rm out} = \widetilde{\sigma}^{\rm sc}_{\rm out} - \sum_\ell \frac{\widetilde{n}_\ell}{\varepsilon^\ell_{\rm out}}, \tag{3.21}$$

where $\widetilde{\sigma}^{\rm sc}_{\rm in}$ and $\widetilde{\sigma}^{\rm sc}_{\rm out}$ are the polarization charges due to the external charge on the inner and outer boundaries respectively and $\varepsilon^\ell_{\rm in}$ and $\varepsilon^\ell_{\rm out}$ behave as dielectric constants for the polarization charge on the inner and outer boundaries respectively due to the induced charge on the ℓth cylinder $\widetilde{n}_\ell$. We express the polarization charges due to the external charge as

$$\widetilde{\sigma}^{\rm sc}_{\rm in} \equiv \frac{\mathcal{R}_{\rm in}\frac{\partial\widetilde{\Phi}_{\rm sc}}{\partial r}|_{r_{\rm in}} + \mathcal{R}_{\rm in}\mathcal{R}_{\rm out}r_{\rm out}g'(r_{\rm in},r_{\rm out})\frac{\partial\widetilde{\Phi}_{\rm sc}}{\partial r}|_{r_{\rm out}}}{1 - r_{\rm out}g'(r_{\rm in},r_{\rm out})r_{\rm in}g'(r_{\rm out},r_{\rm in})\mathcal{R}_{\rm in}\mathcal{R}_{\rm out}}, \tag{3.22}$$

$$\widetilde{\sigma}^{\rm sc}_{\rm out} \equiv \frac{\mathcal{R}_{\rm out}\frac{\partial\widetilde{\Phi}_{\rm sc}}{\partial r}|_{r_{\rm out}} + \mathcal{R}_{\rm in}\mathcal{R}_{\rm out}r_{\rm in}g'(r_{\rm out},r_{\rm in})\frac{\partial\widetilde{\Phi}_{\rm sc}}{\partial r}|_{r_{\rm in}}}{1 - r_{\rm out}g'(r_{\rm in},r_{\rm out})r_{\rm in}g'(r_{\rm out},r_{\rm in})\mathcal{R}_{\rm in}\mathcal{R}_{\rm out}}, \tag{3.23}$$

where $g'(r_1,r_2)$ is the derivative of the radial Green's function $g(r_1,r_2;m,k)$ with respect to the first argument r_1 and where we have dropped the labels m and k. We define $\varepsilon^\ell_{\rm in}$ and $\varepsilon^\ell_{\rm out}$ as

$$\varepsilon^\ell_{\rm in} \equiv \frac{\epsilon_{\rm nt}[\mathcal{R}^{-1}_{\rm in}\mathcal{R}^{-1}_{\rm out} - r_{\rm out}g'(r_{\rm in},r_{\rm out})r_{\rm in}g'(r_{\rm out},r_{\rm in})]}{\mathcal{R}^{-1}_{\rm out}R_\ell g'(r_{\rm in},R_\ell) + r_{\rm out}g'(r_{\rm in},r_{\rm out})R_\ell g'(r_{\rm out},R_\ell)}, \tag{3.24}$$

$$\varepsilon^\ell_{\rm out} \equiv \frac{\epsilon_{\rm nt}[\mathcal{R}^{-1}_{\rm in}\mathcal{R}^{-1}_{\rm out} - r_{\rm out}g'(r_{\rm in},r_{\rm out})r_{\rm in}g'(r_{\rm out},r_{\rm in})]}{\mathcal{R}^{-1}_{\rm in}R_\ell g'(r_{\rm out},R_\ell) + r_{\rm in}g'(r_{\rm out},r_{\rm in})R_\ell g'(r_{\rm in},R_\ell)}. \tag{3.25}$$

3.3 Nanotube's Induced Electron Density

Following the procedure of solution described by Doerr and Yu [150], so that $\Phi = \Phi_{\rm sc} + \Phi_{\rm nt} + \Phi_{\rm in} + \Phi_{\rm out}$ from Eqn. (3.11), we may now write the FB transform of the total electric potential in terms of the induced electron density on the ℓth fluid as

$$\begin{aligned}\widetilde{\Phi}(R_j) = \widetilde{\Phi}_{\rm sc} &- \sum_\ell \frac{R_\ell}{\epsilon_{\rm nt}}g(R_j,R_\ell)\widetilde{n}_\ell + r_{\rm in}g(R_j,r_{\rm in})\widetilde{\sigma}^{\rm sc}_{\rm in} - \sum_\ell \frac{r_{\rm in}}{\varepsilon^\ell_{\rm nt}}g(R_j,r_{\rm in})\widetilde{n}_\ell \\ &+ r_{\rm out}g(R_j,r_{\rm out})\widetilde{\sigma}^{\rm sc}_{\rm out} - \sum_\ell \frac{r_{\rm out}}{\varepsilon^\ell_{\rm nt}}g(R_j,r_{\rm out})\widetilde{n}_\ell.\end{aligned} \tag{3.26}$$

We obtain by substituting Eqn. (3.26) into the constitutive equation for the jth cylinder, Eqn. (3.6), a system of N coupled equations

$$\sum_{\ell}\left[\delta_{j\ell}\chi_j^{-1}+\frac{R_\ell}{\epsilon_{\rm nt}}g(R_j,R_\ell)+\frac{r_{\rm in}}{\varepsilon_{\rm in}^{\ell}}g(R_j,r_{\rm in})+\frac{r_{\rm out}}{\varepsilon_{\rm out}^{\ell}}g(R_j,r_{\rm out})\right]\widetilde{n}_\ell$$
$$=\widetilde{\Phi}_{\rm sc}(R_j)+r_{\rm in}g(R_j,r_{\rm in})\widetilde{\sigma}_{\rm in}^{\rm sc}+r_{\rm out}g(R_j,r_{\rm out})\widetilde{\sigma}_{\rm out}^{\rm sc}, \tag{3.27}$$

where χ_j is the response function of the induced number density of the jth fluid to the total electric potential, $\widetilde{n}_j=\chi_j\widetilde{\Phi}$, defined by

$$\chi_j\equiv\frac{n_j^0(k^2+m^2/R_j^2)}{\alpha_j(k^2+m^2/R_j^2)+\beta(k^2+m^2/R_j^2)^2-\omega^2-i\gamma\omega}, \tag{3.28}$$

where we take the limit $\gamma\to 0^+$. We will also find it useful to write Eqn. (3.27) as a matrix equation of the form

$$\mathbf{\mathcal{M}}\widetilde{\mathbf{n}}=\widetilde{\mathbf{\Phi}}, \tag{3.29}$$

where

$$\mathcal{M}_{j\ell}\equiv\chi_j^{-1}\delta_{j\ell}+\frac{R_\ell}{\epsilon_{\rm nt}}g(R_j,R_\ell)+\frac{r_{\rm in}}{\varepsilon_{\rm in}^{\ell}}g(R_j,r_{\rm in})+\frac{r_{\rm out}}{\varepsilon_{\rm out}^{\ell}}g(R_j,r_{\rm out}), \tag{3.30}$$
$$\widetilde{\Phi}_j\equiv\widetilde{\Phi}_{\rm sc}(R_j)+r_{\rm in}g(R_j,r_{\rm in})\widetilde{\sigma}_{\rm in}^{\rm sc}+r_{\rm out}g(R_j,r_{\rm out})\widetilde{\sigma}_{\rm out}^{\rm sc}. \tag{3.31}$$

Finally, once the external perturbing potential is defined, combining Eqn. (3.27) with the definitions (3.22) and (3.23) of $\widetilde{\sigma}_{\rm in}^{\rm sc}$ and $\widetilde{\sigma}_{\rm out}^{\rm sc}$ respectively, gives a "material" equation to be solved for the induced electron densities $\widetilde{n}_j$ in terms of the screened external potential. Using Eqns. (3.20) and (3.21), along with Eqn. (3.14) and its counterpart on the outer boundary, we may then find the total induced potential throughout the system.

Chapter 4

Ion Channelling through Nanotubes

In the following chapter, we apply the 2D hydrodynamic model for the electronic response of CNTs, developed in Chapters 2 and 3, to ion channelling through CNTs. In other words, we will be modelling an ion beam incident on the CNT in a direction approximately parallel to the nanotube axis.

Although not yet realized experimentally, several studies have already been made of ion channelling through CNTs, bundles, and ropes [7, 8, 87, 88, 89, 200, 201, 202, 203], predicting its feasibility and advantages when compared with traditional single crystal channelling methods. Because atoms in a single crystal typically are densely packed, ions channelled through the crystal will eventually undergo Rutherford scattering or energy losses which force the ion out of the channel. This is often called the *dechannelling* process. However, CNTs have much wider channels (~ 14 Å), when compared with crystal lattices. This should mean a weaker dechannelling process, and hence longer channelling distances will be observed in CNTs when compared with single crystal channels. This also means that CNTs should have a wider acceptance angle (~ 1 rad), and require lower minimum ion energies ($\lesssim 100$ eV). Finally, the ability of CNTs to bend should allow for full 3D control of the incoming ion beam's deflection, something which is not possible with the planar channelling of bent single crystals.

The potential applications of ion channelling through CNTs include the creation and transport of highly focused nanoscale ion beams and their use for ion implantation and manufacturing of electronics at the nanoscale, targeted drug delivery and radiation therapy in medicine at the cellular level, manipulation of low-energy ions in plasma deposition technologies, control of

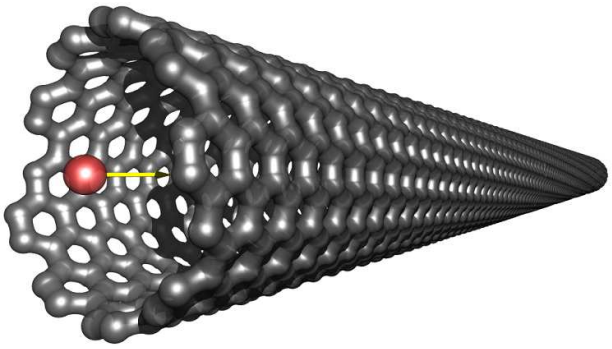

Figure 4.1: Schematic of ion channelling through an (11,9) nanotube.

molecular transport in biological research, and the extraction, steering and collimation of ion beams from high-energy particle accelerators [204].

To model ions being channelled through a CNT, shown schematically in Fig. 4.1, we consider the screened external potential in Eqn. (3.27) to be due to an ion of charge Q moving parallel to the nanotube axis with speed v at position $\mathbf{r}_0 = \{r_0, \varphi_0, vt\}$, having intermediate energy of ~ 1 MeV. This yields a FB transform of the screened external potential of

$$\widetilde{\Phi}_{\rm sc}(r; m, k, \omega) = \frac{2\pi}{\epsilon_{\rm nt}(\omega)} Q g(r, r_0; m, k) \delta(\omega - kv) e^{-im\varphi_0}. \tag{4.1}$$

However, before calculating the electronic response of CNTs to channelled ions, we calculate the intrinsic properties of a nanotube-dielectric system given via plasmon hybridization.

4.1 Plasmon Dispersion

A plasmon is the quantum or quasi-particle of collective oscillation of an electron fluid's charge density. The plasmon energies of a system may be calculated via a dispersion relation between the frequency ω, or plasma frequency, and the angular and longitudinal wave numbers m and k respectively. This dispersion relation yields the plasma frequencies ω, or plasmon energies $\hbar\omega$, at which "peaks" occur in the induced charge density in Eqn. (3.27), or simply the normalized intensity as shown in Fig. 1.2. The dispersion relation is obtained by letting $\gamma = 0$ and setting the denominator of $\mathfrak{M}^{-1}\widetilde{\mathbf{\Phi}}$ from Eqn. (3.29) equal to zero, giving

$$\det|\mathfrak{M}|[\mathcal{R}_{\rm in}^{-1}\mathcal{R}_{\rm out}^{-1} - r_{\rm out} g'(r_{\rm in}, r_{\rm out}) r_{\rm in} g'(r_{\rm out}, r_{\rm in})] = 0 \tag{4.2}$$

where from Eqns. (3.16) and (3.18)

$$\mathcal{R}_{\rm in}^{-1} = \frac{4\pi}{\epsilon_{\rm nt}-\epsilon_{\rm in}}\left[\epsilon_{\rm nt} - (\epsilon_{\rm nt}-\epsilon_{\rm in}|\kappa_{\rm in}|I'_m(|\kappa_{\rm in}|)K_m(|\kappa_{\rm out}|)\right], \tag{4.3}$$

$$\mathcal{R}_{\rm out}^{-1} = \frac{4\pi}{\epsilon_{\rm out}-\epsilon_{\rm nt}}\left[\epsilon_{\rm nt} + (\epsilon_{\rm nt}-\epsilon_{\rm out}|\kappa_{\rm out}|I_m(|\kappa_{\rm out}|)K'_m(|\kappa_{\rm out}|)\right], \tag{4.4}$$

with $\kappa_{\rm in} \equiv kr_{\rm in}$ and $\kappa_{\rm out} \equiv kr_{\rm out}$.

SWNTs with Dielectrics

We now restrict consideration to a SWNT. Using the two-fluid hydrodynamic model [64, 65, 70, 66, 67, 68] we consider the CNT to consist of π and σ fluids superimposed on the cylinder $r = R$ (we take $R = 7$ Å throughout) with equilibrium densities per unit area $n_\pi^0 \approx 0.107$ and $n_\sigma^0 \approx 0.321$ respectively. Bose and Longe [56] have shown that such classical models give results in agreement with RPA models when $1 \ll k_F R$, where $k_F = \sqrt{2\pi n_0}$ is the Fermi momentum. For the CNT system we shall consider, we find $k_F R \approx 22$, which justifies our use of the hydrodynamic model. Equation (3.27) then simplifies to

$$\widetilde{n}_1 = \frac{\widetilde{\Phi}_{\rm sc}(R) + r_{\rm in}g(R,r_{\rm in})\widetilde{\sigma}_{\rm in}^{\rm sc} + r_{\rm out}g(R,r_{\rm out})\widetilde{\sigma}_{\rm out}^{\rm sc}}{\chi^{-1} + \frac{R}{\epsilon_{\rm nt}}g(R,R) + \frac{r_{\rm in}}{\varepsilon_{\rm in}}g(R,r_{\rm in}) + \frac{r_{\rm out}}{\varepsilon_{\rm out}}g(R,r_{\rm out})}, \tag{4.5}$$

where $\chi = \chi_\pi + \chi_\sigma$ is the two-fluid response function and $\widetilde{n}_1 = \widetilde{n}_\pi + \widetilde{n}_\sigma$ is the sum of the induced electron densities of each fluid.

We may obtain from (4.5) a plasmon dispersion relation for ω in terms of the plasmon energies $\Omega_{\rm w}$ and $\Omega_{\rm c}$ for a Drude metal wire and channel respectively, with $\epsilon = 1 - {}^{\omega_p^2}/_{\omega^2}$, [44]

$$\Omega_{\rm w}^2 = +\omega_p^2|\kappa|\varrho_{\rm in}I'_m(|\kappa|\varrho_{\rm in})K_m(|\kappa|\varrho_{\rm in}) \tag{4.6}$$

$$\Omega_{\rm c}^2 = -\omega_p^2|\kappa|\varrho_{\rm out}I_m(|\kappa|\varrho_{\rm out})K'_m(|\kappa|\varrho_{\rm out}) \tag{4.7}$$

and the plasmon energies ω_+ and ω_- for the $\sigma+\pi$ and π branches respectively of a CNT obtained from the two-fluid model, [68]

$$\omega_\pm^2 = \left(\frac{\omega_\pi^2+\omega_\sigma^2}{2}\right) \pm \sqrt{\left(\frac{\omega_\pi^2-\omega_\sigma^2}{2}\right)^2 + \Delta^2}, \tag{4.8}$$

where

$$\omega_{\pi,\sigma}^2 = \Omega_{\pi,\sigma}^2(\kappa^2+m^2)\left[\frac{1}{4R}+\beta\frac{\kappa^2+m^2}{\Omega_{\pi,\sigma}^2R^4}+I_m(|\kappa|)K_m(|\kappa|)\right] \tag{4.9}$$

are respectively the plasmon energies of the non-interacting π and σ fluids, whereas

$$\Delta = \Omega_\pi\Omega_\sigma(\kappa^2+m^2)I_m(|\kappa|)K_m(|\kappa|) \tag{4.10}$$

gives the electrostatic interaction between those fluids, with $\Omega_{\pi,\sigma} = \sqrt{4\pi n_{\pi,\sigma}^0/R}$, and $\kappa \equiv kR$.

The dispersion relations for a CNT encapsulating a metallic wire or encapsulated by a metallic channel are then

$$(\omega^2-\Omega^2)\Omega_{\rm p}^2\Omega_{\rm w}^2(\kappa^2+m^2)I_m(|\kappa|\varrho_{\rm in})K_m^2(|\kappa|)/K_m(|\kappa|\varrho_{\rm in}) = (\omega^2-\Omega_{\rm w}^2)(\omega^2-\omega_+^2)(\omega^2-\omega_-^2) \tag{4.11}$$

and

$$(\omega^2-\Omega^2)\Omega_{\rm p}^2\Omega_{\rm c}^2(\kappa^2+m^2)I_m^2(|\kappa|)K_m(|\kappa|\varrho_{\rm out})/I_m(|\kappa|\varrho_{\rm out}) = (\omega^2-\Omega_{\rm c}^2)(\omega^2-\omega_+^2)(\omega^2-\omega_-^2), \tag{4.12}$$

respectively, where

$$\Omega^2 = \frac{\Omega_\pi^2\Omega_\sigma^2}{2R\Omega_{\rm p}^2}(\kappa^2+m^2)+\frac{\beta}{R^4}(\kappa^2+m^2)^2 \tag{4.13}$$

and $\Omega_{\rm p}^2 = \Omega_\pi^2+\Omega_\sigma^2 = 4\pi n_0/R$ with $n_0 = n_\pi^0+n_\sigma^0 \approx 0.428$ being the equilibrium number density per unit area of carbon valence electrons in graphene.

Figure 4.2 is an energy-level diagram of plasmon hybridization in a composite nanotube and metal wire/channel system, explained in three stages. First, plasmon hybridization occurs in the nanotube between the σ and π electron fluids, with frequencies ω_π and ω_σ respectively from (4.8), yielding the $\sigma+\pi$ and π plasmons, with frequencies ω_+ and ω_- respectively from (4.9), as shown in Fig. 4.3(a) [68]. Second, plasmon hybridization occurs between the $\sigma+\pi$ nanotube plasmon and the metal wire/channel plasmon branches with frequencies $\Omega_{\rm w/c}$ from (4.6) and (4.7) respectively as shown in Fig. 4.3(b), yielding antisymmetrically coupled (antibonding) and symmetrically coupled (bonding) metal-$(\sigma+\pi)$ plasmons with frequencies $\omega_{\rm D+}^a$ and $\omega_{\rm D+}^s$

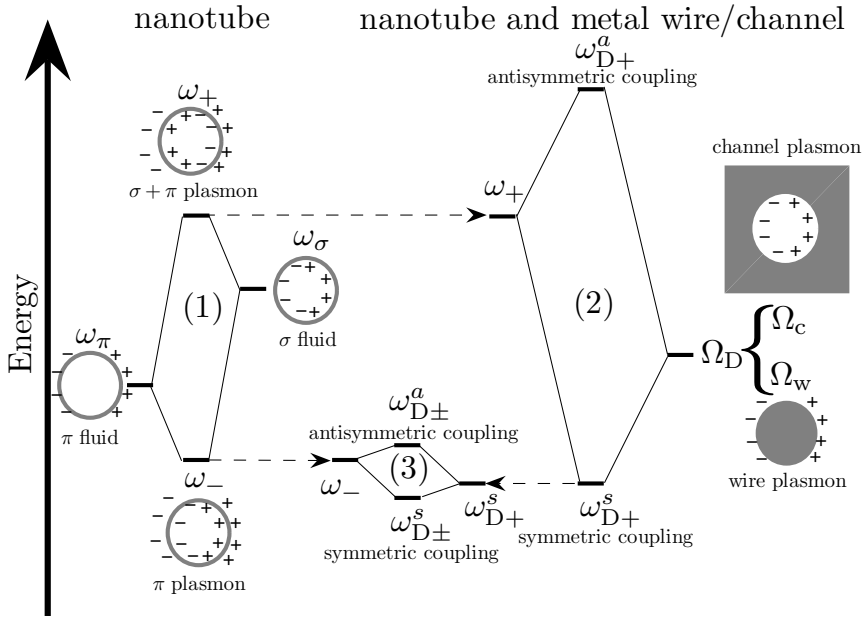

Figure 4.2: Energy-level diagram describing plasmon hybridization in a CNT (left) between (1) the σ and π electron fluids yielding the $\sigma+\pi$ and π plasmons and in a nanotube and metal wire/channel (right) between (2) the $\sigma+\pi$ nanotube plasmon and the metal wire/channel plasmon branches, yielding antisymmetrically coupled (antibonding) and symmetrically coupled (bonding) metal-$(\sigma+\pi)$ plasmons and (3) the symmetrically coupled (bonding) metal-$(\sigma+\pi)$ plasmon and the π nanotube plasmon, yielding antisymmetrically coupled (antibonding) and symmetrically coupled (bonding) π-metal-$(\sigma+\pi)$ plasmons [39, 147].

respectively. Third, plasmon hybridization occurs between the symmetrically coupled (bonding) metal-$(\sigma+\pi)$ plasmon and the π nanotube plasmon, yielding antisymmetrically coupled (antibonding) and symmetrically coupled (bonding) π-metal-$(\sigma+\pi)$ plasmons, with frequencies $\omega^a_{\mathrm{D}\pm}$ and $\omega^s_{\mathrm{D}\pm}$ respectively.

The plasmon hybridization between the π and symmetrically coupled metal-$(\sigma+\pi)$ plasmons is a much weaker coupling than those between the nanotube fluids or the $\sigma+\pi$ and metal plasmons, due to the large energy separation between the π plasmon and the higher energy $\sigma+\pi$ and metal plasmons. The antisymmetrically and symmetrically coupled metal-$(\sigma+\pi)$ plasmon

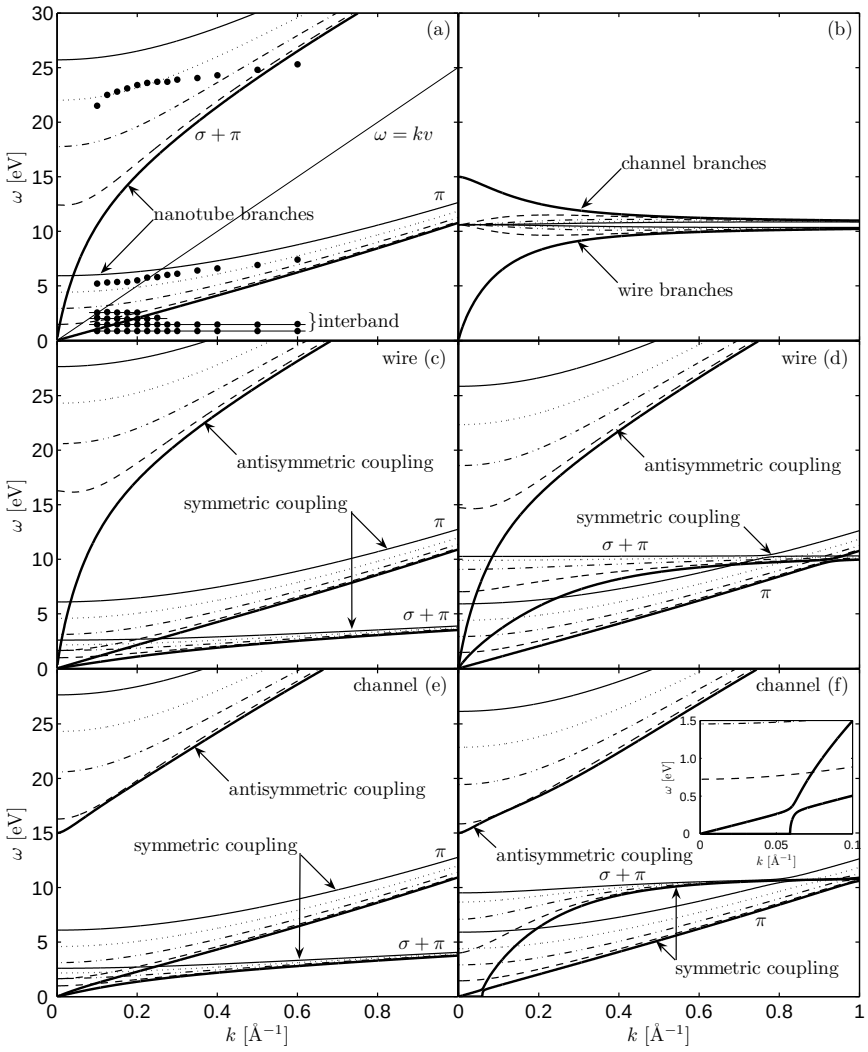

Figure 4.3: The plasmon energy ω in eV versus longitudinal wave number k in Å^{-1}, of (a) a CNT from our model [68] with experimental points (•) from Pichler *et al.* [16, 43] (*see Fig. 1.2*) of radius $R = 7$ Å showing the kinematic resonance condition $\omega = kv$, (b) an aluminum wire of radius $r_{\rm in} = 7$ Å and channel of radius $r_{\rm out} = 7$ Å [154], a CNT of radius $R = 7$ Å encapsulating an aluminum wire of radius (c) $r_{\rm in} = 7$ Å and (d) $r_{\rm in} = 6$ Å, and a CNT of radius $R = 7$ Å encapsulated in an aluminum channel of radius (e) $r_{\rm out} = 7$ Å and (f) $r_{\rm out} = 8$ Å, using $\omega_p \approx 15.0$ eV from Abril *et al.* [153] plotted versus k in Å^{-1} for $m = 0$ (——), 1 (- - - -), 2 (- · - · -), 3 (·····), and 4 (——) [147].

branches will thus have the same qualitative behaviour as the plasmon branches obtained from a single-fluid model. Although in principle a coupling exists between the higher energy antisymmetrically coupled metal-$(\sigma+\pi)$ plasmon and the two lower energy antisymmetrically coupled and symmetrically coupled π-metal-$(\sigma+\pi)$ plasmons, this coupling is very weak due to the large energy separation between these modes [39].

The plasmon energies from the two-fluid model [68] and experimental points [16, 43] for a CNT are shown along with the kinematic resonance condition $\omega = kv$ [62] in Fig. 4.3(a), while those for a metallic channel [44, 45] and a metallic wire [154] are shown in Fig. 4.3(b). The low energy interband plasmon energies measured by Pichler *et al.* are related to excitations of localized electrons, arising from the van Hove singularities in the nanotube band structure [16, 43]. Since these band structure effects occur at such low energies, by applying the kinematic resonance condition $\omega = kv$, we may argue that the band structure will contribute to the ion stopping force and self energy only at low velocities. For ion channelling, we are primarily interested in fast ion interactions, where the ions have velocities paraxial to the nanotube larger than the Fermi velocity ($v > v_F = \sqrt{2\pi n_0}$), so that band structure effects may be neglected. Note that both the $\sigma+\pi$ and π plasmon branches in the cylindrically symmetric $m = 0$ mode vanish at $k = 0$, which disagrees with results obtained when band structure contributions are included. However, when performing calculations for off-axis ion channelling, cylindrical symmetry is broken and higher order m modes, which do not vanish at $k = 0$, begin to dominate.

To improve our model of the combined system, we use both zero and 1 Å as a separation distance between the layers of the dielectric materials and the nanotube, as done by Östling *et al.* [59]. Figures 4.3(c) and 4.3(d) show a CNT of radius $R = 7$ Å encapsulating metallic wires of radii $r_{\rm in} = 7$ Å and $r_{\rm in} = 6$ Å respectively, while Figs. 4.3(e) and 4.3(f) show a CNT encapsulated in metallic channels of radii $r_{\rm out} = 7$ Å and $r_{\rm out} = 8$ Å respectively.

Note the elevation of the high energy antisymmetrically coupled metal-$(\sigma+\pi)$ plasmon branches $\omega^a_{\rm D+}$ in the combined systems shown in Figs. 4.3(c–f), when compared with the $\sigma+\pi$ and metallic plasmon branches shown in Figs. 4.3(a) and 4.3(b) respectively. In particular, the $m = 0$ mode of the antisymmetrically coupled metal-$(\sigma+\pi)$ plasmon for a nanotube encapsulated in a metal channel, shown in Fig. 4.3(e), has a plasma frequency of $\omega^a_{\rm D+} \approx \omega_p + \frac{\kappa^2}{2\omega_p}\left[\Omega_{\rm p}^2 - \omega_p^2/2\right]\left[-\ln(|\kappa|/2) - \gamma_0\right]$ for $\kappa = kR \ll 1$, where γ_0 is Euler's constant. However, as k increases, we find the antisymmetrically coupled metal-$(\sigma+\pi)$ plasmon exhibits

quasi-acoustic behaviour. Conversely, in Figs. 4.3(c) and 4.3(e) the antisymmetrically coupled π-metal-$(\sigma+\pi)$ plasmon branches appear remarkably unchanged from the carbon nanotube quasi-acoustic π branches ω_- shown in Fig. 4.3(a). This is due to the large energy separation between the π branches ω_- and the metal wire and channel branches $\Omega_{\rm w}$ and $\Omega_{\rm c}$. However, at long wavelengths ($k \ll 1$), the antisymmetrically coupled π-metal-$(\sigma+\pi)$ plasmon branches differ substantially from the nanotube π branches. For $r_{\rm out} = r_{\rm in} = R$, the $m = 0$ antisymmetrically coupled π-metal-$(\sigma+\pi)$ plasmon branch, shown in Figs. 4.3(c) and 4.3(e), has a quasi-acoustic plasma frequency of $\omega^a_{\rm D\pm} \approx \frac{\sqrt{6}}{4} k v_F$ for $k \ll 1$. As k increases, the plasma frequency approaches the nanotube's quasi-acoustic π plasma frequency, so that $\omega^a_{\rm D\pm} \approx \omega_- \approx \frac{\sqrt{3}}{4} k v_F$ [68]. Physically, at long wavelengths, the metal wire/channel will interact collectively with the entire electron gas, so that even the weak coupling with the π fluid will have an effect on the low-energy plasma frequencies.

We also find in Figs. 4.3(c) and 4.3(e) that the presence of a metal wire or channel suppresses the symmetrically coupled π-metal-$(\sigma+\pi)$ plasma frequency branches $\omega^s_{\rm D\pm}$ below the nanotube π branches ω_- shown in Fig. 4.3(a). Physically, this is because the electrostatic interaction between the σ and π electron fluids is much weaker than the electrostatic interaction between the nanotube electron fluids and the perfectly conducting metal boundary layers when $r_{\rm out} = r_{\rm in} = R$. At long wavelengths, the $m = 0$ mode of the symmetrically coupled π-metal-$(\sigma+\pi)$ plasmon shows quasi-acoustic behaviour, with plasma frequency $\omega^s_{\rm D\pm} \approx \frac{\sqrt{2}}{4} k v_F$ for $k \ll 1$. As k increases, we find that the symmetrically coupled π-metal-$(\sigma+\pi)$ plasmon exhibits 1-D behaviour.

All m modes from the metallic channel system are higher than those from the metallic wire system, with the separation decreasing with increasing m, as shown in Figs. 4.3(c–e). This is as expected from observing the metallic systems alone as shown in Fig. 4.3(b). It is remarkable that the nanotube π branches with frequencies ω_- and the antisymmetrically coupled metal-$(\sigma+\pi)$ channel/wire branches with frequencies $\omega^a_{\rm D+}$ are independent of the size of the gap between the nanotube and the metal boundary, whereas the symmetrically coupled metal-$(\sigma+\pi)$ branches with frequencies ω^s_+ are strongly affected by this gap. As the separation between the nanotube and the dielectric boundary $\Delta r_b = |R - r_{\rm in,out}|$ increases, the coupling between the nanotube $\sigma+\pi$ plasmon branch and the metal wire/channel branches weakens. The symmetrically coupled metal-$(\sigma+\pi)$ plasmon branch moves from an energy below that of the π plasmon branch

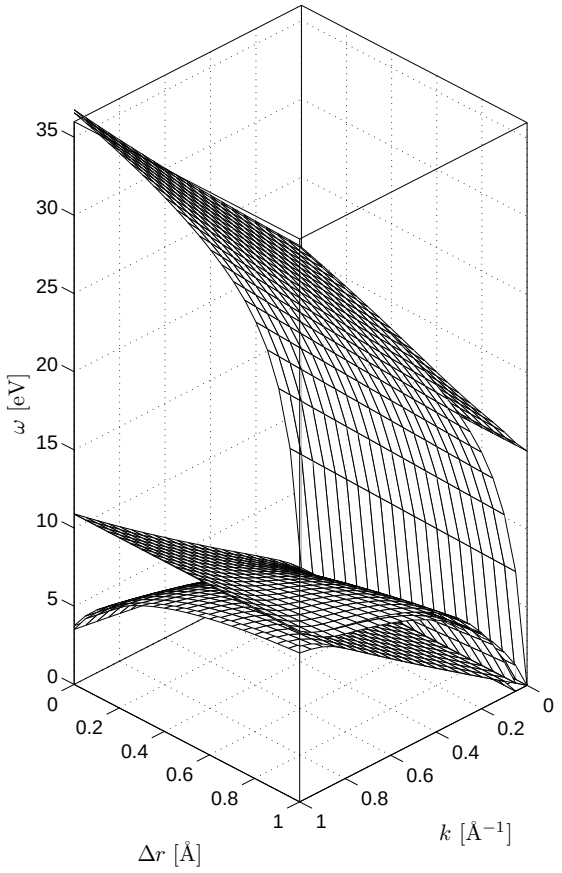

Figure 4.4: The plasmon energy ω in eV of a CNT of radius $R = 7$ Å plotted versus k in Å^{-1} and the tube-boundary gap $\Delta r_b = |R - r_{\mathrm{in,out}}|$ in Å for $m = 0$. Each pair of branches arise from an aluminum channel (upper) and wire (lower) respectively with $\omega_p \approx 15.0$ eV from Abril *et al.* [153, 147]

for $\Delta r_b = 0$ to one crossing the π plasmon branch for $\Delta r_b \approx 1$ Å. The antisymmetrically and symmetrically coupled π-metal-$(\sigma + \pi)$ plasmons thus "bounce" between the plasma frequencies $\omega^s_{\mathrm{D}+}$ and ω_-, due to avoided crossings, illustrated in the inset of Fig. 4.3(f), maintaining a minimal separation of ≈ 0.2 eV.

These avoided crossings induce a cutoff wave number k_C for $m = 0$ in the symmetrically coupled metal-$(\sigma+\pi)$ channel plasmon branch with frequency $\omega^s_{\mathrm{D}\pm}$, which occurs when $\omega^2_+\omega^2_- =$

$\Omega^2\Omega_{\rm p}^2\kappa^2 I_0^2(|\kappa|)K_0(|\kappa|\varrho_{\rm out})/I_0(|\kappa|\varrho_{\rm out})$. For $\Delta r_b \approx 1$ Å, this cutoff is $k_C \approx 0.06$ Å^{-1}, below which the symmetrically coupled π-metal-$(\sigma+\pi)$ plasmon branch is completely imaginary. Thus overdamping occurs at large wavelengths for nanotubes encapsulated in metal channels. This is further illustrated in Fig. 4.4, which shows how the plasmon dispersions for $m = 0$ of the combined system change as the tube-boundary gap Δr_b increases. We note that the upper two antisymmetrically coupled metal-$(\sigma+\pi)$ branches for a wire/channel are only weakly dependent on Δr_b, while the persistence of the nanotube's two degenerate acoustic π branches gives rise to a plane-like structure. Conversely, the two nearly degenerate symmetrically coupled metal-$(\sigma+\pi)$ branches undergo a series of avoided crossings due to plasmon hybridization with the π branches, moving from underneath the corresponding π plane at $\Delta r_b = 0$ to lying above that plane at $\Delta r_b = 1$ Å for the range of wave numbers $0 < k < 1$ Å^{-1}.

DWNTs and MWNTs in Vacuum

We will now consider the case of a DWNT in vacuum, which we model as two electron fluids, each with equilibrium density $n_{1,2}^0 \approx 0.428$, confined to cylindrical shells of radii R_1 and R_2 respectively. In this case, $\epsilon_{\rm in} = \epsilon_{\rm out} = \epsilon_{\rm nt} = 1$, so that the dispersion relation of Eqn. (4.2) yields expressions for the DWNT plasmon branches analogous to the $\sigma+\pi$ and π branches of Eqn. (4.8). These are for each m

$$\omega_\pm^2 = \frac{\omega_1^2+\omega_2^2}{2} \pm \sqrt{\left(\frac{\omega_1^2-\omega_2^2}{2}\right)^2 + \Delta^2}, \tag{4.14}$$

where

$$\omega_{1,2}^2 = \Omega_{1,2}^2(\kappa_{1,2}^2+m^2)\left[\frac{1}{4R_{1,2}} + \frac{\kappa_{1,2}^2+m^2}{4\Omega_{1,2}^2R_{1,2}^4} + I_m(|\kappa_{1,2}|)K_m(|\kappa_{1,2}|)\right] \tag{4.15}$$

are the squares of the plasma frequencies of the individual electron fluids on the cylinders, whereas

$$\Delta^2 = \Omega_1^2\Omega_2^2(\kappa_1^2+m^2)(\kappa_2^2+m^2)I_m^2(|\kappa_1|)K_m^2(|\kappa_2|) \tag{4.16}$$

describes the electrostatic interaction between the two fluids, with $\kappa_1 \equiv kR_1$ and $\kappa_2 \equiv kR_2$.

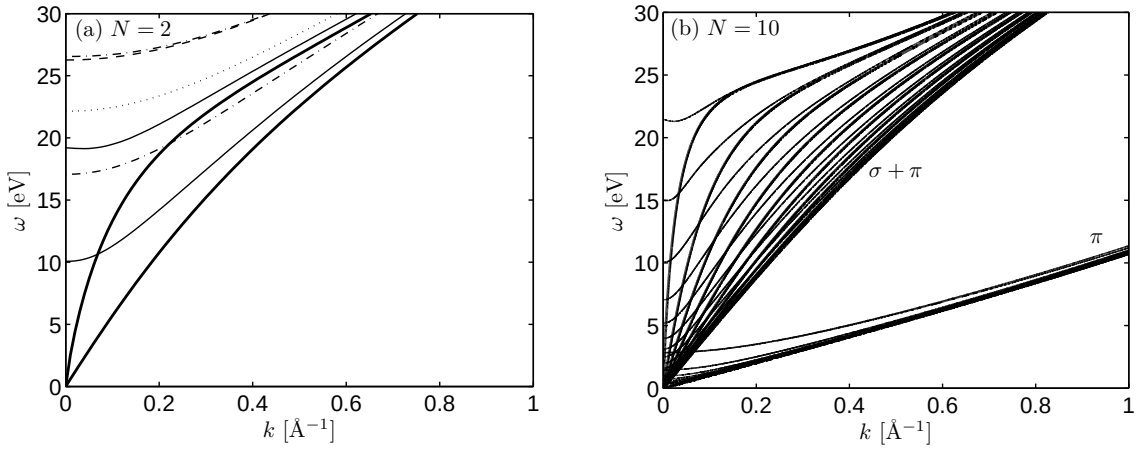

Figure 4.5: The plasmon energy ω in eV versus longitudinal wave number k in Å^{-1} for (a) DWNT with radii $R_1 = 3.6$ Å and $R_2 = 7$ Å and (b) $N = 10$ MWNT with radii $R_n = 3.6 + 3.4n$ Å for $m = 0$ (——), 1 (——), 2 (- - - -), 3 (·····), and 4 (- - - -) [145, 148].

In Fig. 4.5(a), we consider a DWNT with the inner and outer radii $R_1 = 3.6$ Å, and $R_2 = 7$ Å, respectively, with a separation $d = R_2 - R_1 = 3.4$ Å, chosen to match the typical inter-wall distance in MWNTs. The two groups of resonant plasmon dispersions from Eqn. (4.14), $\omega_+(m,k)$ and $\omega_-(m,k)$, are shown in Fig. 4.5(a) versus the longitudinal wave number k for angular wave numbers $m = 0$, 1, 2, 3, and 4. It is apparent in Fig. 4.5(a) that the splitting between the two groups of plasmon frequencies in Eqn. (4.14) is rather substantial owing to the strong electrostatic interaction between the two charged fluids. While the upper group of plasmon dispersions exhibits a characteristic dimensional cross-over from a 2D to a one-dimensional electron system [96, 58], the lower group of plasmon frequencies exhibits weaker dispersions with less spreading among the various m-modes. In particular, the $m = 0$ mode in the lower-energy plasmon group exhibits a quasi-linear dispersion in the limit of long wavelengths, which may be derived analytically in the form $\omega_- \approx \sqrt{\dfrac{2R_1R_2}{R_1+R_2}\ln\left(\dfrac{R_1}{R_2}\right)}kv_F \approx 4k$. This quasi-acoustic plasmon mode seems to be a common occurrence when a splitting of plasmon frequencies happens due to the electrostatic interaction, e.g., in the electron-hole plasma of a CNT [205], or in the coupling between two parallel nanotubes [61].

To illustrate the effects of multiple walls on plasmon dispersion, we choose the example of

an $N = 10$ walled CNT with radius of the nth wall given by $R_n = 3.6 + 3.4n$ Å, where we have used an inner radius of $R_1 \approx 3.6$ Å and separation $d = R_{n+1} - R_n \approx 3.4$ Å, as was done for the DWNT case.

Since we are considering the nanotube to be in vacuum, so that $\epsilon_{\rm in} = \epsilon_{\rm out} = \epsilon_{\rm nt} = 1$, the dispersion relation given by Eqn. (4.2) yields $2N$ positive roots for ω defining the plasmon dispersions which are clearly separated into a high-frequency, $\omega_{j,+}(m,k)$, and a low-frequency, $\omega_{j,-}(m,k)$, group (where $1 \leq j \leq N$) for each angular wave number m, as shown in Fig. 4.5(b) for $N = 10$ with $m = 0$ and 1. These groupings are reminiscent of the experimental plasmon branches describing longitudinal oscillations of $\sigma + \pi$ and π electrons on CNTs shown in Fig. 1.2 [16]. Interestingly, the low-frequency π plasmons are much more tightly packed than the high-frequency group. In particular, the $m = 0$ modes of the π plasmons are degenerate with the quasi-acoustic SWNT π plasmon branch $\omega_- \approx \frac{\sqrt{3}}{4} k v_F$ at long wavelengths. This again reinforces the stability of the π plasmon branch, even when significant hybridization occurs between plasmons from the various nanotube walls.

Comparing Fig. 4.5(a) and Fig. 4.5(b), we see that plasma hybridization between the electron fluids of different nanotube walls leads to a "thickening" of the high-frequency $\sigma + \pi$ plasmon group at medium wavelengths, while the qualitative behaviour of the plasmon branches remains unchanged at small and long wavelengths.

4.2 Electron Density and Electric Potential

Using the induced electron density per unit area, $n_1(\mathbf{r}_R, t)$, on a nanotube of radius R, where $\mathbf{r}_R = \{R, \varphi, z\}$ is the coordinate on the cylinder, we may determine all quantities relevant to ion channelling, such as the induced potential $\Phi_{\rm ind}(\mathbf{r}, t)$, the stopping force, and the image potential. Beginning with the simple model of a single electron fluid, of equilibrium density $n_0 \approx 0.428$, confined to a cylindrical shell of radius R, we will calculate the electron density perturbation induced by an ion of charge Q moving paraxially with speed v at position $\mathbf{r}_0 = \{r_0, \varphi_0, vt\}$ in the laboratory frame of reference. Employing this single-fluid model, we obtain by substituting Eqn. (4.1) for $\widetilde{\Phi}_{\rm sc}$ into Eqn. (3.27) and performing the inverse FB transform, the induced electron

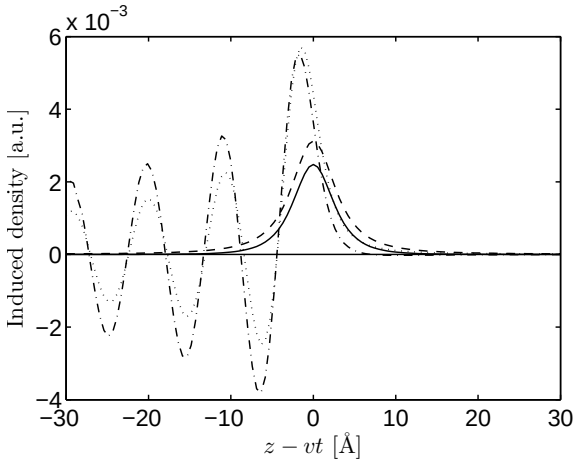

Figure 4.6: The axial dependence of the surface electron density n_1 in in the plane $\varphi = \varphi_0$ on a single wall carbon nanotube with radius $R = 7.4$ Å, induced by protons moving paraxially with speed $v = 0$ at radial distances $r_0 = R/2$ (——) and $r_0 = 3R/2$ (- - - -), and speed $v = 3$ at radial distances $r_0 = R/2$ (- · - · -) and $3R/2$ (·····) [144].

density

$$n_{\rm one}(\mathbf{r}_R, t) = \frac{Q}{R^2} \sum_m \int \frac{d\kappa}{(2\pi)^2} \frac{\Omega_{\rm p}^2(\kappa^2 + m^2) e^{im(\varphi-\varphi_0)} e^{i\kappa(z/R - \varpi t)} I_m(|\kappa|\varrho_{0<}) K_m(|\kappa|\varrho_{0>})}{\Omega_{\rm p}^2(\kappa^2 + m^2) \left[\frac{1}{4R} + \frac{\kappa^2+m^2}{4\Omega_{\rm p}^2 R^4} + I_m(|\kappa|) K_m(|\kappa|)\right] - \kappa\varpi(\kappa\varpi + i\gamma)} \tag{4.17}$$

where we have used the plasma frequency for a non-interacting electron gas of density n_0, $\Omega_{\rm p} \equiv \sqrt{4\pi n_0/R}$, $\varpi \equiv v/R$, and the dimensionless variables $\kappa \equiv kR$, $\varrho_{0<} \equiv \min(1, r_0/R)$, $\varrho_{0>} \equiv \max(1, r_0/R)$.

In Fig. 4.6 we show the z-dependence of the induced electron density calculated using the single-fluid model. We consider a nanotube of radius $R = 7.4$ Å, with an ion travelling paraxially with speed $v = 0$ and $v = 3$ at $r_0 = R/2$ and $r_0 = 3R/2$. For a stationary ion, we find that the induced electron density has a bell-like shape, which is stationary in the ion's moving frame of reference. For ions travelling at speeds much higher than the electron fluid's Fermi velocity $v_F = \sqrt{2\pi n_0} \approx 1.6$, electrons in the fluid are unable to "keep up" with the moving ion's electric field, and oscillations in the induced electron density occur. These oscillations, called the "wake

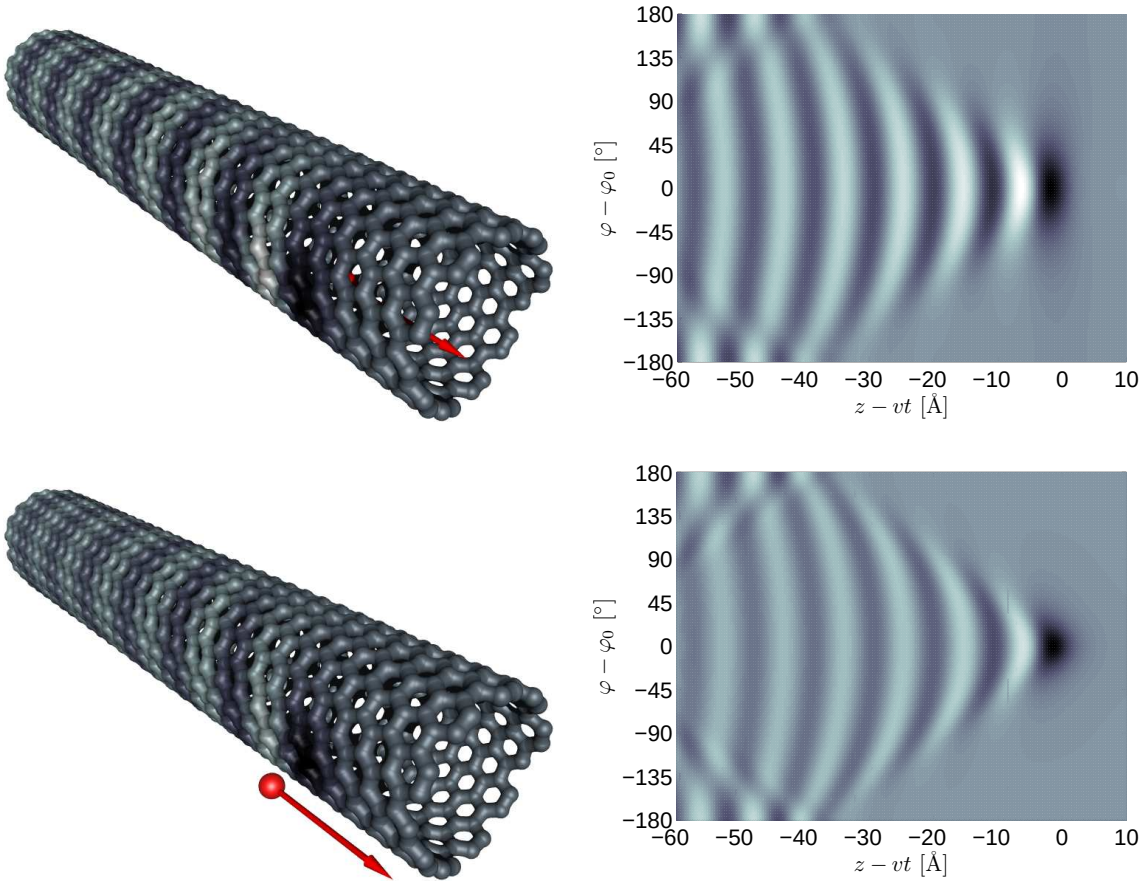

Figure 4.7: Electron number density n_1 on an (11,9) SWNT of radius $R = 6.89$ Å, induced by an ion moving paraxially with speed $v = 3$ at $r_0 = R/2$ (top) and $r_0 = 3R/2$ (bottom).

effect", can be seen in Fig. 4.6 for the induced electron density due to an ion moving paraxially with speed $v = 3$.

In Fig. 4.7, we show calculations of the single-fluid induced electron density on an (11,9) SWNT of radius $R = 6.89$ Å, due to an ion travelling paraxially with speed $v = 3$ to the nanotube at $r_0 = R/2$ and $r_0 = 3R/2$. Regions of higher and lower electron density are darker and lighter respectively. The two left panes show the induced electron density superimposed on the lattice structure of an (11,9) SWNT. The two right panes of Fig. 4.7 are plots of the induced electron density after being "unraveled" into a 2D plot. The 2D plots of the induced electron

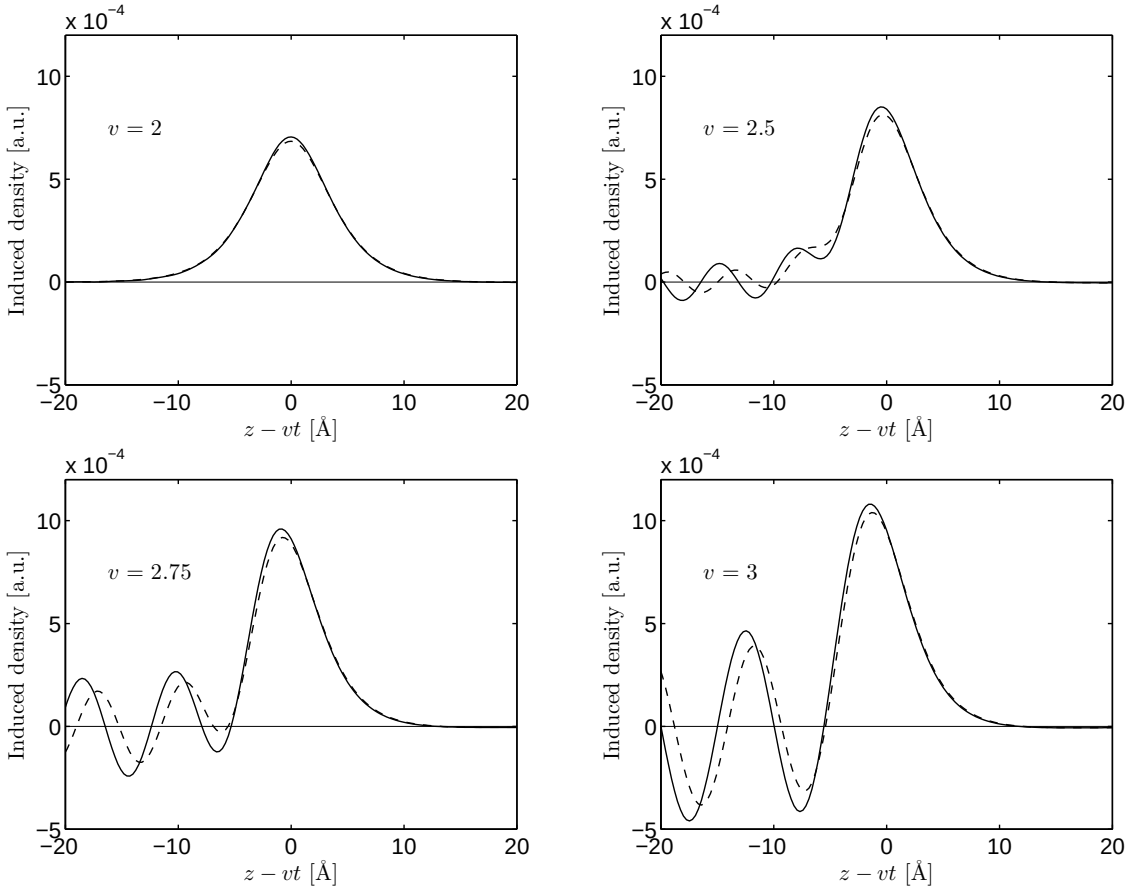

Figure 4.8: Induced electron densities $n_{\rm one}$ (- - - -) and $n_{\rm two}$ (——) from the single-fluid and two-fluid models respectively, versus distance $(z - vt)$ in Å, for a proton moving along the axis of a nanotube with radius $R = 7$ Å, at speeds $v = 2, 2.5, 2.75$ and 3 [68].

density both clearly show a "V" shape wake pattern trailing the ion's position, which begins to interfere with itself at $z_0 - vt \approx 40$ Å behind the ion, once the wake pattern encircles the nanotube. In comparing the induced electron density for $r_0 = R/2$ (upper) and $r_0 = 3R/2$ (lower), we notice that the wake pattern is more localized when the ion is outside the nanotube, due to the nanotube's cylindrical geometry.

We now compare the single-fluid model for the induced electron density with the two-fluid model for the induced electron density in a vacuum, from which we obtain by substituting Eqn.

(4.1) for $\widetilde{\Phi}_{\rm sc}$ into Eqn. (4.5)

$$n_{\rm two}(\mathbf{r}_R,t)=\frac{Q}{R^2}\sum_m\int\frac{d\kappa}{(2\pi)^2}\frac{\Omega_{\rm p}^2(\kappa^2+m^2)e^{im(\varphi-\varphi_0)}e^{i\kappa(z/R-\varpi t)}I_m(|\kappa|\varrho_{0<})K_m(|\kappa|\varrho_{0>})}{[\omega_+^2(m,\kappa)-\kappa\varpi(\kappa\varpi+i\gamma)][\omega_-^2(m,\kappa)-\kappa\varpi(\kappa\varpi+i\gamma)]} \quad (4.18)$$

where $\omega_\pm^2$ are given by Eqn. (4.8).

Figures 4.8 and 4.9 show the induced electron density on a SWNT of radius $R=7$ Å due to an ion travelling along the nanotube axis, calculated using both the single-fluid and two-fluid models. Since $I_m(0)=\delta_{m0}$ [169], by cylindrical symmetry, only the $m=0$ terms contribute in our calculations of the induced electron density.

In Fig. 4.8, we see that the threshold for excitations of the $\sigma+\pi$ plasmon is $v\gtrsim 2$. We find that above this threshold, both the single-fluid and two-fluid models exhibit the usual wake effect trailing the ion with increasing v. Apart from minor differences in the periods and phases of these oscillations, the single-fluid and the two-fluid models give remarkably similar results for speeds $v\gtrsim 2$. On the other hand, for almost all v values in the low-speed range, $0<v<2$, our calculations show that $n_{\rm one}$ and $n_{\rm two}$ are practically on top of each other, as shown in Fig. 4.8(a), both describing a symmetrical, bell-shaped accumulation of electrons on the nanotube wall which screens the channelled ion.

In Fig. 4.9 we show the induced electron density for an ion moving at speeds near the π plasmon phase velocity, given by the kinematic condition to be $v=\frac{\sqrt{3}}{4}v_F\approx 0.71$. This reveals expected, yet qualitatively surprising, differences in the z dependences of the single-fluid and two-fluid induced electron densities, $n_{\rm one}$ and $n_{\rm two}$ respectively. Namely, while the single-fluid model maintains an almost rigidly-shaped bell curve $n_{\rm one}(z-vt)$, the two-fluid model gives rise to the development of a strong asymmetry in the induced electron density $n_{\rm two}(z-vt)$ in the range of speeds shown in Fig. 4.9. The most surprising result is that $n_{\rm two}(z-vt)$ exhibits oscillations for $v\approx 0.72$, shown in Fig. 4.9(b), which *precede* the ion ($z-vt>0$). In contrast, the wake patterns shown in Fig. 4.8(b), Fig. 4.8(c) and Fig. 4.8(d) all *trail* the ion. Our calculations show that this physically puzzling behaviour of the two-fluid model is accompanied by the strong, out-of-phase individual polarizations of the σ and π fluids, similar to the earlier observations in the electron-hole plasma on nanotubes [205]. We finally note that the calculations also show that, while both induced densities $n_{\rm one}$ and $n_{\rm two}$ are insensitive to the variations in (small) values of γ for high speeds, $v>2$, shown in Fig. 4.8, the oscillations in $n_{\rm two}$, shown in Fig. 4.9(b), are heavily damped when both the friction γ and the nanotube radius R increase.

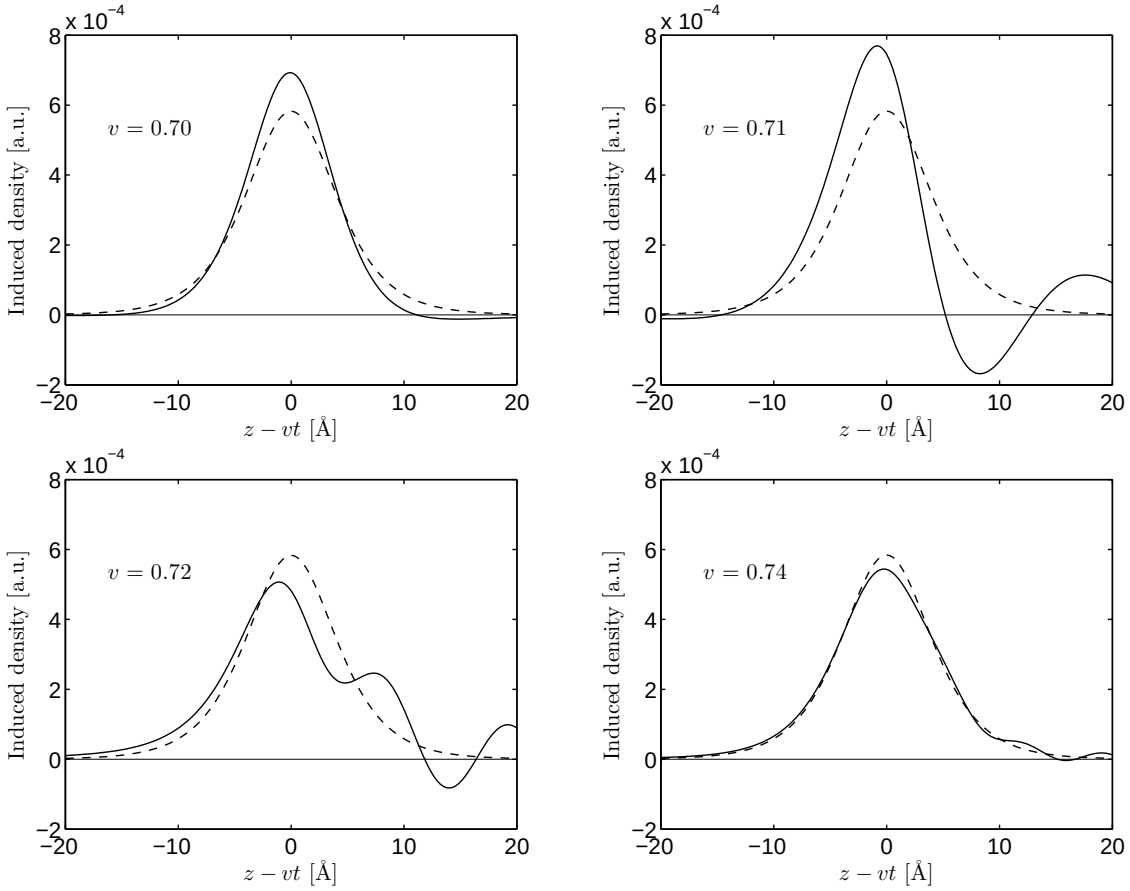

Figure 4.9: Induced electron densities $n_{\rm one}$ (- - - -) and $n_{\rm two}$ (——) from the single-fluid and two-fluid models respectively, versus distance $(z - vt)$ in Å, for a proton moving along the axis of a nanotube with radius $R = 7$ Å, at speeds $v = 0.70$, 0.71, 0.72, and 0.74, near the group velocity of the π plasmon, $v_g = \frac{\sqrt{3}}{4} v_F \approx 0.71$ [68].

The induced electric field from a nanotube due to an ion moving parallel to the nanotube axis, may be calculated using the FB transform of the induced electron density from a single-fluid model, from Eqn. (3.20), to obtain

$$\Phi_{\rm ind}(\mathbf{r}, t) \tag{4.19}$$
$$= -\frac{4\pi Q}{R} \sum_m \int \frac{d\kappa \Omega_{\rm p}^2 (\kappa^2 + m^2) e^{im(\varphi - \varphi_0)} e^{i\kappa(z/R - \varpi t)} I_m(|\kappa| \varrho_{0<}) I_m(|\kappa| \varrho_<) K_m(|\kappa| \varrho_{0>}) K_m(|\kappa| \varrho_>)}{(2\pi)^2 \Omega_{\rm p}^2 (\kappa^2 + m^2) \left[\frac{1}{4R} + \frac{\kappa^2 + m^2}{4\Omega_{\rm p}^2 R^4} + I_m(|\kappa|) K_m(|\kappa|) \right] - \kappa\varpi(\kappa\varpi + i\gamma)}$$

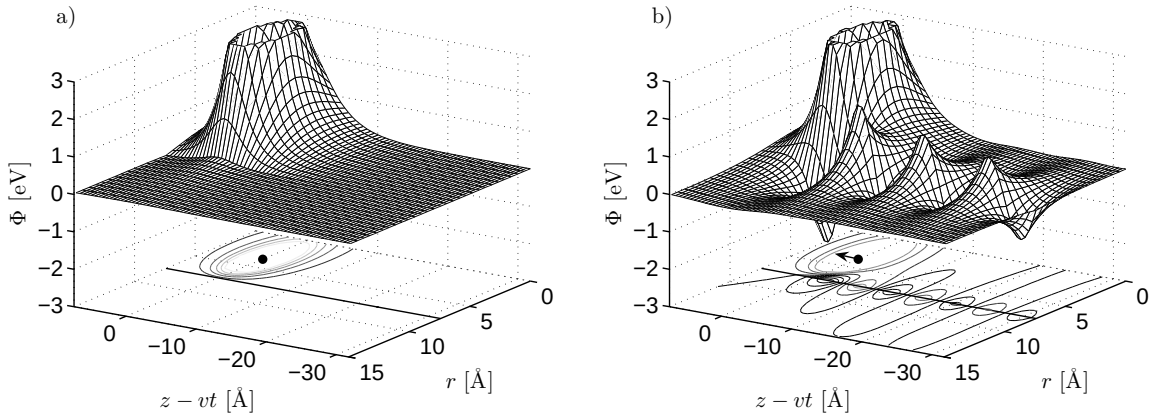

Figure 4.10: Total potential Φ in eV plotted versus r in Å and $(z - vt)$ in Å in the plane $\phi = \phi_0$ for a proton moving paraxially at $r_0 = R/2 \approx 3.7$ Å in a SWNT of radius $R = 7.4$ Å, at speed (a) $v = 0$ and (b) $v = 3$. The level curves show the increments $\Delta\Phi = 0.5$ eV [144].

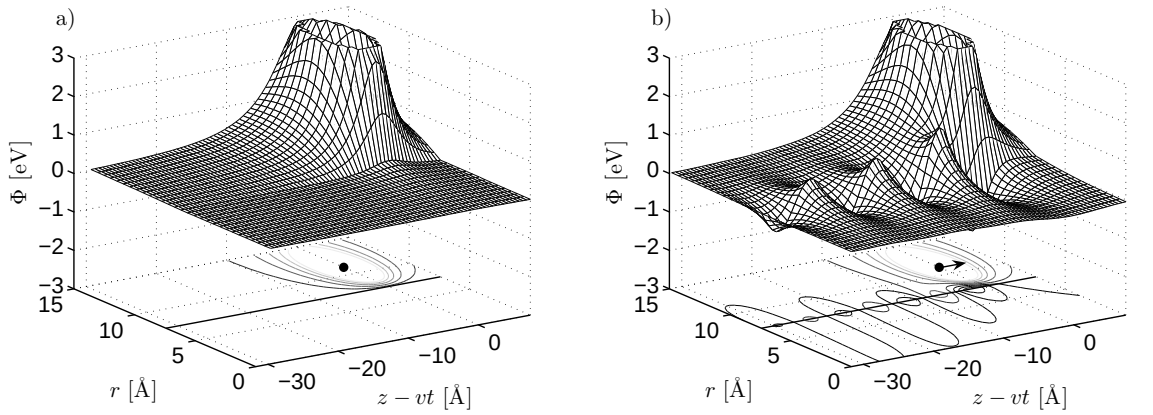

Figure 4.11: Total potential Φ in eV plotted versus r in Å and $(z - vt)$ in Å in the plane $\varphi = \varphi_0$ for a proton moving paraxially at $r_0 = 3R/2 \approx 11.1$ Å outside a SWNT of radius $R = 7.4$ Å, at speed (a) $v = 0$ and (b) $v = 3$. The level curves show the increments $\Delta\Phi = 0.5$ eV [144].

where $\varrho_< \equiv \min(1, r/R)$ and $\varrho_> \equiv \max(1, r/R)$.

We now use Eqn. (4.19) to calculate the 3D spatial variation of the *total* potential Φ for an ion with charge $Q = 1$ at the distances $r_0 = 3.7$ Å and $r_0 = 11.1$ Å from the axis of a nanotube

of radius $R = 7.4$ Å, and show the results in Fig. 4.10 and Fig. 4.11 for the r and z dependence of Φ in the plane $\varphi = \varphi_0$ (defined by the position of the particle). In Fig. 4.10, we show the cases of particles inside the nanotube ($r_0 = 3.7$ Å) at speeds (a) $v = 0$ and (b) $v = 3$. One can observe from Fig. 4.10(a) that, in the static case, the Coulomb potential of the charged particle is effectively screened by the nanotube, so that there is very little "leakage" of that potential outside the nanotube wall. Nevertheless, the magnitude of the leaking potential in Fig. 4.10(a) may be sufficient to provide longitudinal localization for the toroidal image states around nanotubes, as suggested in Ref. [51]. On the other hand, the case of a charge moving at $v = 3$ in Fig. 4.10(b) shows a wake potential trailing the particle with quite pronounced oscillations along the z-axis. These are radially localized at the nanotube surface ($r = R$) and are effectively decayed at the axis of the nanotube ($r = 0$) and at radial distances of $r \gtrsim 2R$. In particular, one notices in Fig. 4.10(b) the development of a relatively deep and long-ranged potential well, lying outside the nanotube in the proximity of the charged particle, which results from the electron fluid "over-compensating" in screening the Coulomb potential of the particle inside the nanotube. Such a well may capture another charged particle outside the nanotube and drag it in a state which has been identified in the case of the bulk solid as a "wake riding" state [206]. Of course, other potential minima seen in the wake potential in Fig. 4.10(b) can give rise to a similar effect. Finally, the results for the total potential Φ in the case of charged particles outside the nanotube with $R = 7.4$ Å, which are placed at $r_0 = 11.1$ Å, are shown in Fig. 4.11 for the speeds (a) $v = 0$ and (b) $v = 3$. The results shown in this figure are surprisingly symmetric with respect to those in Fig. 4.10 for particles inside the nanotube of the same radius, so that similar conclusions may be drawn from Fig. 4.11.

4.3 Stopping Force

The stopping force on an ion of charge Q travelling paraxially to the SWNT with speed v at $\mathbf{r}_0(t) = \{r_0, \varphi_0, vt\}$, in the laboratory frame of reference, is the force opposing the ion's motion. Its magnitude equals the usual (wrongly-named) "stopping power", defined by $S \equiv Q \left.\frac{\partial \Phi_{\rm ind}}{\partial z}\right|_{\mathbf{r}=\mathbf{r}_0}$. This quantity describes, in our model, the energy loss of a channelled particle per unit path length due to the collective electron excitations on the nanotube wall, which are modified by the electrostatic coupling with the polarization of any dielectric media inside or outside the nanotube,

giving rise to the effective surface charge $\sigma_{\rm in}$ or $\sigma_{\rm out}$ on the dielectric boundary at $r = r_{\rm in}$ or $r = r_{\rm out}$ respectively.

For a single ion of charge Q at $\mathbf{r} = \mathbf{r}_0(t)$, moving with speed v paraxially to the nanotube, the screened perturbing potential is

$$\widetilde{\Phi}_{\rm sc} = \frac{2\pi Q}{\epsilon_{\rm sc}(\omega)} g(r, r_0; m, k)\delta(\omega - kv)e^{-im\varphi_0}, \tag{4.20}$$

where $\epsilon_{\rm sc}(\omega)$ is the dielectric function of the region the ion is travelling in. The stopping force S may be calculated using the definition $S = Q\,\frac{\partial}{\partial z}\Phi_{\rm ind}\big|_{\mathbf{r}=\mathbf{r}_0(t)}$, where $\Phi_{\rm ind} = \Phi_{\rm nt} + \Phi_{\rm in} + \Phi_{\rm out} + \Phi_{\rm bulk}$ is the total potential induced by the ion in the system, with $\Phi_{\rm bulk} = (1 - \epsilon_{\rm sc})\Phi_{\rm sc}$ being the potential due to the polarization of the region in which the ion travels. Note that at large wave number, $kR \gg 1$, where any momentum dependence in the dielectric function would be expected to contribute, the FB transform of the stopping force has a factor of $e^{-k|R-r_0|}/k$, so that the effects of momentum dependence on the dielectric function may be neglected when $k \gg 1/|R - r_0|$.

SWNTs in Vacuum

From Eqn. (4.19) for the induced electric potential on a SWNT from a single-fluid model, we obtain for the single-fluid stopping force, $S_{\rm one}$,

$$S_{\rm one} = \frac{4\pi Q}{R^2}{\rm Im}\left[\sum_m \int \frac{d\kappa}{(2\pi)^2} \frac{\Omega_{\rm p}^2\kappa(\kappa^2+m^2)I_m^2(|\kappa|\varrho_{0<})K_m^2(|\kappa|\varrho_{0>})}{\Omega_{\rm p}^2(\kappa^2+m^2)\left[\frac{1}{4R} + \frac{\kappa^2+m^2}{4\Omega_{\rm p}^2R^4} + I_m(|\kappa|)K_m(|\kappa|)\right] - \kappa\varpi(\kappa\varpi + i\gamma)}\right]. \tag{4.21}$$

Similarly, from Eqn. (4.18), we obtain for the two-fluid stopping force, $S_{\rm two}$,

$$S_{\rm two} = \frac{4\pi Q}{R^2}{\rm Im}\left[\sum_m \int \frac{d\kappa}{(2\pi)^2} \frac{\Omega_{\rm p}^2\kappa(\kappa^2+m^2)I_m^2(|\kappa|\varrho_{0<})K_m^2(|\kappa|\varrho_{0>})}{[\omega_+^2(m,\kappa) - \kappa\varpi(\kappa\varpi + i\gamma)][\omega_-^2(m,\kappa) - \kappa\varpi(\kappa\varpi + i\gamma)]}\right], \tag{4.22}$$

where $\omega_\pm(m,\kappa)$ are the $\sigma + \pi$ and π plasma frequencies from the two-fluid model, given in Eqn. (4.8).

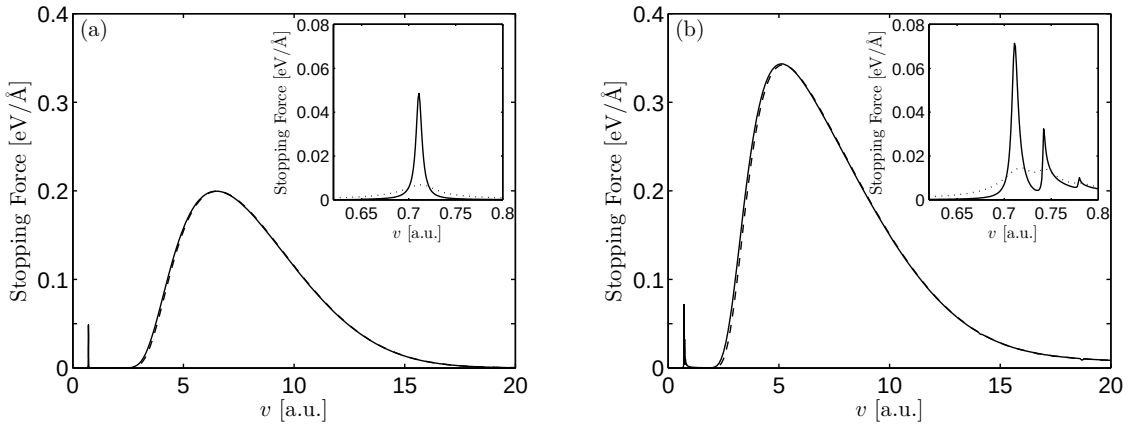

Figure 4.12: Stopping forces $S_{\rm one}$ (- - - -) and $S_{\rm two}$ with friction coefficient $\gamma = 10^{-3}\Omega_{\rm p}$ (——) and $\gamma = 10^{-2}\Omega_{\rm p}$ (·····) in eV/Å from the single-fluid and two-fluid models respectively, plotted versus speed v for a proton moving paraxially at (a) $r_0 = 0$ and (b) $r_0 = R/2$ to a single wall CNT of radius $R = 7$ Å [68].

We first show in Fig. 4.12(a) the results for a proton moving along the axis ($r_0 = 0$) of a SWNT with radius $R = 7$ Å, in which case, by cylindrical symmetry, only the $m = 0$ angular wave numbers contribute to either $S_{\rm one}$ or $S_{\rm two}$. In Fig. 4.12(a), we have used a friction coefficient of $\gamma = 10^{-3}\Omega_{\rm p}$ and, not surprisingly, the two curves $S_{\rm one}$ and $S_{\rm two}$ are found to be almost on top of each other, except for a narrow peak in $S_{\rm two}$ at $v = \frac{\sqrt{3}}{4}v_F \approx 0.71$, which is absent from $S_{\rm one}$. It can be argued that the broad parts of both curves in Fig. 4.12(a) describe the excitation of the high-energy $\sigma + \pi$ plasmon with $m = 0$ for speeds $v \gtrsim 2$, whereas the solitary peak in $S_{\rm two}$ describes the excitation of the low-energy acoustic π plasmon with $m = 0$ when the proton speed satisfies the kinematic condition for the π plasma frequency of $\omega_- \approx \frac{\sqrt{3}}{4}v_F k \approx 0.71k$ at long wavelengths. As was shown earlier for $S_{\rm one}$ [55, 144], we have also verified here that the bulk parts of the stopping force curves for $v \gtrsim 2$ in Fig. 4.12(a) are insensitive to the variations in (small) values of γ. However, owing to the linear dispersion of the acoustic π plasmon with $m = 0$, the peak structure at $v \approx 0.71$ is quite sensitive to this variation, which is illustrated in the inset of Fig. 4.12(a) for two values of the friction constant, $\gamma = 10^{-3}\Omega_{\rm p}$ and $\gamma = 10^{-2}\Omega_{\rm p}$. These results suggest a possibility of having a drift instability at $v = \frac{\sqrt{3}}{4}v_F$ [61], which could provide a means of probing the collective electron excitations on nanotubes. However, these results also

point to the need of a careful examination of the role of various damping mechanisms for the low-frequency plasmon modes.

Finally, in order to illustrate the effects of the plasmon excitations with $m \neq 0$ on the stopping force, we show in Fig. 4.12(b) the results for $S_{\rm one}$ and $S_{\rm two}$ for an proton moving at a distance $r_0 = R/2$ from the axis of a SWNT of radius $R = 7$ Å. Again, the two curves are on top of each other in Fig. 4.12(b) for speeds v above the threshold for $\sigma + \pi$ plasmon excitations, and they both closely reproduce the data obtained earlier, including those based on the dielectric function in RPA [55]. In the low-speed region, $S_{\rm two}$ displays multiple peaks, which are shown in the inset of Fig. 4.12(b) for $\gamma = 10^{-3}\Omega_{\rm p}$ and $\gamma = 10^{-2}\Omega_{\rm p}$, exhibiting the sensitivity of these peaks to damping. For the smaller γ value, one can easily identify in Fig. 4.12(b) several peaks corresponding to the excitations of the π plasmons with angular wave numbers $m = 0$, 1, 2, and 3, in a nice correspondence with the π plasmon dispersion curves shown in Fig. 4.3(a).

SWNTs with Encapsulating Dielectrics and Metal Clamps

Using the two-fluid model, we now study the case of a CNT of radius $R = 7$ Å encapsulated by either insulating or metallic media and look for the corresponding effect on the stopping force for ions moving paraxially. As encapsulating materials we consider silicon dioxide (SiO_2), amorphous carbon, aluminum, and nickel. We model silicon dioxide as a dielectric medium restricted from the inter-tube region, as found experimentally [19, 20, 21], so that $\epsilon_{\rm in} = \epsilon_{\rm nt} = 1$ and $\epsilon_{\rm out} = \epsilon_{\rm SiO_2}$, where we use a dielectric constant of $\epsilon_{\rm SiO_2} \approx 3.9$ [151].

In Appendix C we provide a detailed discussion of the optical dielectric functions we used to model amorphous carbon, aluminum, and nickel surrounding the nanotube, with dielectric boundary separation $\Delta r_b = |r_{\rm out} - R|$ between the outside dielectric boundary and the nanotube radius. Fig. 4.13 shows a schematic of a metal clamp encapsulating an (11,9) SWNT.

Figure 4.14(a) shows the effect of an insulating dielectric medium of SiO_2 encapsulating a CNT of radius $R = 7$ Å, on the stopping force for protons moving paraxially at $r_0 = 0$. From this figure we find a significant reduction in the high-speed stopping force, accompanied by an increase in low-speed stopping, giving rise to reductions in both the magnitude and the position of the main stopping peak. For example, for a model of a "thin" nanotube, $r_{\rm in} = R = r_{\rm out}$, we find the stopping force peak position is reduced to half the value in vacuum. On the other hand, the inset displayed in Fig. 4.14(a) shows that the low-speed peak in

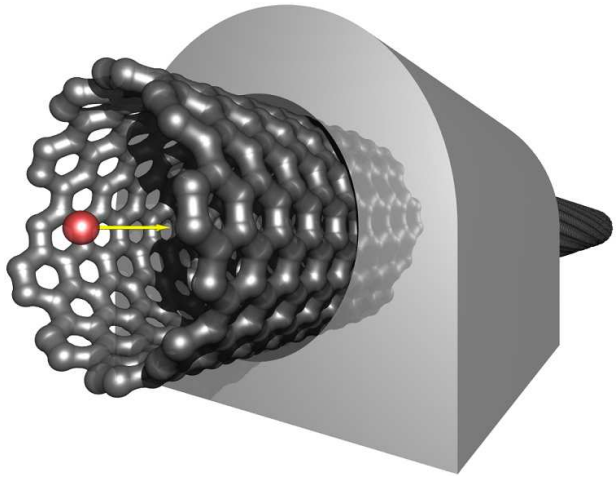

Figure 4.13: Schematic of an (11,9) SWNT encapsulated by a metal clamp.

stopping is only mildly affected by encapsulating the nanotube in SiO_2. Physically, the encapsulating dielectric medium "screens" the electrostatic potential induced on the nanotube by a factor $\Theta \equiv 1 + \frac{(\epsilon_{SiO_2}-1)|\kappa_{out}|I_m(|\kappa_{out}|)K'_m(|\kappa_{out}|)}{1-(\epsilon_{SiO_2}-1)|\kappa_{out}|I_m(|\kappa_{out}|)K'_m(|\kappa_{out}|)} \frac{I_m(|\kappa|)K_m(|\kappa_{out}|)}{I_m(|\kappa_{out}|)K_m(|\kappa|)}$, where $0 < \Theta < 1$ and $\kappa_{out} \equiv kr_{out}$. When $R = r_{out}$, this simplifies to $\Theta = \frac{1}{1-(\epsilon_{SiO_2}-1)|\kappa|I_m(|\kappa|)K'_m(|\kappa|)}$. This "screening" lowers the upper nanotube $\sigma + \pi$ plasmon branch shown in Fig. 4.3(a) and reduces both the position and magnitude of the main high-speed stopping peak. However, the location of the lower π plasmon branch in Fig. 4.3(a) is independent of the electrostatic potential and thus the encapsulating SiO_2, with $\omega_- \approx \frac{\sqrt{3}}{4}kv_F$ for $m = 0$ [68]. This means that the presence of silicon dioxide has little effect on the low-speed stopping peak's position. Since the magnitude of the low-speed stopping peak, shown in the inset of Fig. 4.14(a), is mainly dependent on the friction coefficient γ as previously discussed [68], the magnitude of the low-speed stopping peak is only mildly affected by encapsulating the nanotube in SiO_2.

The presence of amorphous carbon surrounding nanotubes, named α-CNTs by Nishino *et al.* [22] often occurs during their formation. Figure 4.14(b) shows the effect of an amorphous carbon layer surrounding the nanotube on the stopping force for protons moving along the nanotube axis, using $\epsilon_C(\omega)$. We find that the amorphous layer causes a reduction in the stopping force's peak, while significantly raising the high-speed "tail". This is due to the optical nature of the high energy antisymmetrically coupled dielectric-$(\sigma + \pi)$ channel plasmon, which tends to the bulk plasma frequency ω_p at long wavelengths as shown in Figs. 4.3(e) and 4.3(f), as expected for

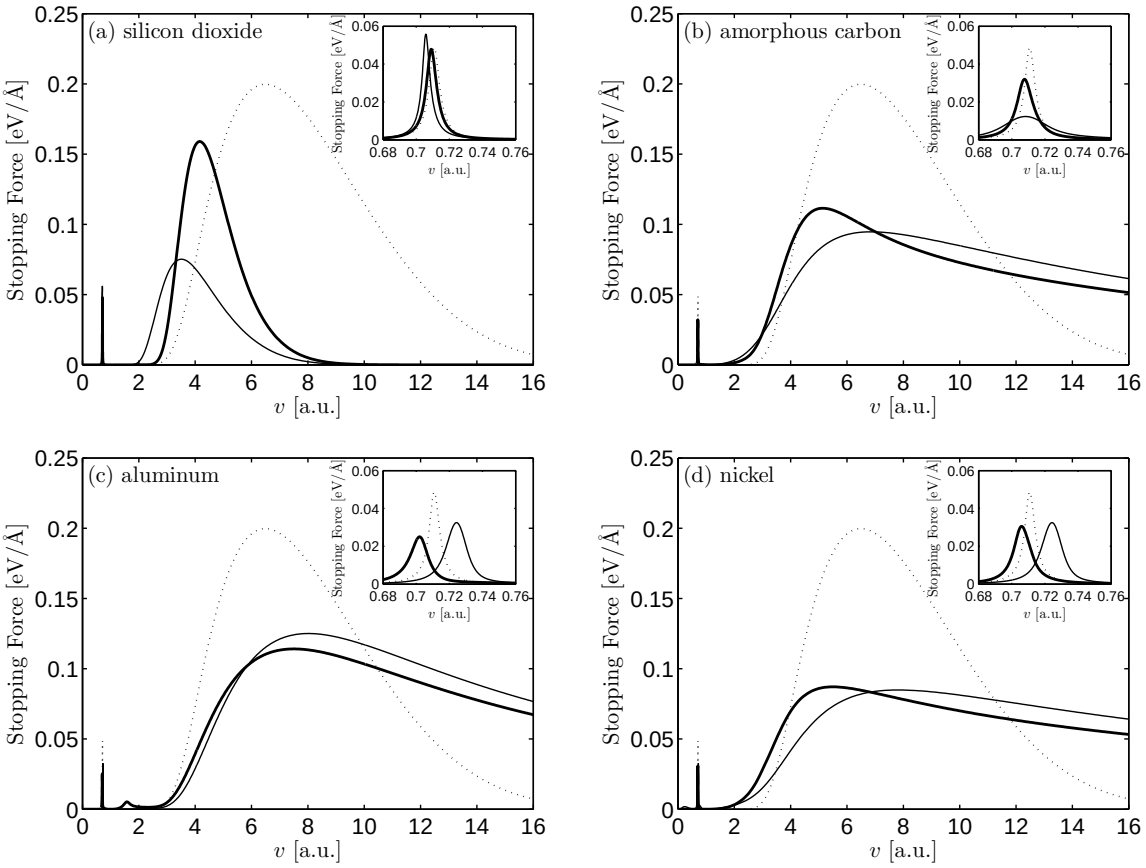

Figure 4.14: The stopping force in eV/Å on an proton travelling paraxially at $r_0 = 0$ with speed v in due to a CNT of radius $R = 7$ Å in vacuum (·····) and encapsulated by a channel with radius $r_{\text{out}} = 7$ Å (——), and $r_{\text{out}} = 8$ Å (——), of (a) silicon dioxide, $\epsilon_{\text{in}} = \epsilon_{\text{nt}} = 1$ and $\epsilon_{\text{out}} = \epsilon_{\text{SiO}_2} \approx 3.9$, (b) amorphous carbon, $\epsilon_{\text{in}} = \epsilon_{\text{nt}} = 1$ and $\epsilon_{\text{out}} = \epsilon_{\text{C}}(\omega)$, (c) aluminum, $\epsilon_{\text{in}} = \epsilon_{\text{nt}} = 1$ and $\epsilon_{\text{out}} = \epsilon_{\text{Al}}(\omega)$, and (d) nickel, $\epsilon_{\text{in}} = \epsilon_{\text{nt}} = 1$ and $\epsilon_{\text{out}} = \epsilon_{\text{Ni}}(\omega)$. We make use of a Drude type dielectric function [152] for amorphous carbon $\epsilon_{\text{C}}(\omega)$, aluminum $\epsilon_{\text{Al}}(\omega)$, and nickel $\epsilon_{\text{Ni}}(\omega)$, using the fitting parameters given in Tables C.1, C.2, and C.3 respectively from Abril *et al.* [153] and Kwei *et al.* [158, 147].

a Drude model dielectric. Applying the kinematic resonance condition, we notice that the high energy plasmon is crossed as v increases, which raises the high-speed stopping "tail". The quasi-

acoustic behaviour of the high energy plasmon acts to "smooth" the high-speed peak lowering the peak height. This suggests that when amorphous carbon surrounds the nanotube, the stopping force is not negligible (≈ 0.1 eV/Å) even at higher speeds ($v \approx c/8$). Since an amorphous carbon layer is a potential model for CNT "bundles" and "ropes", these results have important applications to the area of ion channelling [47, 48, 49, 200, 87, 201]. In addition, the inset shows that the low-speed peak in stopping is also reduced in magnitude by the presence of amorphous carbon around the nanotube.

In Fig. 4.14(c), we show the stopping force on an ion moving with speed v along the axis of a CNT in an aluminum channel, modelled using the Drude model dielectric function $\epsilon_{\rm Al}(\omega)$. Although less physically realizable than other metallic coatings [23], due to aluminum's tendency to "clump" into nano-rings [27], the single sharp peak of aluminum's dielectric function provides a means of comparison with the plasmon energy calculations shown in Figs. 4.3 and 4.4. The elevation of the antisymmetrically coupled metal-$(\sigma + \pi)$ channel plasmon branches to higher frequencies, seen in Fig. 4.3(e) and 4.3(f), causes a shift of the main stopping force peak to higher speeds, while the lowering of the symmetrically coupled metal-$(\sigma + \pi)$ branches causes a reduction of stopping at lower speeds, when compared to stopping in a nanotube alone. The intricacies of the avoided crossings due to plasmon hybridization between the symmetrically coupled $\sigma + \pi$-metallic and π branches in the presence of the aluminum channel, shown in Fig. 4.3(f) and Fig. 4.4, gives rise to multiple low-speed peaks in the stopping force, as well as to a peculiar nonmonotonic shift of the main low-speed peak derived from the quasi-acoustic π plasmon branch $m = 0$, as shown in the inset of Fig. 4.14(c), and the suppressed low-speed peaks at $v \approx 0.2$ for $\Delta r_b = 0$ and $v \approx 1.579$ for $\Delta r_b = 1$ Å derived from the symmetrically coupled metal-$(\sigma + \pi)$ plasmon branch for $m = 0$.

In Fig. 4.14(d) and Fig. 4.15 we model the stopping force due to a metallic channel of nickel [26, 24, 25] using $\epsilon_{\rm Ni}(\omega)$, with an encapsulated CNT of radius $R = 7$ Å, for protons moving paraxially at r_0 = 0, 3 Å, and 5 Å. The stopping forces given previously for a metallic channel by Arista [44], and a CNT [68] are provided for comparison with the coupled nanotube–metallic channel system. One can observe a reduction of the main stopping peak in the combined system in comparison with the nanotube alone, as well as a rise in the high-speed tail, due to the quasi-acoustic antisymmetrically coupled metal-$(\sigma + \pi)$ branch, as discussed for amorphous carbon. However, these effects are less pronounced than in the cases of amorphous carbon and aluminum

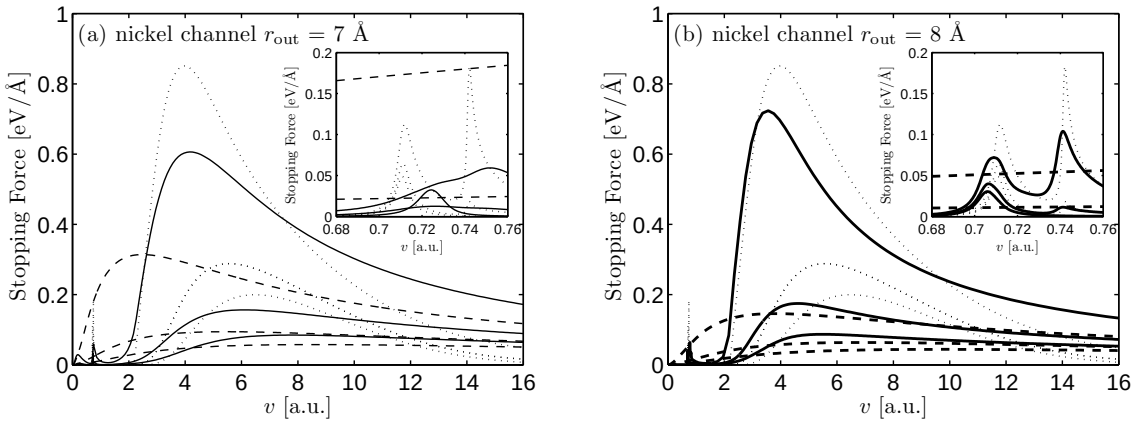

Figure 4.15: The stopping force in eV/Å on a proton travelling paraxially at r_0 = 0 (lower), 3 Å (middle), and 5 Å (upper) with speed v, due to a CNT of radius $R = 7$ Å in vacuum (·····) and encapsulated by a nickel channel, $\epsilon_{\rm in} = \epsilon_{\rm nt}$ = 1, and $\epsilon_{\rm out} = \epsilon_{\rm Ni}(\omega)$, plotted for (a) $r_{\rm out} = 7$ Å (——), and (b) $r_{\rm out} = 8$ Å (——), and for metallic channels alone of radius (a) $r_{\rm out} = 7$ Å (- - - -) and (b) $r_{\rm out} = 8$ Å (- - - -) [44]. We make use of a Drude type dielectric function [152] for nickel, $\epsilon_{\rm Ni}(\omega)$, using the fitting parameters given in Table C.3 from Kwei *et al.* [158, 147].

channels, shown in Figs. 4.14(b) and 4.14(c), respectively. This is due to the broadness of the nickel dielectric function, when compared with the simpler dielectrics functions of amorphous carbon and aluminum, as shown in Fig. C.1 of Appendix C. It is interesting to note that, for zero gap between the nanotube and the channel, the presence of nickel strongly amplifies the low-speed stopping of the nanotube as the proton gets closer to the nanotube walls, yielding a third peak due to the symmetrically coupled metal-$(\sigma + \pi)$ plasmon branches. However, for $\Delta r_b = 1$ Å, the peak due to the symmetrically coupled metal-$(\sigma + \pi)$ plasmon branches is completely suppressed in a nickel channel, unlike the case of an aluminum channel shown in Fig. 4.14(c).

In Fig. 4.16 we model the stopping force due to a metallic wire of nickel [28, 26, 23, 29], using $\epsilon_{\rm Ni}(\omega)$ from Kwei *et al.* [158] for the dielectric function of nickel, encapsulated by a CNT of radius $R = 7$ Å. The stopping forces given previously for a metallic wire by Arista, [154] and a CNT [68], are provided for comparison with the coupled nanotube–metallic wire system. In Fig. 4.16, we see a broadening of the main stopping peak of the combined system towards higher speeds, when compared to an isolated nanotube, which represents a significant reduction

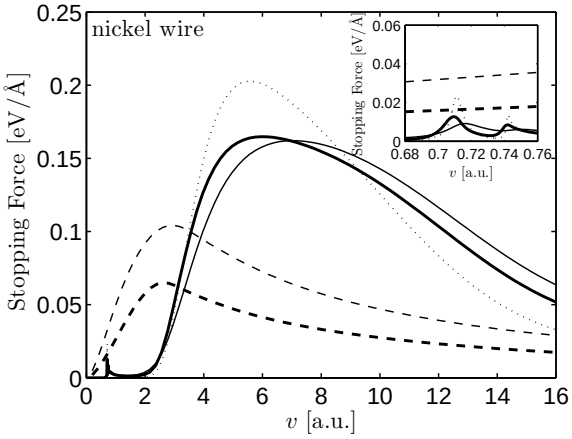

Figure 4.16: The stopping force in eV/Å on an proton travelling paraxially at $r_0 = 3R/2 = 10.5$ Å with speed v due to a carbon nanotube of radius $R = 7$ Å in vacuum (·····) and encapsulating nickel wire of radius $r_{\rm in} = 7$ Å (——), and $r_{\rm in} = 6$ Å (——), and for metallic wires alone of radius $r_{\rm in} = 7$ Å (- - - -) and $r_{\rm in} = 6$ Å (- - - -) [44]. We make use of a Drude type dielectric function [152] for nickel, $\epsilon_{\rm Ni}(\omega)$, using the fitting parameters given in Table C.3 from Kwei *et al.* [158, 147].

of the low-speed stopping and an even more substantial increase in the high speed stopping of the nickel wire alone. This indicates that nanotubes should provide effective "insulation" for encapsulated nano-wires, especially at low speeds. The low-speed inset of Fig. 4.16 shows the stopping force in the range $v \in [0.08, 0.09]\Omega_{\rm p}R \approx$ [0.67,0.76]. The substantial stopping force due to a bare nickel wire is nearly completely suppressed by the presence of the encapsulating nanotube, whereas the two peaks coming from the $m = 0$ and $m = 1$ branches of the π plasmons appear to be substantially broadened by the presence of nickel.

As discussed in Appendix C, we may model a CNT immersed in water, as shown schematically in Fig. 4.17, using the Drude-type dielectric function for water developed by Emfietzoglou *et al.* [207, 208] based on the optical data of Hayashi *et al.* [209]. We find that the stopping force for SWNTs surrounded by water is strongly effected by both the dielectric boundary separation $\Delta r_b \equiv |r_{\rm out} - R|$ between the dielectric boundary layer and the nanotube wall, and the cutoff of the dielectric function at the ionization energy $E_c = 7$ eV.

Figure 4.18 shows the stopping force in eV/Å versus speed v of an proton travelling paraxially

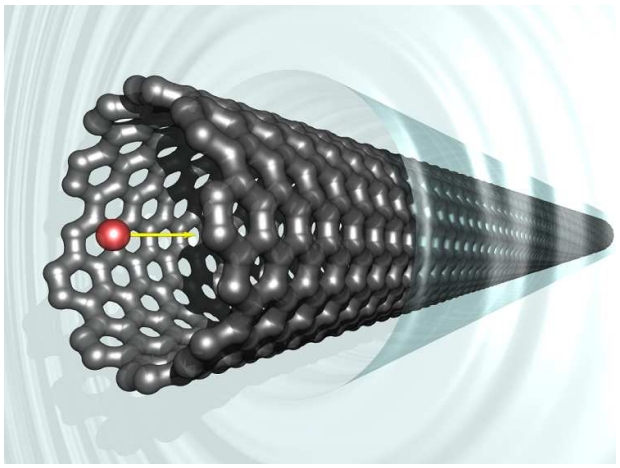

Figure 4.17: Schematic of an (11,9) SWNT immersed in water.

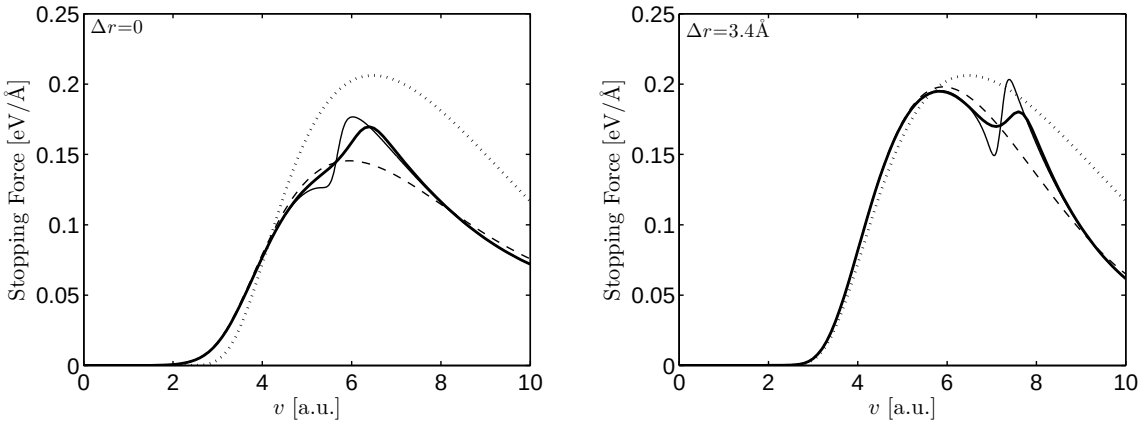

Figure 4.18: The stopping force in eV/Å, plotted versus speed v in on an proton travelling paraxially at r_0 = 0 due to an (11,9) SWNT of radius $R = 6.89$ Å alone (·····), and surrounded by water with boundary separation $\Delta r_b = |r_{\text{out}} - R|$ = 0 and 3.4 Å, calculated using a dielectric function with a sharp cutoff (——), no cutoff (- - - -), and a smoothed cutoff (——) [149].

at $r_0 = 0$, for a dielectric boundary separation of $\Delta r_b = 0$ and 3.4 Å, calculated using a sharp cutoff, smooth cutoff, and no cutoff of the ionization energy at $E_c = 7$ eV. One notices from this figure that the stopping force at the axis of the nanotube is rather insensitive to the presence of water for low proton speeds, as opposed to the high-speed region. More interestingly, structures

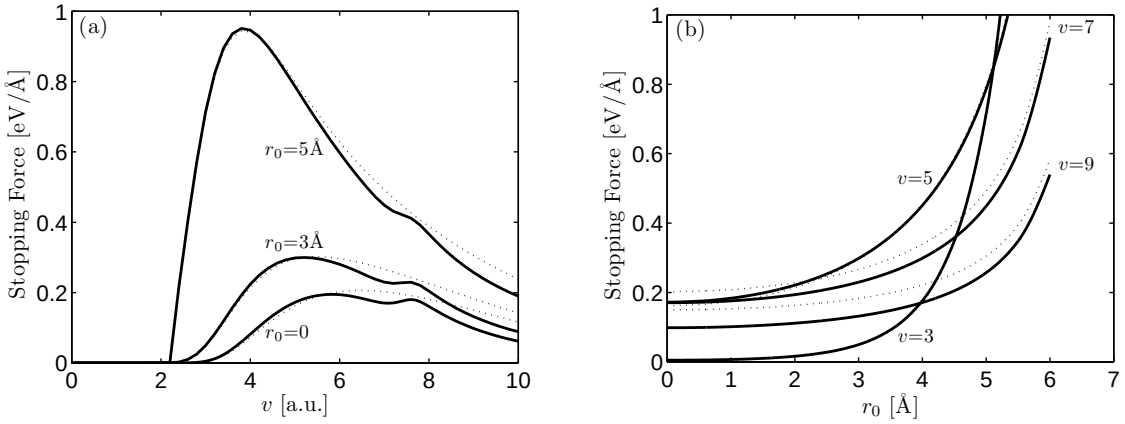

Figure 4.19: The stopping force in eV/Å plotted versus (a) speed v for a proton travelling paraxially at $r_0 = 0$, 3, and 5 Å, and (b) radial distance r_0 in Å for a proton travelling paraxially with speed $v = 0$, 3, 5, 7, and 9 due to a single-walled (11,9) CNT of radius $R = 6.89$ Å alone (·····), and in water with boundary at $r_{\rm out} = 10.29$ Å (——) [149].

appear in the stopping force curve related to the ionization threshold at E_C in the imaginary part of the dielectric function. These structures are more pronounced for sharper transition regions Δ of the cutoff at E_C as defined in Appendix C, and their positions depend on the separation Δr_b between the nanotube and the water boundary. Given the strong dependence of our results on the parameters Δ and Δr_b, it is desirable to physically motivate the values to be used in modelling the effects of water on the nanotube's dielectric response.

Figure 4.19(a) shows the stopping force in eV/Å versus speed v for a proton travelling paraxially at $r_0 = 0$, 3, and 5 Å, for a dielectric boundary separation of $\Delta r_b \approx 3.4$ Å, calculated using a smooth cutoff of the ionization energy at $E_C = 7$ eV. Figure 4.19(b) shows the stopping force in eV/Å versus radial distance r_0 in Å for an ion travelling paraxially with speed $v = 0$, 3, 5, 7, and 9, for a dielectric boundary separation of $\Delta r_b \approx 3.4$ Å, calculated using a smooth cutoff of the ionization energy at $E_C = 7$ eV. These figures confirm that the above conclusions on the effects of water on stopping force are also true when the proton gets close to the nanotube wall.

As shown in Fig. 4.18 and Fig. 4.19, the main effect of the surrounding water is to reduce the magnitude of the stopping force for protons channelled at high speeds. This may be explained by considering the resonance condition, $\omega = kv$, for electronic excitations in the system by the pro-

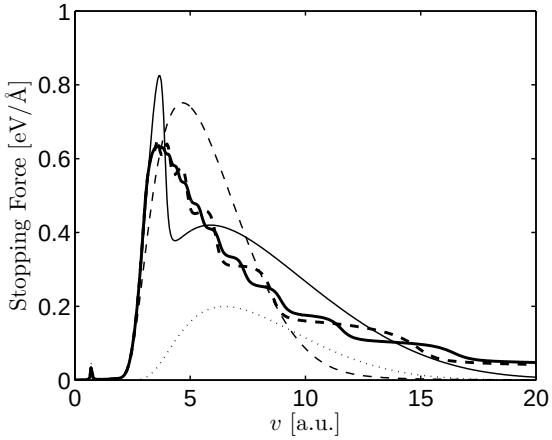

Figure 4.20: Stopping force in eV/Å versus speed v for a proton moving along the axis of a SWNT with radius $R = 3.6$ Å (- - - -), $R = 7$ Å (·····), DWNT with radii $R_1 = 3.6$ Å and $R_2 = 7$ Å (——), MWNTs with radii $R_n = 3.6 + 3.4n$ Å, with $N = 10$ walls (- - - -) and $N = 20$ walls (——) [145, 148].

ton moving paraxially at speed v, as follows. At low frequencies (say, $\omega \approx 5$ eV), the dielectric function of water may be approximated as $\epsilon_{\rm w} \approx 1.9$, so that the surrounding water "screens" the electrostatic interaction between the nanotube electrons. This suppresses the nanotube's plasmon frequency at long wavelengths, thus reducing the high-speed magnitudes of the stopping force and self energy. On the other hand, at high frequencies (say, $\omega > 17$ eV), the real part of the dielectric function of water tends to one, so that, at shorter wavelengths, the nanotube's plasmon frequency is unchanged by the presence of water. This leaves both the stopping force and self energy for protons channelled at low speeds largely unaffected by the surrounding water.

DWNTs and MWNTs in Vacuum

We now calculate the velocity dependence of the stopping force for a particle moving along the axis ($r_0 = 0$) of a DWNT, and show the results in Fig. 4.20(a). For the sake of comparison, also shown in Fig. 4.20(a) are the stopping forces for the cases of a particle moving along the axis of SWNTs, having radii $R = 3.6$ Å and $R = 7$ Å. It should be noted that only the $m = 0$ plasmon modes can contribute to the energy losses in the case $r_0 = 0$, since $I_m(0) = \delta_{m,0}$

due to cylindrical symmetry. Clearly, there exists an overall threshold of $v \gtrsim 2$ for the plasmon excitation. While the SWNT cases show the characteristic, broadly peaked structures seen earlier [55, 143], the stopping in the DWNT shows some novel structure at $v \approx 4$ in the form of a relatively narrow peak superimposed on the low-velocity slope of a broad structure. This broad structure takes intermediate values between the two SWNT cases at the intermediate velocities, but clearly surpasses them both at higher speeds, indicating a strong positive interference, or in-phase motion of the two fluids on a DWNT. On the other hand, the narrow peak at phase speed $v \approx 4$ is likely a consequence of a large-amplitude, out-of-phase motion of those fluids [61, 205], which is triggered by the close matching of the projectile speed and the phase velocity of the quasi-linear, lower $m = 0$ plasmon mode in Fig. 4.5(a). This resonant increase of the energy deposition into the collective excitation modes indicates the onset of a possible drift instability of the charged fluids on a DWNT [61].

The results shown in Fig. 4.20(b) display unexpectedly strong effects of the increasing number of nanotube walls, in the form of uneven interference patterns. We find that the bulk of its high- and intermediate- speed dependence comes from the high-frequency group of $\sigma + \pi$ plasmons in Fig. 4.5(b), with an apparent threshold at about $v \gtrsim 2$. On the other hand, the low-frequency $m = 0$ mode of degenerate π plasmons gives much weaker stopping force in the sub-threshold region in the form of a narrow peak for proton speeds v satisfying the kinematic condition for the π plasmon $\omega_- = \frac{\sqrt{3}}{4} v_F k \approx 0.71k$.

In Fig. 4.21, we study situations where the projectile still moves parallel to the nanotube axis, but at finite radial distances of $r_0 = R_1 - d/2 = 1.9$ Å, (inside the inner cylinder), $r_0 = (R_1 + R_2)/2 = 5.3$ Å, (midway between the two cylindrical surfaces), and $r_0 = R_2 + d/2 = 8.7$ Å, (outside the outer cylinder), so that it always stays at the fixed distance $d/2 = 1.7$ Å, from the nearest wall(s) of the DWNT. In such cases, all m modes contribute to the plasmon excitations. The results for stopping forces in these three cases are shown in Fig. 4.21, indicating that the narrowly-peaked structure at $v \approx 4$ has been partly merged into the broad structures in the cases of the particle travelling inside or outside the nanotube, whereas the particle moving in between the two cylindrical surfaces shows the most massive energy losses with the narrow peak completely disappeared, or immersed into the broad structure.

In Fig. 4.22, we show how the stopping force S depends on radial distance r_0 in a MWNT with $N = 10$ walls for proton speeds $v = 1$, 6 and 10. S is seen to increase sharply at all

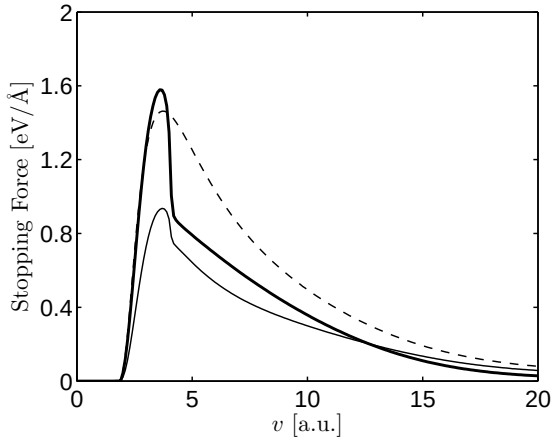

Figure 4.21: Stopping force in eV/Å versus speed v for a proton moving parallel to the axis of a DWNT with radii $R_1 = 3.6$ Å and $R_2 = 7$ Å at the radial distances $r_0 = R_1 - d/2$ (——), $r_0 = R_2 + d/2$ (——), and $r_0 = (R_1 + R_2)/2$ (- - - -), where $d = R_2 - R_1 = 3.4$ Å [145].

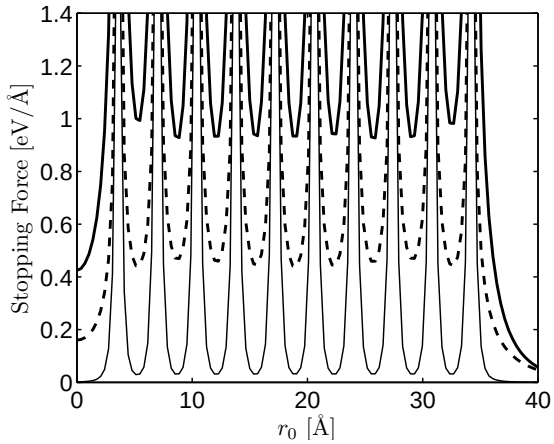

Figure 4.22: Stopping force in eV/Å versus radial distance r_0 in Å for a proton moving paraxially through a $N = 10$ walled nanotube at speeds $v = 1$ (——), $v = 6$ (——), and $v = 10$ (- - - -) [148].

displayed speeds as the proton approaches the nanotube walls. More interestingly, although the sub-threshold stopping at $v = 1$ is obviously suppressed in the central region and outside the

nanotube, it is seen to take small but non-negligible values in the inter-wall regions, owing to increasing contributions of the $m > 0$ modes of π plasmons as r_0 takes increasing values.

4.4 Self Energy (Image Potential)

The self energy, or image potential $E_{\rm self}$, for a single ion of charge Q at $\mathbf{r} = \mathbf{r}_0(t)$ is defined by $E_{\rm self} = (Q/2)\Phi_{\rm ind}(\mathbf{r}_0(t), t)$, where $\Phi_{\rm ind} = \Phi_{\rm nt} + \Phi_{\rm in} + \Phi_{\rm out} + \Phi_{\rm bulk}$ is the total potential induced by the ion on the system, and $\Phi_{\rm bulk} = (1 - \epsilon_{\rm sc})\Phi_{\rm sc}$ is the potential induced in the bulk by the ion, with $\Phi_{\rm sc}$ defined via (4.20). As with the stopping force, for large wave numbers, $kR \gg 1$, the FB transform of the image potential has a factor of $e^{-k|R-r_0|}/k$, so that the dielectric function's momentum dependence may be neglected when $k \gg 1/|R - r_0|$.

CNTs in Vacuum

The most important quantities, relevant to the effects of the nanotube polarization on the motion of the external charge, are its self-energy and the energy loss rates, which are calculated from the local properties of the "induced" potential at the position of the charge. We show in Fig. 4.23(a) and 4.24(a) the dependence of the self-energy on the radial position r_0 and the speed v for a proton moving parallel to the axis of a nanotube with radius $R = 7.4$ Å. For low speeds, one can identify in Figs. 4.23(a) and 4.24(a) the potential well outside the nanotube which gives rise to the toroidal image states [51] and [82], whereas an approximately symmetrical well exists inside the nanotube, which would provide a force pulling away a channelled charged particle toward the walls of the nanotube [202]. Once the speed exceeds the threshold value for the onset of the wake effect, it appears from Figs. 4.23(a) and 4.24(a) that the potential wells on both sides become substantially shallower but nevertheless remain rather long-ranged. The dependence of the self-energy on the projectile velocity v and the radial distance r_0 from the axis of the DWNT is shown in Figs. 4.23(b) and 4.24(b), clearly exhibiting attractive wells close to the surfaces of each of the two cylinders, which become shallower with increasing projectile speed. An intriguing ridge in the self-energy occurs for all radial distances (except midway between the two cylinders), at a speed of $v \approx 4$, which is clearly in correlation with the onset of a drift instability seen in the stopping force in Fig. 4.20(a) and Fig. 4.21.

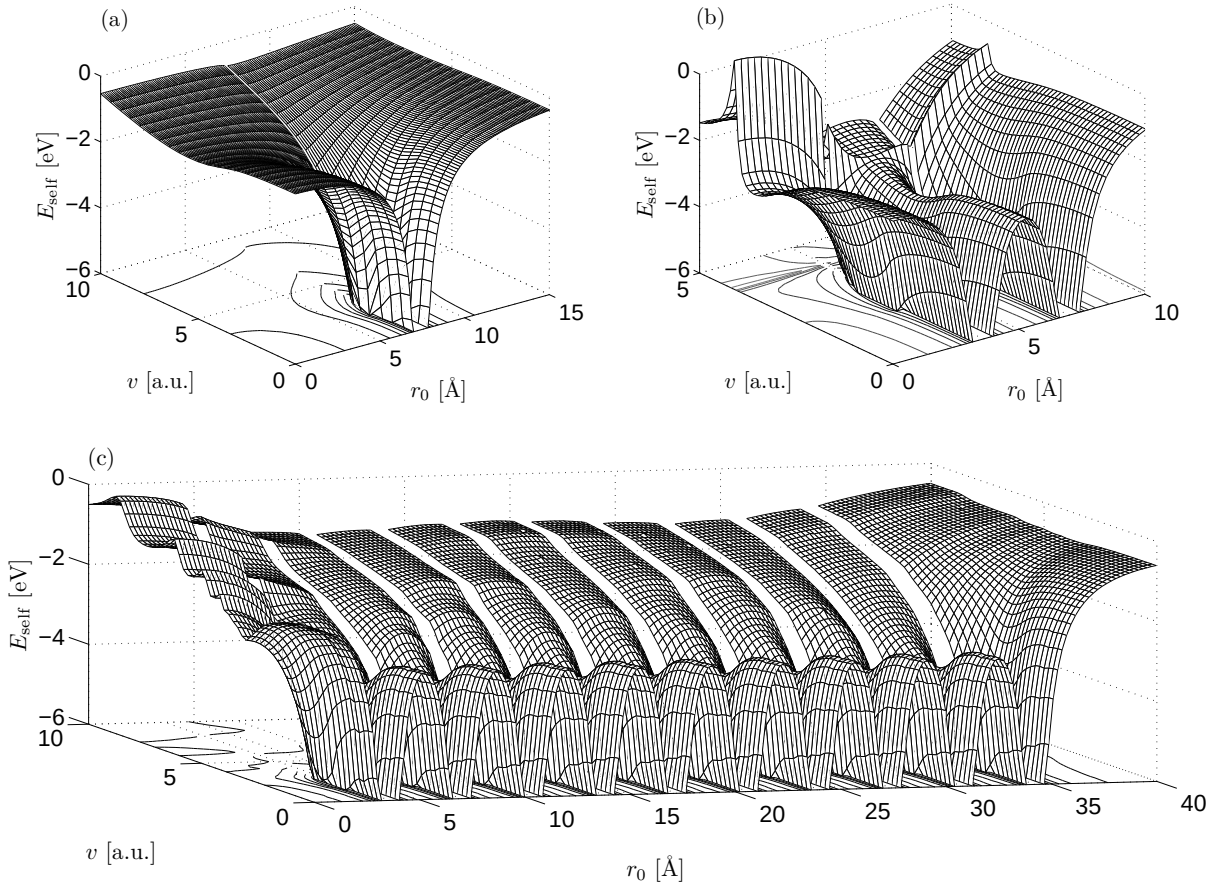

Figure 4.23: The self energy (image potential) $E_{\rm self}$ in eV versus position r_0 in Å and speed v for a proton moving paraxially to (a) SWNT of radius $R = 7.4$ Å, (b) DWNT of radii $R_1 = 3.6$ Å and $R_2 = 7$ Å, and (c) $N = 10$ MWNT with radii $R_n = 3.6 + 3.4n$ Å. The level curves show the increments $\Delta E_{\rm self} = 1$ eV [144, 145, 148].

In Figs. 4.23(c) and 4.24(c), we show the dependences of self-energy on speed v and on radial distance r_0 for a proton traversing paraxially a MWNT with $N = 10$ walls. It is interesting to notice that the interference patterns in the v-dependence, which are most pronounced inside the innermost cylinder, gradually disappear when the proton trajectory traverses the outer walls, so that the proton self-energy outside the outermost wall resembles the dynamical image potential above the surface of a thick slab of graphite. It is also interesting to note that the proton self-

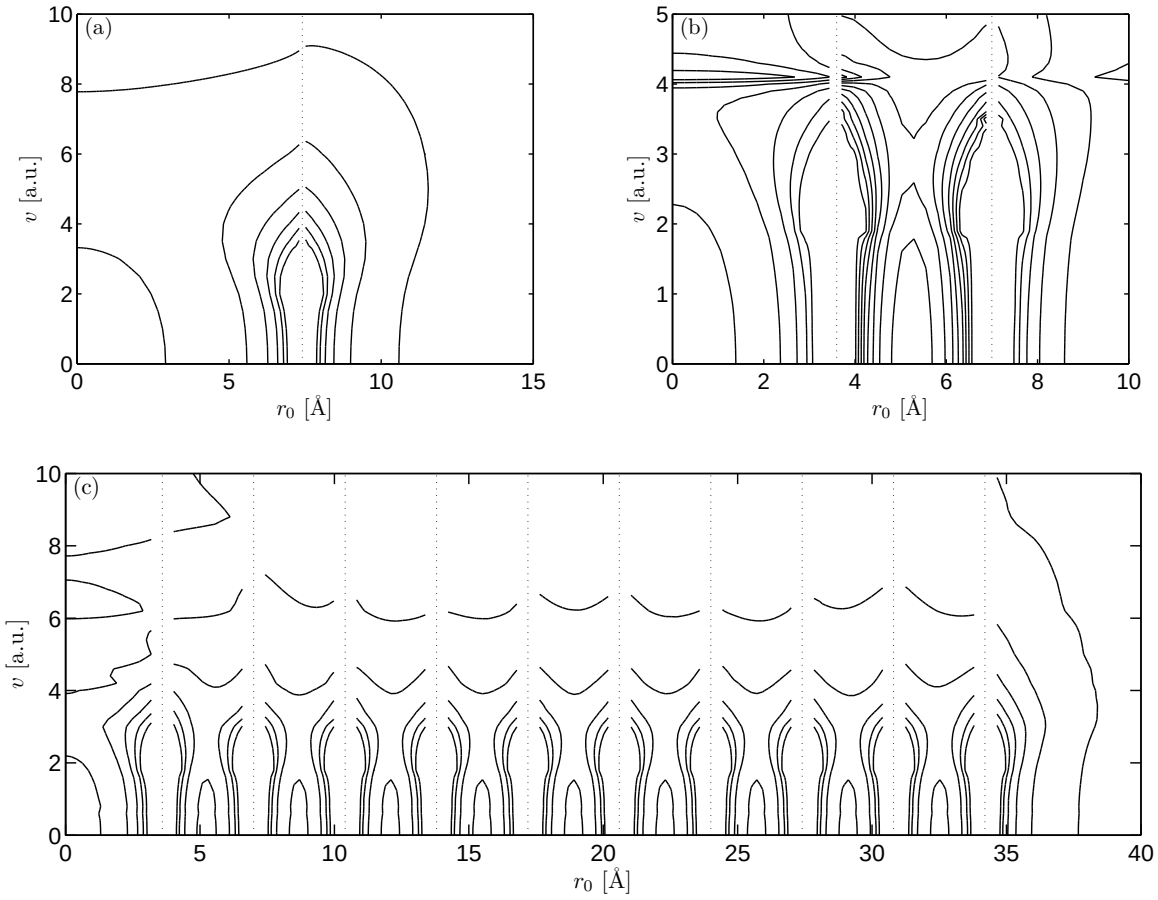

Figure 4.24: The self energy (image potential) $E_{\rm self}$ in eV versus position r_0 in Å and speed v for a proton moving paraxially to (a) SWNT of radius $R = 7.4$ Å, (b) DWNT of radii $R_1 = 3.6$ Å and $R_2 = 7$ Å, and (c) $N = 10$ MWNT with radii $R_n = 3.6 + 3.4n$ Å. The level curves show the increments $\Delta E_{\rm self} = 1$ eV [144, 145, 148].

energy is consistently much lower in the inter-wall regions than outside of the nanotube or inside its central region, especially at low proton speeds, indicating that the inter-wall regions may be energetically more favourable for proton intercalation in MWNTs.

In order to illustrate the differences in the self-energy among SWNTs, DWNTs, and MWNTs, we next consider a proton moving along the axis ($r_0 = 0$) of an N-walled nanotube, and calculate the dependences of self-energy on proton speed v for $N = 1$, 2, 10, and 20 walls. The results,

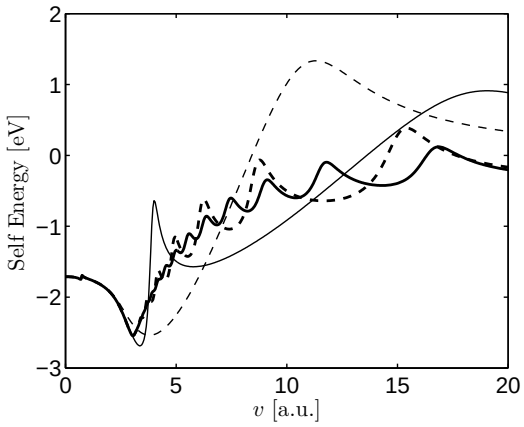

Figure 4.25: The self energy (image potential) in eV versus speed v for a proton moving along the axis of a SWNT with radius $R = 3.6$ Å (- - - -), DWNT with radii $R_1 = 3.6$ Å and $R_2 = 7$ Å (——), MWNTs with radii $R_n = 3.6 + 3.4n$ Å, with $N = 10$ walls (- - - -) and $N = 20$ walls (——) [145, 148].

shown in Fig. 4.25, display unexpectedly strong effects of the increasing number of nanotube walls, in the form of uneven interference patterns. While the effects of π plasmons are seen to be quite negligible at $v \approx \frac{\sqrt{3}}{4} v_F \approx 0.71$, one notices that the self-energy can take positive values for certain high speeds, $v \gg 1$, depending on the number of nanotube walls.

SWNTs with Dielectrics

The optical dielectric function of a nickel clamp surrounding a SWNT, shown schematically in Fig. 4.13, or a nickel clamp embedded in a SWNT, is described in detail in Appendix C. Figure 4.26 shows the speed dependence of the self energy for a proton travelling paraxially at $r_0 = 0$, 3, and 5 Å inside a CNT of radius $R = 7$ Å encapsulated in nickel channels of radii $r_{\rm out} = 7$ Å and $r_{\rm out} = 8$ Å respectively, with the self energies for the nanotube and nickel channels alone provided for comparison. We notice that the image potentials for the nanotube alone and the nickel channels alone are quite different, so that the image potential for the combined system interpolates between them in such a way that it follows the potential for the nanotube alone in the low-speed regime, $v \lesssim 0.25\ \Omega_{\rm p} R \approx 2$, and approaches the channel potentials at high speeds.

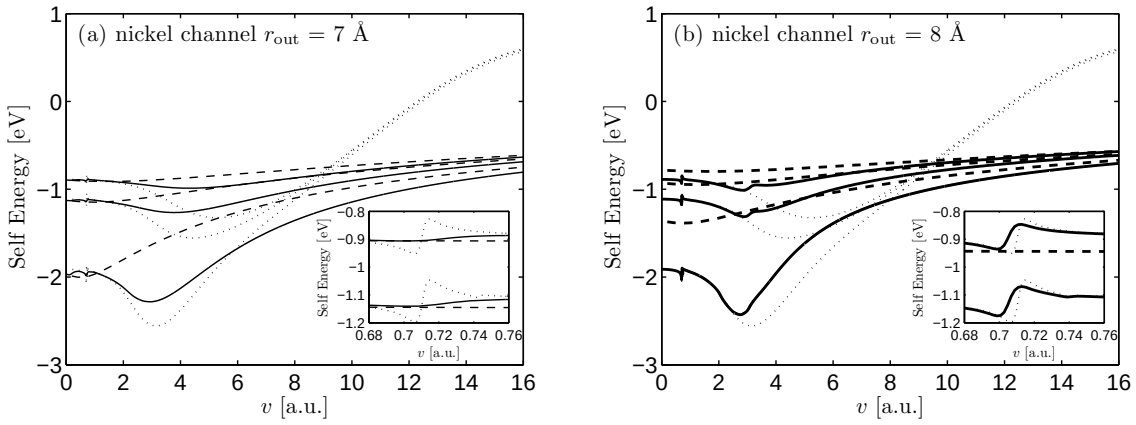

Figure 4.26: The self energy (image potential) in eV on a proton travelling paraxially at r_0 = 0 (upper), 3 Å (middle), and 5 Å (lower), with speed v, due to a CNT of radius $R = 7$ Å in vacuum (·····) and encapsulated by a nickel channel of radius (a) $r_{\rm out} = 7$ Å (——), and (b) $r_{\rm out} = 8$ Å (——), and for metallic channels alone of radius (a) $r_{\rm out} = 7$ Å (- - - -) and (b) $r_{\rm out} = 8$ Å (- - - -). We make use of a Drude type dielectric function [152] for nickel, $\epsilon_{\rm Ni}(\omega)$, using the fitting parameters given in Table C.3 from Kwei *et al.* [158, 147].

This may be explained by applying the kinematic resonance condition $\omega = kv$ to the dielectric-$(\sigma + \pi)$ channel plasmons shown in Fig. 4.3(e) and Fig. 4.3(f), and noticing that they behave qualitatively like the nanotube $\sigma + \pi$ plasmon branches at low speeds, and the metal channel plasmon branches at very high speeds.

Figure 4.27 shows the radial dependence of the self energy for a proton travelling paraxially with speed $v = 0$, $0.5\ \Omega_{\rm p}R \approx 4.217$, and $1\ \Omega_{\rm p}R \approx 8.435$, inside a nanotube encapsulated in a nickel channel Fig. 4.27(a) and Fig. 4.27(b) and outside a nanotube encapsulating a nickel wire Fig. 4.27(c) and Fig. 4.27(d). The cases for a nanotube alone are also shown for comparison. While the effects of the nickel channel are seen in Fig. 4.27(a) and Fig. 4.27(b) to be fairly strong except at zero speed, one notices in Fig. 4.27(c) and Fig. 4.27(d) that, even at higher speeds, for a proton sufficiently far from the nanotube, the nanotube almost completely screens the encapsulated nickel wire. At low speeds, which are of interest for toroidal electron image states around CNTs [51, 52], our results indicate that there will be very little, if any, influence on the wave function and the energy levels of such states coming from an embedded nickel wire.

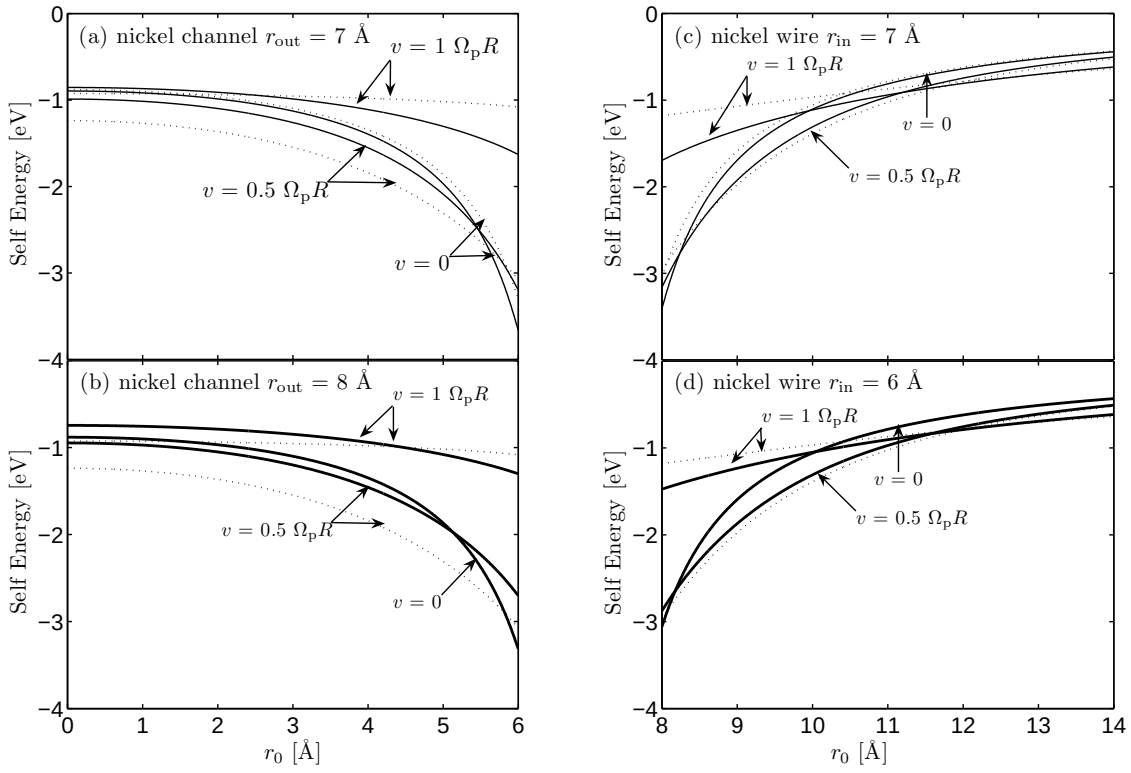

Figure 4.27: The self energy (image potential) in eV on a proton travelling paraxially at r_0 in Å, with speed $v = 0, 0.5\ \Omega_{\rm p}R \approx 4.217$, and $1\ \Omega_{\rm p}R \approx 8.435$, due to a CNT of radius $R = 7$ Å in vacuum (·····) and encapsulated by a nickel channel of radius (a) $r_{\rm out} = 7$ Å (——) and (b) $r_{\rm out} = 8$ Å (——), and encapsulating a nickel wire of radius (c) $r_{\rm in} = 7$ Å (——) and (d) $r_{\rm in} = 6$ Å (——) [44]. We make use of a Drude type dielectric function [152] for nickel, $\epsilon_{\rm Ni}(\omega)$, using the fitting parameters given in Table C.3 from Kwei *et al.* [158, 147].

As discussed in Appendix C and Sect. 4.3, we may model a CNT immersed in water as shown in Fig. 4.17, using the Drude-type optical dielectric function for water developed by Emfietzoglou *et al.* [207, 208] based on the optical data of Hayashi *et al.* [209]. As with the stopping force, we find that the image potential for SWNTs surrounded by water is strongly effected by both the dielectric boundary separation between the dielectric boundary layer and the nanotube wall, and the method of cutoff of the dielectric function at $E_c = 7$ eV.

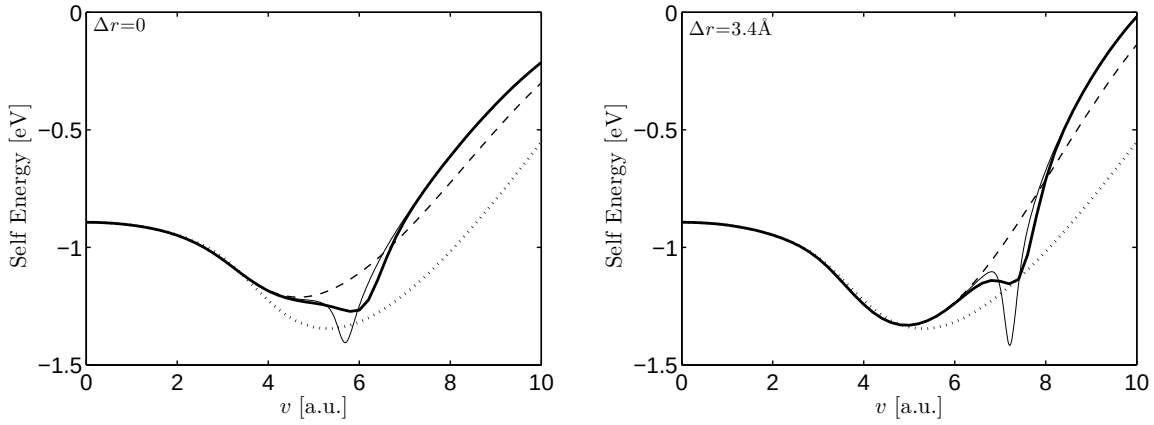

Figure 4.28: The self energy in eV, plotted versus speed v of a proton travelling paraxially at r_0 = 0 due to an (11,9) SWNT of radius $R = 6.89$ Å alone (·····), and surrounded by water with boundary separation $\Delta r_b = |r_{\rm out} - R|$ = 0 and 3.4 Å, calculated using a dielectric function with a sharp cutoff (——), no cutoff (- - - -), and a smoothed cutoff (——) [149].

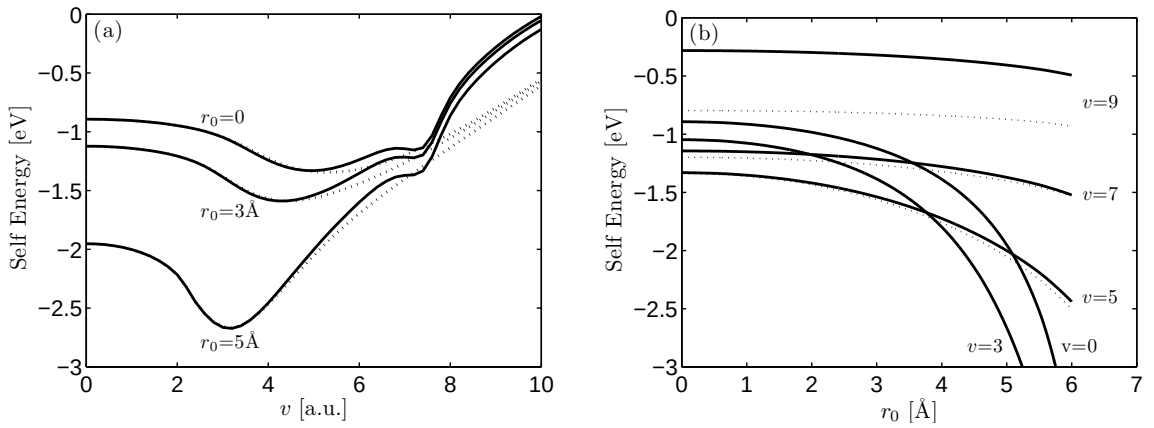

Figure 4.29: The self energy (image potential) in eV plotted versus (a) speed v for a proton travelling paraxially at $r_0 = 0$, 3, and 5 Å and (b) radial distance r_0 in Å for a proton travelling paraxially with speed $v = 0$, 3, 5, 7, and 9 due to a single-walled (11,9) CNT of radius $R = 6.89$ Å alone (·····), and in water with boundary at $b = 10.29$ Å (——) [149].

Figure 4.28 shows the self energy in eV versus speed v of a proton travelling paraxially at $r_0 = 0$ for a dielectric boundary separation of $\Delta r_b = 0$ and 3.4 Å, calculated using a sharp cutoff, smooth cutoff, and no cutoff of the ionization energy at $E_c = 7$ eV. As with the stopping force calculations shown in Fig. 4.18, one notices in Fig. 4.28 that the self energy at the axis of the nanotube is insensitive to the presence of water for low proton speeds, as opposed to the high-speed region. There also appear structures in the self-energy curve related to the ionization threshold at E_C in the imaginary part of the dielectric function. As with the stopping force shown in Fig. 4.18, these structures are more pronounced for sharper transition regions Δ of the cutoff at E_C discussed in Appendix C, and their positions depend on the separation Δr_b between the nanotube and the water boundary. Given the strong dependence of both the stopping force and self energy on the parameters Δ and Δr_b, it is desirable to physically motivate the values to be used in modelling the effects of water on the nanotube's dielectric response.

Figure 4.29(a) shows the self energy in eV versus speed v for a proton travelling paraxially at $r_0 = 0$, 3, and 5 Å, for a dielectric boundary separation of $\Delta r_b \approx 3.4$ Å, calculated using a smooth cutoff of the ionization energy at $E_C = 7$ eV. Figure 4.29(b) shows the self energy in eV, versus radial distance r_0 in Å for an ion travelling paraxially with speed $v = 0$, 3, 5, 7, and 9, for a dielectric boundary separation of $\Delta r_b \approx 3.4$ Å, calculated using a smooth cutoff of the ionization energy at $E_C = 7$ eV. These figures confirm that the above conclusions on the effects of water on stopping and image force are also true when the proton gets close to the nanotube wall.

Chapter 5

3D Kitagawa Model

In the development of the 2D hydrodynamic model, we assumed that all valence electrons on the CNT were confined to a thin cylindrical shell. This same assumption is used in 2D RPA models [102] and in the study of thin macroscopic cylindrical conductors. However, SWNTs typically have radii of ~ 7 Å, whereas the "atomic radius" of a carbon atom is ~ 0.7 Å. This makes the assumption of a 2D equilibrium electron density questionable for the case of CNTs.

In the following chapter we will use a Thomas-Fermi [162], Thomas-Fermi-Dirac [163], Molière [164, 165], and Cruz [166, 167] model to calculate the radial equilibrium electron density $n_0(r)$ on a CNT in the jellium approximation for the carbon ions. Using these densities in a 3D Kitagawa model [161], we calculate the total stopping force on ions moving paraxial to the nanotube, which we shall compare with the stopping force obtained via the 2D hydrodynamic model.

5.1 Density Functional Theory in 3D

Following Parr and Yang's method (pp. 105–109 [127]), which was outlined in Chapter 2, we now obtain a density functional for the ground state energy of a 3D electron gas. Once again, we must obtain expressions for the Thomas-Fermi kinetic energy, T_{TF}, and the Dirac exchange energy, K, given in Eqns. (2.19) and (2.20) respectively, in terms of the 3D electron density n.

As we did in Chapter 2, we begin by assuming the spatial orbitals are plane waves, so that

$$\psi(\mathbf{k};\mathbf{r}) = \frac{e^{i\mathbf{k}\cdot\mathbf{r}}}{\sqrt{V}}, \tag{5.1}$$

$$\rho(\mathbf{r},\mathbf{r}') = \frac{2}{V}\sum_{\text{occupied }\mathbf{k}} e^{i\mathbf{k}\cdot(\mathbf{r}-\mathbf{r}')} \tag{5.2}$$

$$= \frac{1}{4\pi^3}\int_0^{k_F} dk k^2 \int d\phi \int d\theta e^{i\mathbf{k}\cdot(\mathbf{r}-\mathbf{r}')}\sin\theta, \tag{5.3}$$

where we have approximated the summation over occupied atomic levels by an integration over wave vector $\mathbf{k}$. The density $n(\mathbf{r}) = \rho(\mathbf{r},\mathbf{r})$ is then given by

$$n(\mathbf{r}) = \frac{k_F^3}{3\pi^2}. \tag{5.4}$$

Using Eqn. (5.3) for the 3D electron density matrix in Eqn. (2.19) we find the Thomas-Fermi kinetic energy term $T_{\text{TF}}[n]$ can be written

$$T_{\text{TF}}[n] = \frac{3}{10}(3\pi^2)^{2/3}\iiint d^3\mathbf{r}\; n^{5/3}(\mathbf{r}), \tag{5.5}$$

as shown in Appendix D.1 following the procedure of Parr and Yang pp. 106–108 [127]. The 3D Dirac exchange energy term may be obtained from Eqn. (2.20) to be

$$K[n] = \frac{3}{4}\left(\frac{3}{\pi}\right)^{1/3}\iiint d^3\mathbf{r}\; n^{4/3}(\mathbf{r}), \tag{5.6}$$

as shown in Appendix D.2. The full 3D Thomas-Fermi-Dirac-von Weizsäcker density functional is then given by

$$F[n] = \iiint d^3\mathbf{r}\left(C_{\text{TF}}n^{5/3}(\mathbf{r}) - C_x n^{4/3}(\mathbf{r}) + \frac{\lambda_W}{8}\frac{\|\vec{\nabla}n(\mathbf{r})\|^2}{n(\mathbf{r})} + \frac{1}{2}\iiint d^3\mathbf{r}'\,\frac{n(\mathbf{r}')n(\mathbf{r})}{\|\mathbf{r}-\mathbf{r}'\|}\right), \tag{5.7}$$

where $C_{\text{TF}} \equiv \frac{3}{10}(3\pi^2)^{2/3}$, $C_x \equiv \frac{3}{4}\left(\frac{3}{\pi}\right)^{1/3}$, and λ_W is the von Weizsäcker coefficient discussed in Chapter 2.

5.2 Equilibrium Electron Density

In the 2D hydrodynamic model, we assume that the electron density is confined to a thin cylindrical shell. Using this assumption, in Chapter 2 we obtained via Eqn. (2.56), the $\mathcal{O}(1)$ equation, an equilibrium electron density of $n_0(r) = Z\sigma_a\delta(r-R)$, where Z is the number of valence electrons per atom in the electron fluid, and σ_a is the atomic density. To evaluate the validity of this 2D approximation, we now employ a jellium approximation to calculate the radial equilibrium electron density per unit volume $n_0(r)$.

Thomas-Fermi Model

Following the method of Leys *et al.* [162], we begin by calculating the radial equilibrium electron density $n_0(r)$ numerically using the $\mathcal{O}(1)$ equation for the electron density, Eqn. (2.56). The functional derivative of the 3D density functional from Eqn. (5.7) is given by

$$\frac{\delta F[n]}{\delta n} = \frac{5}{3}C_{\mathrm{TF}}n^{2/3}(\mathbf{r}) - \frac{4}{3}C_x n^{1/3}(\mathbf{r}) + \frac{\lambda_W}{8}\left[\frac{\|\vec{\nabla}n(\mathbf{r})\|^2}{n^2(\mathbf{r})} - 2\frac{\nabla^2 n(\mathbf{r})}{n(\mathbf{r})}\right] + \iiint d^3\mathbf{r}'\,\frac{n(\mathbf{r}')}{\|\mathbf{r}-\mathbf{r}'\|}. \tag{5.8}$$

Substituting Eqn. (5.8) for $n_0(r)$ into the gradient of Eqn. (2.56), we find

$$\nabla^2\Phi_{\mathrm{at}} = \nabla^2\frac{\delta F[n_0]}{\delta n_0}, \tag{5.9}$$

so that

$$\begin{aligned} -4\pi Z\sigma_a\delta(r-R) = {} & \frac{5}{3}C_{\mathrm{TF}}\nabla^2 n_0^{2/3}(r) - \frac{4}{3}C_x\nabla^2 n_0^{1/3}(r) \\ & + \frac{\lambda_W}{8}\nabla^2\left[\frac{\|\vec{\nabla}n_0(r)\|^2}{n_0^2(r)} - 2\frac{\nabla^2 n_0(r)}{n_0(r)}\right] - 4\pi n_0(r), \end{aligned} \tag{5.10}$$

where the confining atomic potential Φ_{at} has been modelled using the jellium approximation for a SWNT.

Considering a simplified Thomas-Fermi model, $C_x = \lambda_W = 0$, we may write Eqn. (5.10) for $n_0(r)$ as

$$4\pi n_0(r) = \frac{(3\pi^2)^{2/3}}{2}\left[\frac{\partial^2}{\partial r^2} + \frac{1}{r}\frac{\partial}{\partial r}\right] n_0^{2/3}(r), \qquad r \neq R. \tag{5.11}$$

It is shown in Appendix E from Eqn. (5.10) that the boundary condition

$$-Z\sigma_a R = \frac{(3\pi^2)^{2/3}}{8\pi}\left[\left.\frac{\partial n_0^{2/3}(r)}{\partial r}\right|_{R^+} - \left.\frac{\partial n_0^{2/3}(r)}{\partial r}\right|_{R^-}\right], \tag{5.12}$$

holds on the nanotube wall, while the normalization condition

$$\int_0^\infty n_0(r) r dr = Z\sigma_a R, \tag{5.13}$$

ensures there is a unique solution $n_0(r)$.

By exploiting the symmetry of the system, we find the radial electric field on the nanotube axis should be zero, giving the further condition, as discussed in Appendix E, that

$$\left.\frac{\partial n_0(r)}{\partial r}\right|_{r=0} = 0. \tag{5.14}$$

We may now solve the system of Eqns. (5.11–5.14) for $n_0(r)$ numerically using a backward difference scheme employing a "shooting" method. In this scheme, using a small step $\Delta r_s/R \ll 1$, we make the approximations

$$\frac{\partial n_0(j\Delta r_s)}{\partial r} \approx \frac{n_j - n_{j-1}}{\Delta r_s} \tag{5.15}$$

$$\frac{\partial^2 n_0(j\Delta r_s)}{\partial r^2} \approx \frac{n_{j+1} - 2n_j + n_{j-1}}{\Delta r_s^2} \tag{5.16}$$

where $n_j \equiv n_0(j\Delta r_s)$. Employing Eqns. (5.15) and (5.16) we may approximate Eqn. (5.11) by

$$n_{j+1} \approx \frac{12\pi}{(3\pi^2)^{2/3}} n_j^{4/3}\Delta r_s^2 + \left[2 - \frac{1}{j}\right] n_j + \left[\frac{1}{j} - 1\right] n_{j-1} + \frac{1}{3n_j}(n_j - n_{j-1})^2 \tag{5.17}$$

The boundary condition at the nanotube wall, Eqn. (5.12) may similarly be approximated by

$$n_{j_R+1} \approx -\frac{12\pi}{(3\pi)^{2/3}} Z\sigma_a n_{j_R}^{1/3}\Delta r_s + 2n_{j_R} - n_{j_R-1}, \tag{5.18}$$

where $j_R \equiv R/\Delta r_s$. To close our numerical scheme, we need to impose the two boundary conditions given by Eqns. (5.13) and (5.14). We may impose Eqn. (5.14) by requiring

$$n_1 = n_0(0), \tag{5.19}$$

but we may not impose the normalization condition

$$\sum_j \frac{j\Delta r_s n_j \Delta r_s}{Z\sigma_a R} = 1 \tag{5.20}$$

a priori. We instead impose the normalization condition by employing a "shooting" method. We begin by choosing the value for the equilibrium electron density at the origin to be the mid-point of a suitable range, i.e. $[0, 1]$, so that we use the starting value $n_s = 1/2$. The electron density is then calculated via the numerical scheme, and its "norm", $\sum_j \frac{j\Delta r_s n_j \Delta r_s}{Z\sigma_a R}$, is calculated. If the calculated density has a norm greater than one, we know the starting value used was too large, and we calculate again choosing the value for the equilibrium electron density at the origin to be the mid-point of the range $[0, n_s]$. If the calculated density has a norm less than one, we know the starting value used was too small, and we calculate again choosing the value for the equilibrium electron density at the origin the be the mid-point of the range $[n_s, 1]$. This procedure is repeated until the normalization condition is satisfied. By employing this form of shooting method, it will take a logarithmic number of steps, $\log(1/\epsilon)$, to obtain the starting value $n_s = n_0(0)$ within an error ϵ.

Figure 5.1 shows the radial equilibrium electron density calculated for four valence electrons ($Z = 4$) and six valence electrons ($Z = 6$) using the Thomas-Fermi model. As shown in Fig. 5.1, the Thomas-Fermi model gives an unrealistically long-ranged electron density, as is discussed by March [163]. To obtain a more realistic radial equilibrium electron density, we employ the Thomas-Fermi-Dirac model.

Thomas-Fermi-Dirac Model

The Thomas-Fermi-Dirac model is obtained by neglecting the von Weizsäcker term in Eqn. (5.10), to obtain in analogy to Eqns. (5.11) and (5.12),

$$4\pi n_0(r) = \frac{(3\pi^2)^{2/3}}{2}\left[\frac{\partial^2}{\partial r^2} + \frac{1}{r}\frac{\partial}{\partial r}\right] n_0^{2/3}(r) - \left(\frac{3}{\pi}\right)^{1/3}\left[\frac{\partial^2}{\partial r^2} + \frac{1}{r}\frac{\partial}{\partial r}\right] n_0^{1/3}(r), \tag{5.21}$$

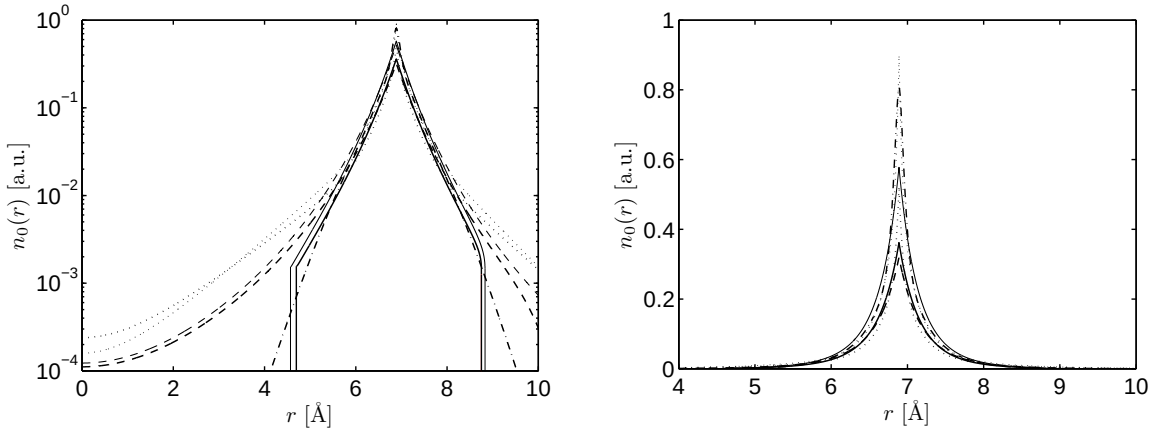

Figure 5.1: The radial equilibrium density n_0, versus radial distance r in Å on an (11,9) SWNT of radius $R = 6.89$ Å, calculated for four valence electrons using a Thomas-Fermi model (- - - -), Thomas-Fermi-Dirac model (——), and Molière model (·····), and for six valence electrons using a Thomas-Fermi model (- - - -), Thomas-Fermi-Dirac model (——), Molière model (·····), and Cruz model (- - - -) [168].

with the boundary condition, as discussed in Appendix E, of

$$-4\pi Z\sigma_a R = \left[\frac{\partial}{\partial r}\left[\frac{(3\pi^2)^{2/3}}{2}n_0^{2/3}(r) - \left(\frac{3}{\pi}\right)^{1/3} n_0^{1/3}(r)\right]\right|_{R^+} - \frac{\partial}{\partial r}\left[\frac{(3\pi^2)^{2/3}}{2}n_0^{2/3}(r) - \left(\frac{3}{\pi}\right)^{1/3} n_0^{1/3}(r)\right]\Bigg|_{R^-}\Bigg], \tag{5.22}$$

and Eqns. (5.13) and (5.14). Employing a backward difference scheme using the shooting method, as discussed for the Thomas-Fermi model, we may solve the approximations to Eqns. (5.21) and (5.22) of

$$n_{j+1} \approx \left[2 - \frac{1}{j}\right] n_j - \left[1 - \frac{1}{j}\right] n_{j-1} + \frac{1}{3n_j}(n_j - n_{j-1})^2 + \frac{12\pi n_j^{4/3}\Delta r_s^2 + \left(\frac{3}{\pi}\right)^{1/3} \frac{1}{3n_j^{4/3}}(n_j - n_{j-1})^2}{(3\pi^2)^{2/3} - \left(\frac{3}{\pi}\right)\frac{1}{n_j^{1/3}}} \tag{5.23}$$

$$n_{j_R+1} \approx 2n_{j_R} - n_{j_R-1} - \frac{12\pi Z\sigma_a \Delta r_s n_{j_R}^{2/3}}{(3\pi^2)^{2/3} n_{j_R}^{1/3} - \left(\frac{3}{\pi}\right)^{1/3}} \tag{5.24}$$

However, the Thomas-Fermi-Dirac model gives an unphysical truncation of the electron density away from the surface, as discussed by March [163]. For this reason, our numerical scheme is unable to satisfy the normalization condition when we start our calculation at the nanotube axis. To account for this truncation, we "shoot" for the location of truncation, in a manner similar to that used for the calculation of the starting value. This truncation is due to cancellation between the positive Thomas-Fermi kinetic energy and the negative Dirac exchange energy. Figure 5.1 shows the radial equilibrium electron density calculated for four valence electrons ($Z = 4$) and six valence electrons ($Z - 6$) using the Thomas-Fermi-Dirac model. As shown in Fig. 5.1, the Thomas-Fermi-Dirac model yields an unphysical truncation of the electron density, as is discussed by March [163].

Thomas-Fermi-Molière Model

Alternatively, we may use the Molière approximation [164, 165] to the radial equilibrium electron density, $n_0(r)$, which is obtained by assuming the total electrostatic potential for a single carbon atom $\Phi_{\rm C}(\mathbf{r})$, has the form

$$\Phi_{\rm C}(\mathbf{r}) = \frac{Z_{\rm C}}{r}\varphi(r/a_m), \tag{5.25}$$

where $Z_{\rm C}$ is the number of valence electrons per carbon atom, a_m is a screening length, given in Thomas-Fermi theory by $a_m = (9\pi^2/128Z_{\rm C})^{1/3} \approx 0.8853 Z_{\rm C}^{-1/3}$, and $\varphi(r/a_m)$ is a screening function, which is a sum of exponentials,

$$\varphi(r/a_m) = \sum_{\ell=1}^{3} \alpha_\ell e^{-\beta_\ell r/a_m}, \tag{5.26}$$

where $\alpha_\ell \approx \{0.1, 0.55, 0.35\}$ and $\beta_\ell \approx \{6.0, 1.2, 0.3\}$.

By assuming that the carbon atoms are "smeared out" into a 2D cylindrical distribution, that is applying the jellium approximation to the atomic density, we find that the total electrostatic potential due to the positive ionic background $\Phi_{\rm at}(\mathbf{r})$ is given by

$$\Phi_{\rm at}(\mathbf{r}) = \iiint d^3\mathbf{r}'\ \sigma_a \delta(r' - R)\Phi_{\rm C}(\mathbf{r}'). \tag{5.27}$$

Using from Ref. [210]

$$\iiint d^3\mathbf{r}'\,\delta(r'-R)\frac{e^{-\lambda\|\mathbf{r}-\mathbf{r}'\|}}{\|\mathbf{r}-\mathbf{r}'\|} = 4\pi R I_0\left(\lambda r_<\right) K_0\left(\lambda r_>\right) \tag{5.28}$$

where $r_< \equiv \min(r,R)$ and $r_> \equiv \max(r,R)$, we find

$$\Phi_{\mathrm{at}}(r) = 4\pi\sigma_a Z_{\mathrm{C}} R \sum_{\ell=1}^{3} \alpha_\ell I_0\left(\frac{\beta_\ell r_<}{a_m}\right) K_0\left(\frac{\beta_\ell r_>}{a_m}\right) \tag{5.29}$$

from Ref. [210]. Employing Poisson's equation, we find $n_0(r) = \frac{1}{4\pi}\nabla^2\Phi_{\mathrm{at}}(r)$, so that

$$n_0(r) = \frac{\sigma_a Z_{\mathrm{C}} R}{a_m^2} \sum_{\ell=1}^{3} \alpha_\ell \beta_\ell^2 I_0\left(\frac{\beta_\ell r_<}{a_m}\right) K_0\left(\frac{\beta_\ell r_>}{a_m}\right). \tag{5.30}$$

Figure 5.1 shows the radial equilibrium density $n_0(r)$ obtained from the Molière model, for $Z_{\mathrm{C}} = 4$ valence electrons and $Z_{\mathrm{C}} = 6$ valence electrons, on a single-wall CNT of radius $R = 6.89$ Å. Since the Molière model is derived from Thomas-Fermi theory, it is not surprising to note the substantial "tails" in the equilibrium electron density, which even surpass those obtained numerically from the Thomas-Fermi model. We may then say that the Molière model yields an equilibrium electron density which differs the most from a 2D jellium model. For this reason, we generally use the Molière model for the equilibrium electron density when comparing the stopping force obtained from the 3D Kitagawa model [161] with that obtained using the 2D hydrodynamic model.

Cruz Model

The equilibrium electron density $n_0(r)$ may also be calculated by employing the electron density for a free carbon atom at position $\mathbf{r}'$, $\rho_{\mathrm{at}}(\|\mathbf{r}-\mathbf{r}'\|)$, obtained using the Cruz approximation [166, 167]. In this model, the electron density for a free carbon atom is assumed to be a sum of the squares of angularly averaged Slater-type atomic orbitals,

$$\rho_{\mathrm{at}}(\|\mathbf{r}-\mathbf{r}'\|) = 2\sum_i |\phi_i(\|\mathbf{r}-\mathbf{r}'\|)|^2, \tag{5.31}$$

where the sum is taken over doubly occupied normalized non-orthogonal orbitals,

$$\phi_i(\|\mathbf{r}-\mathbf{r}'\|) = \sqrt{\frac{2^{2n_i+1}\zeta_i^{2n_i+1}}{4\pi(2n_i)!}}\|\mathbf{r}-\mathbf{r}'\|^{n_i-1}e^{-\zeta_i\|\mathbf{r}-\mathbf{r}'\|}, \tag{5.32}$$

where n_i is the principal atomic number of the ith atomic orbital and ζ_i are variational parameters which are obtained by minimizing the 3D Thomas-Fermi-Dirac-von Weizsäcker energy functional with $\lambda_W = 1/8$. For carbon, the 1s, 2s and 2p orbitals are doubly occupied, so that Cruz *et al.* obtained for the variational parameters $\zeta_{1\mathrm{s}} = 5.57071$, $\zeta_{2\mathrm{s}} = 2.70341$, and $\zeta_{2\mathrm{p}} = 1.23526$ [167]. The electron density for a free carbon atom is then

$$\rho_{\mathrm{at}}(\|\mathbf{r}-\mathbf{r}'\|) = \frac{2\zeta_{1\mathrm{s}}^3}{\pi} e^{-2\zeta_{1\mathrm{s}}\|\mathbf{r}-\mathbf{r}'\|} + \frac{2\zeta_{2\mathrm{s}}^5}{3\pi}\|\mathbf{r}-\mathbf{r}'\|^2 e^{-2\zeta_{2\mathrm{s}}\|\mathbf{r}-\mathbf{r}'\|} + \frac{2\zeta_{2\mathrm{p}}^5}{3\pi}\|\mathbf{r}-\mathbf{r}'\|^2 e^{-2\zeta_{2\mathrm{p}}\|\mathbf{r}-\mathbf{r}'\|}. \tag{5.33}$$

We model the equilibrium electron density of a CNT, $n_0(r)$, by again employ the jellium approximation as was done for the Molière model, so that

$$n_0(r) = \iiint d^3\mathbf{r}'\ \sigma_a \delta(r'-R)\rho_{\mathrm{at}}(\|\mathbf{r}-\mathbf{r}'\|). \tag{5.34}$$

We now evaluate the equilibrium electron density using Eqn. (5.28) by rewriting the electron density for a free carbon atom as

$$\rho_{\mathrm{at}}(\|\mathbf{r}-\mathbf{r}'\|) = -\frac{\zeta_{1\mathrm{s}}^3}{\pi}\frac{\partial}{\partial\zeta_{1\mathrm{s}}}\frac{e^{-2\zeta_{1\mathrm{s}}\|\mathbf{r}-\mathbf{r}'\|}}{\|\mathbf{r}-\mathbf{r}'\|} - \frac{\zeta_{2\mathrm{s}}^5}{12\pi}\frac{\partial^3}{\partial\zeta_{2\mathrm{s}}^3}\frac{e^{-2\zeta_{2\mathrm{s}}\|\mathbf{r}-\mathbf{r}'\|}}{\|\mathbf{r}-\mathbf{r}'\|} - \frac{\zeta_{2\mathrm{p}}^5}{12\pi}\frac{\partial^3}{\partial\zeta_{2\mathrm{p}}^3}\frac{e^{-2\zeta_{2\mathrm{p}}\|\mathbf{r}-\mathbf{r}'\|}}{\|\mathbf{r}-\mathbf{r}'\|}. \tag{5.35}$$

The equilibrium electron density from the Cruz model is then given by

$$\begin{aligned} n_0(r) = &-4\sigma_a R\zeta_{1\mathrm{s}}^3\frac{\partial}{\partial\zeta_{1\mathrm{s}}}I_0(2\zeta_{1\mathrm{s}}r_<)K_0(2\zeta_{1\mathrm{s}}r_>) \\ &-\frac{\sigma_a R}{3}\left[\zeta_{2\mathrm{s}}^5\frac{\partial^3}{\partial\zeta_{2\mathrm{s}}^3}I_0(2\zeta_{2\mathrm{s}}r_<)K_0(2\zeta_{2\mathrm{s}}r_>) + \zeta_{2\mathrm{p}}^5\frac{\partial^3}{\partial\zeta_{2\mathrm{p}}^3}I_0(2\zeta_{2\mathrm{p}}r_<)K_0(2\zeta_{2\mathrm{p}}r_>)\right]. \end{aligned} \tag{5.36}$$

Figure 5.1 shows the radial equilibrium electron density calculated using Cruz's model. We see in Fig. 5.1 that Cruz's model gives a much shorter-ranged equilibrium electron density, especially when compared with the Thomas-Fermi and Molière models. Further, the Cruz approximation yields an electron density which "interpolates" the Thomas-Fermi-Dirac model electron density, without truncation.

5.3 Induced Electron Density

The *induced electron density* is the linear order correction $n_1(\mathbf{r},t)$ satisfying Eqn. (2.61), the $\mathcal{O}(\lambda)$ equation. We shall now find it useful to define the reduced density functional $G[n]$ as the

energy density functional $F[n]$ with the classical Coulomb interaction energy removed, so that

$$\frac{\delta G[n]}{\delta n} = \frac{5C_{\rm TF}}{3}n^{2/3}(\mathbf{r}) - \frac{4C_x}{3}n^{1/3}(\mathbf{r}) + \frac{\lambda_W}{8}\left(\frac{\|\vec{\nabla}n(\mathbf{r})\|^2}{n^2(\mathbf{r})} - 2\frac{\nabla^2 n(\mathbf{r})}{n(\mathbf{r})}\right). \tag{5.37}$$

Substituting Eqn. (5.37) into the $\mathcal{O}(\lambda)$ equation, we find

$$\frac{\partial^2 n_1}{\partial t^2} + \gamma\frac{\partial n_1}{\partial t} = \vec{\nabla}\cdot\left(n_0\vec{\nabla}\left[\left(\frac{\delta G[n]}{\delta n}\right)_1 + \iiint d^3\mathbf{r}'\,\frac{n_1(\mathbf{r}')}{\|\mathbf{r}-\mathbf{r}'\|} - \Phi_{\rm ext}\right]\right). \tag{5.38}$$

Given that n_0 is a function of r alone in cylindrical coordinates, we take the Fourier transform with respect to $\{t, \varphi, z\} \rightarrow \{\omega, m, k\}$, and use Poisson's equation for $\Phi_{\rm ind}$ and $\Phi_{\rm ext}$, to obtain

$$\begin{aligned}\omega(\omega+i\gamma)\widetilde{n}_1(r) = &-\left[n_0\frac{\partial^2}{\partial r^2} + \frac{n_0}{r}\frac{\partial}{\partial r} + \frac{\partial n_0}{\partial r}\frac{\partial}{\partial r}\right]\left[\frac{\delta G[\widetilde{n}]}{\delta\widetilde{n}}\right]_1 \\ &+\left(k^2 + \frac{m^2}{r^2}\right)\left[\frac{\delta G[\widetilde{n}]}{\delta\widetilde{n}}\right]_1 + 4\pi n_0[\widetilde{n}_1(r) - \widetilde{\rho}_{\rm ext}(r)] \\ &-\frac{\partial n_0}{\partial r}\frac{\partial}{\partial r}\int dr' r' g(r,r';m,k)[\widetilde{n}_1(r') - \widetilde{\rho}_{\rm ext}(r')],\end{aligned} \tag{5.39}$$

where $g(r,r';m,k) = 4\pi I_m(|k|r_>)K_m(|k|r_<)$, $r_< = \min(r,r')$, and $r_> = \max(r,r')$. In Eqn. (5.39) and hereafter, for compactness we drop the dependence on r in $n_0(r)$ and the dependences on m, k, and ω in $\widetilde{n}_1$ and $\widetilde{\rho}_{\rm ext}$.

Considering a simplified perfect conductor model, $C_{\rm TF} = C_x = \lambda_W = 0$, letting $\omega_p(r)$ denote the local plasma frequency , given by $\omega_p^2(r) \equiv 4\pi n_0(r)$, employing the dimensionless units $\kappa \equiv kR$ and $\varrho \equiv r/R$ where R is the nanotube radius, and the combined frequency $\Omega^2 \equiv \omega(\omega + i\gamma)$, we may derive Kitagawa's [161] expression for the induced density,

$$\widetilde{n}_1(r) = \frac{\omega_p^2\widetilde{\rho}_{\rm ext}}{\omega_p^2 - \Omega^2} - \frac{\partial\omega_p^2}{\partial\varrho}\int d\varrho'\varrho'\frac{|\kappa|g'(\varrho,\varrho';m,\kappa)[\widetilde{\rho}_{\rm ext}(\varrho') - \widetilde{n}_1(\varrho')]}{4\pi(\omega_p^2(\varrho) - \Omega^2)}, \tag{5.40}$$

where $g'(\varrho,\varrho';m,\kappa) \equiv I'_m(|\kappa|\varrho)K_m(|\kappa|\varrho')\Theta(\varrho'-\varrho) + I_m(|\kappa|\varrho')K'_m(|\kappa|\varrho)\Theta(\varrho-\varrho')$, where Θ is the Heaviside step function.

Employing Picard's method to solve this first order integral equation, we assume the integral operator in the second term of (5.40) is a contractive mapping, so that $\widetilde{n}_1 = \widetilde{n}_1^{(0)} + \widetilde{n}_1^{(1)} + \widetilde{n}_1^{(2)} + \cdots$,

where

$$\widetilde{n}_1^{(0)} = \frac{\omega_p^2 \widetilde{\rho}_{\text{ext}}}{\omega_p^2 - \Omega^2} \tag{5.41}$$

$$\widetilde{n}_1^{(1)} = -\frac{\partial \omega_p^2}{\partial \varrho} \int d\varrho' \frac{\varrho' |\kappa| g'(\varrho, \varrho'; m, \kappa)[\widetilde{\rho}_{\text{ext}}(\varrho') - \widetilde{n}_1^{(0)}(\varrho')]}{4\pi[\omega_p^2(\varrho) - \Omega^2]} \tag{5.42}$$

$$= \frac{\partial \omega_p^2}{\partial \varrho} \int d\varrho' \frac{\varrho' \Omega^2 \widetilde{\rho}_{\text{ext}}(\varrho') |\kappa| g'(\varrho, \varrho'; m, \kappa)}{4\pi[\omega_p^2(\varrho) - \Omega^2][\omega_p^2(\varrho') - \Omega^2]} \tag{5.43}$$

$$\widetilde{n}_1^{(j)} = \frac{\partial \omega_p^2}{\partial \varrho} \int d\varrho' \frac{\varrho' |\kappa| g'(\varrho, \varrho'; m, \kappa) \widetilde{n}_1^{(j-1)}(\varrho')}{4\pi[\omega_p^2(\varrho) - \Omega^2]}. \tag{5.44}$$

In Appendix F we show that the second term of (5.40) is indeed a contractive mapping in the high frequency regime, that is, provided $\Omega \gg \omega_p(0) \approx 0.036$.

The FB transform of the linearized induced potential $\widetilde{\Phi}_{\text{ind}}$ is given in terms of the density correction $\widetilde{n}_1$ by

$$\widetilde{\Phi}_{\text{ind}}(\varrho; m, \kappa, \omega) = -R^2 \int d\varrho' \varrho' g(\varrho, \varrho'; m, \kappa) \widetilde{n}_1(\varrho'; m, \kappa, \omega). \tag{5.45}$$

We now separate the induced potential into a *local* and *non-local* contribution. The local contribution to the induced potential is the potential due to electrons at the location of the external charge, so that

$$\widetilde{\Phi}_{\text{ind}}^l(\varrho; m, \kappa, \omega) = -R^2 \int d\varrho' \varrho' g(\varrho, \varrho'; m, \kappa) \widetilde{n}_1^{(0)}(\varrho'; m, \kappa, \omega) \tag{5.46}$$

$$= -R^2 \int d\varrho' \varrho' g(\varrho, \varrho'; m, \kappa) \frac{\omega_p^2(\varrho') \widetilde{\rho}_{\text{ext}}(\varrho')}{\omega_p^2(\varrho') - \Omega^2}. \tag{5.47}$$

This means that as the ion approaches the nanotube wall, where the equilibrium electron density is highest, the local contribution to the induced potential will begin to dominate. The non-local contribution to the induced potential is the potential due to distant collisions with the nanotube electrons, i.e. $\widetilde{n}_1^{(1)}$, so that

$$\widetilde{\Phi}_{\text{ind}}^n(\varrho; m, \kappa, \omega) = -R^2 \int d\varrho' \varrho' g(\varrho, \varrho'; m, \kappa) \widetilde{n}_1^{(1)}(\varrho'; m, \kappa, \omega) \tag{5.48}$$

$$= -R^2 \int d\varrho' \int d\varrho'' \varrho'' \varrho' \frac{\partial \omega_p^2}{\partial \varrho'} \frac{\Omega^2 \widetilde{\rho}_{\text{ext}}(\varrho'') g(\varrho, \varrho'; m, \kappa) |\kappa| g'_m(\varrho', \varrho''; m, \kappa)}{4\pi[\omega_p^2(\varrho') - \Omega^2][\omega_p^2(\varrho'') - \Omega^2]}. \tag{5.49}$$

This means that in near the nanotube axis, where the equilibrium electron density is "small", the non-local contribution to the induced potential will begin to dominate. Applying Kitagawa's approximation [161], the induced potential $\widetilde{\Phi}_{\rm ind} \approx \widetilde{\Phi}^l_{\rm ind} + \widetilde{\Phi}^n_{\rm ind}$ for $\omega_p^2 \ll \Omega^2$.

5.4 Stopping Force

Defining the *stopping force* as $S \equiv Q\,\frac{\partial \Phi_{\rm ind}}{\partial z}\big|_{\mathbf{r}=\mathbf{r}_0}$, we find is the sum of a local and non-local stopping force, $S = S_l + S_n$, so that

$$S = \sum_m \iint \frac{d\kappa d\omega}{(2\pi)^3 R} e^{im\varphi_0} e^{i\kappa z_0/R} e^{-i\omega t} \widetilde{S}(\varrho_0; m, \kappa, \omega), \tag{5.50}$$

$$\widetilde{S}_l = -QRi \int d\varrho \frac{\varrho \kappa g_m(\varrho_0, \varrho; m, \kappa)\omega_p^2(\varrho)\widetilde{\rho}_{\rm ext}(\varrho)}{\omega_p^2(\varrho) - \Omega^2}, \tag{5.51}$$

$$\widetilde{S}_n = -QRi \int d\varrho \int d\varrho' \frac{\partial \omega_p^2}{\partial \varrho} \frac{\kappa|\kappa|\Omega^2 \widetilde{\rho}_{\rm ext}(\varrho') g(\varrho_0, \varrho; m, \kappa) g'(\varrho, \varrho'; m, \kappa)\varrho'\varrho}{4\pi[\omega_p^2(\varrho) - \Omega^2][\omega_p^2(\varrho') - \Omega^2]}. \tag{5.52}$$

If we assume our external perturbative potential, $\Phi_{\rm ext}$, is due to an ion travelling paraxially with constant speed $v = R\varpi$, the Fourier transform of the external charge density is then $\widetilde{\rho}_{\rm ext}(\varrho; m, \kappa, \omega) = \frac{2\pi}{R^2\varrho} Q\delta(\varrho - \varrho_0)\delta(\omega - \kappa\varpi)e^{-im\varphi_0}$.

Local Stopping Force

The local stopping force is then

$$S_l = -\frac{Q^2 i}{4\pi^2 R^2} \sum_m \int d\kappa \frac{\kappa g(\varrho_0, \varrho_0; m, \kappa)\omega_p^2(\varrho_0)}{\omega_p^2(\varrho_0) - \kappa\varpi(\kappa\varpi + i\gamma)} \tag{5.53}$$

$$= \frac{Q^2}{4\pi^2 R^2} {\rm Im}\left[\sum_m \int d\kappa \frac{\kappa g(\varrho_0, \varrho_0; m, \kappa)\omega_p^2(\varrho_0)}{\omega_p^2(\varrho_0) - \kappa\varpi(\kappa\varpi + i\gamma)}\right]. \tag{5.54}$$

In Appendix G, by employing the Sokhotsky-Plemelj Formula described by Vladimirov pp. 75–79 [211], the above integral is found to be

$$S_l = \frac{Q^2\omega_p^2(\varrho_0)}{v^2} \sum_{m=-\infty}^{\infty} I_m\left(\varrho_0 \frac{\omega_p(\varrho_0)}{\varpi}\right) K_m\left(\varrho_0 \frac{\omega_p(\varrho_0)}{\varpi}\right). \tag{5.55}$$

The above classical expression for the local stopping force diverges since we are calculating the stopping force arising from electrons at the same position as the ion. This is often remedied by truncating the series in m at $m_c \sim Rvm_e/\hbar$ for example. However, following the method of Vager and Gemmell [212], we note that quantum mechanically, the channelled ion wave packet is "smeared out" with an extension $\sim \hbar/m_e v = \lambda_e$, that is, the electron's de Broglie wavelength. To calculate the local stopping force, we evaluate the derivative in the z direction of the induced potential at $\mathbf{r}_0' = \{r_0 + \lambda_e, \varphi, z\}$, so that

$$S_l = \frac{Q^2\omega_p^2(\varrho_0)}{v^2} \sum_{m=-\infty}^{\infty} I_m\left(\frac{\varrho_0\omega_p(\varrho_0)}{\varpi}\right) K_m\left(\frac{\varrho_0\omega_p(\varrho_0)}{\varpi} + \frac{\lambda_e\omega_p(\varrho_0)}{R\varpi}\right). \tag{5.56}$$

From Prudnikov (5.9.2.9) [213], we have

$$\sum_{m=-\infty}^{\infty} I_m(w)K_m(z) = K_0\left(\sqrt{w^2 + z^2 - 2wz}\right) \tag{5.57}$$

so that using $v = R\varpi$,

$$S_l = \frac{Q^2\omega_p^2(\varrho_0)}{v^2} K_0\left(\frac{\lambda_e\omega_p(\varrho_0)}{v}\right). \tag{5.58}$$

Non-Local Stopping Force

The non-local contribution to the stopping force is given by

$$S_n = -\frac{Q^2 i}{16\pi^3 R^2} \sum_m \int d\kappa \int d\varrho \frac{\partial\omega_p^2}{\partial\varrho} \frac{\varrho|\kappa|\kappa^3\varpi^2 g(\varrho_0, \varrho; m, \kappa) g'(\varrho, \varrho_0; m, \kappa)}{[\omega_p^2(\varrho) - \kappa^2\varpi^2][\omega_p^2(\varrho_0) - \kappa^2\varpi^2]} \tag{5.59}$$

$$= \frac{Q^2}{16\pi^3 R^2} \mathrm{Im}\left[\sum_m \int d\kappa \int d\varrho \frac{\partial\omega_p^2}{\partial\varrho} \frac{\varrho|\kappa|\kappa^3\varpi^2 g(\varrho_0, \varrho; m, \kappa) g'(\varrho, \varrho_0; m, \kappa)}{[\omega_p^2(\varrho) - \kappa^2\varpi^2][\omega_p^2(\varrho_0) - \kappa^2\varpi^2]}\right]. \tag{5.60}$$

Again employing the Sokhotsky-Plemelj Formula, as discussed in Appendix G, we obtain for the non-local stopping force

$$\begin{aligned} S_n = & \frac{Q^2}{16\pi^2 v^2} \sum_m \int d\varrho \varrho \frac{\partial \omega_p^2}{\partial \varrho} \frac{1}{\varpi[\omega_p^2(\varrho_0) - \omega_p^2(\varrho)]} \\ & \left[\omega_p^3(\varrho) g\left(\varrho_0, \varrho; m, \frac{\omega_p(\varrho)}{\varpi}\right) g'\left(\varrho, \varrho_0; m, \frac{\omega_p(\varrho)}{\varpi}\right) \right. \\ & \left. - \omega_p^3(\varrho_0) g\left(\varrho_0, \varrho; m, \frac{\omega_p(\varrho_0)}{\varpi}\right) g'\left(\varrho, \varrho_0; m, \frac{\omega_p(\varrho_0)}{\varpi}\right) \right] \qquad (5.61) \\ = & \frac{Q^2}{16\pi^2 v^2} \sum_m \int d\varrho \varrho \frac{\partial \omega_p^2}{\partial \varrho} F(\varrho, \varrho_0, \omega_p(\varrho), \omega_p(\varrho_0), \varpi), \qquad (5.62) \end{aligned}$$

where

$$F = \begin{cases} \dfrac{f\left(\frac{\omega_p(\varrho)}{\varpi}\right) - f\left(\frac{\omega_p(\varrho_0)}{\varpi}\right)}{[\omega_p^2(\varrho_0) - \omega_p^2(\varrho)]/\varpi^2}, & \omega_p(\varrho) \neq \omega_p(\varrho_0) \\ \left.\dfrac{\partial f(x)}{\partial x}\right|_{x=\omega_p(\varrho_0)/\varpi} & \text{otherwise} \end{cases} \qquad (5.63)$$

$$f(x) = x^3 g_m(\varrho_0, \varrho; m, x) g'(\varrho, \varrho_0; m, x). \qquad (5.64)$$

In Fig. 5.2 we have shown the speed dependence of the stopping force for protons moving paraxially at $r_0 = 0$, 3, and 5 Å to an (11,9) SWNT of radius $R = 6.89$ Å. Comparison is made between the stopping force obtained from the 2D hydrodynamic model and that obtained using a 3D Kitagawa model [161] employing a Molière equilibrium electron density. We find that the non-local contribution to the stopping force gives fairly close agreement with the 2D model for sufficiently high speeds ($v \gtrsim 5$). This agrees with Kitagawa's suggestion [161] that the non-local contribution to the stopping force is due to distant collisions with the target electrons. However, we find that at shorter distances from the nanotube wall ($r_0 \gtrsim 3$ Å), the local contribution to the stopping force becomes significant, giving a much higher total stopping force from the 3D Kitagawa model [161] in the near-wall region. This may be explained by noting that the local contribution to the stopping force is due to the electrons at the protons location. We may see this effect more clearly in Fig. 5.3, which shows the radial dependence of the stopping force for protons with paraxial speeds $v = 5$, 7, and 9, since the 3D Kitagawa model applies to only the high frequency regime ($\omega_p(0) \ll \Omega$) [161].

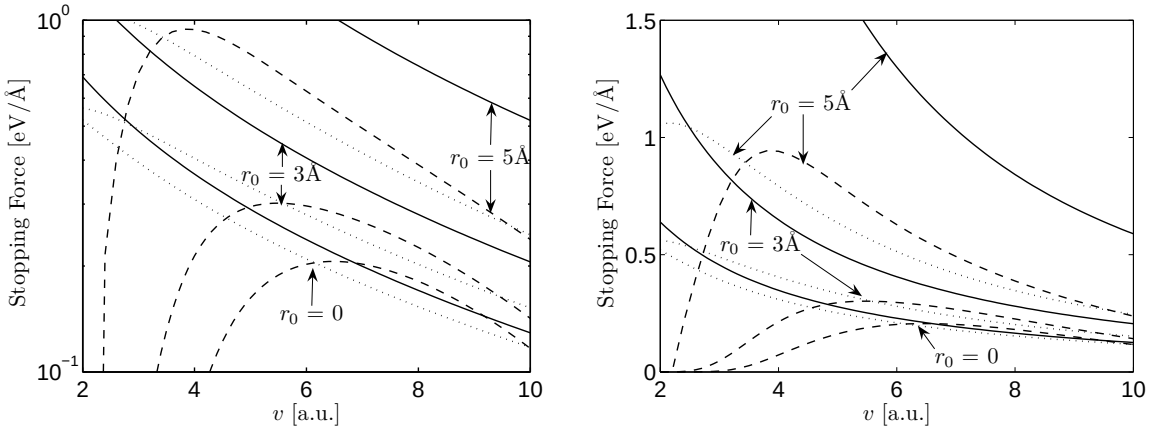

Figure 5.2: The total stopping force $S = S_l + S_n$ (——), with the non-local stopping force contribution S_n (·····), and the 2D hydrodynamic model stopping force (- - - -), plotted versus speed v for an proton moving paraxially at $r_0 = 0$, 3 Å, and 5 Å to a single wall (11,9) CNT of radius $R = 6.89$ Å [168].

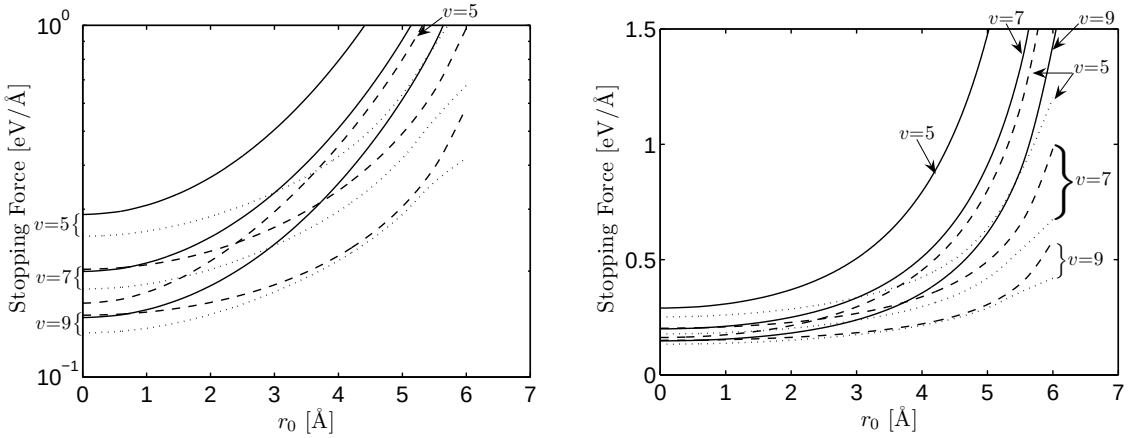

Figure 5.3: The total stopping force $S = S_l + S_n$ (——), the non-local stopping force contribution S_n (·····), and the 2D hydrodynamic model stopping force (- - - -), plotted versus radial distance r_0 in Å for an proton moving paraxially with speed $v = 5$, 7, and 9, in an (11,9) SWNT of radius $R = 6.89$ Å [168].

In Fig. 5.4 we explore how the 3D Kitagawa model for the stopping force depends on the

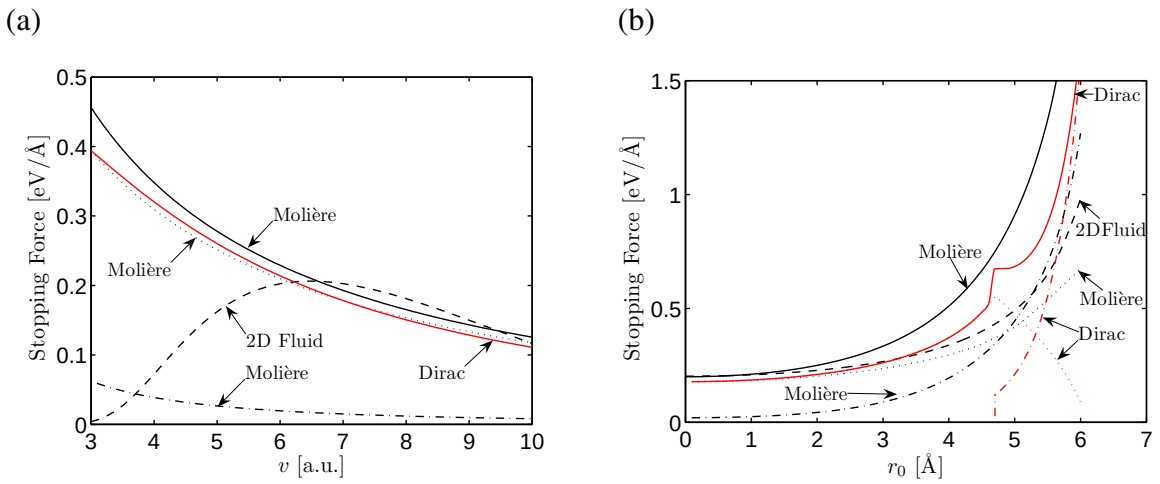

Figure 5.4: The total stopping force $S = S_l + S_n$ (——), the local stopping force contribution S_l (- · - · -), the non-local stopping force contribution S_n (·····), from the Thomas-Fermi-Molière (Molière) and Thomas-Fermi-Dirac (Dirac) models, and the 2D hydrodynamic (2D Fluid) model stopping force (- - - -), plotted versus (a) speed v for a proton at $r_0 = 0$, and (b) radial distance r_0 in Å for a proton moving paraxially with speed $v = 7$, in an (11,9) SWNT of radius $R = 6.89$ Å [168].

choice of equilibrium electron density model, by employing both the Molière and Thomas-Fermi-Dirac models. Figure 5.4(a) shows the speed dependence of the stopping force for a proton travelling on the axis of an (11,9) SWNT of radius $R = 6.89$ Å, for the Molière, Thomas-Fermi-Dirac (Dirac), and 2D hydrodynamic (2D Fluid) models. We note that both the Molière and Dirac total stopping forces are in fair agreement with the 2D hydrodynamic model stopping force on the nanotube axis, as seen in Fig. 5.4(a). We also note that the truncation of the Dirac equilibrium electron density results in no contribution from the local stopping force being felt for protons more than 4 Å from the nanotube wall. For this reason, the non-local Molière and the total Dirac stopping forces are in close agreement for protons near the axis ($r_0 \lesssim 3$ Å), as seen in Fig. 5.4(b) for protons travelling paraxially with speed $v = 7$. We also see in Fig 5.4(b) that at sufficiently high speeds, the relative importance of the local and non-local stopping force contributions switches near the nanotube wall ($r_0 \gtrsim 4$ Å). While this change is smooth for the Molière model, the truncation of the equilibrium electron density in the Dirac model introduces

a "jump" in the total stopping force at $r_0 \approx 4.2$ Å.

Chapter 6

Dicluster and Dipole Channelling through Nanotubes

In the previous chapters, we considered the electronic response of CNTs to channelled ions. We now consider their electronic response to ion and molecular clusters under channelling conditions. In particular, the Coulomb explosion of H_2^+ and H_3^+ molecules under channelling conditions, as studied by Zhou *et al.* [214], is of great interest to the area of hydrogen storage in CNTs. Also, the channelling of water molecules through CNTs may be studied by employing a point dipole model.

Using the single-fluid 2D hydrodynamic model for the induced electric potential of a SWNT, which we derived in Chapter 4, we may obtain the image potential, total potential, dynamic-polarization force, and total stopping force for channelled diclusters and dipoles.

6.1 Induced Electric Potential

Applying the single-fluid 2-D hydrodynamic model for a SWNT, discussed in Chapters 3 and 4, we may write the total induced potential at position $\mathbf{r}$ in the laboratory frame of reference, in terms of the FB transform of the linearized induced electron number density per unit area on the nanotube, $\widetilde{n}_1(m,\kappa,\omega)$, as

$$\Phi_{\rm ind}(\mathbf{r},t) = -4\pi \sum_m \iint \frac{d\kappa d\omega}{(2\pi)^3} e^{i(m\varphi+\kappa z/R-\omega t)} I_m(|\kappa|\varrho_<) K_m(|\kappa|\varrho_>) \widetilde{n}_1(m,\kappa,\omega), \qquad (6.1)$$

where I_m and K_m are Modified Bessel functions of the first and second kind respectively, with $\varrho_< \equiv \min(1, r/R)$ and $\varrho_> \equiv \max(1, r/R)$.

Using the 2-D Hydrodynamic Model, we obtain for the FB transform of the linearized induced electron density

$$\widetilde{n}_1(m,\kappa,\omega) = \frac{\widetilde{\Phi}_{\rm ext}(R;m,\kappa,\omega)}{\chi^{-1}(m,\kappa,\omega) + 4\pi R I_m(|\kappa|)K_m(|\kappa|)} \tag{6.2}$$

where $\widetilde{\Phi}_{\rm ext}(R;m,\kappa,\omega)$ is the FB transform of the external potential from the ions and χ is the susceptibility, $\chi^{-1}\widetilde{n}_1 = \widetilde{\Phi}$. From Eqn. (3.28), the susceptibility in a single-fluid model is

$$\chi(m,\kappa,\omega) = \left[\frac{\alpha}{n_0} + \frac{\beta}{n_0}\frac{\kappa^2+m^2}{R^2} - \frac{R^2}{n_0}\frac{\omega(\omega+i\gamma)}{\kappa^2+m^2}\right]^{-1}, \tag{6.3}$$

where $n_0 \approx 0.428$ is the equilibrium electron number density on the nanotube, $\alpha \equiv \pi n_0$, and $\beta \equiv 1/4$.

The FB transform of the external potential from the N ions is the sum of Coulomb potentials for the pth ion of charge Q_p moving parallel to the nanotube axis with speeds $v_p = R\varpi_p$ at positions $\mathbf{r}_p = \{\varrho_p R, \varphi_p, z_p\}$ in the moving centre of mass frame of reference, is then given by

$$\widetilde{\Phi}_{\rm ext}(R;m,\kappa,\omega) = \sum_{p=1}^{N} 8\pi^2 Q_p \delta(\omega - \kappa\varpi_p) I_m(|\kappa|\varrho_{p<}) K_m(|\kappa|\varrho_{p>}) e^{-im\varphi_p} e^{-i\kappa z_p/R}, \tag{6.4}$$

where $\varrho_{p<} \equiv \min(1, r_p/R)$ and $\varrho_{p>} \equiv \max(1, r_p/R)$.

Substituting Eqn. (6.4) for $\widetilde{\Phi}_{\rm ext}(R;m,\kappa,\omega)$ into Eqns. (6.2) and (6.1), we obtain for the total induced potential

$$\Phi_{\rm ind}(\mathbf{r},t) = \\ -\sum_{p=1}^{N}\frac{4\pi Q_p}{R}\sum_m \int \frac{d\kappa}{\pi} \frac{e^{im(\varphi-\varphi_p)+i\kappa(z/R-z_p/R-\varpi_p t)} I_m(|\kappa|\varrho_<) K_m(|\kappa|\varrho_>) I_m(|\kappa|\varrho_{p<}) K_m(|\kappa|\varrho_{p>})}{R^{-1}\chi^{-1}(m,\kappa,\kappa\varpi_p) + 4\pi I_m(|\kappa|)K_m(|\kappa|)}. \tag{6.5}$$

6.2 Total Potential Energy

As discussed in Chapter 4 and by Zhou *et al.* [214], the total self-energy of a cluster of N ions, $E_{\rm self}$, is given by

$$E_{\rm self} = \frac{1}{2}\sum_{q=1}^{N} Q_q \Phi_{\rm ind}(\mathbf{r}_q + v_q t \mathbf{e}_z, t) \tag{6.6}$$

$$= -\sum_{p,q=1}^{N} \frac{4\pi Q_p Q_q}{R} \sum_m \int \frac{d\kappa}{2\pi} \frac{e^{im\Delta\varphi_p^q + i\kappa(\Delta z_p^q/R + \Delta\varpi_p^q t)} I_m(|\kappa|\varrho_{q<}) K_m(|\kappa|\varrho_{q>}) I_m(|\kappa|\varrho_{p<}) K_m(|\kappa|\varrho_{p>})}{R^{-1}\chi^{-1}(m,\kappa,\kappa\varpi_p) + 4\pi I_m(|\kappa|) K_m(|\kappa|)}, \tag{6.7}$$

where $\Delta\varphi_p^q \equiv \varphi_q - \varphi_p$, $\Delta z_p^q \equiv z_q - z_p$, $\Delta\varpi_p^q \equiv \varpi_q - \varpi_p$, and $\mathbf{e}_z$ is a unit vector parallel to the nanotube axis. The total self-energy includes a contribution from each ion's non-interacting self-energy, and vicinage parts coming from interferences in the self-energy due to the spatial correlation among the constituent ions [214].

The *total* potential energy of the system U_T is the sum of the repulsive atomic potential arising from the interaction between the ions and individual carbon atoms on the nanotube, $U_{\rm at}$, the Coulomb interaction potential between the N ions, $V_{\rm C}$, and the total self-energy, $E_{\rm self}$.

The total potential energy is then

$$U_T = \sum_{p=1}^{N} \sum_{q=p+1}^{N} \frac{Q_p Q_q}{\|\mathbf{r}_p - \mathbf{r}_q\|} + U_{\rm at} + E_{\rm self} \tag{6.8}$$

If we now consider the problem of two ions of equal coaxial speed $v = R\varpi$, with separation $\Delta\rho \equiv \|\mathbf{r}_1 - \mathbf{r}_2\|$, our problem simplifies to

$$U_T = \frac{Q_1 Q_2}{\Delta\rho} + U_{\rm at} - \frac{4\pi}{R}\sum_m \int \frac{d\kappa}{2\pi} \left[\frac{Q_1^2 I_m^2(|\kappa|\varrho_{1<}) K_m^2(|\kappa|\varrho_{1>}) + Q_2^2 I_m^2(|\kappa|\varrho_{2<}) K_m^2(|\kappa|\varrho_{2>})}{R^{-1}\chi^{-1}(m,\kappa,\kappa\varpi) + 4\pi I_m(|\kappa|) K_m(|\kappa|)} \right.$$
$$\left. + \frac{2Q_1 Q_2 \cos(m\Delta\varphi + \kappa\Delta z/R) I_m(|\kappa|\varrho_{1<}) K_m(|\kappa|\varrho_{1>}) I_m(|\kappa|\varrho_{2<}) K_m(|\kappa|\varrho_{2>})}{R^{-1}\chi^{-1}(\kappa,m,u) + 4\pi I_m(|\kappa|) K_m(|\kappa|)} \right]. \tag{6.9}$$

To model the atomic potential energy for the ion cluster, $U_{\rm at}$, we employ either a Molière atomic potential, as used by Zhou *et al.*, or a Doyle-Turner atomic potential, as employed by Borka *et al.* when modelling the rainbow effect in ion channelling through SWNTs [215] and DWNTs [216].

Molière Atomic Potential

The Molière atomic potential, U_{M}, is given from Eqn. (5.29) to be

$$U_{\mathrm{M}} = 4\pi \sum_{p=1}^{N} Q_p \sigma_a Z_{\mathrm{C}} \sum_{\ell=1}^{3} \alpha_\ell I_0 \left(\frac{\beta_\ell r_{p<}}{a_m} \right) K_0 \left(\frac{\beta_\ell r_{p>}}{a_m} \right), \tag{6.10}$$

where $Z_{\mathrm{C}} = 6$ is the atomic number of carbon, and Q_p is the charge of the pth ion in the cluster. As discussed in Chapter 5 and by March [163], the Molière model gives an unrealistically long-ranged potential energy. For ions travelling at intermediate speeds, the Doyle-Turner atomic potential may provide more realistic results.

Doyle-Turner Atomic Potential

The Doyle-Turner atomic potential U_{DT}, has been applied to CNTs by both Zhevhago and Glebov [217] and Borka *et al.* [215, 216]. In cylindrical coordinates, the radial Doyle-Turner atomic potential has the form

$$U_{\mathrm{DT}} = \sum_{p=1}^{N} \frac{32\pi Q_p Z_{\mathrm{C}} R}{3^{3/2}\ell_{\mathrm{C}}^2} \sum_{j=1}^{4} a_j b_j^2 e^{-b_j^2(r^2+R^2)} I_0(2b_j^2 rR), \tag{6.11}$$

where $Z_{\mathrm{C}} = 6$ is the atomic number of carbon, $\ell_{\mathrm{C}} \approx 0.144$ nm is the atomic spacing in the nanotube, $a_j \equiv \{3.222, 5.270, 2.012, 0.5499\} \times 10^{-4}$ nm^2 and $b_j \equiv \{10.330, 18.694, 37.456, 106.88\}$ nm^{-1} are fitting parameters. For $r/R \gg 0$, the Doyle-Turner atomic potential can be approximated by a sum of Gaussians of the form

$$U_{\mathrm{DT}} \approx \sum_{p=1}^{N} \frac{32\pi Q_p Z_{\mathrm{C}} R}{3^{3/2}\ell_{\mathrm{C}}^2} \sum_{j=1}^{4} a_j b_j^2 e^{-b_j^2(r-R)^2}. \tag{6.12}$$

The Doyle-Turner atomic potential is therefore rather short-ranged, and most applicable at high ion speeds.

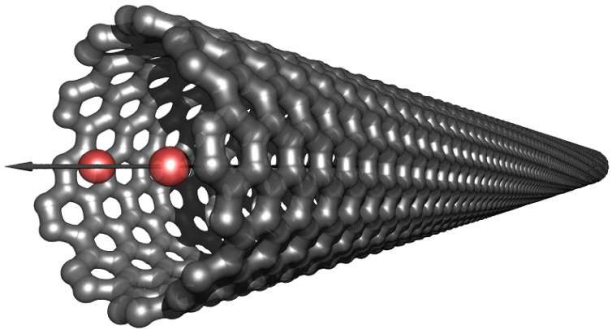

Figure 6.1: Schematic of two ions centred at the origin of an (11,9) nanotube.

6.3 Diclusters – Two Ions of Equal Charge $Q_1 = Q_2 = Q$

When both ions are inside the nanotube at equal radial distances, so that $r_1, r_2 \leq R$ the total potential energy is then

$$U_T = \frac{Q_1 Q_2}{\Delta\rho} + U_{\rm at} - \frac{2}{R}\sum_m\!\!\!\!\!\!\int d\kappa \frac{[Q_1^2 I_m^2(|\kappa|\varrho_1) + Q_2^2 I_m^2(|\kappa|\varrho_2)]K_m^2(|\kappa|)}{R^{-1}\chi^{-1}(m,\kappa,\kappa\varpi) + 4\pi I_m(|\kappa|)K_m(|\kappa|)}$$
$$-\frac{4}{R}\sum_m\!\!\!\!\!\!\int d\kappa \frac{Q_1 Q_2 \cos(m\Delta\varphi + \kappa\Delta z/R) I_m(|\kappa|\varrho_1) I_m(|\kappa|\varrho_2) K_m^2(|\kappa|)}{R^{-1}\chi^{-1}(m,\kappa,\kappa\varpi) + 4\pi I_m(|\kappa|)K_m(|\kappa|)}. \quad (6.13)$$

For the case of two ions of equal charge $Q_1 = Q_2 = Q$ at equal distances x_0 from the nanotube axis, so that $\varrho_1 = \varrho_2 = \varrho_0 \equiv x_0/R$, our expression for the total potential energy simplifies further to

$$U_T = \frac{Q^2}{\Delta\rho} + U_{\rm at} - \frac{4Q^2}{R}\sum_m\!\!\!\!\!\!\int d\kappa \frac{I_m^2(|\kappa|\varrho_0)K_m^2(|\kappa|)[1+\cos(m\Delta\varphi + \kappa\Delta z/R)]}{R^{-1}\chi^{-1}(m,\kappa,\kappa\varpi) + 4\pi I_m(|\kappa|)K_m(|\kappa|)}. \quad (6.14)$$

Centre of Mass on Nanotube Axis

When the two ions have their centre of mass located on the nanotube axis as shown in Fig. 6.1, so that $\Delta\varphi = \pi$ and $\varrho_1 = \varrho_2 = \varrho_0 \leq 1$, their positions in Cartesian coordinates are given by $\mathbf{r}_{1,2} = \pm(x_0\mathbf{e}_x + z_0\mathbf{e}_z) \equiv \pm\{x_0, 0, z_0\}$, where $\mathbf{e}_x$ is a unit vector perpendicular to the nanotube axis, and $\mathbf{e}_z$ is a unit vector in the longitudinal direction. The problem then simplifies further to

$$U_T = \frac{Q^2}{\Delta\rho} + U_{\rm at} - \frac{4Q^2}{R}\sum_m\!\!\!\!\!\!\int d\kappa \frac{I_m^2(|\kappa|\varrho_0)K_m^2(|\kappa|))[1+(-1)^m\cos\kappa\Delta z/R]}{R^{-1}\chi^{-1}(m,\kappa,\kappa\varpi) + 4\pi I_m(|\kappa|)K_m(|\kappa|)}. \quad (6.15)$$

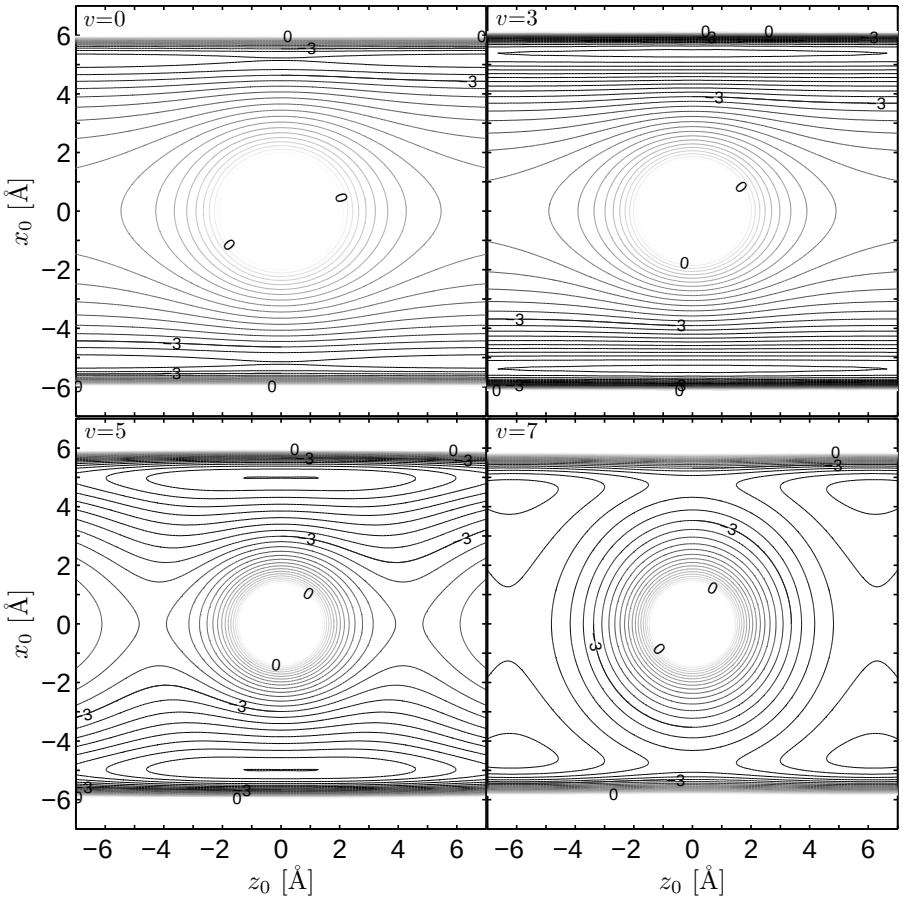

Figure 6.2: The total potential, $U_T = U_{\rm DT} + E_{\rm self} + V_{\rm C}$, in eV, for a Doyle-Turner potential, with contours separated by 0.2 eV, for two protons at positions $\mathbf{r}_{1,2} = \pm\{x_0, 0, z_0\}$, in the moving centre of mass frame of reference, with speed $v = 0$, 3, 5, and 7, where $R = 7$ Å is the nanotube radius.

Figures 6.2 and 6.3 are contour plots of the total potential energy, using the Doyle-Turner and Molière atomic potentials respectively, for two protons with centre of mass at the origin, positions $\mathbf{r}_{1,2} = \pm(x_0\mathbf{e}_x + z_0\mathbf{e}_z) \equiv \pm\{x_0, 0, z_0\}$, and common coaxial speeds (a) $v = 0$, (b) $v = 3$, (c) $v = 5$, and (d) $v = 7$.

We note that the potential "wells" in Fig. 6.2 and Fig. 6.3 are due to collective oscillations

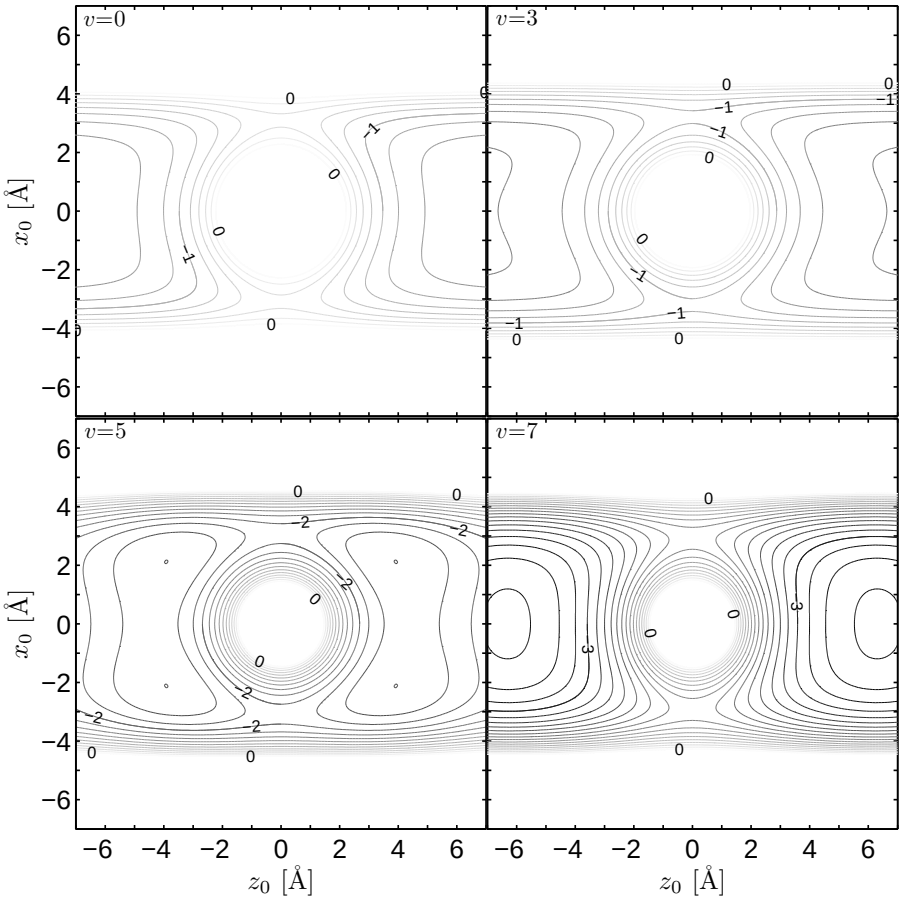

Figure 6.3: The total potential, $U_T = U_{\rm M} + E_{\rm self} + V_{\rm C}$, in eV, for a Molière potential, with contours separated by 0.2 eV, for two protons at positions $\mathbf{r}_{1,2} = \pm\{x_0, 0, z_0\}$, in the moving centre of mass frame of reference, with speed $v = 0$, 3, 5, and 7, where $R = 7$ Å is the nanotube radius.

of the electron gas on the nanotube. These minima in the total potential occur when the trailing proton is "wake riding", that is, following in the potential wells of the leading proton's wake. These minima indicate that diclusters moving with common paraxial speeds $v \gtrsim 2$, that is at speeds above that at which collective oscillations of the electron fluid occur, are loosely "bonded" when they are channelled through the nanotube. In comparing Fig. 6.2 and Fig. 6.3, we note that

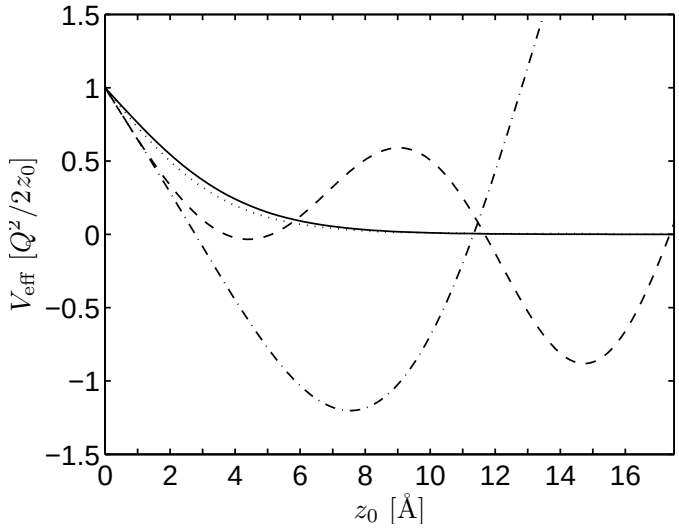

Figure 6.4: The effective potential $V_{\rm eff}$ in units of the Coulomb potential $V_{\rm C} = \frac{Q^2}{2z_0}$, for two protons at positions $\mathbf{r}_{1,2} = \pm\{0, 0, z_0\}$, in the moving centre of mass frame of reference, moving paraxially with speed $v = 0$ (——), $v = 3$ (·····), $v = 5$ (- - - -), and $v = 7$ (- · - ·), to a CNT of radius $R = 7$ Å.

the shorter ranged Doyle-Turner atomic potential gives much deeper potential wells than the longer-ranged Molière atomic potential.

We note here that the dynamic-polarization force from the nanotube on the dicluster may be obtained by taking the gradient of the induced potential. This dynamic-polarization force has two contributions. First, the stopping force in the $-z$-direction, which is obtained by differentiating the potential with respect to the axial coordinate z. Second, the image force in the radial r-direction, which is obtained by differentiating the potential with respect to the radial coordinate r. Since the integrand of the induced potential is an even function of the angular wave number m, and differentiating with respect to the angular coordinate φ multiplies the integrand by a factor of im, we know that there can be no force due to the induced potential which acts in the φ-direction.

If both ions are on the nanotube axis, so that $\varrho_0 = 0$, and their separation is $\Delta\rho = \Delta z$, using that $U_{\rm at}(0)$ is a constant, and $I_m(0) = \delta_{m0}$ from Abramowitz and Stegun [169], we obtain

$$U_T = \frac{Q^2}{\Delta z}\left[1 - \frac{\Delta z}{\pi R}\int d\kappa \frac{K_0^2(|\kappa|)[1 + \cos\kappa\Delta z/R]}{\frac{1}{4\pi R}\chi^{-1}(0, \kappa, \kappa\varpi) + I_0(|\kappa|)K_0(|\kappa|)}\right] + U_{\rm at}(0). \qquad (6.16)$$

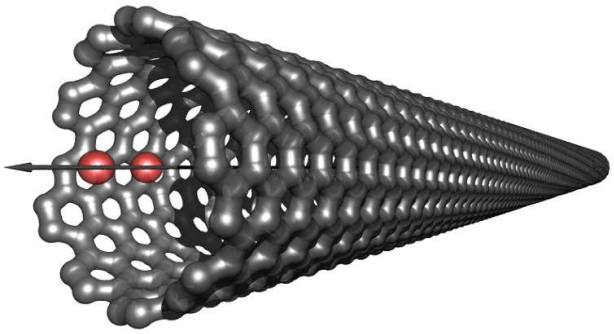

Figure 6.5: Schematic of two ions aligned with the axis of an (11,9) nanotube

Up to a constant factor, the effective potential between the ions is then given by

$$V_{\text{eff}} = \frac{Q^2}{\Delta z}\left[1 - \frac{\Delta z}{\pi R}\int d\kappa \frac{K_0^2(|\kappa|)\cos(\kappa\Delta z/R)}{\frac{1}{4\pi R}\chi^{-1}(0,\kappa,\kappa\varpi) + I_0(|\kappa|)K_0(|\kappa|)}\right]. \tag{6.17}$$

The calculation of V_{eff} is shown in Fig. 6.4, for an ion separation of zero to five radii. We find that the ions are nearly completely screened from each other by the nanotube after a separation of three radii.

In Fig. 6.4 we see that at high speeds, $v \gtrsim 5$, the minima of the effective potential is at $\Delta z \approx 10$ Å and $\Delta z \approx 30$ Å when $v = 5$ and $\Delta z \approx 15$ Å when $v = 7$.

If both ions are at $z = 0$, so that $\Delta z = 0$ and $\Delta\rho = 2r_0$, the problem simplifies to

$$U_T = \frac{Q^2}{2r_0} + U_{\text{at}} - \frac{Q^2}{\pi R}\sum_m \int d\kappa \frac{I_m^2(|\kappa|\varrho_0)K_m^2(|\kappa|)[1+(-1)^m]}{\frac{1}{4\pi R}\chi^{-1}(0,\kappa,\kappa\varpi) + I_m(|\kappa|)K_m(|\kappa|)}. \tag{6.18}$$

Only when m is even is the integral non-zero, so that

$$U_T = \frac{Q^2}{2r_0} + U_{\text{at}} - \frac{2Q^2}{\pi R}\sum_m \int d\kappa \frac{I_{2m}^2(|\kappa|\varrho_0)K_{2m}^2(|\kappa|)}{\frac{1}{4\pi R}\chi^{-1}(0,\kappa,\kappa\varpi) + I_{2m}(|\kappa|)K_{2m}(|\kappa|)}. \tag{6.19}$$

Aligned with Nanotube Axis

When the two ions are in a coaxial orientation inside the nanotube as shown in Fig. 6.5, so that $\Delta\varphi = 0$, $\Delta\rho = \Delta z$, and $\varrho_1 = \varrho_2 = \varrho_0 \leq 1$, their positions in Cartesian coordinates are given by $\mathbf{r}_{1,2} = x_0\mathbf{e}_x \pm z_0\mathbf{e}_z \equiv \{x_0, 0, \pm z_0\}$. The problem then simplifies to

$$U_T = \frac{Q^2}{\Delta z} + U_{\text{at}} - \frac{4Q^2}{R}\sum_m \int d\kappa \frac{I_m^2(|\kappa|\varrho_0)K_m^2(|\kappa|)[1+\cos\kappa\Delta z/R]}{R^{-1}\chi^{-1}(m,\kappa,\kappa\varpi) + 4\pi I_m(|\kappa|)K_m(|\kappa|)}. \tag{6.20}$$

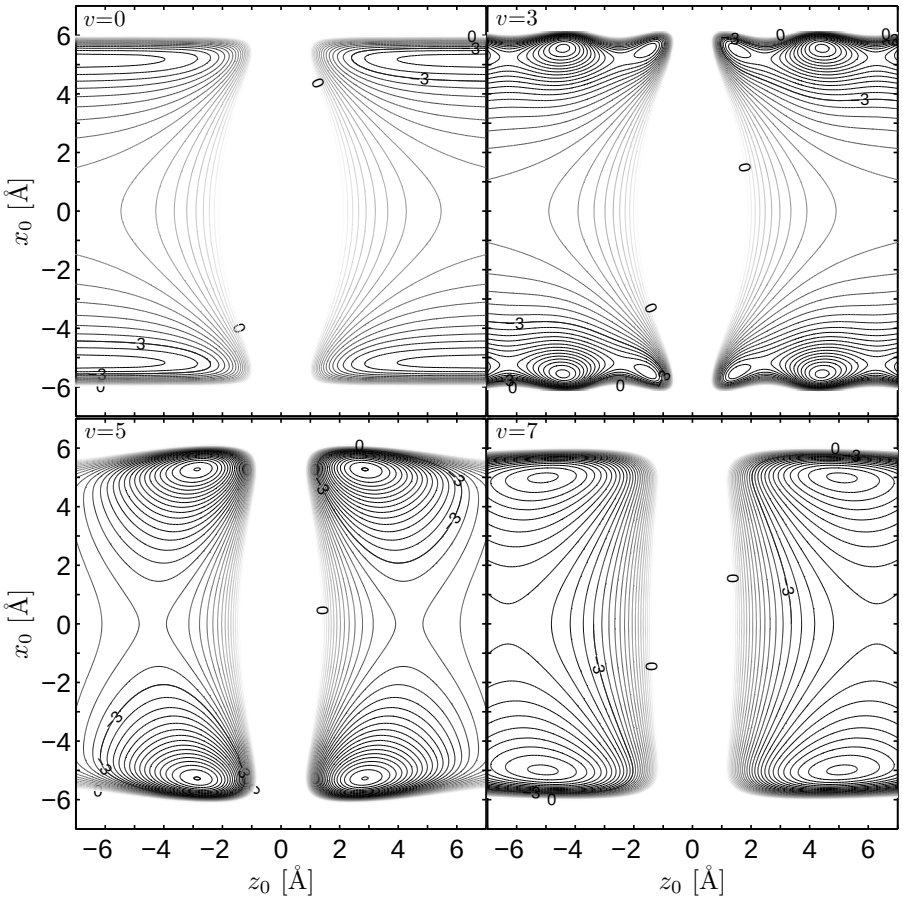

Figure 6.6: The total potential, $U_T = U_{\rm DT} + E_{\rm self} + V_{\rm C}$, in eV, for a Doyle-Turner potential, with contours separated by 0.2 eV, for two protons at positions $\mathbf{r}_{1,2} = \{x_0, 0, \pm z_0\}$, in the moving centre of mass frame of reference, with speed $v = 0$, 3, 5, and 7, where $R = 7$ Å is the nanotube radius.

Figures 6.6 and 6.7 are contour plots of the total potential energy, using the Doyle-Turner and Molière atomic potentials respectively, for two protons oriented parallel to the nanotube axis, with positions $\mathbf{r}_{1,2} = x_0\mathbf{e}_x \pm z_0\mathbf{e}_z \equiv \{x_0, 0, \pm z_0\}$ and common coaxial speeds $v = 0$, $v = 3$, $v = 5$, and $v = 7$. Considering Fig. 6.6, we note the deep potential wells for $v = 5$ of approximately 4.6 eV, which occur when the protons are radially aligned at $\mathbf{r}_{1,2} \approx \pm 5\mathbf{e}_x$. These

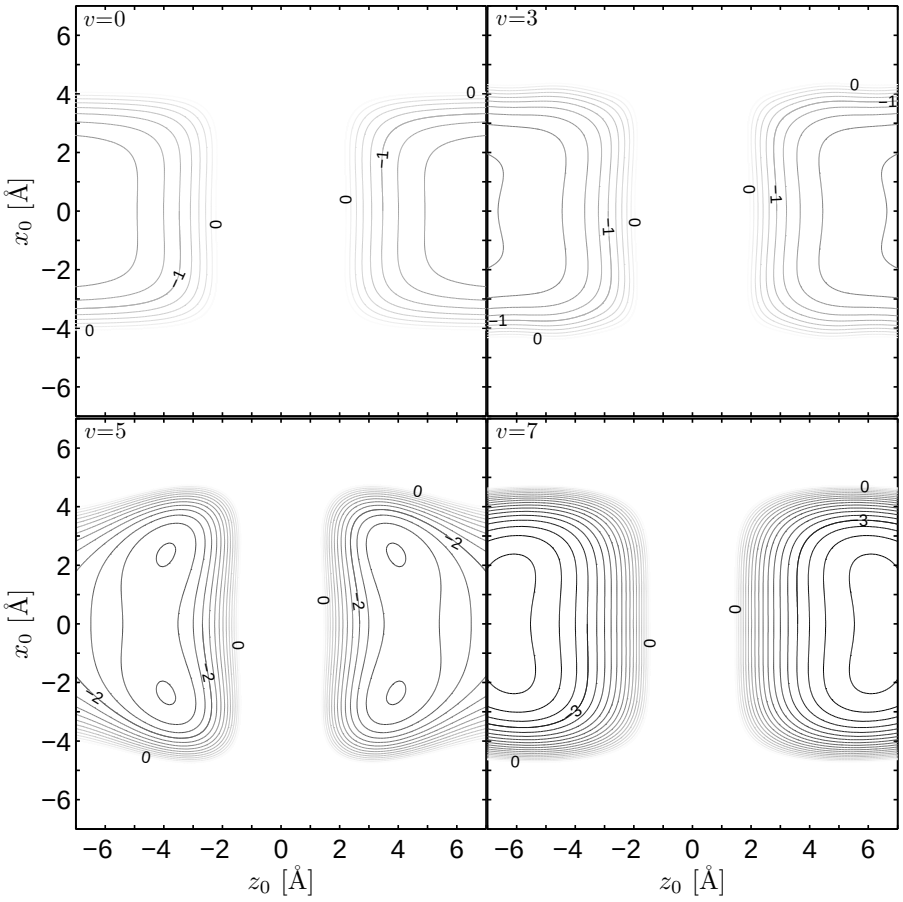

Figure 6.7: The total potential, $U_T = U_{\rm M} + E_{\rm self} + V_{\rm C}$, in eV, for a Molière potential, with contours separated by 0.2 eV, for two protons at positions $\mathbf{r}_{1,2} = \{x_0, 0, \pm z_0\}$, in the moving centre of mass frame of reference, with speed $v = 0$, 3, 5, and 7, where $R = 7$ Å is the nanotube radius.

potential wells are somewhat shallower than for $v = 3$, and located closer to the nanotube axis. For $v = 7$, their potential wells are of approximately 4.0 eV, located at $\mathbf{r}_{1,2} \approx \pm 4.55\mathbf{e}_x + 6.30\mathbf{e}_z$ Å. We also note the much broader and shallower wells shown in Fig. 6.7, due to the longer-ranged Molière atomic potential.

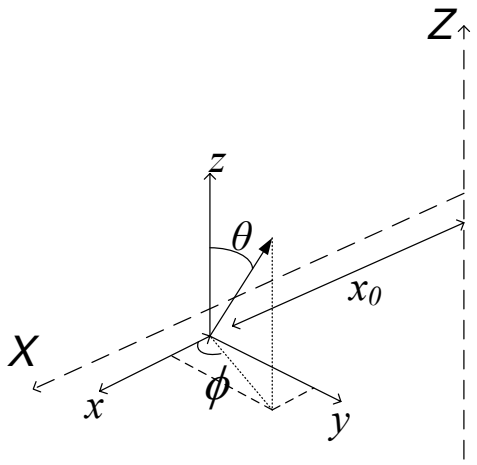

Figure 6.8: Spherical coordinate angles ϕ and θ relative to the nanotube axis (z-axis) and the dipole position x_0 (x-axis).

6.4 Dipoles – Ions of Opposite Charge $Q_1 = -Q_2 = Q$

We now consider two ions of opposite charges, $Q_1 = -Q_2 = Q$, at positions in the moving centre of mass frame of reference $\mathbf{r}_1$ and $\mathbf{r}_2$. In cylindrical coordinates their positions are given by $\mathbf{r}_{1,2} = \{x_0 \pm \frac{1}{2}\Delta r, \pm\frac{1}{2}\Delta\varphi, \pm\frac{1}{2}\Delta z\}$ with separation $\Delta\rho = \sqrt{\Delta r^2 + (4x_0^2 - \Delta r^2)\sin^2(\Delta\varphi/2) + \Delta z^2}$. The electrostatic dipole moment, $\boldsymbol{\mu}$, for a system with charge density $\rho(\mathbf{r})$ is defined by Jackson [199] as

$$\boldsymbol{\mu} = \iiint d^3\mathbf{r}'\ \mathbf{r}'\rho(\mathbf{r}'). \tag{6.21}$$

For our system of two opposite charges $\boldsymbol{\mu} = Q(\mathbf{r}_1 - \mathbf{r}_2) = \{\mu_r, \mu_\varphi, \mu_z\}$, so that $\|\boldsymbol{\mu}\| = Q\Delta\rho = \mu = \sqrt{\mu_r^2 + \mu_\varphi^2 + \mu_z^2}$, where $\mu_r = Q\Delta r$, $\mu_\varphi = Q\sqrt{4x_0^2 - \Delta r^2}\sin(\Delta\varphi/2)$, and $\mu_z = Q\Delta z$. If both ions are located inside the nanotube, so that $x_0 \pm \frac{1}{2}\Delta r < R$, the self energy when the ions have equal paraxial speeds $v = R\varpi$ is

$$\begin{aligned} E_{\text{self}} = &-\frac{8Q^2}{R}\sum_m\int d\kappa \frac{\sin^2\left(\frac{m}{2}\Delta\varphi + \frac{1}{2}\kappa\Delta z/R\right) I_m(|\kappa|[\varrho_0 + \frac{1}{2}\Delta\varrho])I_m(|\kappa|[\varrho_0 - \frac{1}{2}\Delta\varrho])K_m^2(|\kappa|)}{R^{-1}\chi^{-1}(m,\kappa,\kappa\varpi) + 4\pi I_m(|\kappa|)K_m(|\kappa|)} \\ &-\frac{2Q^2}{R}\sum_m\int d\kappa \frac{[I_m(|\kappa|[\varrho_0 + \frac{1}{2}\Delta\varrho]) - I_m(|\kappa|[\varrho_0 - \frac{1}{2}\Delta\varrho])]^2 K_m^2(|\kappa|)}{R^{-1}\chi^{-1}(m,\kappa,\kappa\varpi) + 4\pi I_m(|\kappa|)K_m(|\kappa|)}, \end{aligned} \tag{6.22}$$

where we have used the dimensionless units $\varrho_0 \equiv x_0/R$, $\Delta\varrho \equiv \Delta r/R$ and $\kappa \equiv kR$.

To calculate the self energy for a point dipole, we take the limit $Q \to \infty$ and $\Delta\rho \to 0$ while their product μ remains constant. Substituting $\Delta r = \mu_r/Q$, $\Delta\varphi = 2\arcsin\left(\mu_\varphi/\sqrt{4Q^2x_0^2-\mu_r^2}\right) \approx \mu_\varphi/Qx_0 + \mathcal{O}(Q^{-2})$, and $\Delta z = \mu_z/Q$ while taking the limit $Q \to \infty$ we find

$$E_{\rm self} = -\frac{2}{R^3}\sum_m\int d\kappa \frac{[(\frac{m}{\kappa\varrho_0}\mu_\varphi + \mu_z)^2 I_m^2(|\kappa|\varrho_0) + \mu_r^2[I_m'(|\kappa|\varrho_0)]^2]\kappa^2 K_m^2(|\kappa|)}{R^{-1}\chi^{-1}(m,\kappa,\varpi) + 4\pi I_m(|\kappa|)K_m(|\kappa|)} \tag{6.23}$$

$$= -\frac{2\mu^2}{R^3}\sum_m\int d\kappa \frac{[(\frac{m}{\kappa\varrho_0}\sin\phi\sin\theta + \cos\theta)^2 I_m^2(|\kappa|\varrho_0) + \cos^2\phi\sin^2\theta[I_m'(|\kappa|\varrho_0)]^2]\kappa^2 K_m^2(|\kappa|)}{R^{-1}\chi^{-1}(m,\kappa,\varpi) + 4\pi I_m(|\kappa|)K_m(|\kappa|)}, \tag{6.24}$$

where the dipole orientation angles in spherical coordinates, $\{\phi, \theta\}$, are depicted in Fig. 6.8.

In Fig. 6.9 and Fig. 6.10, we show the dependence of the self energy on orientation of the dipole, for a point dipole located at $x_0 = R/2 = 3.5$ Å inside a SWNT of radius $R = 7$ Å. Figure 6.9 shows the relative magnitude of the self-energy at each paraxial speed $v = 0$, 3, 5, and 7. Alternatively Fig. 6.10 shows the self-energy via the shape of each 3D surface, allowing comparison between the self-energies for each paraxial speed $v = 0$, 3, 5, and 7. We note that for $v = 0$, 5, and 7, the self energy is minimized when the dipole is oriented perpendicular to the nanotube axis, that is, the direction of motion. However, at medium speeds, $v = 3$, we find the self-energy is minimized when the point dipole is oriented parallel to the radial direction, that is, the x-direction, while the self-energy is independent of the angle of orientation in the yz-plane.

Figure 6.11 shows the radial position dependence of the self-energy for a dipole oriented in the yz-plane, so that $\phi = 90°$, and θ is the angle in the yz-plane relative to the direction of motion. Figure 6.12 shows the radial position dependence of the self-energy for a dipole oriented in the xz-plane, so that $\phi = 0°$, and θ is the angle in the xz-plane relative to the direction of motion. Figure 6.13 shows the radial position dependence of the self-energy for a dipole oriented in the xy-plane, so that $\theta = 90°$, and ϕ is the azimuthal angle in the xy-plane relative to the radial direction. We note that the absolute values of the self-energies shown in Fig. 6.11, Fig. 6.12, and Fig. 6.13, are two orders of magnitude smaller than those obtained for single ions in Chapter 4 and diclusters in Sect. 6.3, for dipole moments $\mu \sim 1$.

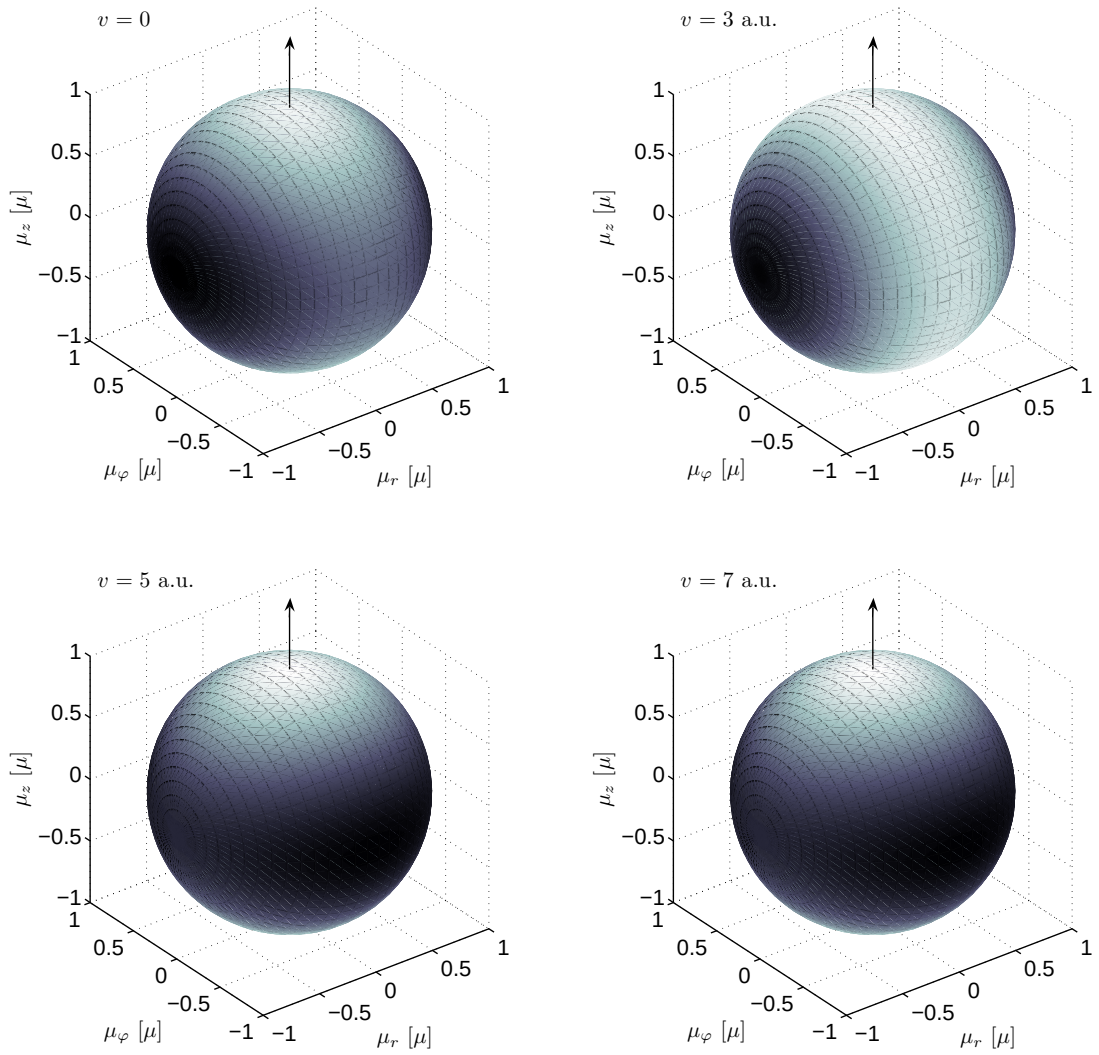

Figure 6.9: The self energy E_{self} for a point dipole with dipole vector $\boldsymbol{\mu}$ at $x_0 = 3.5$ Å, inside a nanotube of radius R = 7 Å, moving with paraxial speed $v = 0$ (-13.6×10^{-3} eV/$\mu^2 \leq E_{\text{self}} \leq -6.88 \times 10^{-3}$ eV/μ^2), $v = 3$ (-21.6×10^{-3} eV/$\mu^2 \leq E_{\text{self}} \leq -14.4 \times 10^{-3}$ eV/μ^2), $v = 5$ (-11.2×10^{-3} eV/$\mu^2 \leq E_{\text{self}} \leq 1.6 \times 10^{-3}$ eV/μ^2), and $v = 7$ (-5.6×10^{-3} eV/$\mu^2 \leq E_{\text{self}} \leq 4.0 \times 10^{-3}$ eV/μ^2).

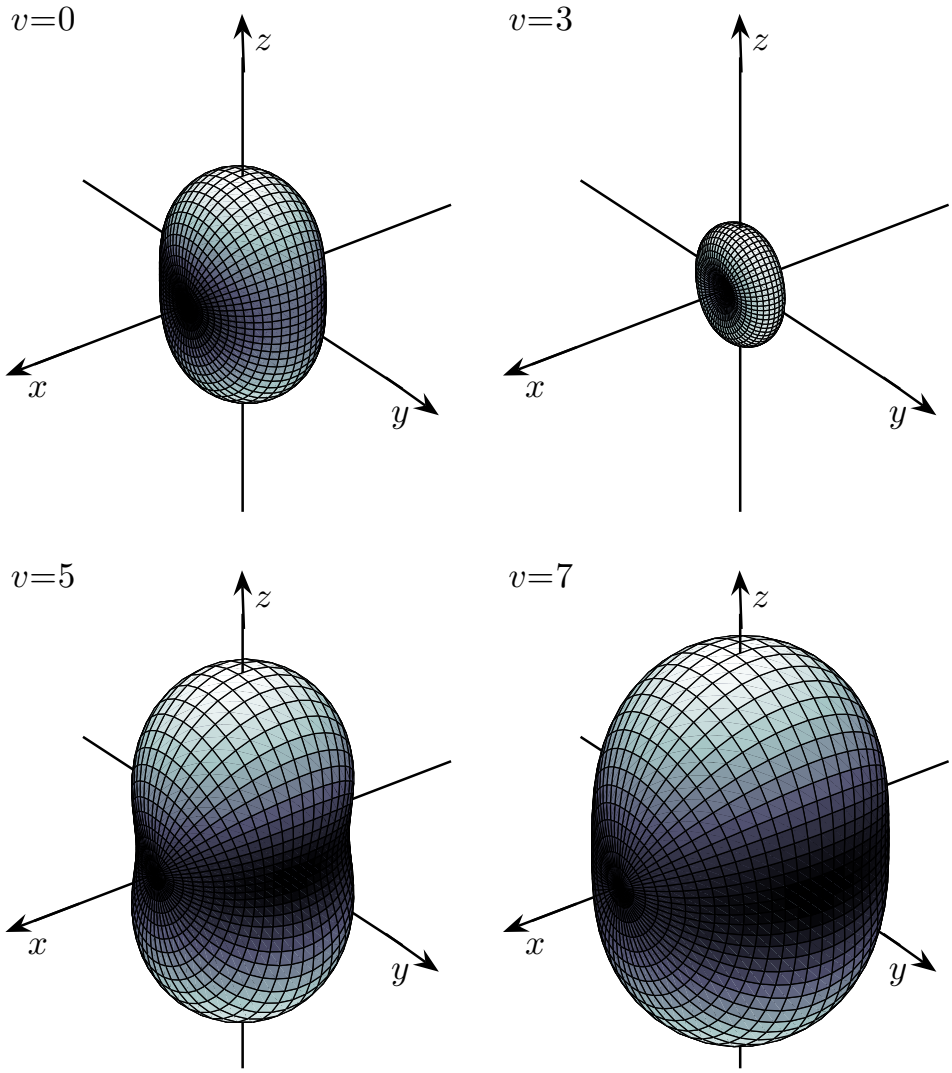

Figure 6.10: The self energy E_{self} for a point dipole with dipole vector $\boldsymbol{\mu}$ at $x_0 = 3.5$ Å, inside a nanotube of radius R = 7 Å, moving with paraxial speed $v = 0$ (-13.6×10^{-3} eV/$\mu^2 \leq E_{\text{self}} \leq -6.88 \times 10^{-3}$ eV/μ^2), $v = 3$ (-21.6×10^{-3} eV/$\mu^2 \leq E_{\text{self}} \leq -14.4 \times 10^{-3}$ eV/μ^2), $v = 5$ (-11.2×10^{-3} eV/$\mu^2 \leq E_{\text{self}} \leq 1.6 \times 10^{-3}$ eV/μ^2), and $v = 7$ (-5.6×10^{-3} eV/$\mu^2 \leq E_{\text{self}} \leq 4.0 \times 10^{-3}$ eV/μ^2).

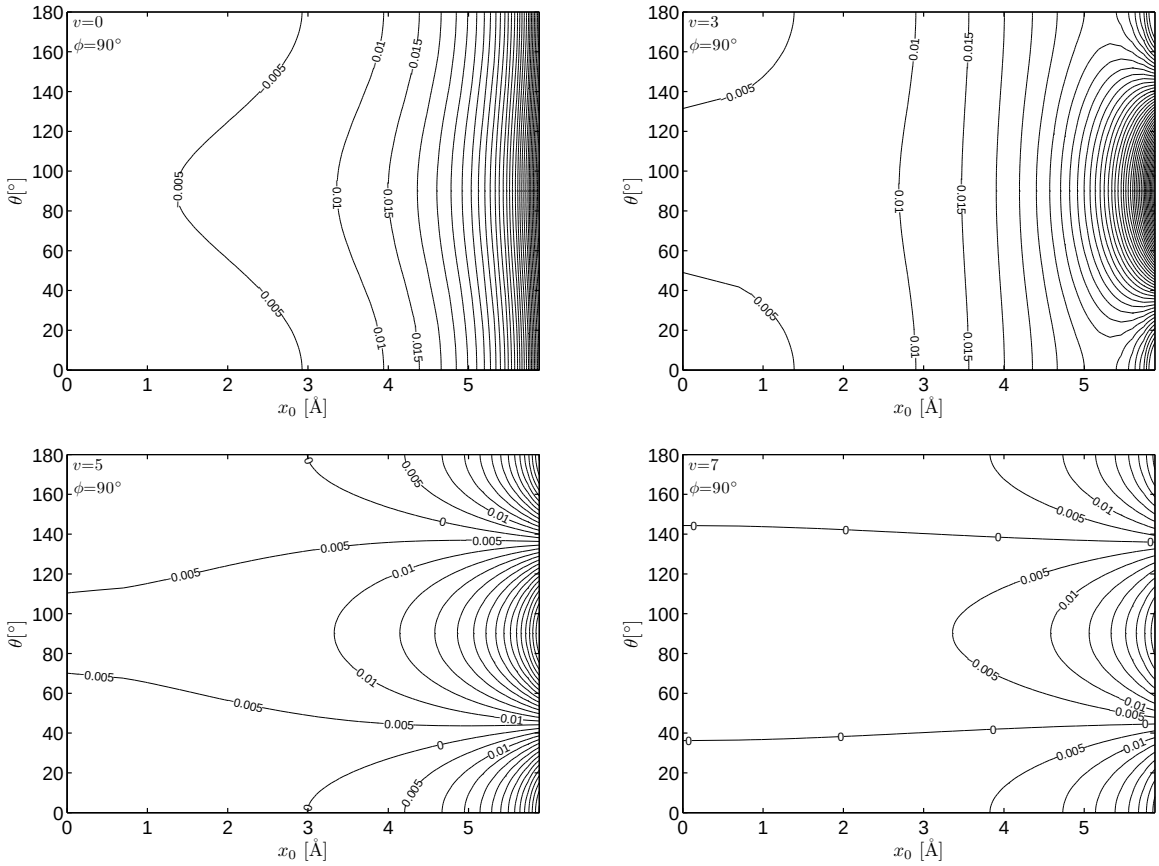

Figure 6.11: The self energy E_{self} in eV for a point dipole $\boldsymbol{\mu}$ at $\phi = 90°$, so that θ is an angle in the yz-plane relative to the direction of motion, located at radial position x_0 in Å, and moving with speed $v = 0, 3, 5,$ and 7 parallel to the axis of a CNT of radius $R = 7$ Å.

6.5 Stopping Force

Using the definition of stopping force described in Chapter 4, for the case of two ions of equal charge $Q_1 = Q_2 = Q$ at equal radial distances, so that $\varrho_1 = \varrho_2 = \varrho_0$, the stopping force of the dicluster is given by

$$S = \frac{8Q^2}{R^2}\mathrm{Im}\left[\sum_m \int d\kappa \frac{\kappa I_m^2(|\kappa|\varrho_0)K_m^2(|\kappa|)[1+\cos(m\Delta\varphi + \kappa\Delta z/R)]}{R^{-1}\chi^{-1}(m,\kappa,\kappa\varpi) + 4\pi I_m(|\kappa|)K_m(|\kappa|)}\right]. \tag{6.25}$$

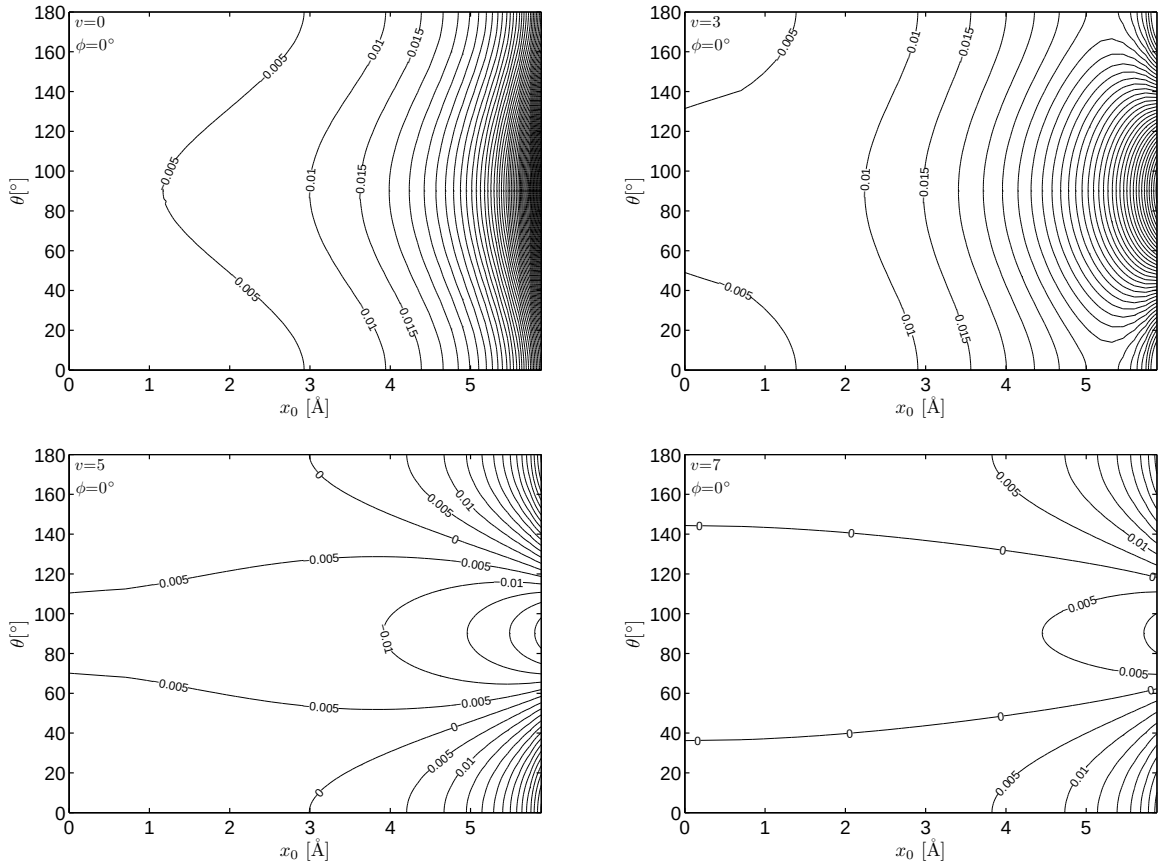

Figure 6.12: The self energy $E_{\rm self}$ in eV for a point dipole $\boldsymbol{\mu}$ at $\phi = 0$, so that θ is an angle in the xz-plane relative to the direction of motion, located at radial position x_0 in Å, and moving with speed $v = 0, 3, 5,$ and 7 parallel to the axis of a CNT of radius $R = 7$ Å.

The stopping force on a point dipole may be similarly calculated from the induced electric potential by $S \equiv Q\ \frac{\partial}{\partial z}\Phi_{\rm ind}\big|_{\mathbf{r}=\mathbf{r}_0}$, so that

$$S = \frac{4\mu^2}{R^3}{\rm Im}\left[\sum_m \int d\kappa \frac{[(\frac{m}{\kappa\varrho_0}\sin\phi\sin\theta + \cos\theta)^2 I_m^2(|\kappa|\varrho_0) + \cos^2\phi\sin^2\theta[I_m'(|\kappa|\varrho_0)]^2]\kappa^3 K_m^2(|\kappa|)}{R^{-1}\chi^{-1}(m,\kappa,\varpi) + 4\pi I_m(|\kappa|)K_m(|\kappa|)}\right], \tag{6.26}$$

where the dipole orientation angles in spherical coordinates, $\{\phi, \theta\}$, are depicted in Fig. 6.8.

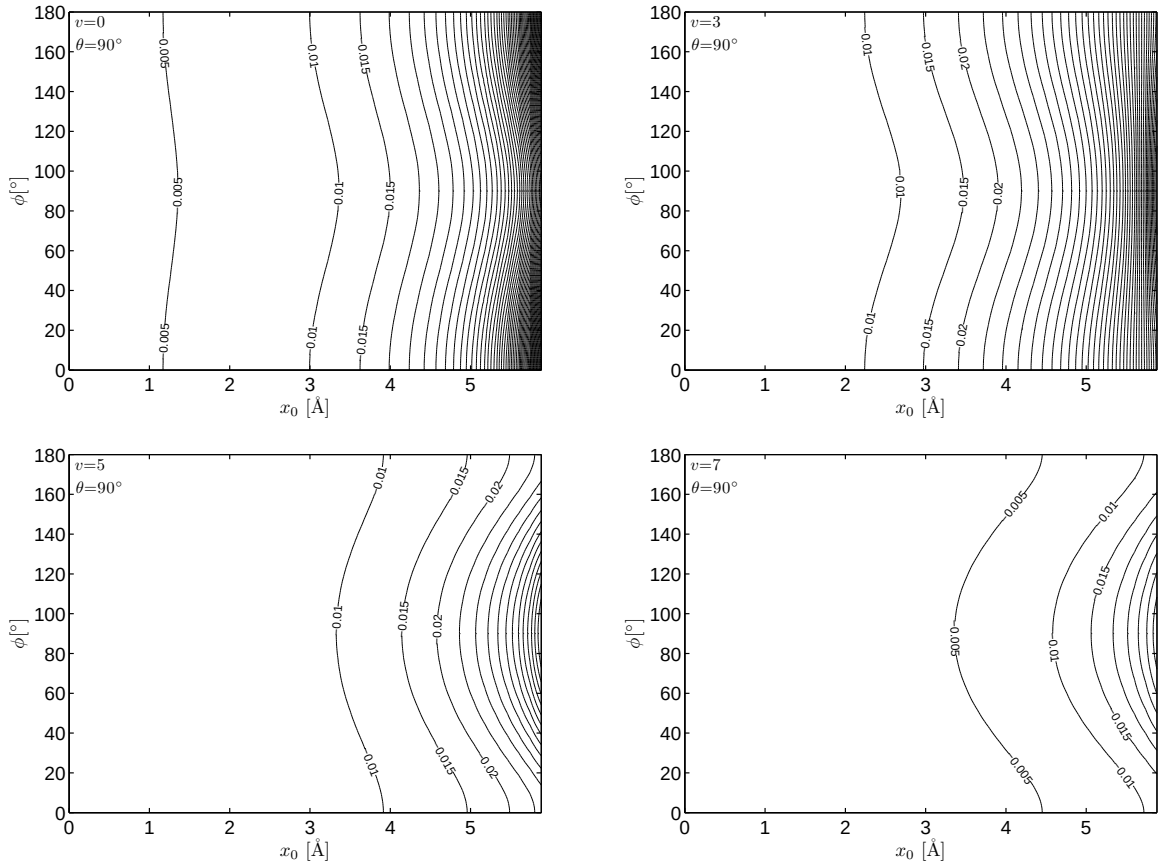

Figure 6.13: The self energy E_{self} in eV for a point dipole $\boldsymbol{\mu}$ at $\theta = 90°$, so that ϕ is an angle in the xy-plane relative to the radial position x_0 in Å, moving with speed $v = 0, 3, 5,$ and 7 parallel to the axis of a CNT of radius $R = 7$ Å.

Figure 6.14 shows the dependence of the stopping force in eV/Åμ^2 on the dipole's paraxial speed v. We find that, as with the self energy, the stopping force on dipoles is approximately two orders of magnitude smaller than the stopping for single ions. This suggests that the dynamic-polarization force has little effect on channelled molecules such as water molecules. Further, for $v \gtrsim 6$, the stopping force is much greater when the dipole is oriented perpendicular to the direction of motion (z-direction). We find that at these high speeds, the stopping force is independent of the azimuthal angle ϕ in the xy-plane. However, for medium speeds ($3 \lesssim v \lesssim 5$), the stopping force is minimized when the dipole is oriented in the angular direction (y-direction).

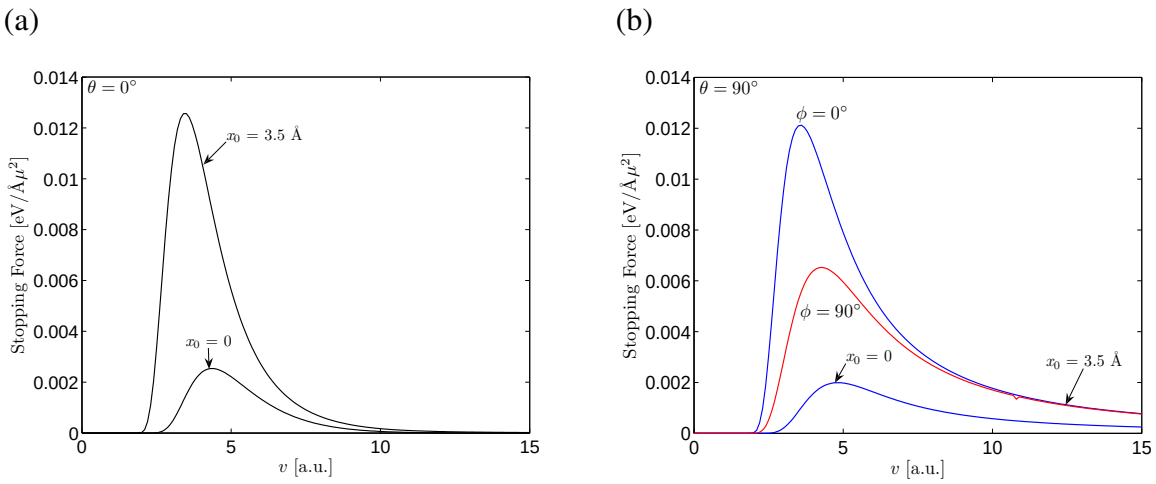

Figure 6.14: The stopping force in eV/Åμ^2 for a point dipole $\boldsymbol{\mu}$ in the (a) z-direction ($\theta = 0°$) and in the (b) x-direction ($\theta = 90°, \phi = 0°$) and y-direction ($\theta = 90°, \phi = 90°$), at $x_0 = 0$ and 3.5 Å, moving with speed v parallel to the axis of a CNT of radius $R = 7$ Å.

We also find that the stopping force is generally maximized for all orientations when the dipole is travelling with paraxial speed $v \approx 4$

Chapter 7

Oblique Ion Trajectories Near Nanotubes

In the previous chapters, we have concentrated on ions under near-channelling conditions, so that their velocities were nearly parallel to the nanotube axis. However, such an experimental setup has yet to be realized. Predominantly, the electronic interaction between ion beams and CNT, via EELS or atomic force microscopy (AFM), consists of ion beams at oblique angles to the nanotube axis. For this reason, EELS at oblique trajectories has been both modelled [42, 218, 219, 220] and measured [16]. In this chapter, we give expressions for both the energy loss, $\Delta E_{\rm loss}$, and deflection angle, $\Delta\theta$, for ions travelling at oblique angles outside a SWNT, shown schematically in Fig. 7.1, where the 2-D hydrodynamic model is most applicable. We also assume that the ions travel uniformly with constant velocity

7.1 Energy Loss

We define the energy loss, $\Delta E_{\rm loss}$, as the work done by the induced force on the external perturbing charge moving on trajectory $\mathbf{r} = \mathbf{r}_0(t)$. This may be written as the negative integral of the induced force along the path length,

$$\Delta E_{\rm loss} = -\int \mathbf{F}_{\rm ind} \cdot d\mathbf{r} \tag{7.1}$$

$$= -\int_{-\infty}^{\infty} dt \mathbf{F}_{\rm ind}(\mathbf{r}_0(t), t) \cdot \mathbf{v}_0(t), \tag{7.2}$$

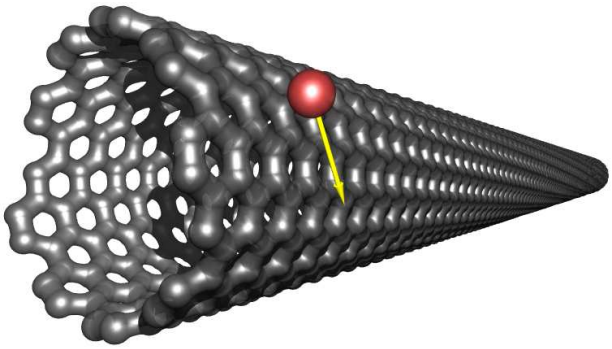

Figure 7.1: Schematic of an (11,9) SWNT and an ion with an oblique trajectory.

where $\mathbf{v}_0(t) \equiv \dfrac{d\mathbf{r}_0}{dt}$.

Considering the induced force to be the Lorentz force due to the induced charge density, we may write $\mathbf{F}_{\rm ind}$ as

$$\mathbf{F}_{\rm ind}(\mathbf{r}_0(t),t) = Q\mathbf{E}_{\rm ind}(\mathbf{r}_0(t),t) \tag{7.3}$$

where Q is the charge of the perturbing ion.

Writing this in terms of the induced scalar potential, $\Phi_{\rm ind}$, we obtain

$$\mathbf{F}_{\rm ind}(\mathbf{r}_0(t),t) = -Q\left[\vec{\nabla}\Phi_{\rm ind}(\mathbf{r},t)\right]_{\mathbf{r}=\mathbf{r}_0(t)}. \tag{7.4}$$

We can thus express the energy loss in terms of the scalar and vector potential as

$$\begin{aligned}\Delta E_{\rm loss} =& Q\int_{-\infty}^{\infty}dt\left[\left(\mathbf{v}_0\cdot\vec{\nabla}+\frac{\partial}{\partial t}\right)\Phi_{\rm ind}(\mathbf{r},t)\right]_{\mathbf{r}=\mathbf{r}_0(t)}\\ &-Q\int_{-\infty}^{\infty}dt\left[\frac{\partial}{\partial t}\Phi_{\rm ind}(\mathbf{r},t)\right]_{\mathbf{r}=\mathbf{r}_0(t)}\end{aligned} \tag{7.5}$$

Since $\frac{d}{dt} = \mathbf{v}_0\cdot\vec{\nabla}+\frac{\partial}{\partial t}$, by setting the potential to be equal to zero for $t=\pm\infty$, i.e. $\Phi_{\rm ind}\to 0$ as $t\to\pm\infty$, we obtain

$$\Delta E_{\rm loss} = -Q\int_{-\infty}^{\infty}dt\left[\frac{\partial}{\partial t}\Phi_{\rm ind}(\mathbf{r},t)\right]_{\mathbf{r}=\mathbf{r}_0(t)} \tag{7.6}$$

Introducing the Fourier time transform

$$\Phi_{\rm ind}(\mathbf{r},t) = \int_{-\infty}^{\infty}\frac{d\omega}{2\pi}e^{-i\omega t}\widehat{\Phi}_{\rm ind}(\mathbf{r},\omega), \tag{7.7}$$

we obtain

$$\Delta E_{\rm loss} = -Q\int_{-\infty}^{\infty}\frac{d\omega}{2\pi i}\omega\int_{-\infty}^{\infty}dte^{-i\omega t}\widehat{\Phi}_{\rm ind}(\mathbf{r}_0(t),\omega). \tag{7.8}$$

We may now define the plasmon excitation probability function, also called the energy-loss probability per energy unit, $\mathcal{P}(\omega)$ as $2i$ times the imaginary, or odd, part of the ω integrand in equation (7.8) by

$$\Delta E_{\rm loss} = \int_0^{\infty}d\omega\omega\mathcal{P}(\omega), \tag{7.9}$$

$$\mathcal{P}(\omega) = -\frac{Q}{\pi}{\rm Im}\left[\int_{-\infty}^{\infty}dte^{-i\omega t}\widehat{\Phi}_{\rm ind}(\mathbf{r}_0(t),\omega)\right]. \tag{7.10}$$

From the two-fluid 2-D Hydrodynamic model for a SWNT of radius R, the induced electric potential on the nanotube is given by

$$\widehat{\Phi}_{\rm ind} = -\sum_m\int\frac{dk}{(2\pi)^2}\frac{e^{im\varphi}e^{ikz}Rg(r,R;m,k)\widetilde{\Phi}_{\rm ext}(R;m,k,\omega)}{\chi^{-1}(m,k,\omega)+Rg(R,R;m,k)} \tag{7.11}$$

where $g(r,r';m,k)$ is the radial Green's function in cylindrical coordinates, derived in Appendix B, $\chi\equiv\chi_\pi+\chi_\sigma$ is the sum of the susceptibilities of the two fluids, and χ_π^{-1} and χ_σ^{-1} are given by

$$\chi_{\pi,\sigma}^{-1} \equiv \frac{\alpha_{\pi,\sigma}}{n^0_{\pi,\sigma}} + \frac{\beta(k^2+\frac{m^2}{R^2})}{n^0_{\pi,\sigma}} - \frac{\omega(\omega+i\gamma)}{n^0_{\pi,\sigma}(k^2+\frac{m^2}{R^2})}, \tag{7.12}$$

with $n^0_\pi \approx 0.107$, $n^0_\sigma \approx 0.321$.

We may express the external perturbing ion's velocity in Cartesian coordinates as $\mathbf{v}_0 = v_\perp\mathbf{e}_y + v_\parallel\mathbf{e}_z$, where $v_\perp\mathbf{e}_y$ is the ion's velocity component perpendicular to the nanotube axis, and $v_\parallel\mathbf{e}_z$ is the ion's velocity component parallel to the nanotube axis. The ion's position in the laboratory frame of reference is then $\mathbf{r}_0(t) = \{r_0(t),\varphi_0(t),z_0(t)\}$, where

$$r_0(t) = \sqrt{r_{\rm min}^2+v_\perp^2t^2}, \tag{7.13}$$

$$\varphi_0(t) = \arctan\left(\frac{v_\perp t}{r_{\rm min}}\right), \tag{7.14}$$

$$z_0(t) = v_\parallel t, \tag{7.15}$$

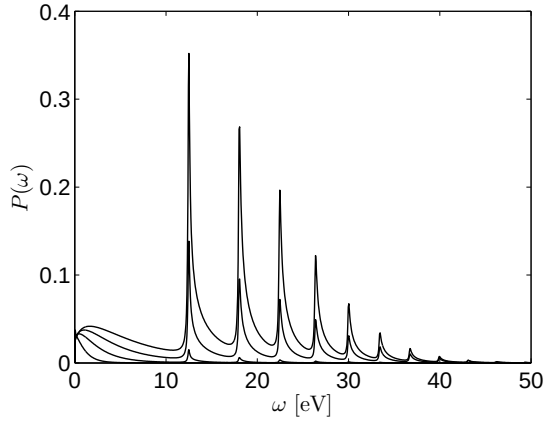

Figure 7.2: The probability function $\mathcal{P}(\omega)$ of undergoing energy loss ω in eV for a proton travelling perpendicular to the nanotube with speed $v_\perp = 1$, 2, 3, and 4 and closest approach $r_{\min} = 10.5$ Å to the nanotube of radius $R = 7$ Å.

and $r_{\min} = \min_t r_0(t)$ is the ion's distance of closest approach to the nanotube axis, which we take to be in the x-direction of our Cartesian coordinate system. We find the Fourier transform of the ion's potential is then given by

$$\widetilde{\Phi}_{\text{ext}} = Q\int_{-\infty}^{\infty} d\tau e^{i\omega\tau} e^{-im\varphi_0(\tau)} e^{-ikz_0(\tau)} g(r, r_0(\tau); m, k). \tag{7.16}$$

The integral over time t in $\mathcal{P}(\omega)$ for an ion outside the SWNT, that is $r_{\min} > R$, is then

$$J_E(m, k, \omega) \equiv \int_{-\infty}^{\infty} dt e^{-i\omega t} e^{im\varphi_0(t)} e^{ikz_0(t)} K_m(|k| r_0(t)), \tag{7.17}$$

and the Fourier transform of the ion's potential is

$$\widetilde{\Phi}_{\text{ext}}(r; m, k, \omega) = 4\pi Q I_m(|k| r) J_E(m, k, \omega). \tag{7.18}$$

In Appendix H, the integral $J_E(m, k, \omega)$ is evaluated to be

$$J_E(m, k, \omega) = \pi \frac{e^{-\frac{r_{\min}}{v_\perp}\sqrt{(\omega - kv_\parallel)^2 + k^2 v_\perp^2}}}{\sqrt{(\omega - kv_\parallel)^2 + k^2 v_\perp^2}} \left(\frac{\omega - kv_\parallel + \sqrt{(\omega - kv_\parallel)^2 + k^2 v_\perp^2}}{kv_\perp} \right)^m . \tag{7.19}$$

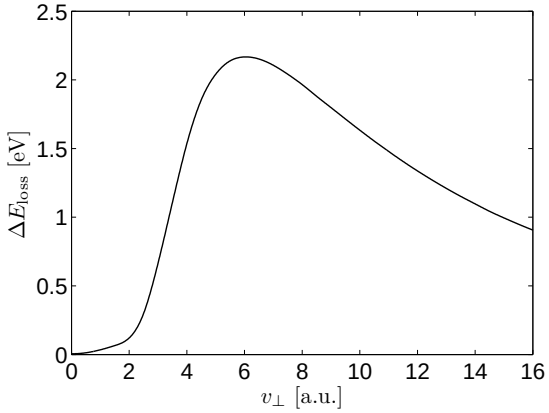

Figure 7.3: The energy loss, $\Delta E_{\rm loss}$, in eV for a proton travelling perpendicular to the nanotube with speed $v_\perp$ in atomic units and closest approach $r_{\rm min} = 10.5$ Å to the nanotube of radius $R = 7$ Å.

The probability function $\mathcal{P}(\omega)$ thus simplifies to

$$\mathcal{P}(\omega) = \frac{Q^2}{\pi^2}\mathrm{Im}\left[\sum_m \int dk \frac{I_m^2(|k|R)J_E^2(m,k,\omega)}{(4\pi R)^{-1}\chi^{-1}(m,k,\omega) + I_m(|k|R)K_m(|k|R)}\right]. \qquad (7.20)$$

In Fig. 7.2, we show the probability function $\mathcal{P}(\omega)$ of undergoing energy loss ω in eV for a proton travelling perpendicularly to the nanotube. We note the significant peaks in $\mathcal{P}(\omega)$ due to the higher m modes of the plasmon branches, which begin to dominate the electronic response outside the nanotube.

Figure 7.3 shows calculations of the energy loss for a proton moving perpendicular to the nanotube axis with a closest approach of $r_{\rm min} = 3R/2$ to a nanotube of radius $R = 7$ Å. A naïve comparison with stopping force calculations, which give the energy loss *per unit path length*, suggests the energy loss calculations shown in Fig. 7.3 are in qualitative agreement with our stopping force calculations. By comparing Fig. 7.3 with the stopping force at $3R/2$ for a proton moving parallel to the nanotube axis, we find that our energy loss calculation behaves qualitatively as a stopping force acting over ~ 10 Å, which is of the order of the nanotube diameter of ~ 14 Å.

7.2 Deflection Angle

The change in the ion's momentum perpendicular to it's trajectory, $\Delta\mathbf{p}_\perp$, is given by

$$\Delta\mathbf{p}_\perp = \int_{-\infty}^{\infty} dt \mathbf{F}_{\rm ind}^\perp(\mathbf{r}_0(t), t), \tag{7.21}$$

where $\mathbf{F}_{\rm ind}^\perp$ is the component of the induced force which acts perpendicularly to the ion's trajectory, given by $\mathbf{F}_{\rm ind}^\perp = \dfrac{(\mathbf{v}_0 \times \mathbf{F}_{\rm ind}) \times \mathbf{v}_0}{v_0^2}$.

The angle of the ion's deflection by the nanotube, $\Delta\boldsymbol{\theta}$, may be approximated for small deflection angles, by

$$\Delta\boldsymbol{\theta} \approx \frac{\Delta\mathbf{p}_\perp}{p_0} = \frac{1}{Mv_0}\int_{-\infty}^{\infty} dt \mathbf{F}_{\rm ind}^\perp(\mathbf{r}_0(t), t), \tag{7.22}$$

where $p_0 = Mv_0$ is the ion's total momentum, M is the ion's mass, and $v_0 = \sqrt{v_\parallel^2 + v_\perp^2}$ is the ion's speed.

Considering the ion to be outside the SWNT, $r_{\rm min} > R$, with the x-axis of our Cartesian coordinate system in the direction of closest approach $r_{\rm min}$, we now restrict consideration to the case of trajectories perpendicular to the nanotube axis, so that the ion's velocity is in the y-direction, with $\mathbf{v}_0 = v_\perp \mathbf{e}_x$ and $v_\parallel = 0$. The ion's deflection angle $\Delta\boldsymbol{\theta}$ is then in the xy-plane, so that $\Delta\boldsymbol{\theta} = \Delta\theta_x \mathbf{e}_x$, and is given by

$$\Delta\theta_x \approx \frac{\Delta p_x}{p_0} = \frac{1}{Mv_0}\int_{-\infty}^{\infty} dt \mathbf{F}_{\rm ind} \cdot \mathbf{e}_x, = -\frac{Q}{Mv_0}\int_{-\infty}^{\infty} dt \left[(\mathbf{e}_x \cdot \vec{\nabla})\Phi_{\rm ind}(\mathbf{r}, t)\right]_{\mathbf{r}=\mathbf{r}_0(t)}, \tag{7.23}$$

where Δp_x is the component of the change in the ion's momentum in the x-direction.

Working with the Fourier transform of the induced potential $\widetilde{\Phi}_{\rm ind}$, which from Eqn. (7.11) is

$$\widetilde{\Phi}_{\rm ind} = -\frac{4\pi R I_m(|k|R) K_m(|k|r)\widetilde{\Phi}_{\rm ext}(R; m, k, \omega)}{\chi^{-1}(m, k, \omega) + Rg(R, R; m, k)}, \tag{7.24}$$

we find that when the ion remains outside the nanotube, $r_{\rm min} > R$, the gradient of the induced potential is then given by

$$\vec{\nabla}\Phi_{\rm ind} = \sum_m \iint \frac{dk d\omega}{(2\pi)^3} e^{im\varphi} e^{ikz} e^{-i\omega t} \widetilde{\Phi}_{\rm ind}(r; m, k, \omega) \left[|k| \frac{K_m'(|k|r)}{K_m(|k|r)}\, \mathbf{e}_r + i\frac{m}{r}\, \mathbf{e}_\varphi + ik\, \mathbf{e}_z\right] \tag{7.25}$$

where

$$\mathbf{e}_r = \cos\varphi\,\mathbf{e}_x + \sin\varphi\,\mathbf{e}_y, \tag{7.26}$$

$$\mathbf{e}_\varphi = \sin\varphi\,\mathbf{e}_x - \cos\varphi\,\mathbf{e}_y. \tag{7.27}$$

The ion's velocity is then

$$\mathbf{v}_0 = v_\perp \mathbf{e}_y = \frac{v_\perp^2 t}{\sqrt{r_{\min}^2 + v_\perp^2 t^2}}\mathbf{e}_r - \frac{v_\perp r_{\min}}{\sqrt{r_{\min}^2 + v_\perp^2 t^2}}\mathbf{e}_\varphi. \tag{7.28}$$

Working with the Fourier transform of the induced potential, given by equation (7.25), we find

$$\Delta\theta_x \approx -\frac{Q}{Mv_0}\int_{-\infty}^{\infty} dt \left[\left(\cos\varphi\frac{\partial}{\partial r} + \frac{\sin\varphi}{r}\frac{\partial}{\partial\varphi}\right)\Phi_{\rm ind}(\mathbf{r},t)\right]_{\mathbf{r}=\mathbf{r}_0(t)} \tag{7.29}$$

$$\Delta\theta_x \approx -\frac{Q}{Mv_0}\int_{-\infty}^{\infty} dt \sum_m \iint \frac{dk d\omega}{(2\pi)^3} e^{im\varphi_0(t)} e^{-i\omega t}\widetilde{\Phi}_{\rm ind}(r_0(t);m,k,\omega) \times \left[|k|\frac{K_m'(|k|r_0(t))}{K_m(|k|r_0(t))}\cos\varphi_0(t) + i\frac{m\sin\varphi_0(t)}{r_0(t)}\right]. \tag{7.30}$$

The integral over time t in $\Delta\theta_x$ thus becomes for $r_{\min} > R$

$$J_\theta(m,k,\omega) \equiv \int_{-\infty}^{\infty} dt e^{im\varphi_0(t)} e^{-i\omega t}\left[|k|K_m'(|k|r_0(t))\cos\varphi_0(t) + imK_m(|k|r_0(t))\frac{\sin\varphi_0(t)}{r_0(t)}\right]. \tag{7.31}$$

After substitution of Eqn. (7.24) for $\widetilde{\Phi}_{\rm ind}$ and Eqn. (7.18) for $\widetilde{\Phi}_{\rm ext}$ into Eqn. (7.30), we may express the deflection angle in the xy-plane in terms of $J_E(m,k,\omega)$ and $J_\theta(m,k,\omega)$ as

$$\Delta\theta_x \approx \frac{Q^2}{2\pi^2 Mv_0}\int_{-\infty}^{\infty} d\omega \sum_m \int dk \frac{I_m^2(kR)J_E(m,k,\omega)J_\theta(m,k,\omega)}{(4\pi R)^{-1}\chi^{-1}(m,k,\omega) + I_m(|k|R)K_m(|k|R)}. \tag{7.32}$$

Although Eqn. (7.32) is a closed form expression for the deflection angle in the xy-plane, the sum over angular wave number m, and the three integrals over frequency ω, longitudinal wave number k, and time t, make a direct numerical calculation of (7.32) difficult using a language such as Matlab. For this reason, we have begun porting our numerical codes to Fortran, with the anticipation of a substantial improvement in our code's runtime.

Chapter 8

Conclusion

8.1 Summary of Results

We have derived a simple, parameter free version of the two-fluid hydrodynamic model for the electronic response of the electrons on a SWNT, which treats the σ and π electrons as separate 2D charged fluids constrained to the same cylindrical surface. The strong electrostatic interaction between the fluids gives rise to splitting of the collective-excitation frequencies into two sets which closely follow the experimental dispersion curves for the high-energy $\sigma + \pi$ plasmons and the low-energy π plasmons. In particular, the $m = 0$ mode of the π plasmons exhibits a quasi-acoustic, linear dispersion versus the longitudinal wave number [68]. Calculations of the induced electron density on the nanotube and the stopping force for a charged particle moving parallel to the nanotube axis show that, at particle speeds above the threshold for $\sigma + \pi$ plasmon excitations, the two-fluid model essentially follows the results of the single-fluid model. Conversely, the low particle speed range reveals some novel effects due to π plasmon excitations in the two-fluid model. In particular, when the particle speed matches the phase velocity of the acoustic π plasmon, the induced density shows oscillations which precede the position of the particle, in contrast to the usual wake oscillations, whereas the speed-dependence of the stopping force of the particle displays peaked structures around that phase velocity. It has been found that, while the high-speed stopping force is insensitive to the friction coefficient, the low-speed peaks are quite dependent on it. This finding points to a need to further improve the proposed two-fluid model by carefully examining the role of damping at lower plasmon frequencies.

We have also formulated a hydrodynamic model for the dielectric response of a MWNT, represented by a set of concentric cylindrical surfaces, each occupied by a 2D electron fluid. Calculations have been completed for a two-cylinder nanotube, showing that the strong electrostatic interaction between the two fluids on these cylinders gives rise to splitting of the collective-excitation frequencies into two sets for various angular modes m, with the lower $m = 0$ mode exhibiting a quasi-acoustic, linear dispersion versus the longitudinal wave number k. Calculations of the stopping force for a charged particle, which moves at speed v, parallel to the nanotube axis at radial distances inside, outside, or in between the two cylinders, show typical broad peaks above the plasmon-excitation threshold phase speed of $v \approx 2$, as well as a narrow peak at $v \approx 4$, matching the phase velocity of the quasi-acoustic low-energy plasmon. Calculations of the self-energy of a charged particle moving paraxially show the typical long-ranged attractive wells for radial distances close to the cylinder walls, which diminish with increasing speed v, with an intriguing jump in the self-energy across the speed $v \approx 4$ for all radial distances.

These findings indicate that richness in the plasmon dispersions of MWNTs may exert a profound influence on the dynamics of charged-particle interactions with MWNTs, especially when conditions are met for a drift instability of the electron fluids. The multitude of plasmon dispersion curves in the presence of multiple walls gives rise to rather strong interference patterns in the velocity dependences of both the stopping force and the self-energy for fast ions moving paraxially inside the nanotube. It is expected that, if larger values of the friction coefficients in those fluids are used, the interference patterns would be significantly washed-out [68]. As the radial position of an ion increases into regions between the nanotube walls, and eventually reaches regions far outside the nanotube, the interference patterns also tend to disappear. The low-frequency group of π plasmons exerts relatively weak effects on the low-speed stopping force and self-energy, so that the bulk of these quantities at intermediate and high speeds may be satisfactorily described by a single-fluid model [144] for the combined $\sigma+\pi$ electron oscillations.

We have studied the plasmon hybridization in the UV region taking place when a single-walled CNT either is encapsulated in a solid channel or encapsulates a solid nano-wire. For the case of aluminum, we have shown that the antisymmetrically coupled plasmon dispersion curves are always above the nanotube curves, whose low-energy, quasi-acoustic plasmon π branches exhibit a remarkable insensitivity to the presence of metal, due to their large separation from the metallic wire and channel branches. Conversely, the symmetrically coupled metal-$(\sigma + \pi)$

branches occur at low energies and are forced through plasmon hybridization to undergo avoided crossings with the π branches, depending on the size of the gap between the nanotube and the metal.

Further, we have studied the energy losses and the dynamical image potential, which are both determined by the plasmon excitations, for fast ions moving parallel to the nanotube axis. In the case of insulating materials, such as SiO_2, the nanotube's high-speed stopping is significantly suppressed and its low-speed stopping raised, whereas in the cases of amorphous carbon and metals, the opposite is generally true. We have paid particular attention to nickel, as it is known to be one of the metals that most readily binds to CNTs, both inside and outside. Moreover, we have found that the dynamical image potential inside a nanotube encapsulated in a nickel channel follows the potential inside an isolated nanotube at low speeds, but approaches the potential inside an isolated nickel channel at high speeds. For an ion moving parallel to a nanotube encapsulating a nickel nanowire, we have found that the dynamical image potential at large distance from the nanotube closely follows that of an isolated nanotube, indicating that an efficient shielding of the embedded metal takes place.

However, near the nanotube wall, the accuracy of the 2D hydrodynamic model becomes questionable. To better model channelling in the near wall region, and determine the region of validity of the 2D hydrodynamic model, we have also studied the 3D Kitagawa model. Given the limitation of the 3D model of the electron gas to high frequencies, and therefore high ion speeds, one can deduce with a reasonable degree of confidence several conclusions of relevance for ion channelling at the energies of about 1 MeV/amu, or higher. In the central regions of CNTs where the electron density is low, the stopping due to distant collisions with target electrons is reasonably well described by both the 2D hydrodynamic model and the non-local contribution of the 3D model. As the ion approaches the nanotube wall, close collisions with the nanotube electrons give a significant increase in energy losses, which is well described by the local contribution from the 3D model, whereas the 2D model becomes increasingly inadequate already within several ångströms of the nanotube wall.

We have also applied the 2D hydrodynamic model to dicluster channelling, where we find that for diclusters with common paraxial speed $v \gtrsim 2$, the collective oscillations of the induced electric potential give rise to "wells" in the total electric potential. These minima occur when the trailing ion is located in a potential well of the leading ion's wake, often called "wake riding". We

also find that the longer-ranged Molière atomic potential provides a more substantial reduction of the electron fluid's screening ability, when compared with the shorter-ranged Doyle-Turner atomic potential. This leads to narrower and deeper potential wells when using the Doyle-Turner atomic potential when compared with the wide shallow wells obtained from the Molière atomic potential.

We have found that both the self-energy and stopping force for point dipole channelling are approximately two orders of magnitude smaller than the respective values for single ions or di-clusters, when $\mu \sim 1$. Since the dipole moment of water is $\mu_{\mathrm{H_2O}} \approx 0.73$, this suggests that individual water molecules should have minimal electrostatic interactions with CNTs. However, the well-known hydrophobicity of CNTs [38] brings the point-dipole model into question, suggesting that other interactions, such as the induced dipole moment, may dominate the electrostatic interaction between water molecules and nanotubes.

Finally, we have considered the energy losses and deflection angles for ions travelling at oblique angles to the nanotube axis. We find that the plasmon excitation probability function, $\mathcal{P}(\omega)$, also called variously the frequency dependent loss probability and the energy-loss probability per energy unit, consists of a series of sharp peaks arising from various m modes of the plasmon energies. We also find that the energy loss ΔE_{loss}, is substantial when compared with the stopping force for ions travelling paraxially at the same distance from the nanotube. Although we are able to provide a closed form expression for the deflection angle, calculation of the sum over angular wave number m, and the three integrals over frequency ω, longitudinal wave number k, and time t, make a numerical result difficult to obtain.

8.2 Applications of the 2D Hydrodynamic Model

In general, our results are possibly very relevant for the ongoing studies of ion channelling through CNTs, which may be part of a rope assembled on a solid substrate and clamped by a metal, since both the ion stopping and the image force may be quite sensitive to the presence of a polarizable medium surrounding a nanotube. In that context, it is interesting to mention that Fink *et al.* recently grew CNTs in etched ion tracks in films of SiO_2 and other materials, providing a system in which ion channelling in CNTs may be realized [221]. Also quite recently, Zhu *et al.* published the first evidence of ion channelling in carbon nanotubes, by incorporating

an array of well-ordered carbon nanotubes in a porous anodic aluminum oxide membrane [222]. The 2D hydrodynamic model has already been used in MD simulations of proton and cluster channelling through long SWNTs by Zhou *et al.* [50, 214], and MD simulations of the rainbow effect in proton channelling through SWNTs and DWNTs by Borka *et al.* [215, 216]. On the other hand, our results also imply that an embedded metal wire in a CNT will probably exert very little influence on the electron image states around the nanotube.

8.3 Future Work

Many potential applications and extensions of the 2D hydrodynamic model are open at present, but we shall mention here only a few of immediate interest.

It is worth noting that the 3D Kitagawa model assumes that internal interactions between electrons contribute only to the equilibrium electron density, and may be neglected when calculating the linear correction to the induced electron density. This apparent inconsistency could be resolved by retention of the $\frac{\delta G[n]}{\delta n}$ term in Eqn. (5.39) when calculating the induced electron density. Such a calculation would amount to use of the full 3D density functional $F[n]$. This should provide more accurate calculations of the induced electron density, especially in the "near wall" region, since the cylindrical geometry of the density functional $F[n]$ is retained. Such accurate calculations of both the image potential and stopping force in the near wall region are needed for the MD simulation of ion channelling through nanotubes [214, 50], and the calculation of the rainbow effect in such systems [215, 216]. However, the "shooting method", which was used to calculate the radial equilibrium electron density, becomes intractable for the 3D problem, since the boundary condition on the induced electron density is an integral over all three spatial coordinates $\iiint n(r) r dr d\varphi dz = Q$, where Q is the ion's charge.

The 2D hydrodynamic model could also be improved by allowing the equilibrium electron density to be a function of angular and longitudinal position, so that $n_0 \equiv n_0(\varphi, z)$. This amounts to removal of the jellium approximation. The use of a 2D position dependent equilibrium electron density would allow the incorporation into our calculation of a nanotube's chirality, which determines whether a nanotube is semiconducting or metallic [2]. The results we have presented here are most applicable to chiral nanotubes with large unit cells, such as an (11,9) SWNT with a unit cell of ≈ 70 Å in length. For these nanotubes, the jellium approximation is highly accurate

for fast ion channelling, since the electron density contains no “grooves”. However, “grooves” are found in the electron density of non-chiral nanotubes such as the (10,10) armchair SWNT.

Briefly, other possible extensions and applications of the present study of carbon nanotubes include

- Calculation of ion self-energy in channelling based on a 3D model
- Calculation of ion deflection angles for oblique trajectories
- Channelling and oblique incidence of polarizable molecules
- Modelling of boron nitride nanotubes
- Non-linear corrections to the hydrodynamic model
- Modelling dielectric response of CNT ropes or bundles
- Ion charge-state effects on channelling and oblique incidence
- Modelling dielectric response of finite-length CNTs
- Effects of external laser and magnetic fields
- Modelling CNTs in a plasmon sheath region

Appendix A

2D Density-Functional Theory Calculations

A.1 Hohenberg-Kohn Theorem

We will begin our discussion of DFT by proving the following simplified version of Theorem 2.1 given by Hohenberg and Kohn [223], and discussed by Parr and Yang pp. 51–56 [127].

Theorem A.1 (First Hohenberg-Kohn)
The external potential $V_{\mathrm{ext}}(\mathbf{r})$ is determined, within a trivial additive constant, by the electron density $n(\mathbf{r})$.

Proof

Let Ψ and Ψ' be wavefunctions for the electron number density $n(\mathbf{r}) = \Psi^*(\mathbf{r})\Psi(\mathbf{r}) = \Psi'^*(\mathbf{r})\Psi'(\mathbf{r})$. Now let Ψ and Ψ' be ground state wavefunctions for the Hamiltonians $\widehat{\mathcal{H}}$ and $\widehat{\mathcal{H}}'$ with ground state energies E_0 and E_0' respectively. We now assume that $E_0 \neq E_0'$, so that the

ground state energy is not unique for a given electron number density $n(\mathbf{r})$.

$$
\begin{aligned}
E_0 &= \iiint d^3\mathbf{r}\ \Psi^*(\mathbf{r})\widehat{\mathcal{H}}\Psi(\mathbf{r}) && \text{(A.1)}\\
&< \iiint d^3\mathbf{r}\ \Psi'^*(\mathbf{r})\widehat{\mathcal{H}}\Psi'(\mathbf{r}) && \text{(A.2)}\\
&= \iiint d^3\mathbf{r}\ \Psi'^*(\mathbf{r})\widehat{\mathcal{H}}'\Psi'(\mathbf{r}) + \iiint d^3\mathbf{r}\ \Psi'^*(\mathbf{r})(\widehat{\mathcal{H}} - \widehat{\mathcal{H}}')\Psi'(\mathbf{r}) && \text{(A.3)}\\
&= E_0' + \iiint d^3\mathbf{r}\ n(\mathbf{r})[V_{\rm ext}(\mathbf{r}) - V'_{\rm ext}(\mathbf{r})], && \text{(A.4)}
\end{aligned}
$$

where $V_{\rm ext}(\mathbf{r})$ and $V'_{\rm ext}(\mathbf{r})$ are the external potentials for the Hamiltonians $\widehat{\mathcal{H}}$ and $\widehat{\mathcal{H}}'$ respectively. Similarly for E_0' we find

$$
E_0' < E_0 - \iiint d^3\mathbf{r}\ n(\mathbf{r})[V_{\rm ext}(\mathbf{r}) - V'_{\rm ext}(\mathbf{r})], \qquad \text{(A.5)}
$$

so that summing Eqns. (A.4) and (A.5) we find $E_0 + E_0' < E_0' + E_0$, which is a contradiction. Thus there cannot be two different external potentials $V_{\rm ext}(\mathbf{r})$ that give the same electron density $n(\mathbf{r})$ for their ground states.

A.2 Density $n(\mathbf{r}_\infty)$ on a Plane

For an electron gas confined to a 2D plane, with Cartesian coordinates $\mathbf{r}_\infty \equiv \{x, y; z = 0\}$, we may approximate the wave functions by

$$
\psi(k_x, k_y; x, y) = \frac{e^{ik_x x} e^{ik_y y}}{L}, \qquad \text{(A.6)}
$$

where $k_x = 2\pi n_x/L$, $k_y = 2\pi n_y/L$; $n_x, n_y \in \{0, \pm 1, \ldots\}$, and L is the length of the infinite potential well which confines the electron gas to the plane. The energy is then from the Schrödinger equation

$$
E(k_x, k_y) = \frac{k_x^2 + k_y^2}{2}. \qquad \text{(A.7)}
$$

The density matrix in terms of the wavefunctions $\psi(k_x, k_y; x, y)$ is then

$$
\rho(\mathbf{r}_\infty, \Delta r) = \frac{1}{2\pi^2}\int dk \int d\theta k e^{ik\Delta r\cos\theta}. \qquad \text{(A.8)}
$$

The planar density is then given by

$$n(\mathbf{r}_\infty) \;=\; \rho(\mathbf{r}_\infty,\mathbf{r}_\infty) = \frac{1}{2\pi^2}\int_0^{k_F} dkk \int_{-\pi}^{\pi} d\theta = \frac{k_F}{2\pi} = \frac{E_F}{\pi} \quad . \tag{A.9}$$

We may calculate $\rho(\mathbf{r}_\infty, \Delta r)$ by utilizing the integral form of the Bessel function of the first kind

$$J_0(z) \;=\; \frac{1}{\pi}\int_0^{\pi} d\theta e^{iz\cos\theta}, \tag{A.10}$$

given by Abramowitz and Stegun [169]. We then find

$$\rho(\mathbf{r}_\infty, \Delta r) \;=\; \frac{1}{\pi}\int_0^{k_F} dkkJ_0(k\Delta r). \tag{A.11}$$

Employing the recurrence relation

$$z^n J_{n-1}(z) \;=\; \frac{d}{dz} z^n J_n(z) \tag{A.12}$$

from Abramowitz and Stegun [169], we find

$$\rho(\mathbf{r}_\infty, \Delta r) \;=\; \frac{k_F}{\pi\Delta r} J_1(k_F\Delta r) = \frac{\sqrt{2\pi n}}{\Delta r\pi} J_1(\sqrt{2\pi n}\Delta r). \tag{A.13}$$

A.3 Density $n(\mathbf{r}_R)$ on a Cylinder

The electron density $n(\mathbf{r}_R) = \rho(\mathbf{r}_R, \mathbf{r}_R)$ on a cylinder may be written in terms of the Fermi energy E_F using Eqn. (2.25) as

$$n(\mathbf{r}_R) = \frac{1}{\pi^2 R} \sum_{\ell=-\lfloor \ell_F \rfloor}^{\lfloor \ell_F \rfloor} \sqrt{2E_F - \frac{\ell^2}{R^2}} \tag{A.14}$$

$$= \frac{1}{\pi^2 R^2} \sum_{\ell=-\lfloor \ell_F \rfloor}^{\lfloor \ell_F \rfloor} \sqrt{\ell_F^2 - \ell^2} \tag{A.15}$$

We now rewrite our summation using the Euler-Maclaurin formula

$$\sum_{k=m}^{n} f(k) = \int_m^n f(x)dx + \frac{1}{2}\left(f(n) + f(m)\right) + \frac{1}{12}\left(f'(n) - f'(m)\right) + \varepsilon(f,m,n) \tag{A.16}$$

$$|\varepsilon(f,m,n)| \leq \frac{1}{120}\int_m^n |f'''(x)|dx. \tag{A.17}$$

to obtain

$$n(\mathbf{r}_R) = \frac{1}{\pi^2 R^2}\left(\int_{-\lfloor \ell_F\rfloor+1}^{\lfloor \ell_F\rfloor-1}\sqrt{\ell_F^2-\ell^2}d\ell + 2\sqrt{\ell_F^2-\lfloor \ell_F\rfloor^2}+\sqrt{\ell_F^2-(\lfloor \ell_F\rfloor-1)^2}\right.$$
$$\left.-\frac{1}{6}\frac{\lfloor \ell_F\rfloor-1}{\sqrt{\ell_F^2-(\lfloor \ell_F\rfloor-1)^2}}+\varepsilon\left(\ell_F,\lfloor \ell_F\rfloor\right)\right) \tag{A.18}$$
$$= \frac{\ell_F^2}{\pi^2 R^2}\left(\arcsin\left(\frac{\lfloor \ell_F\rfloor-1}{\ell_F}\right)+\frac{\lfloor \ell_F\rfloor}{\ell_F}\sqrt{1-\frac{(\lfloor \ell_F\rfloor-1)^2}{\ell_F^2}}\right.$$
$$\left.+\frac{2}{\ell_F}\sqrt{1-\frac{\lfloor \ell_F\rfloor^2}{\ell_F^2}}+\frac{\lfloor \ell_F\rfloor-1}{6\ell_F^2\sqrt{\ell_F^2-(\lfloor \ell_F\rfloor-1)^2}}+\frac{1}{\ell_F^2}\varepsilon\left(\ell_F,\lfloor \ell_F\rfloor\right)\right) \tag{A.19}$$

where

$$\left|\varepsilon\left(\ell_F,\lfloor \ell_F\rfloor\right)\right| \leq \frac{1}{60}\frac{\ell_F^2}{(\ell_F^2-(\lfloor \ell_F\rfloor-1)^2)^{3/2}} \tag{A.20}$$

We now define a parameter $\epsilon^2 = \ell_F - \lfloor \ell_F\rfloor < 1$. Expanding in terms of $\frac{1}{\ell_F}$ we obtain

$$n(\mathbf{r}_R) = \frac{\ell_F^2}{\pi^2 R^2}\left[\frac{\pi}{2}+\left[2\sqrt{2}\epsilon-\frac{16\epsilon^4+20\epsilon^2+3}{6\sqrt{2\epsilon^2+2}}\right]\ell_F^{-3/2}+\frac{1}{\ell_F^2}\varepsilon\left(\ell_F,\lfloor \ell_F\rfloor\right)+\mathcal{O}\left(\ell_F^{-5/2}\right)\right] \tag{A.21}$$
$$= n_{\text{plane}}\left[1+\left[\frac{4\sqrt{2}}{\pi}\epsilon-\frac{16\epsilon^4+20\epsilon^2+3}{3\pi\sqrt{2\epsilon^2+2}}\right]\ell_F^{-3/2}+\frac{2}{\pi\ell_F^2}\varepsilon\left(\ell_F,\lfloor \ell_F\rfloor\right)+\mathcal{O}\left(\ell_F^{-5/2}\right)\right] \tag{A.22}$$

where the error is bounded above by

$$\left|\frac{2}{\pi\ell_F^2}\varepsilon\left(\ell_F,\lfloor \ell_F\rfloor\right)\right| \leq \frac{1}{30\pi}\left(\ell_F^2-(\lfloor \ell_F\rfloor-1)^2\right)^{-3/2} \tag{A.23}$$
$$= \frac{(\epsilon^2+1)^{-2}}{60\pi\sqrt{2\epsilon^2+2}}\ell_F^{-3/2}+\mathcal{O}\left(\ell_F^{-5/2}\right). \tag{A.24}$$

The density $n(\mathbf{r}_R)$ may thus be approximated by the planar density $n_{\text{plane}}(\mathbf{r}_\infty$ with relative error $\varepsilon^n_{\text{plane}}$ given by

$$\varepsilon^n_{\text{plane}} = \left\|\frac{n(\mathbf{r}_R)-n_{\text{plane}}(\mathbf{r}_\infty)}{n_{\text{plane}}(\mathbf{r}_\infty)}\right\|_\infty \tag{A.25}$$
$$= \frac{2}{\pi}\max_\epsilon\left|2\sqrt{2}\epsilon-\frac{16\epsilon^4+20\epsilon^2+3}{6\sqrt{2\epsilon^2+2}}\pm\frac{1}{60(2\epsilon^2+2)^{3/2}}\right|\ell_F^{-3/2}+\mathcal{O}\left(\ell_F^{-5/2}\right) \tag{A.26}$$
$$\approx 0.302\ell_F^{-3/2}+\mathcal{O}\left(\ell_F^{-5/2}\right). \tag{A.27}$$

A.4 $-\nabla^2_{\mathbf{r}_R}\rho(\mathbf{r}_R,\mathbf{r}'_R)\big|_{\mathbf{r}'_R=\mathbf{r}_R}$ on a Cylinder

To calculate the diagonal elements of the Laplacian of the density matrix $-\nabla^2_{\mathbf{r}_R}\rho(\mathbf{r}_R,\mathbf{r}'_R)$, we first make the following change of coordinates

$$\overline{\mathbf{r}}_R = \frac{1}{2}\left(\mathbf{r}_R + \mathbf{r}'_R\right) \tag{A.28}$$

$$\Delta\mathbf{r}_R = \mathbf{r}_R - \mathbf{r}'_R = \{0, \Delta\varphi, \Delta z\}, \tag{A.29}$$

so that we may write the Laplacian in the new coordinates as

$$\nabla^2_{\mathbf{r}_R} = \frac{1}{4}\nabla^2_{\overline{\mathbf{r}}_R} + \vec{\nabla}_{\overline{\mathbf{r}}_R}\vec{\nabla}_{\Delta\mathbf{r}_R} + \nabla^2_{\Delta\mathbf{r}_R} \tag{A.30}$$

using the Chain Rule. We may rewrite the Thomas-Fermi term in the new coordinates as

$$T_{\mathrm{TF}} = -\frac{1}{2}\iint d^2\overline{\mathbf{r}}_R\,\left(\frac{1}{4}\nabla^2_{\overline{\mathbf{r}}_R} + \vec{\nabla}_{\overline{\mathbf{r}}_R}\vec{\nabla}_{\Delta\mathbf{r}_R} + \nabla^2_{\Delta\mathbf{r}_R}\right)\rho(\overline{\mathbf{r}}_R,\Delta\mathbf{r}_R)\Big|_{\Delta\mathbf{r}_R=0} \tag{A.31}$$

Evaluating the integrand of T_{TF} term by term, we find

$$\vec{\nabla}_{\Delta\mathbf{r}_R}\rho(\overline{\mathbf{r}}_R,\Delta\mathbf{r}_R)|_{\Delta\mathbf{r}_R=0} = \frac{1}{\pi^2 R}\int_{-\lfloor\ell_F\rfloor}^{\lfloor\ell_F\rfloor} d\ell\left(\frac{1}{R}\frac{\partial}{\partial\Delta\varphi} + \frac{\partial}{\partial\Delta z}\right)e^{i\ell\Delta\varphi}\frac{\sin(k_F(\ell)\Delta z)}{\Delta z}\Big|_{\Delta\mathbf{r}_R=0} \tag{A.32}$$

$$= \frac{1}{\pi^2 R}\int_{-\lfloor\ell_F\rfloor}^{\lfloor\ell_F\rfloor} d\ell e^{i\ell\Delta\varphi}\left[\left[\frac{i\ell}{R} - \frac{1}{\Delta z}\right]\frac{\sin(k_F\Delta z)}{\Delta z} + \frac{\cos(k_F\Delta z)k_F}{\Delta z}\right]d\ell\Big|_{\Delta\mathbf{r}_R=0} = 0 \tag{A.33}$$

since $k_F(\ell)$ is an even function of ℓ.

For the $\nabla^2_{\Delta\mathbf{r}_R}$ term we find

$$-\nabla^2_{\Delta\mathbf{r}_R}\rho(\overline{\mathbf{r}}_R,\Delta\mathbf{r}_R)|_{\Delta\mathbf{r}_R=0}$$

$$= \frac{1}{\pi^2 R}\sum_{\ell=-\lfloor\ell_F\rfloor}^{\lfloor\ell_F\rfloor} e^{i\ell\Delta\varphi}\left[\frac{\ell^2}{R^2} + k_F^2 - \frac{2}{\Delta z^2} + \frac{2\cos(k_F\Delta z)}{\sin(k_F\Delta z)\Delta z}\right]\frac{\sin(k_F\Delta z)}{\Delta z}\Big|_{\Delta\mathbf{r}_R=0} \tag{A.34}$$

$$= \frac{1}{\pi^2 R}\sum_{\ell=-\lfloor\ell_F\rfloor}^{\lfloor\ell_F\rfloor}\left(\frac{\ell^2}{R^2} + \frac{1}{3}k_F^2(\ell)\right)k_F(\ell) \tag{A.35}$$

$$= \frac{1}{\pi^2 R^4}\sum_{\ell=-\lfloor\ell_F\rfloor}^{\lfloor\ell_F\rfloor}\ell^2\sqrt{\ell_F^2-\ell^2} + \frac{1}{3}\left(\ell_F^2-\ell^2\right)^{3/2} \tag{A.36}$$

Applying the Euler-Maclaurin summation formula as before, we obtain the following expansion in terms of ℓ_F^{-1} where $\epsilon^2 = \ell_F - \lfloor \ell_F \rfloor < 1$,

$$
\begin{aligned}
&-\nabla^2_{\Delta \mathbf{r}_R} \rho(\overline{\mathbf{r}}_R, \Delta \mathbf{r}_R)|_{\Delta \mathbf{r}_R = 0} \\
&= \frac{\ell_F^4}{\pi^2 R^4} \left(\frac{\pi}{4} + \left(2\sqrt{2}\epsilon - \frac{16\epsilon^4 + 20\epsilon^2 + 5}{6\sqrt{2\epsilon^2 + 2}} \right) \ell_F^{-3/2} + \frac{1}{\ell_F^4} \varepsilon \left(\ell_F, \lfloor \ell_F \rfloor \right) + \mathcal{O}\left(\ell_F^{-5/2} \right) \right) && \text{(A.37)} \\
&= \pi n_{\text{plane}}^2 \left(1 + \left(\frac{8\sqrt{2}}{\pi}\epsilon - \frac{32\epsilon^4 + 40\epsilon^2 + 10}{3\pi\sqrt{2\epsilon^2 + 2}} \right) \ell_F^{-3/2} + \frac{4}{\ell_F^4 \pi} \varepsilon(\ell_F, \lfloor \ell_F \rfloor) + \mathcal{O}\left(\ell_F^{-5/2} \right) \right) && \text{(A.38)}
\end{aligned}
$$

where the error $\varepsilon \left(\ell_F, \lfloor \ell_F \rfloor \right)$ satisfies

$$
\left| \frac{1}{\ell_F^4} \varepsilon(\ell_F, \lfloor \ell_F \rfloor) \right| \leq \frac{1}{60} (2\epsilon^2 + 2)^{-3/2} \ell_F^{-3/2} + \mathcal{O}\left(\ell_F^{-5/2} \right) \tag{A.39}
$$

Thus we are justified in using the planar density relation, πn_{plane}^2, with relative error $\varepsilon_{\text{plane}}^{\nabla^2 \rho}$

$$
\begin{aligned}
\varepsilon_{\text{plane}}^{\nabla^2 \rho} &= \left\| \frac{\nabla^2_{\Delta \mathbf{r}_R} \rho(\overline{\mathbf{r}}_R, \Delta \mathbf{r}_R)|_{\Delta \mathbf{r}_R = 0} + \pi n_{\text{plane}}^2}{\pi n_{\text{plane}}^2} \right\|_\infty && \text{(A.40)} \\
&= \frac{4}{\pi} \max_\epsilon \left| 2\sqrt{2}\epsilon - \frac{16\epsilon^4 + 20\epsilon^2 + 5}{6\sqrt{2\epsilon^2 + 2}} \pm \frac{1}{60(2\epsilon^2 + 2)^{3/2}} \right| \ell_F^{-3/2} + \mathcal{O}\left(\ell_F^{-5/2} \right) && \text{(A.41)} \\
&\approx 0.3303 \ell_F^{-3/2} + \mathcal{O}\left(\ell_F^{-5/2} \right). && \text{(A.42)}
\end{aligned}
$$

A.5 Exchange Energy Correction on a Plane

The exchange energy correction $K[\rho]$ on a plane is given by

$$
\begin{aligned}
K[\rho] &= \frac{1}{4} \iint d^2 \mathbf{r}_\infty \int d(\Delta r) \int d(\Delta\theta) \Delta r \frac{\rho^2(\mathbf{r}_\infty, \Delta r)}{\Delta r} && \text{(A.43)} \\
&= \frac{1}{4} \iint d^2 \mathbf{r}_\infty \int d(\Delta r) \int d(\Delta\theta) \frac{2\pi n}{\pi^2 \Delta r^2} J_1^2(\sqrt{2\pi n} \Delta r) && \text{(A.44)} \\
&= \iint d^2 \mathbf{r}_\infty \, n(\mathbf{r}_\infty) \int d(\Delta r) \frac{J_1^2(\sqrt{2\pi n} \Delta r)}{\Delta r^2} && \text{(A.45)} \\
&= \frac{4}{3} \sqrt{\frac{2}{\pi}} \iint d^2 \mathbf{r}_\infty \, n^{3/2}(\mathbf{r}_\infty). && \text{(A.46)}
\end{aligned}
$$

A.6 von Weizsäcker Kinetic Energy Term

Following the procedure outlined by Kryachko and Ludeña pp. 66, 173, 291–292 [184], we may write the kinetic energy term of the Hartree-Fock ground state energy as

$$T[\rho] = -\frac{1}{2}\iint d^2\mathbf{r}_R \; \nabla^2_{\mathbf{r}_R}\rho(\mathbf{r}_R, \mathbf{r}'_R)|_{\mathbf{r}_R=\mathbf{r}'_R} \tag{A.47}$$

$$= -\frac{1}{2}\iint d^2\mathbf{r}_R \iint d^2\mathbf{r}'_R \; \delta(\mathbf{r}_R - \mathbf{r}'_R)\nabla^2_{\mathbf{r}_R}\rho(\mathbf{r}_R, \mathbf{r}'_R). \tag{A.48}$$

We now assume that the two-electron density matrix $\rho(\mathbf{r}_R, \mathbf{r}'_R)$ is an antisymmetric function of the electron positions, so that $\rho(\mathbf{r}_R, \mathbf{r}'_R) = -\rho(\mathbf{r}'_R, \mathbf{r}_R)$. Then employing the expansion of $\rho(\mathbf{r}_R, \mathbf{r}'_R)$ in terms of spatial wave functions ϕ_i, so that $\rho(\mathbf{r}_R, \mathbf{r}'_R) = 2\sum_{i=1}^{N/2} \phi_i^*(\mathbf{r}_R)\phi_i(\mathbf{r}'_R)$, we find

$$T[\rho] = \frac{1}{2}\iint d^2\mathbf{r}_R \iint d^2\mathbf{r}'_R \; \delta(\mathbf{r}_R - \mathbf{r}'_R)\vec{\nabla}_{\mathbf{r}_R}\vec{\nabla}_{\mathbf{r}'_R}\left(2\sum_{i=1}^{N/2}\phi_i^*(\mathbf{r}_R)\phi_i(\mathbf{r}'_R)\right) \tag{A.49}$$

$$= \iint d^2\mathbf{r}_R \sum_{i=1}^{N/2} \vec{\nabla}_{\mathbf{r}_R}\phi_i^*(\mathbf{r}_R) \cdot \vec{\nabla}_{\mathbf{r}'_R}\phi_i(\mathbf{r}'_R)\Big|_{\mathbf{r}'_R=\mathbf{r}_R} \tag{A.50}$$

$$= \iint d^2\mathbf{r}_R \sum_{i=1}^{N/2} \frac{\vec{\nabla}_{\mathbf{r}_R}\phi_i^*(\mathbf{r}_R)\phi_i(\mathbf{r}_R) \cdot \vec{\nabla}_{\mathbf{r}'_R}\phi_i^*(\mathbf{r}'_R)\phi_i(\mathbf{r}'_R)}{4\phi_i(\mathbf{r}_R)\phi_i^*(\mathbf{r}'_R)}\Bigg|_{\mathbf{r}'_R=\mathbf{r}_R} \tag{A.51}$$

$$= \frac{1}{8}\iint d^2\mathbf{r}_R \sum_{i=1}^{N/2} \frac{[2\vec{\nabla}\phi_i^*(\mathbf{r}_R)\phi_i(\mathbf{r}_R)]^2}{2\phi_i(\mathbf{r}_R)\phi_i^*(\mathbf{r}_R)}. \tag{A.52}$$

When the electron fluid consists of only one doubly occupied orbital, so that $N = 2$ and $n(\mathbf{r}_R) = 2\phi(\mathbf{r}_R)\phi^*(\mathbf{r}_R)$, we obtain the von Weizsäcker term directly from the kinetic energy term, so that

$$T[n] = \frac{1}{8}\iint d^2\mathbf{r}_R \; \frac{[\vec{\nabla}n(\mathbf{r}_R)]^2}{n(\mathbf{r}_R)}. \tag{A.53}$$

Appendix B

Green's Functions in Cylindrical Coordinates

The method of Green's functions in cylindrical coordinates, as discussed by Jackson pp. 125–127 [199], involves finding a function $G(\mathbf{r}, \mathbf{r}')$ which satisfies

$$\nabla^2 G(\mathbf{r}, \mathbf{r}') = -\frac{4\pi}{r}\delta(r - r')\delta(\varphi - \varphi')\delta(z - z'), \tag{B.1}$$

and is symmetric in $\mathbf{r}$ and $\mathbf{r}'$, so that $G(\mathbf{r}, \mathbf{r}') = G(\mathbf{r}', \mathbf{r})$. Once such a function, called the Green's function, is found, the solution to Poisson's equation, Eqn. (2.69), is given by

$$\Phi(\mathbf{r}, t) = \iiint d^3\mathbf{r}'\, G(\mathbf{r}, \mathbf{r}')[\rho_{\text{ext}}(\mathbf{r}', t) - \rho_1(\mathbf{r}', t)]. \tag{B.2}$$

This is seen by calculating the Laplacian of Eqn. (B.2)

$$\begin{aligned}
\nabla^2_{\mathbf{r}}\Phi(\mathbf{r}, t) &= \nabla^2_{\mathbf{r}} \iiint d^3\mathbf{r}'\, G(\mathbf{r}, \mathbf{r}')[\rho_{\text{ext}}(\mathbf{r}', t) - \rho_1(\mathbf{r}', t)] && \text{(B.3)}\\
&= \iiint d^3\mathbf{r}'\, \nabla^2_{\mathbf{r}} G(\mathbf{r}, \mathbf{r}')[\rho_{\text{ext}}(\mathbf{r}', t) - \rho_1(\mathbf{r}', t)] && \text{(B.4)}\\
&= -\int dz' \int dr' \int d\varphi' r' \frac{4\pi}{r}\delta(r - r')\delta(\varphi - \varphi')\delta(z - z')[\rho_{\text{ext}}(\mathbf{r}', t) - \rho_1(\mathbf{r}', t)] && \text{(B.5)}\\
&= -4\pi[\rho_{\text{ext}}(\mathbf{r}, t) - \rho_1(\mathbf{r}, t)]. && \text{(B.6)}
\end{aligned}$$

From Fourier analysis, we know that the Fourier transform of the delta function is the unit

function, so that

$$\delta(z-z') = \int_{-\infty}^{\infty} \frac{dk}{2\pi} e^{ik(z-z')}, \tag{B.7}$$

and since the polar angle φ is a periodic function,

$$\delta(\varphi-\varphi') = \sum_{m=-\infty}^{\infty} \frac{1}{2\pi} e^{im(\varphi-\varphi')}. \tag{B.8}$$

We now introduce a radial Green's function $g(r,r';m,k)$ so that

$$G(\mathbf{r},\mathbf{r}') = \sum_m \int \frac{dk}{(2\pi)^2} e^{ik(z-z')} e^{im(\varphi-\varphi')} g(r,r';m,k). \tag{B.9}$$

Employing Eqn. (B.1), we find after some simplification that $g(r,r';m,k)$ must satisfy

$$\frac{1}{r}\frac{\partial}{\partial r}\left(r\frac{\partial g(r,r';m,k)}{\partial r}\right) - \left(k^2 + \frac{m^2}{r^2}\right) g(r,r';m,k) = -\frac{4\pi}{r}\delta(r-r'). \tag{B.10}$$

Letting $\kappa \equiv kr$, we obtain by multiplying Eqn. (B.10) by r^2,

$$\kappa^2 \frac{\partial^2 g}{\partial \kappa^2} + \kappa \frac{\partial g}{\partial \kappa} - (\kappa^2 + m^2) g = 0, \tag{B.11}$$

when $r \neq r'$. As discussed by Abramowitz and Stegun pp. 374–379 [169], Eqn. (B.11) is the differential equation for modified Bessel's functions, and has linearly independent solutions $I_m(|\kappa|)$ and $K_m(|\kappa|)$. At $r = r'$, the delta function in Eqn. (B.10) introduces a discontinuity in the slope, so that

$$\left.\frac{\partial}{\partial r} g(r,r';m,k)\right|_{r=r'+} - \left.\frac{\partial}{\partial r} g(r,r';m,k)\right|_{r=r'-} = -\frac{4\pi}{r'}. \tag{B.12}$$

Using the symmetric property of the Green's function, and that the Wronskian of $I_m(|\kappa|)$ and $K_m(|\kappa|)$ is

$$I_m(|\kappa|)K'_m(|\kappa|) - I'_m(|\kappa|)K_m(|\kappa|) = -\frac{1}{|\kappa|}, \tag{B.13}$$

the radial Green's function is given by

$$g(r,r';m,k) = 4\pi I_m(|k|r_<) K_m(|k|r_>) \tag{B.14}$$

where $r_> \equiv \max(r, r')$ and $r_< \equiv \min(r, r')$.

The solution to Poisson's equation, Eqn. (2.69), is then in terms of the radial Green's function

$$\Phi(\mathbf{r}, t) = \iiint d^3\mathbf{r}' \sum_m \int \frac{dk}{(2\pi)^2} e^{im(\varphi-\varphi')} e^{ik(z-z')} g(r, r'; m, k)[\rho_{\text{ext}}(\mathbf{r}', t) - \rho_1(\mathbf{r}', t)]. \quad \text{(B.15)}$$

We now introduce the Fourier-Bessel (FB) transform of the Coulomb potential as

$$\frac{1}{\|\mathbf{r} - \mathbf{r}'\|} = \sum_m \int \frac{dk}{(2\pi)^2} e^{im(\varphi-\varphi')} e^{ik(z-z')} g(r, r'; m, k). \quad \text{(B.16)}$$

Appendix C

Modelling Dielectric Media

In the following appendix, we give a brief overview of the dielectric functions and types of materials to be considered when modelling embedding and encapsulating dielectric media in stopping force and image potential calculations.

We model the dielectric function of a channel of amorphous carbon and aluminum using a Drude model for their optical dielectric functions [152, 153] $\epsilon_{\mathrm{C}}(\omega)$ and $\epsilon_{\mathrm{Al}}(\omega)$, which gives a loss function of the form

$$\mathrm{Im}\left[-\epsilon^{-1}(\omega)\right] = \begin{cases} \sum_i \dfrac{A_i \omega_i^2 \gamma_i \omega}{(\omega^2 - \omega_i^2)^2 + \gamma_i^2 \omega^2}, \text{if } \omega < \omega_{i\ \mathrm{edge}} \\ \sum_i \dfrac{A_{i\ \mathrm{sh}} \omega_{i\ \mathrm{sh}}^2 \gamma_{i\ \mathrm{sh}} \omega}{(\omega^2 - \omega_{i\ \mathrm{sh}}^2)^2 + \gamma_{i\ \mathrm{sh}}^2 \omega^2}, \text{otherwise} \end{cases} \tag{C.1}$$

where A_i, γ_i, ω_i, $A_{i\ \mathrm{sh}}$, $\gamma_{i\ \mathrm{sh}}$, $\omega_{i\ \mathrm{sh}}$, and $\omega_{i\ \mathrm{edge}}$ are reproduced in Table C.1 and Table C.2 from Abril *et al.* [153]. In Fig. C.1(a) and Fig. C.1(b) we show the energy-loss functions for amorphous carbon and aluminum, respectively. Note the single high peak in Fig. C.1(b) for aluminum, with $\mathrm{Im}\left[\frac{-1}{\epsilon_{\mathrm{Al}}(\omega_p)}\right] \approx 20$, where $\omega_p \approx 15.0$ eV is the plasma frequency of aluminum. This justifies our use of a dispersionless Drude model for the optical dielectric function of aluminum, that is $\epsilon_{\mathrm{Al}}(\omega) \approx 1 - \frac{\omega_p^2}{\omega^2}$, in Sect. 4.1.

Table C.1: Drude model parameters for carbon (Ref. [153])

i	ω_i	γ_i	A_i
1	0.230	0.21	0.2362
2	0.945	0.49	0.7088

$\omega_{i\ \mathrm{edge}}$	$\omega_{i\ \mathrm{sh}}$	$\gamma_{i\ \mathrm{sh}}$	$A_{i\ \mathrm{sh}}$
10.45	10.5	7.9	0.004078

Table C.2: Drude model parameters for aluminum (Ref. [153])

i	ω_i	γ_i	A_i
1	0.551	0.035	1.1178

$\omega_{i\ \mathrm{edge}}$	$\omega_{i\ \mathrm{sh}}$	$\gamma_{i\ \mathrm{sh}}$	$A_{i\ \mathrm{sh}}$
2.664	3.9	3.0	0.0666

One obtains $\mathrm{Re}\left[\epsilon^{-1}(\omega)\right]$ using the Kramers-Kronig relation [224, 153]

$$\mathrm{Re}\left[\frac{1}{\epsilon(\omega)}\right] = 1 + \begin{cases} \displaystyle\sum_i \frac{A_i\omega_i^2(\omega^2-\omega_i^2)}{(\omega^2-\omega_i^2)^2+\gamma_i^2\omega^2}, \text{if } \omega < \omega_{i\ \mathrm{edge}} \\ \displaystyle\sum_i \frac{A_{i\ \mathrm{sh}}\omega_{i\ \mathrm{sh}}^2(\omega^2-\omega_{i\ \mathrm{sh}}^2)}{(\omega^2-\omega_{i\ \mathrm{sh}}^2)^2+\gamma_{i\ \mathrm{sh}}^2\omega^2}, \text{otherwise} \end{cases} . \tag{C.2}$$

Figure 4.13 shows a schematic of a nickel clamp being used to facilitate ion channelling through CNTs. The dielectric function for nickel $\epsilon_{\mathrm{Ni}}(\omega)$ is modelled by Kwei *et al.* as a superposition of damped linear oscillators [158]. Here $\epsilon_{\mathrm{Ni}}(\omega) = \varepsilon_1(\omega) + i\varepsilon_2(\omega)$, with

$$\varepsilon_1(\omega) = \epsilon_{\mathrm{B}} - \sum_i \frac{A_i'\left(\omega^2-\omega_i^2\right)}{\left(\omega^2-\omega_i^2\right)^2+\omega^2\gamma_i^2}, \tag{C.3}$$

$$\varepsilon_2(\omega) = \sum_i \frac{A_i'\gamma_i\omega}{\left(\omega^2-\omega_i^2\right)^2+\omega^2\gamma_i^2}, \tag{C.4}$$

where ϵ_{B}, A_i', γ_i and ω_i are given in Table C.3. In Fig. C.1(c) we see that the energy-loss function for nickel has a much more substantial "width" than either the aluminum or amorphous carbon

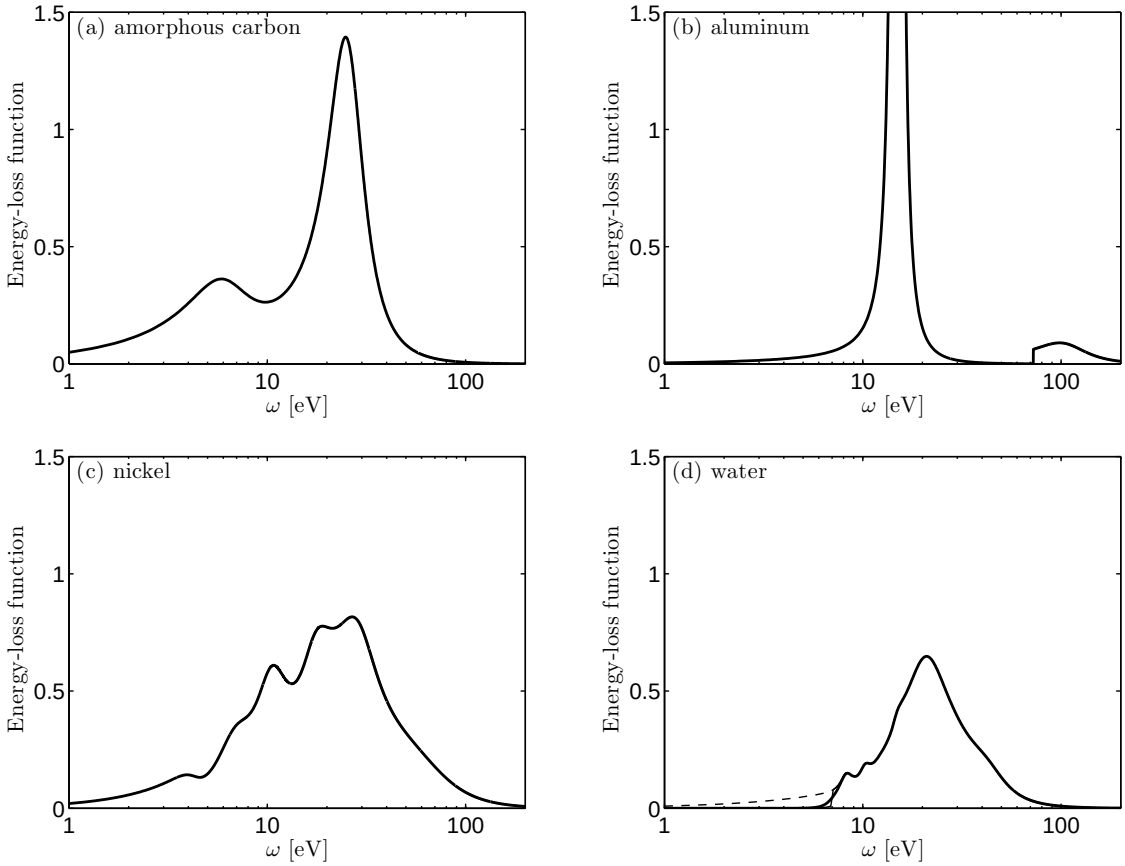

Figure C.1: The energy-loss function $\mathrm{Im}\left[\frac{-1}{\epsilon(\omega)}\right]$ plotted versus ω in eV, for (a) amorphous carbon $\epsilon_{\mathrm{C}}(\omega)$ (——) using the fitting parameters given in Table C.1 from Abril *et al.* [153], (b) aluminum $\epsilon_{\mathrm{Al}}(\omega)$ (——) using the fitting parameters given in Table C.2 from Abril *et al.* [153], (c) nickel $\epsilon_{\mathrm{Ni}}(\omega)$ (——) using the fitting parameters given in Table C.3 from Kwei *et al.* [158], and (d) water $\epsilon_{\mathrm{H_2O}}$ with a sharp cutoff (——), no cutoff (- - - -), and a smoothed cutoff (——) using the fitting parameters given in Table C.4 from Emfietzglou *et al.* [208, 209].

dielectric functions. This arises from the many oscillators, ten in all, used in its construction. For this reason, simple plasmon based analysis of the stopping force and image potential becomes difficult for metals with complicated optical dielectric functions.

We model a SWNT in water, shown schematically in Fig. 4.17, using the Drude-type dielec-

Table C.3: Drude model parameters for nickel, $\epsilon_{\rm B} = 1.02$ (Ref. [158])

A_i' [eV^2]	γ_i [eV]	ω_i [eV]
25	0.01	0
50	2.00	0.45
30	4.00	1.50
60	6.00	3.60
18	1.30	4.60
37	4.20	8.30
95	7.20	14.60
200	18.00	24.00
200	70.00	45.00
545	80.00	58.00

Table C.4: The Drude model parameters for the IXS optical data (Refs. [207, 208, 209])

	Transition, j	E_j [eV]	γ_j [eV]	f_j
		Excitations		
1	(A^1B_1)	8.10	1.90	0.0045
2	(B^1A_1)	10.10	1.95	0.0046
3	(Ryd A+B)	12.10	2.94	0.0030
4	(Ryd C+D)	13.51	5.06	0.0190
5	(diffuse bands)	14.41	2.64	0.0050
		Ionizations		
6	($1b_1$)	16.30	14.00	0.2300
7	($3a_1$)	17.25	10.91	0.1600
8	($1b_2$)	28.00	27.38	0.1890
9	($2a_1$)	42.00	28.68	0.2095
10	(K shell)[1]	450.00	360.00	0.3143

tric function for water developed by Emfietzoglou *et al.* [207, 208], $\epsilon_{\rm w}(\omega) = \varepsilon_1(\omega) + i\varepsilon_2(\omega)$,

where

$$\varepsilon_1(\omega) = 1 + E_p^2 \sum_j^{\text{ioniz}} \left[\frac{f_j(E_j^2 - \omega^2)}{(E_j^2 - \omega^2)^2 + (\gamma_j \omega)^2} \right] + E_p^2 \sum_j^{\text{excit}} \left[\frac{f_j(E_j^2 - \omega^2)[(E_j^2 - \omega^2)^2 + 3(\gamma_j\omega)^2]}{[(E_j^2 - \omega^2)^2 + (\gamma_j \omega)^2]^2} \right], \tag{C.5}$$

$$\varepsilon_2(\omega) = E_p^2 H(\omega - E_C, \Delta) \sum_j^{\text{ioniz}} \left[\frac{f_j \gamma_j \omega}{(E_j^2 - \omega^2)^2 + (\gamma_j \omega)^2} \right] + E_p^2 \sum_j^{\text{excit}} \left[\frac{2 f_j \gamma_j^3 \omega^3}{[(E_j^2 - E^2)^2 + (\gamma_j \omega)^2]^2} \right], \tag{C.6}$$

where E_p is the nominal free-electron plasma energy of liquid water (~ 21.46 eV) and f_j, γ_j, and E_j, are the oscillator strength, damping energy, and transition energy coefficients, respectively, given in Table C.4 based on the optical data of Hayashi *et al.* [209]. The ionization energy cutoff at $E_C = 7$ eV in water is ensured by the function $H(\omega - E_C, \Delta)$ defined by $H(x, \Delta) = 1/(1 + e^{-x/\Delta})$. As shown in Fig. C.1(d) for the energy-loss function, a sharp cutoff, as employed by Emfietzoglou *et al.*, is obtained by letting $\Delta \to 0^+$, a smoothed cutoff, as employed by Dingfelder *et al.* [226], is obtained by taking $\Delta \approx 0.64$ eV, and a dielectric function without an ionization energy cutoff is obtained by letting $\Delta/x \to 0^+$. Moreover, since CNTs are known to be hydrophobic [38], we model the encapsulating water by a dielectric boundary at both $r_{\text{out}} = R$ and $r_{\text{out}} = R + \Delta r_b$, using $\Delta r_b \approx 3.4$ Å, as found from MD simulation by Moulin *et al.* [31].

Appendix D

3D Density-Functional Theory Calculations

D.1 Thomas-Fermi Kinetic Energy

The Thomas-Fermi kinetic energy term, $T_{\mathrm{TF}}[\rho]$, may be written as

$$T_{\mathrm{TF}}[\rho] = -\frac{1}{2}\iiint d^3\mathbf{r}\ \ \nabla^2_{\mathbf{r}}\rho(\mathbf{r},\mathbf{r}')\big|_{\mathbf{r}=\mathbf{r}'}\,. \tag{D.1}$$

To simplify our expression for the spinless density matrix in 3D, we make the following change of coordinates

$$\overline{\mathbf{r}} = \frac{1}{2}\left(\mathbf{r}+\mathbf{r}'\right) \tag{D.2}$$

$$\Delta\mathbf{r} = \mathbf{r}-\mathbf{r}' = \{\Delta r, \Delta\varphi, \Delta z\}, \tag{D.3}$$

so that from Eqn. (5.3), we find

$$\rho(\overline{\mathbf{r}},\Delta\mathbf{r}) = \frac{1}{2\pi^2}\int_0^{k_F} dk k^2 \int_0^{\pi} d\theta e^{ik\|\Delta\mathbf{r}\|\cos\theta}\sin\theta, \tag{D.4}$$

$$= \frac{1}{\pi^2}\int_0^{k_F} dk k \frac{\sin(k\|\Delta\mathbf{r}\|)}{\mathbf{r}} \tag{D.5}$$

$$= 3n(\mathbf{r})\frac{\sin(k_F\|\Delta\mathbf{r}\|)-k_F\|\Delta\mathbf{r}\|\cos(k_F\|\Delta\mathbf{r}\|)}{k_F^3\|\Delta\mathbf{r}\|^3} \tag{D.6}$$

We may write the Laplacian in the new coordinates as

$$\nabla^2_{\mathbf{r}} = \frac{1}{4}\nabla^2_{\overline{\mathbf{r}}} + \vec{\nabla}_{\overline{\mathbf{r}}}\vec{\nabla}_{\Delta\mathbf{r}} + \nabla^2_{\Delta\mathbf{r}} \tag{D.7}$$

using the Chain Rule, so that we may rewrite the Thomas-Fermi term in the new coordinates as

$$T_{\mathrm{TF}} = -\frac{1}{2}\iiint d^3\overline{\mathbf{r}}\ \left(\frac{1}{4}\nabla^2_{\overline{\mathbf{r}}} + \vec{\nabla}_{\overline{\mathbf{r}}}\vec{\nabla}_{\Delta\mathbf{r}} + \nabla^2_{\Delta\mathbf{r}}\right)\rho(\overline{\mathbf{r}},\Delta\mathbf{r})\Big|_{\Delta\mathbf{r}=0}. \tag{D.8}$$

Letting $s \equiv k_F\|\Delta\mathbf{r}\|$, so that in terms of s, the 3D density matrix has the form

$$\rho(\overline{\mathbf{r}},s) = 3n(\overline{\mathbf{r}})\frac{\sin s - s\cos s}{s^3}. \tag{D.9}$$

We now evaluate the gradient of $\rho(\overline{\mathbf{r}},\Delta\mathbf{r})$ with respect to $\Delta\mathbf{r}$, as

$$\vec{\nabla}_{\Delta\mathbf{r}}\rho(\overline{\mathbf{r}},\Delta\mathbf{r})|_{\Delta\mathbf{r}=0} = 3n(\overline{\mathbf{r}})k_F(\overline{\mathbf{r}})\frac{\partial}{\partial s}\frac{\sin s - s\cos s}{s^3}\Big|_{s=0} \tag{D.10}$$

$$= 3n(\overline{\mathbf{r}})k_F(\overline{\mathbf{r}})\frac{\partial}{\partial s}\sum_{n=0}^{\infty}\frac{(-1)^n s^{2n-2}}{(2n+1)!} - \frac{(-1)^n s^{2n-2}}{(2n)!}\Big|_{s=0} \tag{D.11}$$

$$= 3n(\overline{\mathbf{r}})k_F(\overline{\mathbf{r}})\sum_{n=0}^{\infty}\frac{(-1)^n(2n-2)s^{2n-3}}{(2n+1)!} - \frac{(-1)^n(2n-2)s^{2n-3}}{(2n)!}\Big|_{s=0} \tag{D.12}$$

$$= 3n(\overline{\mathbf{r}})k_F(\overline{\mathbf{r}})\left[\frac{-2}{s^3} + \frac{2}{s^3} + \frac{0}{s} - \frac{0}{s} + \frac{2s}{5!} - \frac{2s}{4!} + \mathcal{O}(s^3)\right]_{s=0} = 0. \tag{D.13}$$

The Laplacian of $\rho(\overline{\mathbf{r}},\Delta\mathbf{r})$ with respect to $\Delta\mathbf{r}$ is similarly obtained as

$$\nabla^2_{\Delta\mathbf{r}}\rho(\overline{\mathbf{r}},\Delta\mathbf{r}) = 3n(\overline{\mathbf{r}})k_F(\overline{\mathbf{r}})\frac{1}{s^2}\frac{\partial}{\partial s}s^2\frac{\partial}{\partial s}\frac{\sin s - s\cos s}{s^3}\Big|_{s=0} \tag{D.14}$$

$$= 3n(\overline{\mathbf{r}})k_F(\overline{\mathbf{r}})\frac{1}{s^2}\frac{\partial}{\partial s}\sum_{n=0}^{\infty}\frac{(-1)^n(2n-2)s^{2n-1}}{(2n+1)!} - \frac{(-1)^n(2n-2)s^{2n-1}}{(2n)!}\Big|_{s=0} \tag{D.15}$$

$$= 3n(\overline{\mathbf{r}})k_F(\overline{\mathbf{r}})\frac{1}{s^2}\sum_{n=0}^{\infty}\frac{(-1)^n(2n-2)(2n-1)s^{2n-2}}{(2n+1)!} - \frac{(-1)^n(2n-2)(2n-1)s^{2n-2}}{(2n)!}\Bigg|_{s=0} \tag{D.16}$$

$$= 3n(\overline{\mathbf{r}})k_F(\overline{\mathbf{r}})\sum_{n=0}^{\infty}\frac{(-1)^n(2n-2)(2n-1)s^{2n-4}}{(2n+1)!} - \frac{(-1)^n(2n-2)(2n-1)s^{2n-4}}{(2n)!}\Bigg|_{s=0} \tag{D.17}$$

$$= 3n(\overline{\mathbf{r}})k_F(\overline{\mathbf{r}})\sum_{n=0}^{\infty}\frac{(-1)^n(2n-2)(2n-1)s^{2n-4}}{(2n+1)!} - \frac{(-1)^n(2n-2)(2n-1)s^{2n-4}}{(2n)!}\Bigg|_{s=0} \tag{D.18}$$

$$= 3n(\overline{\mathbf{r}})k_F(\overline{\mathbf{r}})\left[\frac{2}{s^4} - \frac{2}{s^4} + 0 - 0 + \frac{6}{5!} - \frac{6}{4!} + \mathcal{O}(s^2)\right]_{s=0} \tag{D.19}$$

$$= -\frac{3}{5}(3\pi)^{2/3}n^{5/3}(\mathbf{r}) \tag{D.20}$$

Assuming that the 3D electron density is well-behaved, so that $\iiint d^3\mathbf{r}\ \nabla^2 n(\mathbf{r}) = 0$, the Thomas-Fermi kinetic energy term is given by

$$T_{\mathrm{TF}}[n] = \frac{3}{10}(3\pi)^{2/3}\iiint d^3\mathbf{r}\ n^{5/3}(\mathbf{r}). \tag{D.21}$$

D.2 Dirac Exchange Energy

The Dirac exchange energy is given by Eqn. (2.20) to be

$$K[n] = \frac{1}{4}\iiint d^3\mathbf{r}\iiint d^3\mathbf{r}'\ \frac{\|\rho(\mathbf{r},\mathbf{r}')\|^2}{\|\mathbf{r}-\mathbf{r}'\|}. \tag{D.22}$$

Employing the coordinates

$$\overline{\mathbf{r}} = \frac{1}{2}(\mathbf{r}+\mathbf{r}') \tag{D.23}$$

$$\Delta\mathbf{r} = \mathbf{r}-\mathbf{r}' = \{\Delta r, \Delta\varphi, \Delta z\}, \tag{D.24}$$

with $s \equiv k_F \Delta\mathbf{r}$, we may substitute Eqn. (D.9) into our expression for the Dirac exchange energy to obtain

$$K[n] = \frac{1}{4}\iiint d^3\overline{\mathbf{r}} \iiint d^3\Delta\mathbf{r}\ \frac{\|\rho(\overline{\mathbf{r}}, \Delta\mathbf{r})\|^2}{\|\Delta\mathbf{r}\|} \tag{D.25}$$

$$= \pi \iiint d^3\overline{\mathbf{r}} \int ds \frac{\|\rho(\overline{\mathbf{r}}, s)\|^2}{s} \frac{s^2}{k_F^2} \tag{D.26}$$

$$= 3\left(\frac{3}{\pi}\right)^{1/3} \iiint d^3\mathbf{r}\ n^{4/3}(\mathbf{r}) \int_0^\infty ds \frac{(\sin s - s\cos s)^2}{s^5} \tag{D.27}$$

$$= 3\left(\frac{3}{\pi}\right)^{1/3} \iiint d^3\mathbf{r}\ n^{4/3}(\mathbf{r}) \left[\frac{2s^2+1}{8s^4} - \frac{\cos 2s}{8s^4} - \frac{\sin 2s}{4s^3}\right]_{s=0} \tag{D.28}$$

$$= \frac{3}{4}\left(\frac{3}{\pi}\right)^{1/3} \iiint d^3\mathbf{r}\ n^{4/3}(\mathbf{r}). \tag{D.29}$$

Appendix E

Boundary Conditions for the Equilibrium Electron Density $n_0(r)$

For a cylindrical shell of radius R, with atomic density $\sigma_a\delta(r-R)$, and Z valence electrons per atom, the electric potential has the following boundary conditions. First, the electric potential is chosen to be continuous, so that

$$\Phi(R^-) = \Phi(R^+). \tag{E.1}$$

Letting $G[n]$ be the reduced density function, defined as the energy density functional $F[n]$ with the classical Coulomb interaction energy $\iiint d^3\mathbf{r} \iiint d^3\mathbf{r}' \frac{n(\mathbf{r}')n(\mathbf{r})}{\|\mathbf{r}-\mathbf{r}'\|}$ removed, we obtain, from minimizing the electron energy, that

$$\mu_0 = \frac{\delta G[n]}{\delta n} - \Phi, \tag{E.2}$$

where Φ is the total electric potential and μ_0 is the chemical potential. Let n_0 be a solution of Eqn. (E.2). Since Φ is continuous at $r = R$ and μ_0 is a constant, we have $\frac{\delta G[n]}{\delta n}$, and hence n_0, are continuous at $r = R$. Next, by integrating Poisson's equation for the total electric potential,

$$\frac{1}{r}\frac{\partial}{\partial r}\left(r\frac{\partial \Phi}{\partial r}\right) = -4\pi Z\sigma_a\delta(r-R) + 4\pi n_0(r), \tag{E.3}$$

with respect to the radial coordinate from R^- to R^+, we find

$$\int_{R^-}^{R^+} \frac{\partial}{\partial r} r \frac{\partial \Phi}{\partial r} dr = -4\pi Z \sigma_a R \tag{E.4}$$

$$\left.\frac{\partial \Phi}{\partial r}\right|_{R^+} - \left.\frac{\partial \Phi}{\partial r}\right|_{R^-} = -4\pi Z \sigma_a, \tag{E.5}$$

where we have used the fact that the continuity of n_0 at $r = R$ implies $\int_{R^-}^{R^+} n_0(r) dr = 0$. Rewriting Eqn. (E.5) in terms of the equilibrium radial electron density, we obtain an explicit boundary condition for n_0 at $r = R$ of

$$\frac{\partial}{\partial n_0} \left[\frac{\delta G[n_0]}{\delta n_0}\right]_{r=R} \left[\left.\frac{\partial n_0}{\partial r}\right|_{R^+} - \left.\frac{\partial n_0}{\partial r}\right|_{R^-}\right] = -4\pi Z \sigma_a. \tag{E.6}$$

By cylindrical symmetry, the radial component of the electric field must be zero on the cylinder's axis, so that

$$\left.\frac{\partial \Phi}{\partial r}\right|_{r=0} = 0. \tag{E.7}$$

Differentiating Eqn. (E.2) at $r = 0$, we obtain a condition on n_0 on the cylinder's axis of

$$\left.\frac{\partial}{\partial n_0} \frac{\delta G[n_0]}{\delta n_0} \frac{\partial n_0}{\partial r}\right|_{r=0} = 0. \tag{E.8}$$

The Thomas-Fermi model gives a reduced density functional $G[n_0]$ such that $\frac{\partial}{\partial n_0} \frac{\delta G[n_0]}{\delta n_0} \neq 0$, so that

$$\left.\frac{\partial n_0}{\partial r}\right|_{r=0} = 0. \tag{E.9}$$

However, for the Thomas-Fermi-Dirac model, the derivative of the functional derivative of $G[n_0]$ does satisfy $\frac{\partial}{\partial n_0} \frac{\delta G[n_0]}{\delta n_0} = 0$ for some r greater than zero, due to cancellation between the Thomas-Fermi and Dirac exchange terms. This is what causes the unphysical "truncation" of the electron density discussed by March [163].

Appendix F

Region of Validity for Kitagawa's Approximation

To determine the region of validity of Kitagawa's approximation [161], we must find when Eqn.(5.44), that is

$$\widetilde{n}_1^{(j)} = \frac{\partial \omega_p^2}{\partial \varrho} \int d\varrho' \frac{\varrho' |\kappa| g'(\varrho, \varrho'; m, \kappa) \widetilde{n}_1^{(j-1)}(\varrho')}{4\pi[\omega_p^2(\varrho) - \Omega^2]}. \tag{F.1}$$

for $\widetilde{n}_1^{(j)}$ as a function of the previous density term $\widetilde{n}_1^{(j-1)}$, is a contractive mapping.

Employing the norm $\| \cdot \|$ over functions on $[0, \infty)$

$$\|f(x)\| = \int_0^\infty dx |f(x)|, \tag{F.2}$$

we will determine for which values of Ω (F.1) is a contractive mapping, ie. $\|\widetilde{n}_1^{(j)}(\varrho)\varrho\| \leq k\|\widetilde{n}_1^{(j)}(\varrho)\varrho\|$, where $0 \leq k < 1$.

$$\|\widetilde{n}_1^{(j)}(\varrho)\varrho\| = \left\| \frac{\partial \omega_p^2}{\partial \varrho} \int_0^\infty d\varrho' \frac{\varrho' \varrho \frac{\partial}{\partial \varrho} I_m(|\kappa|\varrho_<) K_m(|\kappa|\varrho_>) \widetilde{n}_1^{(j-1)}(\varrho')}{\omega_p^2(\varrho) - \Omega^2} \right\| \tag{F.3}$$

$$\leq \left\| \frac{\frac{\partial \omega_p^2}{\partial \varrho}}{\omega_p^2(\varrho) - \Omega^2} \left[|\kappa \varrho K_m'(|\kappa|\varrho)| \int_0^\varrho d\varrho' |I_m(|\kappa|\varrho') \widetilde{n}_1^{(j-1)}(\varrho') \varrho'| \right. \right.$$

$$\left. \left. + |\kappa \varrho I_m'(|\kappa|\varrho)| \int_\varrho^\infty d\varrho' |K_m(|\kappa|\varrho') \widetilde{n}_1^{(j-1)}(\varrho') \varrho'| \right] \right\| \tag{F.4}$$

$$\leq \left\| \left[\frac{\partial}{\partial \varrho} \ln |\omega_p^2(\varrho) - \Omega^2| \right] |\kappa| \varrho [I'_m(|\kappa|\varrho) K_m(|\kappa|\varrho) - I_m(|\kappa|\varrho) K'_m(|\kappa|\varrho)] \int_0^\infty d\varrho' |\widetilde{n}_1^{(j-1)}(\varrho') \varrho'| \right\|.$$

Employing the identity $I'_\nu(z)K_\nu(z) - I_\nu(z)K'_\nu(z) = 1/z$ [227], and the norm of $\widetilde{n}_1^{(j-1)}(\varrho)\varrho$ defined by Eqn. (F.2), we find

$$\|\widetilde{n}_1^{(j)}(\varrho)\varrho\| \leq \int_0^\infty \left| \frac{\partial}{\partial \varrho} \ln |\omega_p^2(\varrho) - \Omega^2 \right| d\varrho \|\widetilde{n}_1^{(j-1)}(\varrho)\varrho\| \tag{F.5}$$

$$= \ln \left| \frac{-\Omega^2}{\omega_p^2(0) - \Omega^2} \right| \|\widetilde{n}_1^{(j-1)}(\varrho)\varrho\| \tag{F.6}$$

$$= -\ln \left| 1 - \frac{\omega_p^2(0)}{\Omega^2} \right| \|\widetilde{n}_1^{(j-1)}(\varrho)\varrho\| \tag{F.7}$$

$$\approx \left[\frac{\omega_p^2(0)}{\Omega^2} + \frac{1}{2} \frac{\omega_p^4(0)}{\Omega^4} + \mathcal{O}\left(\frac{\omega_p^6(0)}{\Omega^6} \right) \right] \|\widetilde{n}_1^{(j-1)}(\varrho)\varrho\| \tag{F.8}$$

so that to ensure $k = -\ln \left| 1 - \frac{\omega_p^2(0)}{\Omega^2} \right| < 1$, we require $\omega_p(0) < 0.795\Omega$. Thus when $\omega_p(0) \ll \Omega$, we have a contraction mapping, and our series for $\widetilde{n}_1$ converges. Kitagawa neglects corrections to the induced density $\widetilde{n}_1^{(j)}$ for $j \geq 2$, letting $\widetilde{n}_1 \approx \widetilde{n}_1^{(0)} + \widetilde{n}_1^{(1)}$, including "local" and "non-local" contributions [161]. We may estimate the error introduced by truncating the density series as

$$\frac{\int_0^\infty \sum_{j=2}^\infty |\widetilde{n}_1^{(j)}(\varrho)| \varrho d\varrho}{\int_0^\infty |\widetilde{n}_1^{(1)}(\varrho)| \varrho d\varrho} \leq -\frac{\ln |1 - \frac{\omega_p^2(0)}{\Omega^2}|}{1 + \ln |1 - \frac{\omega_p^2(0)}{\Omega^2}|} \approx \frac{\omega_p^2(0)}{\Omega^2} + \frac{3}{2} \frac{\omega_p^4(0)}{\Omega^4} + \mathcal{O}\left(\frac{\omega_p^6(0)}{\Omega^6} \right). \tag{F.9}$$

Numerical calculations of $n_0(r)$ as shown in Fig. 5.1 may be used to estimate k using $\omega_p(0) = \sqrt{4\pi n_0(0)} \approx 0.036$. Our series for the linearized induced density applies only for frequencies $\Omega > 0.0453$.

Appendix G

Calculation of Local and Non-local Stopping Forces

G.1 Sokhotsky-Plemelj Formula

The Sokhotsky-Plemelj formula is often used in mathematical physics applications to evaluate analytically integrals of the form $\int_{-\infty}^{\infty} \frac{f(x)}{x-x_0 \pm i\Gamma}$, in the limit $\Gamma \to 0^+$. See Vladimirov pp. 75–79 [211] for a more complete discussion.

Formula 1 (Sokhotsky-Plemelj)
Let $f(x)$ be a continuous function such that $f(x) \to 0$ as $x \to \pm\infty$. Then

$$\lim_{\Gamma \to 0^+} \int dx \frac{f(x)}{x - x_0 \pm i\Gamma} = \mathrm{P.V.} \int dx \frac{f(x)}{x - x_0} \mp i\pi \int dx \delta(x - x_0) f(x). \tag{G.1}$$

Here $\mathrm{P.V.} \int dx \frac{f(x)}{x-x_0}$ denotes the *principal value of the integral* of $\frac{f(x)}{x-x_0}$, which is defined to be

$$\mathrm{P.V.} \int_a^b dx \frac{f(x)}{x - x_0} = \lim_{\epsilon \to 0^+} \int_a^{x_0 - \epsilon} dx \frac{f(x)}{x - x_0} + \int_{x_0+\epsilon}^b dx \frac{f(x)}{x - x_0}. \tag{G.2}$$

We may easily prove the Sokhotsky-Plemelj formula for the case of integration over the real line as follows.

Proof of Formula 1

$$\lim_{\Gamma\to 0^+}\int_{-\infty}^{\infty} dx \frac{f(x)}{x - x_0 \pm i\Gamma}$$

$$= f(x_0)\lim_{\Gamma\to 0^+}\int_{-\infty}^{\infty} dx \frac{x - x_0 \pm \Gamma}{(x-x_0)^2 + \Gamma^2} + \lim_{\Gamma\to 0^+}\int_{-\infty}^{\infty} dx \frac{f(x) - f(x_0)}{x - x_0 \pm i\Gamma} \tag{G.3}$$

$$= f(x_0)\lim_{\Gamma\to 0^+}\left[\ln|(x-x_0)^2 + \Gamma^2| \mp i \arctan\left(\frac{x-x_0}{\Gamma}\right)\right]_{-\infty}^{\infty}$$

$$+ \lim_{\epsilon\to 0^+}\int_{-\infty}^{x_0-\epsilon} dx \frac{f(x) - f(x_0)}{x - x_0} + \int_{x_0+\epsilon}^{\infty} dx \frac{f(x) - f(x_0)}{x - x_0} \tag{G.4}$$

$$= \mp i\pi f(x_0) + \text{P.V.}\int_{-\infty}^{\infty} dx \frac{f(x)}{x - x_0} - f(x_0)\text{P.V.}\int_{-\infty}^{\infty} dx \frac{1}{x - x_0} \tag{G.5}$$

$$= \text{P.V.}\int_{-\infty}^{\infty} dx \frac{f(x)}{x - x_0} \mp i\pi\int_{-\infty}^{\infty} dx\delta(x - x_0)f(x), \tag{G.6}$$

as required.

G.2 Calculation of Local Stopping Force S_l

The local stopping force S_l, due to an ion travelling paraxially with constant speed $v = R\varpi$, is given by Eqn. (5.53) to be

$$S_l = -\frac{Q^2 i}{\pi R^2}\sum_m \int d\kappa \frac{\kappa I_m(|\kappa|\varrho_0)K_m(|\kappa|\varrho_0)\omega_p^2(\varrho_0)}{\omega_p^2(\varrho_0) - \kappa\varpi(\kappa\varpi + i\gamma)}. \tag{G.7}$$

Before we may employ the Sokhotsky-Plemelj formula for the calculation of the above integral, we must first manipulate the integrand into the form $\frac{f(x)}{x - x_0 + i\Gamma}$. This may be done by employing partial fraction decomposition, and dropping terms of order $\mathcal{O}(\gamma^2)$, so that

$$S_l = -\frac{Q^2 i}{\pi R^2}\sum_m \int \frac{\kappa I_m(|\kappa|\varrho_0)K_m(|\kappa|\varrho_0)\omega_p^2(\varrho_0)d\kappa}{\omega_p^2(\varrho_0) - \gamma^2/4 - (\kappa\varpi + i\gamma/2)^2} \tag{G.8}$$

$$= \frac{Q^2 i\omega_p(\varrho_0)}{2\pi R^2}\sum_m \int d\kappa \frac{\kappa I_m(|\kappa|\varrho_0)K_m(|\kappa|\varrho_0)}{\kappa\varpi + i\gamma/2 - \omega_p(\varrho_0)} - \frac{\kappa I_m(|\kappa|\varrho_0)K_m(|\kappa|\varrho_0)}{\kappa\varpi + i\gamma/2 + \omega_p(\varrho_0)}. \tag{G.9}$$

Taking the limit $\gamma \to 0^+$, and employing the Sokhotsky-Plemelj formula (G.1), we find

$$S_l = \frac{Q^2 i\omega_p(\varrho_0)}{2\pi R^2}\sum_m \left[\text{P.V.}\int d\kappa \frac{\kappa I_m(|\kappa|\varrho_0)K_m(|\kappa|\varrho_0)}{\kappa\varpi - \omega_p(\varrho_0)} - \text{P.V.}\int d\kappa \frac{\kappa I_m(|\kappa|\varrho_0)K_m(|\kappa|\varrho_0)}{\kappa\varpi + \omega_p(\varrho_0)}\right.$$
$$\left. -i\pi\int d\kappa \left[\delta(\kappa\varpi - \omega_p(\varrho_0)) - \delta(\kappa\varpi - \omega_p(\varrho_0))\right]\kappa I_m(|\kappa|\varrho_0)K_m(|\kappa|\varrho_0)\right]. \tag{G.10}$$

Combining the two principal value integrals we find

$$S_l = \frac{Q^2\omega_p^2(\varrho_0)}{v^2}\sum_m I_m\left(\varrho_0\frac{\omega_p(\varrho)}{\varpi}\right)K_m\left(\varrho_0\frac{\omega_p(\varrho_0)}{\varpi}\right)$$
$$-\frac{Q^2 i\omega_p^2(\varrho_0)}{\pi R^2}\sum_m \text{P.V.}\int d\kappa \frac{\kappa I_m(|\kappa|\varrho_0)K_m(|\kappa|\varrho_0)}{\kappa^2\varpi^2 - \omega_p^2(\varrho_0)} \tag{G.11}$$
$$= \frac{Q^2\omega_p^2(\varrho_0)}{v^2}\sum_m I_m\left(\varrho_0\frac{\omega_p(\varrho)}{\varpi}\right)K_m\left(\varrho_0\frac{\omega_p(\varrho_0)}{\varpi}\right), \tag{G.12}$$

since the integral is of an odd function.

G.3 Calculation of Non-local Stopping Force S_n

The non-local stopping force S_n, due to an ion travelling paraxially with constant speed $v = R\varpi$, is given by Eqn. (5.59) to be

$$S_n = -\frac{Q^2 i}{16\pi^3 R^2}\sum_m \int d\kappa \int d\varrho \frac{\partial\omega_p^2}{\partial\varrho}\frac{\varrho|\kappa|\kappa^3\varpi^2 g(\varrho_0,\varrho;m,\kappa)g'(\varrho,\varrho_0;m,\kappa)}{[\omega_p^2(\varrho) - (\kappa\varpi + i\gamma/2)^2][\omega_p^2(\varrho_0) - (\kappa\varpi + i\gamma/2)^2]}. \tag{G.13}$$

Using the fractional decomposition for constants A and B of

$$\frac{1}{[x^2 - A^2][x^2 - B^2]} = \frac{1}{A^2 - B^2}\left[\frac{1}{x^2 - A^2} - \frac{1}{x^2 - B^2}\right], \tag{G.14}$$

and employing our results for the local stopping force S_l, we find

$$S_n = \frac{Q^2}{16\pi^2 v^2}\sum_m \int d\varrho\varrho\frac{\partial\omega_p^2}{\partial\varrho}\frac{1}{\varpi[\omega_p^2(\varrho_0) - \omega_p^2(\varrho)]}$$
$$\left[\omega_p^3(\varrho)g\left(\varrho_0,\varrho;m,\frac{\omega_p(\varrho)}{\varpi}\right)g'\left(\varrho,\varrho_0;m,\frac{\omega_p(\varrho)}{\varpi}\right)\right.$$
$$\left. -\omega_p^3(\varrho_0)g\left(\varrho_0,\varrho;m,\frac{\omega_p(\varrho_0)}{\varpi}\right)g'\left(\varrho,\varrho_0;m,\frac{\omega_p(\varrho_0)}{\varpi}\right)\right] \tag{G.15}$$

as required.

Appendix H

Calculation of $J_E(m, k, \omega)$

Let us define the integral over time t in $\mathcal{P}(\omega)$ for $r_{\min} > R$ as

$$J_E(m, k, \omega) \equiv \int_{-\infty}^{\infty} dt e^{-i\omega t} e^{im\varphi_0(t)} e^{ikz_0(t)} K_m(|k| r_0(t)). \tag{H.1}$$

Rewriting in dimensionless variables $w(t) \equiv -\frac{v_\perp t}{r_{\min}}$, $u(k) \equiv k r_{\min}$, and $\xi(k, \omega) \equiv \frac{r_{\min}}{v_\perp}(\omega - k v_\parallel)$, we obtain

$$J_E = \frac{r_{\min}}{v_\perp} \int_{-\infty}^{\infty} dw e^{i\xi w} \left(\frac{1 - iw}{\sqrt{1 + w^2}} \right)^m K_m(u\sqrt{1 + w^2}) \tag{H.2}$$

$$= \frac{r_{\min}}{v_\perp} \left[1 - \frac{d}{d\xi} \right]^m \int_{-\infty}^{\infty} dw e^{i\xi w} \frac{K_m(u\sqrt{1 + w^2})}{(1 + w^2)^{m/2}} \tag{H.3}$$

$$= \frac{r_{\min}}{v_\perp} \left[1 - \frac{d}{d\xi} \right]^m 2 \int_1^{\infty} d\ell \frac{\ell^{1-m} \cos(\xi\sqrt{\ell^2 - 1}) K_m(u\ell)}{\sqrt{\ell^2 - 1}}, \tag{H.4}$$

where we have used the substitution $\ell \equiv \sqrt{1 + w^2}$.

From Glasser [228] and Prudnikov *et al.* (pp. 362, Formula 2.16.16(7)) [213]

$$\int_a^{\infty} x^{1 \pm \nu} \frac{\cos(b\sqrt{x^2 - a^2}) K_\nu(cx) dx}{\sqrt{x^2 - a^2}} = \sqrt{\frac{\pi}{2}} a^{\frac{1}{2} \pm \nu} c^{\pm \nu} (b^2 + c^2)^{\frac{\mp 2\nu - 1}{4}} K_{\mp \nu - \frac{1}{2}}(a\sqrt{b^2 + c^2}), \tag{H.5}$$

so that

$$J_E = \frac{\sqrt{2\pi} r_{\min}}{v_\perp u^m} \left[1 - \frac{d}{d\xi} \right]^m (\xi^2 + u^2)^{\frac{2n-1}{4}} K_{m - \frac{1}{2}}(\sqrt{\xi^2 + u^2}). \tag{H.6}$$

Let $\zeta \equiv \sqrt{\xi^2+u^2} = \dfrac{r_{\min}}{v_\perp}\sqrt{(\omega-kv_\parallel)^2+(kv_\perp)^2}$, so that

$$J_E = \frac{\sqrt{2\pi}r_{\min}}{v_\perp u^m}\left[1-\frac{\xi}{\zeta}\frac{d}{d\zeta}\right]^m \zeta^{m-\frac{1}{2}}K_{m-\frac{1}{2}}(\zeta) \tag{H.7}$$

For ease of notation, let $D \equiv -\dfrac{1}{\zeta}\dfrac{d}{d\zeta}$ and $F_m(\zeta) \equiv \zeta^{m-\frac{1}{2}}K_{m-\frac{1}{2}}(\zeta)$, and consider $(1+\xi D)^m F_m(\zeta)$.

We must first prove the proposition

$$(\xi D)^m = \sum_{k=0}^{[m/2]}(-1)^k(2k-1)!!\binom{m}{2k}\xi^{m-2k}D^{m-k}. \tag{H.8}$$

For $m=0$, we find

$$(\xi D)^0 = (-1)^0(2(0)-1)!!\binom{0}{2(0)}x^{0-2(0)}D^{0-0} = 1 \tag{H.9}$$

since $(-1)!! \equiv 1$, as required.

We assume that the proposition holds for $m \le n$, and we must be sure that the proposition is true for $m = n+1$, i.e.

$$(\xi D)^{n+1} = \sum_{k=0}^{[\frac{n+1}{2}]}(-1)^k(2k-1)!!\binom{n+1}{2k}\xi^{n+1-2k}D^{n+1-k}.$$

We find by the inductive hypothesis that

$$(\xi D)^{n+1} = (\xi D)(\xi D)^n \tag{H.10}$$

$$= (\xi D)\sum_{k=0}^{[n/2]}(-1)^k(2k-1)!!\binom{n}{2k}\xi^{n-2k}D^{n-k}, \tag{H.11}$$

$$= \sum_{k=0}^{[n/2]}(-1)^k(2k-1)!!\binom{n}{2k}(\xi D)\xi^{n-2k}D^{n-k}. \tag{H.12}$$

Using that $\xi D = -\frac{d}{d\xi}$, we find

$$
\begin{aligned}
(\xi D)^{n+1} &= \sum_{k=0}^{[n/2]} (-1)^k (2k-1)!! \binom{n}{2k} \xi^{n+1-2k} D^{n+1-k} \\
&\quad + \sum_{k=0}^{[n/2]} (-1)^k (2k-1)!! \binom{n}{2k} (-1) \frac{d}{d\xi} (\xi^{n-2k}) D^{n-k} \qquad \text{(H.13)} \\
&= \sum_{k=0}^{[n/2]} (-1)^k (2k-1)!! \binom{n}{2k} \xi^{n+1-2k} D^{n+1-k} \\
&\quad + \sum_{k=0}^{[n/2]} (-1)^{(k+1)} (2k-1)!! \binom{n}{2k} (n-2k) \xi^{n-2k-1} D^{n-k}. \qquad \text{(H.14)}
\end{aligned}
$$

By definition of the choose notation

$$
\begin{aligned}
\binom{n}{2k}(n-2k) &= \frac{n!(n-2k)}{(n-2k)!(2k)!} \qquad \text{(H.15)} \\
&= \frac{n!(2k+1)}{(n-(2k+1))!(2k+1)!} \qquad \text{(H.16)} \\
&= (2k+1)\binom{n}{2k+1}, \qquad \text{(H.17)}
\end{aligned}
$$

for $2k \neq n$, so that by changing the limits of for the second summation from $0 \leq k \leq \frac{n}{2}$ to $0 \leq k \leq \frac{n-1}{2}$, we obtain

$$
\begin{aligned}
(\xi D)^{n+1} &= \sum_{k=0}^{[n/2]} (-1)^k (2k-1)!! \binom{n}{2k} \xi^{n+1-2k} D^{n+1-k} \\
&\quad + \sum_{k=0}^{[\frac{n-1}{2}]} (-1)^{(k+1)} (2k+1)!! \binom{n}{2k+1} \xi^{n-2k-1} D^{n-k}. \qquad \text{(H.18)}
\end{aligned}
$$

Changing the limits of the second summation again from $0 \leq k \leq \frac{n-1}{2}$ to $1 \leq k \leq \frac{n+1}{2}$,

with $k \in \mathbb{Z}$ we obtain

$$(\xi D)^{n+1} = \sum_{k=0}^{[n/2]} (-1)^k (2k-1)!! \binom{n}{2k} \xi^{n+1-2k} D^{n+1-k} + \sum_{k=1}^{[\frac{n+1}{2}]} (-1)^k (2k-1)!! \binom{n}{2k-1} \xi^{n+1-2k} D^{n+1-k}. \tag{H.19}$$

Using Pascal's Formula

$$\binom{p}{q-1} = \binom{p+1}{q} - \binom{p}{q}, \tag{H.20}$$

and combining the two summations, we find

$$(\xi D)^{n+1} = \sum_{k=0}^{[\frac{n+1}{2}]} (-1)^k (2k-1)!! \binom{n+1}{2k} \xi^{n+1-2k} D^{n+1-k} \tag{H.21}$$

as required.

From the Binomial Theorem,

$$(1+\xi D)^m = \sum_{n=0}^{m} \binom{m}{n} (\xi D)^n. \tag{H.22}$$

Applying (H.8), we obtain

$$(1+\xi D)^m = \sum_{n=0}^{m} \binom{m}{n} \sum_{k=0}^{[n/2]} (-1)^k (2k-1)!! \binom{n}{2k} \xi^{n-2k} D^{n-k}. \tag{H.23}$$

Letting $p = m - (n-2k)$, $0 \le p \le m$, so that $n = m - p + 2k$, $0 \le k \le \frac{p}{2}$,

$$= \sum_{p=0}^{m} \xi^{m-p} \binom{m}{p} \sum_{k=0}^{[p/2]} (-1)^k (2k-1)!! \binom{p}{2k} D^{m-p+k}. \tag{H.24}$$

From Abramowitz and Stegun (pp. 444, Formulas 10.2.18 & 10.2.22) [169], we have

$$F_{n+2}(\zeta) = (2n+1) F_{n+1}(\zeta) + \zeta^2 F_n(\zeta) \tag{H.25}$$

$$D^k F_n(\zeta) = F_{n-k}(\zeta) \tag{H.26}$$

so that

$$(1+\xi D)^m F_m(\zeta) = \sum_{n=0}^{m} \binom{m}{n} \xi^{m-n} S_n(\zeta), \tag{H.27}$$

where we define $S_n(\zeta)$ by

$$S_n(\zeta) \equiv \sum_{k=0}^{[n/2]} (-1)^k (2k-1)!! \binom{n}{2k} D^{m-n+k} F_m(\zeta) \tag{H.28}$$

$$= \sum_{k=0}^{[n/2]} (-1)^k (2k-1)!! \binom{n}{2k} F_{n-k}(\zeta). \tag{H.29}$$

using (H.26).

Applying the recursion relation (H.25), we find

$$\zeta^2 S_n(\zeta) = \sum_{k=0}^{[n/2]} (-1)^k (2k-1)!! \binom{n}{2k} \zeta^2 F_{n-k}(\zeta) \tag{H.30}$$

$$= \sum_{k=0}^{[\frac{n}{2}]} (-1)^k (2k-1)!! \binom{n}{2k} F_{n+2-k}(\zeta)$$

$$+ \sum_{k=0}^{[\frac{n}{2}]} (-1)^{k+1} (2k-1)!! \binom{n}{2k} (2(n-k)+1) F_{n+1-k}(\zeta). \tag{H.31}$$

Using that

$$\binom{n}{2k} \frac{2(n-k)+1}{2k+1} = \binom{n+2}{2(k+1)} - \binom{n}{2(k+1)} \tag{H.32}$$

by the definition of the choose notation and using Pascal's Formula (H.20), we obtain by relabeling the second summation from $k+1 \to k$

$$\zeta^2 S_n(\zeta) = \sum_{k=0}^{[\frac{n}{2}]} (-1)^k (2k-1)!! \binom{n}{2k} F_{n+2-k}(\zeta)$$

$$+ \sum_{k=1}^{[\frac{n+2}{2}]} (-1)^k (2k-1)!! \left[\binom{n+2}{2k} - \binom{n}{2k} \right] F_{n+2-k}(\zeta). \tag{H.33}$$

Combining the two summations yields

$$\zeta^2 S_n(\zeta) = \sum_{k=0}^{[\frac{n+2}{2}]} (-1)^k (2k-1)!! \binom{n+2}{2k} F_{n+2-k}(\zeta)$$
$$\zeta^2 S_n(\zeta) = S_{n+2}(\zeta). \tag{H.34}$$

Noting that $S_1(\zeta) = F_1(\zeta)$, and by the definition of $F_m(\zeta)$, we find that

$$S_1(\zeta) = \zeta^{1-\frac{1}{2}} K_{1-\frac{1}{2}}(\zeta) = \zeta[\zeta^{-\frac{1}{2}} K_{-\frac{1}{2}}(\zeta)] = \zeta F_0(\zeta), \tag{H.35}$$

using that $K_m(\zeta)$ is an even function of m [169]. Applying (H.34) recursively, we find that

$$S_m(\zeta) = \zeta^m F_0(\zeta), \tag{H.36}$$

giving

$$(1-\xi D)^m F_m(\zeta) = (\xi+\zeta)^m F_0(\zeta) = (\xi+\zeta)^m \frac{K_{-\frac{1}{2}}(\zeta)}{\zeta^{-\frac{1}{2}}} = \sqrt{\frac{\pi}{2}} (\xi+\zeta)^m \frac{e^{-\zeta}}{\zeta}, \tag{H.37}$$

where we have used from Abramowitz and Stegun [169], $K_{-\frac{1}{2}}(\zeta) = \sqrt{\frac{\pi}{2}} \frac{e^{-\zeta}}{\sqrt{\zeta}}$. Substituting (H.37) into equation (H.7), we obtain for the integral

$$J_E(m,k,\omega) = \frac{\pi r_{\min}}{v_\perp} \frac{e^{-\zeta}}{\zeta} \left(\frac{\xi+\zeta}{u}\right)^m \tag{H.38}$$
$$= \pi \frac{e^{-\frac{r_{\min}}{v_\perp}\sqrt{(\omega-kv_\parallel)^2+k^2v_\perp^2}}}{\sqrt{(\omega-kv_\parallel)^2+k^2v_\perp^2}} \left(\frac{\omega-kv_\parallel+\sqrt{(\omega-kv_\parallel)^2+k^2v_\perp^2}}{kv_\perp}\right)^m. \tag{H.39}$$

Bibliography

[1] S. Iijima, "Helical microtubules of graphitic carbon", *Nature* **354**, 56 (Nov. 1991), doi:10.1038/354056a0.

[2] M. S. Dresselhaus, G. Dresselhaus, and P. Avouris, eds., *Carbon Nanotubes: Synthesis, Structure, Properties, and Applications* (Springer, Berlin, 2001).

[3] W. B. Choi, J. U. Chu, K. S. Jeong, E. J. Bae, J. W. Lee, J. J. Kim, and J. O. Lee, "Ultrahigh-density nanotransistors by using selectively grown vertical carbon nanotubes", *Appl. Phys. Lett.* **79**(22), 3696 (2001), doi:10.1063/1.1419236.

[4] K. Keren, R. S. Berman, E. Buchstab, U. Sivan, and E. Braun, "DNA-templated carbon nanotube field-effect transistor", *Science* **302**(5649), 1380 (2003), doi:10.1126/science.1091022.

[5] W. A. Deheer, A. Châtelain, and D. Ugarte, "A carbon nanotube field-emission electron source", *Science* **270**(5239), 1179 (Nov. 1995), doi:10.1126/science.270.5239.1179.

[6] A. Goldoni, L. Petaccia, L. Gregoratti, B. Kaulich, A. Barinov, S. Lizzit, A. Laurita, L. Sangaletti, and R. Larciprete, "Spectroscopic characterization of contaminants and interaction with gases in single-walled carbon nanotubes", *Carbon* **42**(10), 2099 (2004), doi:10.1016/j.carbon.2004.04.011.

[7] S. Bellucci, V. M. Biryukov, Y. A. Chesnokov, V. Guidi, and W. Scandale, "Channeling of high energy beams in nanotubes", *Nucl. Instrum. & Methods Phys. Res. B* **202**, 236 (2003), doi:10.1016/S0168-583X(02)01863-3.

[8] S. Bellucci, V. M. Biryukov, and A. Cordelli, "Channeling of high-energy particles in a multi-wall nanotube", *Phys. Lett. B* **608**, 53 (2005), doi:10.1016/j.physletb.2005.01.003.

[9] J. Wei, H. Zhu, D. Wu, and B. Wei, "Carbon nanotube filaments in household light bulbs", *Appl. Phys. Lett.* **84**, 4869 (2004), doi:10.1063/1.1762697.

[10] H. Ajiki and T. Ando, "Aharonov-Bohm effect in carbon nanotubes", *Physica B* **201**, 349 (1994), doi:10.1016/0921-4526(94)91112-6.

[11] T. Ando, "Theory of electronic states and transport in carbon nano-tubes", *Physics of Semiconductors 2002, Proceedings Institute of Physics Conference Series* **171**, 1 (2003).

[12] T. Ando, T. Nakanishi, and R. Saito, "Berry's phase and absence of back scattering in carbon nanotubes", *J. Phys. Soc. Japan* **67**(8), 2857 (1998), doi:10.1143/JPSJ.67.2857.

[13] Y. J. Jung, Y. Homma, R. Vajtai, Y. Kobayashi, T. Ogino, and P. M. Ajayan, "Straightening suspended single walled carbon nanotubes by ion irradiation", *Nano. Lett.* **4**(6), 1109 (2004), doi:10.1021/nl049550b.

[14] A. V. Krasheninnikov and K. Nordlund, "Irradiation effects in carbon nanotubes", *Nucl. Instrum. & Methods Phys. Res. B* **216**, 355 (2004), doi:10.1016/j.nimb.2003.11.061.

[15] J. A. V. Pomoell, A. V. Krasheninnikov, K. Nordlund, and J. Keinonen, "Ion ranges and irradiation-induced defects in multiwalled carbon nanotubes", *J. Appl. Phys.* **96**(5), 2864 (2004), doi:10.1063/1.1776317.

[16] T. Pichler, M. Knupfer, M. S. Golden, J. Fink, A. Rinzler, and R. E. Smalley, "Localized and delocalized electronic states in single-wall carbon nanotubes", *Phys. Rev. Lett.* **80**(21), 4729 (May 1998), doi:10.1103/PhysRevLett.80.4729.

[17] T. W. Odom, J.-L. Huang, P. Kim, and C. M. Lieber, "Atomic structure and electronic properties of single-walled carbon nanotubes", *Nature* **391**(6662), 62 (Dec. 1998), doi:10.1038/34145.

[18] T. W. Odom, J.-L. Huang, P. Kim, and C. M. Lieber, "Structure and electronic properties of carbon nanotubes", *J. Phys. Chem. B* **104**(13), 2794 (2000), doi:10.1021/jp993592k.

[19] T. Kempa, D. Carnahan, M. Olek, M. Correa, M. Giersig, M. Cross, G. Benham, M. Sennett, Z. Ren, and K. Kempa, "Dielectric media based on isolated metallic nanostructures", *J. Appl. Phys.* **98**, 034310 (2005), doi:10.1063/1.1996836.

[20] J. Nig, J. Zhang, Y. Pan, and J. Guo, "Fabrication and mechanical properties of SiO_2 matrix composits reinforced by carbon nanotube", *Mater. Sci. Eng.* **A313**, 83 (2001), doi:10.1016/S0921-5093(03)00256-9.

[21] C. Xiang, X. Shi, Y. Pan, and J. Guo, "Fabrication and dielectric properties of CNTs/SiO_2 composites", *Key Eng. Mater.* **280–283**, 123 (2005).

[22] H. Nishino, C. Yamaguchi, H. Nakaoka, and R. Nishida, "Carbon nanotube with amorphous carbon wall: α-CNT", *Carbon* **41**(11), 2165 (2003), doi:10.1016/S0008-6223(03)00206-9.

[23] C. Guerret-Piécourt, Y. L. Bourar, A. Loiseau, and H. Pascard, "Relation between metal electronic structure and morphology of metal compounds inside carbon nanotubes", *Nature* **372**(6508), 761 (Dec. 1994), doi:10.1038/372761a0.

[24] W. X. Chen, J. P. Tu, L. Y. Wang, H. Y.Gan, Z. D. Xu, and X. B. Zhang, "Tribological application of carbon nanotubes in a metal-based composite coating and composites", *Carbon* **41**(2), 215 (2003), doi:10.1016/S0008-6223(02)00265-8.

[25] Y. Zhang, N. W. Franklin, R. J. Chen, and H. Dai, "Metal coating on suspended carbon nanotubes and its implication to metal-tube interaction", *Chem. Phys. Lett.* **331**(1), 35 (Nov. 2000), doi:10.1016/S0009-2614(00)01162-3.

[26] S. Ninomiya, Y. Yamazaki, F. Koike, H. Masuda, T. Azuma, K. Komaki, K. Kuroki, and M. Sekiguchi, "Stabilized hollow ions extracted in vacuum", *Phys. Rev. Lett.* **78**(24), 4557 (1997), doi:10.1103/PhysRevLett.78.4557.

[27] V. M. K. Bagci, O. Gülseren, T. Yildirim, Z. Gedik, and S. Ciraci, "Metal nanoring and tube formation on carbon nanotubes", *Phys. Rev. B* **66**, 045409 (2002), doi:10.1103/PhysRevB.66.045409.

[28] J. Bao, K. Wang, Z. Xu, H. Zhang, and Z. Lu, "A novel nanostructure of nickel nanotubes encapsulated in carbon nanotubes", *Chem. Commun.* pp. 208–209 (2003), doi:10.1039/b208539a.

[29] C. H. Liang, G. W. Meng, L. D. Zhang, N. F. Shen, and X. Y. Zhang, "Carbon nanotubes filled partially or completely with nickel", *J. Cryst. Growth* **218**(1), 136 (Sep. 2000), doi:10.1016/S0022-0248(00)00557-1.

[30] Y. Bushuev, S. Davletbaeva, and F. F. Muguet, "Hydration simulations of a carbon nanotube, imerse in water, according to the 3-attractor water model", *Sensors* **5**(4–5), 139 (Apr. 2005), URL http://www.mdpi.org/sensors/papers/s5040139.pdf.

[31] F. Moulin, M. Devel, and S. Picaud, "Molecular dynamics simulations of polarizable nanotubes interacting with water", *Phys. Rev. B* **71**(16), 165401 (Apr. 2005), doi:10.1103/PhysRevB.71.165401.

[32] K. Moloni, M. R. Buss, and R. P. Andres, "Tapping mode scanning force microscopy in water using a carbon nanotube probe", *Ultramicroscopy* **80**(4), 237 (Dec. 1999), doi:10.1016/S0304-3991(99)00107-2.

[33] Z. Zahab, L. Spina, P. Poncharal, and C. Marlière, "Water-vapor effect on the electrical conductivity of a single-walled carbon nanotube mat", *Phys. Rev. B* **62**(15), 10000 (Oct. 2000), doi:10.1103/PhysRevB.62.10000.

[34] W. Kim, A. Javey, O. Vermesh, Q. Wang, Y. Li, and H. Dai, "Hysteresis caused by water molecules in carbon nanotube field-effect transistors", *Nano. Lett.* **3**(2), 193 (Feb. 2003), doi:10.1021/nl0259232.

[35] D. M. Guldi, G. M. A. Rahman, N. Jux, D. Balbinot, U. Hartnagel, N. Tagmatarchis, and M. Prato, "Functional single-wall carbon nanotube nanohybrids–asociating SWNTs with water-soluble enzyme model systems", *J. Am. Chem. Soc.* **127**(27), 9830 (2005), doi:10.1021/ja050930o.

[36] D. N. Futaba, K. Hata, T. Yamada, K. Mizuno, M. Yumura, and S. Iijima, "Kinetics of water-assisted single-walled carbon nanotube synthesis revealed by a time-evolution analysis", *Phys. Rev. Lett.* **95**(5), 056104 (Jul. 2005), doi:10.1103/PhysRevLett.95.056104.

[37] S. Andreev, D. Reichman, and G. Hummer, "Effect of flexibility on hydrophobic behavior of nanotube water channels", *J. Chem. Phys.* **123**(19), 194502 (Nov. 2005), doi:10.1063/1.210529.

[38] L. Zhu, Y. Xiu, D. W. Hess, and C.-P. Wong, "Aligned carbon nanotube stacks by water-assisted selective etching", *Nano. Lett.* **5**(12), 2641 (Dec. 2005), doi:10.1021/nl051906b.

[39] E. Prodan, C. Radloff, N. J. Halas, and P. Nordlander, "A hybridization model for the plasmon response of complex nanostructures", *Science* **302**(5644), 419 (Oct. 2003), doi:10.1126/science.1089171.

[40] E. Prodan, A. Lee, and P. Nordlander, "The effect of a dielectric core and embedding medium on the polarizability of metalic nanoshells", *Chem. Phys. Lett.* **360**, 325 (2002), doi:10.1016/S0009-2614(02)00850-3.

[41] E. Prodan, P. Nordlander, and N. J. Halas, "Effects of dielectric screening on the optical properties of metallic nanoshells", *Chem. Phys. Lett.* **368**, 94 (2002), doi:10.1016/S0009-2614(02)01828-6.

[42] T. Stöckli, J.-M. Bonard, A. Châtelain, Z. L. Wang, and P. Stadelmann, "Collective oscillations in a single-wall carbon nanotube excited by fast electrons", *Phys. Rev. B* **64**, 115424 (2001), doi:10.1103/PhysRevB.64.115424.

[43] J. H. Fink and P. Lambin, in M. S. Dresselhaus, G. Dresselhaus, and P. Avouris, eds., *Carbon Nanotubes: Synthesis, Structure, Properties, and Applications* (Springer, Berlin, 2001), pp. 247–272.

[44] N. R. Arista, "Interaction of ions and molecules with surface modes in cylindrical channels in solids", *Phys. Rev. A* **64**(3), 032901 (Aug. 2001), doi:10.1103/PhysRevA.64.032901.

[45] N. R. Arista and M. A. Fuentes, "Interaction of charged particles with surface plasmons in cylindrical channels in solids", *Phys. Rev. B* **63**, 165401 (2001), doi:10.1103/PhysRevB.63.165401.

[46] K. Tökési, X.-M. Tong, C. Lemell, and J. Burgdörfer, "Energy loss of charged particles at large distances from metal surfaces", *Phys. Rev. A* **72**, 022901 (2005), doi:10.1103/PhysRevA.72.022901.

[47] X. Artru, S. P. Fomin, N. F. Shulǵa, K. A. Ispirian, and N. K. Zhevago, "Carbon nanotubes and fullerites in high-energy and X-ray physics", *Phys. Rep.* **412**, 89 (2005), doi:10.1016/j.physrep.2005.02.002.

[48] S. Bellucci, "Nanotubes for particle channeling, radiation and electron sources", *Nucl. Instrum. & Methods Phys. Res. B* **234**, 57 (2005), doi:10.1016/j.nimb.2005.02.018.

[49] A. V. Krasheninnikov and K. Nordlund, "Multiwalled carbon nanotubes as apertures and conduits for energetic ions", *Phys. Rev. B* **71**, 24508 (2005), doi:10.1103/PhysRevB.71.24508.

[50] D.-P. Zhou, Y.-N. Wang, L. Wei, and Z. L. Mišković, "Dynamic polarization effects in ion channeling through single-wall carbon nanotubes", *Phys. Rev. A* **72**, 023202 (2005), doi:10.1103/PhysRevA.72.023202.

[51] B. E. Granger, P. Král, H. R. Sadeghpour, and M. Shapiro, "Highly extended image states around nanotubes", *Phys. Rev. Lett.* **89**(13), 135506 (Sep. 2002), doi:10.1103/PhysRevLett.89.135506.

[52] M. Zamkov, N. Woody, B. Shan, H. S. Chakraborty, Z. Change, U. Thumm, and P. Richard, "Time-resolved photoimaging of image-potential states in carbon nanotubes", *Phys. Rev. Lett.* **93**(15), 156803 (2004), doi:10.1103/PhysRevLett.93.156803.

[53] A. G. Marinopoulos, L. Reining, A. Rubio, and N. Vast, "Optical and loss spectra of carbon nanotubes: Depolarization effects and intertube interactions", *Phys. Rev. Lett.* **91**, 046402 (2003), doi:10.1103/PhysRevLett.91.046402.

[54] E. Prodan and P. Nordlander, "Plasmon hybridization in spherical nanoparticles", *J. Chem. Phys.* **120**(11), 5444 (Mar. 2004), doi:10.1063/1.1647518.

[55] Y.-N. Wang and Z. L. Mišković, "Interactions of fast ions with carbon nanotubes: self-energy and stopping power", *Phys. Rev. A* **69**, 022901 (2004), doi:10.1103/PhysRevA.69.022901.

[56] P. Longe and S. M. Bose, "Collective excitations in metallic graphene tubules", *Phys. Rev. B* **48**(24), 18239 (1993), doi:10.1103/PhysRevB.48.18239.

[57] S. M. Bose, "Low energy plasmon peaks in the electron energy loss spectra of single-wall carbon nanotubes", *Phys. Lett. A* **289**, 255 (2001), doi:10.1016/S0375-9601(01)00585-0.

[58] C. Yannouleas, E. N. Bogachek, and U. Landman, "Collective excitations of multishell carbon microstructures: Multishell fullerenes and coaxial nanotubes", *Phys. Rev. B* **53**(15), 10225 (1996), doi:10.1103/PhysRevB.53.10225.

[59] D. Östling, D. Tománek, and A. Rosén, "Electronic structure of single-wall, multiwall, and filled carbon nanotubes", *Phys. Rev. B* **55**(20), 13980 (1997), doi:10.1103/PhysRevB.55.13980.

[60] G. Gumbs and G. R. Aĭzin, "Collective excitations in a linear periodic array of cylindrical nanotubes", *Phys. Rev. B* **65**, 195407 (2002), doi:10.1103/PhysRevB.65.195407.

[61] G. Gumbs and A. Balassis, "Effects of coupling on plasmon modes and drift-induced instabilities in a pair of cylindrical nanotubes", *Phys. Rev. B* **68**, 075405 (2003), doi:10.1103/PhysRevB.68.075405.

[62] G. Gumbs and A. Balassis, "Comparison of the stopping power of plasmons and single-particle excitations for nanotubes", *Phys. Rev. B* **71**, 235410 (2005), doi:10.1103/PhysRevB.71.235410.

[63] G. Gumbs, A. Balassis, and P. Fekete, "Image potential for a double-walled cylindrical nanotube", *Phys. Rev. B* **73**, 075411 (2006), doi:10.1103/PhysRevB.73.075411.

[64] J. Cazaux, "Sur la constante dielectrique du graphite dans l'ultraviolet", *Solid State Commun.* **8**(7), 545 (Apr. 1970), doi:10.1016/0038-1098(70)90301-7.

[65] J. Cazaux, "Sur l'anisotropie des pertes d'energie et des constantes optiques du graphite dans l'ultraviolet", *Opt. Commun.* **2**(4), 173 (Sep. 1970), doi:10.1016/0030-4018(70)90009-X.

[66] G. Barton and C. Eberlein, "Plasma spectroscopy proposed for C_{60} and C_{70}", *J. Chem. Phys.* **95**(3), 1512 (Aug. 1991), doi:10.1063/1.461065.

[67] X. Jiang, "Collective plasmon excitations in graphene tubules", *Phys. Rev. B* **54**(19), 13487 (1996), doi:10.1103/PhysRevB.54.13487.

[68] D. J. Mowbray, Z. L. Mišković, F. O. Goodman, and Y.-N. Wang, "Interactions of fast ions with carbon nanotubes: two-fluid model", *Phys. Rev. B* **70**(19), 195418 (Nov. 2004), doi:10.1103/PhysRevB.70.195418.

[69] M. Weissbluth, *Atoms and Molecules* (Academic Press, New York, 1978).

[70] G. Barton, "Some surface effects in the hydrodynamic model of metals", *Rep. Prog. Phys.* **42**, 963 (1979), doi:10.1088/0034-4885/42/6/001.

[71] I. V. Hertel, H. Steger, J. de Vries, B. Weisser, C. Menzel, B. Kamke, and W. Kamke, "Giant plasmon excitation in free C_{60} and C_{70} molecules studied by photoionization", *Phys. Rev. Lett.* **68**, 784 (1992), doi:10.1103/PhysRevLett.68.784.

[72] P. Sigmund, *Particle Penetration and Radiation Effects: General Aspects and Stopping of Swift Point Charges* (Springer, Heidelburg, 2006).

[73] J. M. Pitarke, V. M. Silkin, E. V. Chulkov, and P. M. Echenique, "Surface plasmons in metallic structures", *J. Opt. A: Pure Appl. Opt.* **7**, S73 (2005), URL http://stacks.iop.org/JOptA/7/S73.

[74] T. Stöckli, Z. L. Wang, J.-M. Bonard, P. Stadelmann, and A. Châtelain, "Plasmon excitations in carbon nanotubes", *Phil. Mag. B* **79**(10), 1531 (Oct. 1999), URL http://www.ingentaconnect.com/content/tandf/tphb/1999/00000079/00000010/art00004.

[75] Z. L. Wang, "Valence electron excitations and plasmon oscillations in thin films, surfaces, interfaces and small particles", *Micron* **27**(3–4), 265 (1996), doi:10.1016/0968-4328(96)00011-X.

[76] C. Yannouleas, E. N. Bogachek, and U. Landman, "Dimensionality crossovers of the σ plasmon in coaxial carbon nanotubes", *Phys. Rev. B* **50**(11), 7977 (1994), doi:10.1103/PhysRevB.50.7977.

[77] W. Que, "Theory of plasmons in carbon nanotube bundles", *J. Phys.: Condens. Matter* **14**, 5239 (2002), doi:10.1088/0953-8984/14/20/319.

[78] Y. Kornyushin and W. Que, "Plasma oscillations of the carbon peapod", *J. Phys.: Condens. Matter* **14**, 10203 (2002), doi:10.1088/0953-8984/14/43/317.

[79] G. Y. Slepyan, S. A. Maksimenko, V. P. Kalosha, A. V. Gusakov, and J. Hermann, "High-order harmonic generation by condunction electrons in carbon nanotube ropes", *Phys. Rev. A* **63**, 053808 (2001), doi:10.1103/PhysRevA.63.053808.

[80] G. Y. Slepyan, S. A. Maksimenko, A. Lakhtakia, O. Yevtushenko, and A. V. Guskov, "Electrodynamics of carbon nanotubes: Dynamic conductivity, impedance boundary conditions, and surface wave propagation", *Phys. Rev. B* **60**(24), 17136 (Dec. 1999), doi:10.1103/PhysRevB.60.17136.

[81] G. Y. Slepyan, S. A. Maksimenko, A. Lakhtakia, and O. M. Yevtushenko, "Electromagnetic response of carbon nanotubes and nanotube ropes", *Syn. Metals* **124**(1), 121 (Oct. 2001), doi:10.1016/S0379-6779(01)00445-3.

[82] D. Segal, P. Král, and M. Shapiro, "Shaping of detached image states above suspended nanowires", *Phys. Rev. B* **69**, 153405 (2004), doi:10.1103/PhysRevB.69.153405.

[83] D. Segal, P. Král, and M. Shapiro, "Electric and magnetic-field tuning of tubular image states above suspended nanowires", *Chem. Phys. Lett.* **392**, 314 (2004), doi:10.1016/j.cplett.2004.05.075.

[84] D. Segal, B. E. Granger, H. R. Sadeghpour, P. Král, and M. Shapiro, "Tunable bands of electronic image states in nanowire lattices", *Phys. Rev. Lett.* **94**, 016402 (Jan. 2005), doi:10.1103/PhysRevLett.94.016402.

[85] M. Zamkov, H. S. Chakraborty, A. Habib, N. Woody, U. Thumm, and P. Richard, "Image-potential states of single- and multiwalled carbon nanotubes", *Phys. Rev. B* **70**, 115419 (2004), doi:10.1103/PhysRevB.70.115419.

[86] M. Krčmar, W. M. Saslow, and A. Zangwill, "Electrostatics of conducting nanocylinders", *J. Appl. Phys.* **93**(6), 3495 (Mar. 2003), doi:10.1063/1.1540712.

[87] G. V. Dedkov, "Fullerene nanotubes can be used when transporting gamma-quanta, neutrons, ion beams and radiation from relativistic particles", *Nucl. Instrum. & Methods Phys. Res. B* **143**(4), 584 (1998), doi:10.1016/S0168-583X(98)00388-7.

[88] G. V. Dedkov and B. S. Karamurzov, "Fullerene nanotubes as transporting and focusing elements of nanoscale beam technology", *Surf. Coat. Tech.* **128–129**, 51 (2000), doi:10.1016/S0257-8972(00)00656-3.

[89] G. V. Dedkov, "Characterization of nanotubes as microscale beam manipulators: transmission of neutral atoms and low-energy ions", *Surf. Coat. Tech.* **158–159**, 75 (2002), doi:10.1016/S0257-8972(02)00223-2.

[90] H. Ehrenreich and M. H. Cohen, "Self-consistent field approach to the many-electron problem", *Phys. Rev.* **115**(4), 786 (Aug. 1959), doi:10.1103/PhysRev.115.786.

[91] J. Lindhard, "On the properties of a gas of charged particles", *K. Dan. Vidensk. Selsk. Mat. Fys. Medd.* **28**(8), 1 (1954).

[92] N. W. Ashcroft and N. D. Mermin, *Solid State Physics* (Thomson Learning, Toronto, 1976).

[93] G. D. Mahan, *Many-Particle Physics*, 2nd ed. (Plenum Press, New York, 1990).

[94] M. F. Lin and F. L. Shuy, "Low-frequency electronic excitations in doped carbon nanotubes", *Physica B* **292**, 117 (Oct. 2000), doi:10.1016/S0921-4526(00)00499-3.

[95] M. F. Lin, F. L. Shuy, and R. B. Chen, "Dielectric response of an electron-gas nanotube superlattice", *Phys. Lett. A* **253**, 88 (1999), doi:10.1016/S0375-9601(99)00009-2.

[96] M. F. Lin and K. W.-K. Shung, "Elementary excitations in cylindrical tubules", *Phys. Rev. B* **47**(11), 6617 (1993), doi:10.1103/PhysRevB.47.6617.

[97] M. F. Lin, D. S. Chuu, C. S. Huang, Y. K. Lin, and K. W.-K. Shung, "Collective excitations in a single-layer carbon nanotube", *Phys. Rev. B* **53**(23), 15493 (1996), doi:10.1103/PhysRevB.53.15493.

[98] Y. H. Ho, G. W. Ho, T. S. Li, and M. F. Lin, "Electronic excitations of double-walled armchair carbon nanotubes", *Physica E* **32**, 569 (2006), doi:10.1016/j.physe.2005.12.106.

[99] B. Vasvári, "Collective resonances in carbon nanotubes", *Phys. Rev. B* **55**(12), 7993 (1997), doi:10.1103/PhysRevB.55.7993.

[100] B. Tanatar, "Short-range correlation effects on the plasmons in cylindrical tubules", *Phys. Rev. B* **55**(3), 1361 (Jan. 1997), doi:10.1103/PhysRevB.55.1361.

[101] O. Sato, Y. Tanaka, M. Kobayashi, and A. Hasegawa, "Exotic behaviour of the dielectric function and the plasmons of an electron gas on a tubule", *Phys. Rev. B* **48**(3), 1947 (1993), doi:10.1103/PhysRevB.48.1947.

[102] G. Gumbs, A. Balassis, and C.-Y. Shew, "Plasmon-polaritons for a nanotube in an intense terahertz field", *Europhys. Lett.* **64**(2), 225 (Oct. 2003), doi:10.1209/epl/i2003-00297-5.

[103] L. X. Benedict, S. G. Louie, and M. L. Cohen, "Static polarizabilities of single-wall carbon nanotubes", *Phys. Rev. B* **52**(11), 8541 (Sep. 1995), doi:10.1103/PhysRevB.52.8541.

[104] W. Que, "Littinger parameter g for metallic carbon nanotubes and related systems", *Phys. Rev. B* **66**, 193405 (2002), doi:10.1103/PhysRevB.66.193405.

[105] L. M. Woods and G. D. Mahan, "Electron-phonon effects in graphene and armchair (10,10) signle-wall carbon nanotubes", *Phys. Rev. B* **61**(16), 1051 (Apr. 2000), doi:10.1103/PhysRevB.61.10651.

[106] C. Kittel, *Introduction to Solid State Physics*, 7th ed. (Wiley, New York, 1996).

[107] W.-D. Sheng, "A transfer matrix approach to conductance in quantum waveguides", *J. Phys.: Condens. Matter* **8**(20), 3635 (May 1996), doi:10.1088/0953-8984/8/20/009.

[108] A. Mayer, N. M. Miskovsky, P. H. Cutler, and P. Lambin, "Trasfer-matrix simulations of field emission from bundles of open and closed (5,5) carbon nanotubes", *Phys. Rev. B* **68**, 235401 (2003), doi:10.1103/PhysRevB.68.235401.

[109] V. Menunier, L. Henrard, and P. Lambin, "Energetics of bent carbon nanotubes", *Phys. Rev. B* **57**(4), 2586 (Jan. 1998), doi:10.1103/PhysRevB.57.2586.

[110] A. Mayer, N. M. Miskovsky, and P. H. Cutler, "Transfer-matrix simulations of field emission from a metallic (5,5) carbon nanotube", *Ultramicroscopy* **92**, 215 (2002), doi:10.1016/S0304-3991(02)00136-5.

[111] A. Mayer, N. M. Miskovsky, and P. H. Cutler, "Simulations of field emission from a semiconducting (10,0) carbon nanotube", *J. Vac. Sci. Technol. B* **20**(1), 100 (Jan. 2002), doi:10.1116/1.1428275.

[112] G. I. Márk, L. Tapasztó, László, P. Biró, and A. Mayer, in V. N. Popov and P. Lambin, eds., *Carbon Nanotubes* (Springer, Dordrecht, 2006), URL http://www.springer.com/dal/home/materials?SGWID=1-10041-22-134256226-0.

[113] A. Mayer, "Band structure and transport properties of carbon nanotubes using a local pseudopotential and a trsnsfer-matrix technique", *Carbon* **42**(10), 2057 (2004), doi:10.1016/j.carbon.2004.04.017.

[114] M. B. Nardelli, "Electronic transport in extended systems: Application to carbon nanotubes", *Phys. Rev. B* **60**(11), 7828 (Sep. 1999), doi:10.1103/PhysRevB.60.7828.

[115] S. Han and J. Ihm, "First-principles study of field emission of carbon nanotubes", *Phys. Rev. B* **66**, 241402(R) (2002), doi:10.1103/PhysRevB.66.241402.

[116] V. N. Popov, "Curvature effects on the structural, electronic and optical properties of isolated single-walled carbon nanotubes within a symmetry-adapted non-orthogonal tight-binding model", *New J. Phys.* **6**, 17 (2004), doi:10.1088/1367-2630/6/1/017.

[117] N. Hamada, S. ichi Sawada, and A. Oshiyama, "New one-dimensional conductors: Graphitic microtubules", *Phys. Rev. Lett.* **68**(10), 1579 (Mar. 1992), doi:10.1103/PhysRevLett.68.1579.

[118] Y. I. Pylutskyy, S. S. Durov, O. V. Ogloblya, E. V. Buzaneva, and P. Sharff, "Molecular dynamics simulation of mechanical, vibrational and electronic properties of carbon nanotubes", *Comp. Mater. Sci.* **17**, 352 (2000), doi:10.1016/S0927-0256(00)00051-3.

[119] R. Saito, M. Fujita, G. Dresselhaus, and M. S. Dresselhaus, "Electronic structure of graphene tubules based on C_{60}", *Phys. Rev. B* **46**(3), 1804 (Jul. 1992), doi:10.1103/PhysRevB.46.1804.

[120] A. A. Maarouf, C. L. Kane, and E. J. Mele, "Electronic structure of carbon nanotube ropes", *Phys. Rev. B* **61**(16), 11156 (Apr. 2000), doi:10.1103/PhysRevB.61.11156.

[121] S. C. Chen, F. L. Shyu, C. S. Lue, and M. F. Lin, "Dielectric screening for carbon nanotubes in a gating electric field", *Physica E* **32**, 577 (2006), doi:10.1016/j.physe.2005.12.108.

[122] V. N. Popov, L. Henrard, and P. Lambin, "Electron-phonon and electron-photon interactions and resonant raman scattering from the radial-breathing mode of single-walled carbon nanotubes", *Phys. Rev. B* **72**, 035436 (2005), doi:10.1103/PhysRevB.72.035436.

[123] V. N. Popov and L. Henrard, "Comparative study of the optical properties of single-walled carbon nanotubes within orthogonal and nonorthogonal tight-binding models", *Phys. Rev. B* **70**, 115407 (2004), doi:10.1103/PhysRevB.70.115407.

[124] P. Lambin, F. Triozon, and V. Meunier, in V. N. Popov and P. Lambin, eds., *Carbon Nanotubes* (Springer, Dordrecht, 2006), URL http://www.springer.com/dal/home/materials?SGWID=1-10041-22-134256226-0.

[125] C. Amovilli and N. H. March, "Long-range forces between C nanotubes and between C cages: Some polarizability bounds and scaling approximations yielding interaction energies at intermediate separations", *Carbon* **43**(8), 1634 (Jul. 2005), doi:10.1016/j.carbon.2005.01.027.

[126] F. Léonard and J. Tersoff, "Dielectric response of semiconducting carbon nanotubes", *Appl. Phys. Lett.* **81**(25), 4835 (2002), doi:10.1063/1.1530373.

[127] R. G. Parr and W. Yang, *Density-Functional Theory of Atoms and Molecules* (Oxford University Press, New York, 1989).

[128] J. W. Mintmire, B. I. Dunlap, and C. T. White, "Are fullerene tubules metallic?", *Phys. Rev. Lett.* **68**(5), 631 (Feb. 1992), doi:10.1103/PhysRevLett.68.631.

[129] M. Simeoni, C. D. Luca, S. Picozzi, S. Santucci, and B. Delley, "Interaction between zigzag single-wall carbon nanotubes and polymers: A density-functional study", *J. Chem. Phys.* **122**, 1 (2005), doi:10.1063/1.1925272.

[130] P. Keblinski, S. K. Nayak, P. Zapol, and P. M. Ajayan, "Charge distribution and stability of charged carbon nanotubes", *Phys. Rev. Lett.* **89**(25), 255503 (Dec. 2002), doi:10.1103/PhysRevLett.89.255503.

[131] X. Blase, L. X. Benedict, E. L. Shirley, and S. G. Louie, "Hybridization effects and metallicity in small radius carbon nanotubes", *Phys. Rev. Lett.* **72**(12), 1878 (Mar. 1994), doi:10.1103/PhysRevLett.72.1878.

[132] L. Lou, P. Nordlander, and R. E. Smalley, "Fullerene nanotubes in electric fields", *Phys. Rev. B* **52**, 1429 (1995), doi:10.1103/PhysRevB.52.1429.

[133] D. Sánchez-Portal, E. Artacho, J. M. Soler, A. Rubio, and P. Ordejón, "*Ab initio* structural, elastic, and vibrational properties of carbon nanotubes", *Phys. Rev. B* **59**(19), 12678 (May 1999), doi:10.1103/PhysRevB.59.12678.

[134] A. G. Marinopoulos, L. Wirtz, A. Marini, V. Olevano, A. Rubio, and L. Reining, "Optical absoption and electron energy loss spectra of carbon and boron nitride nanotubes: a first-principles approach", *Appl. Phys. A* **78**, 1157 (2004), doi:10.1007/s00339-003-2467-z.

[135] W. Zhang, Z. Zhu, Z. Xu, Z. Wang, and F. Zhang, "Molecular dynamics study of a low energy carbon ion moving in a single-wall carbon nanotube", *Nano.* **16**, 2681 (2005), doi:10.1088/0957-4484/16/11/036.

[136] C. S. Moura and L. Amaral, "Channeling on carbon nanotubes: A molecular dynamics approach", *J. Phys. Chem. B* **109**, 13515 (2005), doi:10.1021/jp051637d.

[137] A. Udomvech, T. Kerdcharoen, and T. Osotchan, "First principles tudy of Li and Li^+ adsorbed on carbon nanotube: Variation of tubule diameter and length", *Chem. Phys. Lett.* **406**, 161 (2005), doi:10.1016/j.cplett.2005.02.084.

[138] E. J. Mele, P. Král, and D. Tománek, "Coherent control of photocurrents in graphene and carbon nanotubes", *Phys. Rev. B* **61**(11), 7669 (Mar. 2000), doi:10.1103/PhysRevB.61.7669.

[139] H. Ajiki and T. Ando, "Electronic states of carbon nanotubes", *J. Phys. Soc. Japan* **62**(4), 1255 (Apr. 1993), doi:10.1143/JPSJ.62.1255.

[140] V. A. Margulis and T. A. Sizikova, "Theoretical study of third-order nonlinear optical response of semiconductor carbon nanotubes", *Physica B* **245**, 173 (1998), doi:10.1016/S0921-4526(97)00676-5.

[141] V. A. Marguilis and E. A. Gaiduk, "Dielectric function of single-wall carbon nanotubes", *Chem. Phys. Lett.* **341**(1–2), 16 (Jun. 2001), doi:10.1016/S0009-2614(01)00294-9.

[142] V. A. Marguilis and E. A. Gaiduk, "Nature of near-infrared absorption in single-wall carbon nanotubes", *Phys. Lett. A* **281**, 52 (Mar. 2001), doi:10.1016/10.1016/S0375-9601(01)00086-X.

[143] Y.-N. Wang and Z. L. Mišković, "Energy loss of charged particles moving in cylindrical tubules", *Phys. Rev. A* **66**, 042904 (2002), doi:10.1103/PhysRevA.66.042904.

[144] D. J. Mowbray, Z. L. Mišković, F. O. Goodman, and Y.-N. Wang, "Wake effect in interactions of fast ions with carbon nanotubes", *Phys. Lett. A* **329**, 94 (Aug. 2004), doi:10.1016/j.physleta.2004.06.090.

[145] D. J. Mowbray, S. Chung, Z. L. Mišković, F. O. Goodman, and Y.-N. Wang, "Dynamic interactions of fast ions with carbon nanotubes", *Nucl. Instrum. & Methods Phys. Res. B* **230**(1–4), 142 (Apr. 2005), doi:10.1016/j.nimb.2004.12.032.

[146] D. J. Mowbray, S. Chung, and Z. L. Mišković, in V. N. Popov and P. Lambin, eds., *Carbon Nanotubes* (Springer, Dordrecht, 2006), pp. 176–177.

[147] D. J. Mowbray, Z. L. Mišković, and F. O. Goodman, "Ion interactions with carbon nanotubes in dielectric media", *Phys. Rev. B* **74**(19), 195435 (Nov. 2006), doi:10.1103/PhysRevB.74.195435.

[148] S. Chung, D. J. Mowbray, Z. L. Mišković, F. O. Goodman, and Y.-N. Wang, "Dynamic interactions of fast ions with multiwalled carbon nanotubes", *Radiation Phys. Chem.* **76**(3), 524 (May 2007), doi:10.1016/j.radphyschem.2005.09.020.

[149] D. J. Mowbray, Z. L. Mišković, and F. O. Goodman, "Dynamic interactions of ions with carbon nanotubes in water", *Nucl. Instrum. & Methods Phys. Res. B* (2007), (in press).

[150] T. P. Doerr and Y.-K. Yu, "Electrostatics in the presence of dielectrics: The benefits of treating the induced surface charge density directly", *Amer. J. Phys.* **72**(2), 190 (Feb. 2004), doi:10.1119/1.1624115.

[151] J. W. Swart, J. A. Diniz, I. Doi, and M. A. B. de Moraes, "Modification of the refractive index and the dielectric constant of silicon dioxide by means of ion implantation", *Nucl. Instrum. & Methods Phys. Res. B* **166-167**, 171 (2000), doi:10.1016/S0168-583X(99)00650-3.

[152] J. C. Ashley, J. J. Cowan, R. H. Ritchie, V. E. Anderson, and J. Hoelzl, "Straggling and plasmon excitation in the energy loss spectra of electrons transmitted through carbon", *Thin Solid Films* **60**(3), 361 (Jul. 1979), doi:10.1016/0040-6090(79)90082-8.

[153] I. Abril, R. Garcia-Molina, C. D. Denton, F. J. Pérez-Pérez, and N. R. Arista, "Dielectric description of wakes and stopping powers in solids", *Phys. Rev. A* **58**(1), 357 (Jul. 1998), doi:10.1103/PhysRevA.58.357.

[154] J. L. Gervasoni and N. R. Arista, "Plasmon excitations in cylindrical wires by external charged particles", *Phys. Rev. B* **68**(23), 235302 (Dec. 2003), doi:10.1103/PhysRevB.68.235302.

[155] S. Roberts, "Optical properties of nickel and tungsten and their interpretation according to Drude's formula", *Phys. Rev.* **114**(1), 104 (Apr. 1959), doi:10.1103/PhysRev.114.1959.

[156] P. B. Johnson and R. W. Christy, "Optical constants of transition metals: Ti, V, Cr, Mn, Fe, Co, Ni, Pd", *Phys. Rev. B* **9**(12), 5056 (Jun. 1974), doi:10.1103/PhysRevB.9.5056.

[157] P. B. Johnson and R. W. Christy, "Optical constants of copper and nickel as a function of temperature", *Phys. Rev. B* **11**(4), 1315 (Feb. 1975), doi:10.1103/PhysRevB.11.1315.

[158] C. M. Kwei, Y. F. Chen, C. J. Tung, and J. P. Wang, "Electron inelastic mean free paths for plasmon excitations and interband transitions", *Surf. Sci.* **293**(3), 202 (Aug. 1993), doi:10.1016/0039-6028(93)90314-A.

[159] T. J. Moravec, J. C. Rife, and R. N. Dexter, "Optical constants of nickel, iron, and nickel-iron alloys in the vacuum ultraviolet", *Phys. Rev. B* **13**(8), 3297 (Apr. 1976), doi:10.1103/PhysRevB.13.3297.

[160] R. H. Ritchie and A. L. Marusak, "The surface plasmon dispersion relation for an electron gas", *Surf. Sci.* **4**(3), 234 (1966), doi:10.1016/0039-6028(66)90003-3.

[161] M. Kitagawa, "Calculation of the stopping power at the surface of a solid", *Nucl. Instrum. & Methods Phys. Res. B* **33**, 409 (1988), doi:10.1016/0168-583X(88)90595-2.

[162] F. E. Leys, C. Amovilli, I. A. Howard, N. H. March, and A. Rubio, "Surface charge model of a carbon nanotube: self-consistent field from Thomas-Fermi theory", *J. Phys. Chem. Solids* **64**(8), 1285 (2003), doi:10.1016/S0022-3697(03)00133-1.

[163] N. H. March, *Electron density theory of atoms and molecules* (Academic Press, London, 1992).

[164] D. S. Gemmell, "Channeling and related effects in the motion of charged particles through crystals", *Rev. Mod. Phys.* **49**(1), 129 (Jan. 1974), doi:10.1103/RevModPhys.46.129.

[165] G. Molière, "Therorie der Streuung schneller geladener Teilchen I. Einzelstreuung am abgeschirmten Coulomb-Feld", *Z. Naturforsch. A* **2**(3), 133 (1947).

[166] S. A. Cruz, C. Díaz-García, A. P. Pathak, and J. Soullard, "Pressure dependence of the mean excitation energy of atomic systems", *Nucl. Instrum. & Methods Phys. Res. B* **230**, 46 (Apr. 2005), doi:10.1016/j.nimb.2004.12.015.

[167] S. A. Cruz, C. Díaz-Carcía, and G. Covarrubias, "Statistical atomic models with complete neglect of differential overlap for the study of free and confined systems", *Interntl. J. Quant. Chem.* **102**(5), 897 (2005), doi:10.1002/qua.20452.

[168] D. J. Mowbray, J. Zuloaga, Z. L. Mišković, and F. O. Goodman, "Stopping power for ion channeling through carbon nanotubes", *Radiat. Effects & Defects in Solids* (2007), (in press).

[169] M. Abramowitz and I. A. Stegun, *Handbook of Mathematical Functions with Formulas, Graphs, and Mathematical Tables*, ninth ed. (Dover Publications, Inc., New York, 1970), URL http://www.math.sfu.ca/ cbm/aands/.

[170] F. Bloch, "Stopping power of atoms with many electrons", *Z. Phys.* **81**, 363 (1933).

[171] A. L. Fetter, "Electrodynamics of a layered electron gas. I. single layer", *Ann. Phys.* **81**(2), 367 (Dec. 1973), doi:10.1016/0003-4916(73)90161-9.

[172] A. L. Fetter, "Electrodynamics of a layered electron gas. II. periodic array", *Ann. Phys.* **88**(1), 1 (Nov. 1974), doi:10.1016/0003-4916(74)90397-2.

[173] M. K. Harbola and A. Banerjee, "Many-electron problem in terms of the density: from Thomas-Fermi to modern Density-Functional theory", *J. Theor. Comp. Chem.* **2**(2), 301 (2003), doi:10.1142/S021963360300046X.

[174] N. Argaman and G. Makov, "Density functional theory: An introduction", *Amer. J. Phys.* **68**(1), 69 (Jan. 2000), doi:10.1119/1.19375.

[175] S. Lundqvist and N. H. March, *Theory of the Inhomogeneous Electron Gas* (Plenum Press, New York, 1983).

[176] J. R. Smith, "Self-consitent many-electron theory of electron work functions and surface potential charcteristics for selected metals", *Phys. Rev.* **181**(2), 522 (1969), doi:10.1103/PhysRev.181.522.

[177] S. C. Ying, J. R. Smith, and W. Kohn, "Self-consistent screening of charges embedded in a metal surface", *J. Vac. Sci. & Tech.* **9**(2), 575 (Mar. 1972), doi:10.1116/1.1317722.

[178] S. C. Ying, "Hydrodynamic response of inhomogeneous metallic systems", *Il Nuovo Cimento* **B 23**(1), 270 (1974).

[179] S. C. Ying, J. R. Smith, and W. Kohn, "Density-functional theory of chemisorption on metal surfaces", *Phys. Rev. B* **11**(4), 1483 (1975), doi:10.1103/PhysRevB.11.1483.

[180] M. Levy, "Universal variational functionals of electron densities, first-order density matrices, and natural spin-orbitals and solution of the v-representability problem", *Proc. Natl. Acad. Sci. USA* **76**(12), 6062 (Dec. 1979), URL http://www.pnas.org/cgi/content/abstract/76/12/6062.

[181] M. Levy, "Electron densities in search of Hamiltonians", *Phys. Rev. A* **26**(3), 1200 (Sep. 1982), doi:10.1103/PhysRevA.26.1200.

[182] B. P. van Zyl and E. Zaremba, "Thomas-Fermi-Dirac-von Weizsäcker hydrodynamics in laterally modulated electronic systems", *Phys. Rev. B* **59**(3), 2079 (1999), doi:10.1103/PhysRevB.59.2079.

[183] C. F. von Weizsäcker, "Zur theorie dier kernmassen", *Z. Phys.* **96**, 431 (1935).

[184] E. S. Kryachko and E. V. Ludeña, *Energy Density Functional Theory of Many-Electron Systems* (Kluwer Academic Publishers, Dordrecht, 1990).

[185] A. Holas, P. M. Kozlowski, and N. H. March, "Kinetic energy density and Pauli potential: dimensionality dependence, gradient expansions and non-locality", *J. Phys. A: Math. Gen.* **24**(18), 4249 (Sep. 1991), doi:10.1088/0305-4470/24/18/013.

[186] K. Yonei and Y. Tomishima, "On the Weizsäcker correction to the Thomas-Fermi theory of atoms", *J. Phys. Soc. Japan* **20**, 1051 (1965), doi:10.1143/JPSJ.20.1051.

[187] E. H. Lieb, "Thomas-Fermi and related theories of atoms and molecules", *Rev. Mod. Phys.* **53**(4), 603 (Oct. 1981), doi:10.1103/RevModPhys.53.603.

[188] R. M. Dreizler and J. da Providencia, eds., *Density Functional Methods in Physics* (Plenum, New York, 1985).

[189] P. R. Acharya, L. J. Bartolotti, S. B. Sears, and R. G. Parr, "An atomic kinetic energy functional with full Weizsäcker correction", *Proc. Nat. Acad. Sci. USA* **77**(12), 6978 (Dec. 1980), URL http://www.pnas.org/cgi/content/abstract/77/12/6978.

[190] J. L. Gázquez and J. Robles, "On the atomic kinetic energy functionals with full weizsäcker correction", *J. Chem. Phys.* **76**(3), 1467 (Feb. 1982), doi:10.1063/1.443107.

[191] P. R. Acharya, "Comment on the derivation of atomic kinetic energy functionals with full weizsäcker correction", *J. Chem. Phys.* **78**(4), 2101 (Feb. 1983), doi:10.1063/1.444924.

[192] E. Teller, "On the stability of molecules in the Thomas-Fermi theory", *Rev. Mod. Phys.* **34**(4), 627 (Oct. 1962), doi:10.1103/RevModPhys.34.627.

[193] B. M. Deb and S. K. Ghosh, "QFD and single-particle density", *Single-Particle Density in Physics* (1987).

[194] E. Runge and E. K. U. Gross, "Density-functional theory for time-dependent systems", *Phys. Rev. Lett.* **52**, 997 (1984), doi:10.1103/PhysRevLett.52.997.

[195] H. Goldstein, C. Poole, and J. Safko, *Classical Mechanics*, 3rd ed. (Addison Wesley, San Francisco, 2002).

[196] L. J. F. Broer, "Generalized fluid dynamics and quantum mechanics", *Physica* **76**(2), 364 (Sep. 1974), doi:10.1016/0031-8914(74)90204-3.

[197] D. Lurie, *Particles and Fields* (Interscience, New York, 1968).

[198] A. Eguiluz and J. J. Quinn, "Hydrodynamic model for surface plasmons in metals and degenerate semiconductors", *Phys. Rev. B* **14**(4), 1347 (1976), doi:10.1103/PhysRevB.14.1347.

[199] J. D. Jackson, *Classical Electrodynamics*, 3rd ed. (Wiley, New York, 1999).

[200] L. A. Gevorgian, K. A. Ispirian, and R. K. Ispirian, "High energy particle channeling in nanotubes", *Nucl. Instrum. & Methods Phys. Res. B* **145**, 155 (1998), doi:10.1016/S0168-583X(98)00327-9.

[201] N. K. Zhevago and V. I. Glebov, "Channeling of fast charged and neutral particles in nanotubes", *Phys. Lett. A* **250**, 360 (Dec. 1998), doi:10.1016/S0375-9601(98)00850-0.

[202] N. K. Zhevago and V. I. Glebov, "Computer simulations of fast particle propagation through straight and bent nanotubes", *Phys. Lett. A* **310**(4), 301 (2003), doi:10.1016/S0375-9601(03)00241-X.

[203] A. A. Greenenko and N. F. Shul'ga, "Fast ion passing through straight and bent nanotubes", *Nucl. Instrum. & Methods Phys. Res. B* **205**, 767 (2003), doi:10.1016/S0168-583X(03)00583-4.

[204] Z. L. Mišković, "Ion channeling through carbon nanotubes", *Radiat. Effects & Defects in Solids* (2007), (in press).

[205] O. Sato, M. Kobaryashi, Y. Tanaka, and A. Hasegawa, "Acoustic plasma wave in a quantum-size cylindrical electron-hole plasma", *Phys. Rev. B* **52**(7), 4677 (Aug. 1995), doi:10.1103/PhysRevB.52.4677.

[206] J. Burgdörfer, "Dynamic screening and wake effects on electronic excitation in ion-solid and ion-surface collisions", *Nucl. Instrum. & Methods Phys. Res. B* **67**, 1 (Apr. 1992), doi:10.1016/0168-583X(92)95760-O.

[207] D. Emfietzoglou and H. Nikjoo, "The effect of model approximations on single-collision distributions of low-energy electrons in liquid water", *Radiat. Res* **163**(1), 98 (Jan. 2005), doi:10.1667/RR3281.

[208] D. Emfietzoglou, F. A. Cucinotta, and H. Nikjoo, "A complete dielectric reponse model for liquid water: A solution of the Bethe ridge problem", *Radiat. Res.* **164**(2), 202 (Aug. 2005), doi:10.1667/RR3399.

[209] H. Hayashi, N. Watanabe, Y. Udagawa, and C.-C. Kao, "The complete optical spectrum of liquid water measured by inelastic x-ray scattering", *Proc. Nat. Acad. Sci. USA* **97**(12), 6264 (Jun. 2000), doi:10.1073/pnas.110572097.

[210] J. Zuloaga, *Hydrodynamic Modeling of Dielectric Response in Graphene and Carbon Nanotubes*, Master's thesis, University of Waterloo (2006), URL http://etd.uwaterloo.ca/etd/jzuloaga2006.pdf.

[211] V. S. Vladimirov, *Equations of Mathematical Physics* (Marcel Dekker, New York, 1971).

[212] Z. Vager and D. S. Gemmell, "Polarization induced in a solid by the passage of fast charged partic les", *Phys. Rev. Lett.* **37**(20), 1352 (Nov. 1976), doi:10.1103/PhysRevLett.37.1352.

[213] A. P. Prudnikov, Y. A. Brychkov, and O. I. Marichev, *Integrals and Series: Volume 2: Special Functions* (Gordon and Breach Science Publishers, 1998).

[214] D.-P. Zhou, Y.-H. Song, Y.-N. Wang, and Z. L. Mišković, "Coulomb explosions and stopping of molecular ions channeled through carbon nanotubes", *Phys. Rev. A* **73**, 033202 (2006), doi:10.1103/PhysRevA.73.033202.

[215] D. Borka, S. Petrović, N. Nešković, D. J. Mowbray, and Z. L. Mišković, "Influence of the dynamical image potential on the rainbows in ion channeling through short carbon nanotubes", *Phys. Rev. A* **73**(6), 062902 (Jun. 2006), doi:10.1103/PhysRevA.73.062902.

[216] D. Borka, S. Petrović, N. Nešković, D. J. Mowbray, and Z. L. Mišković, "Influence of the dynamic polarization effect on the angular distributions of protons channeled in double-wall carbon nanotubes", *Nucl. Instrum. & Methods Phys. Res. B* (2007), (in press).

[217] N. K. Zhevhago and V. I. Glebov, "Diffraction and channeling in nanotubes", *J. Exp. Theor. Phys.* **91**(3), 504 (2000), doi:10.1134/1.1320084.

[218] D. Taverna, M. Kociak, V. Charbois, and L. Henrard, "Electron energy-loss spectrum of an electron passing near a locally anisotropic nanotube", *Phys. Rev. B* **66**, 235419 (2002), doi:10.1103/PhysRevB.66.235419.

[219] D. Taverna, M. Kociak, V. Charbois, L. Henrard, O. Stephan, and C. Colliex, "Simulations of electron energy-loss spectra of an electron passing near a locally anisotropic nanotube", *J. Electron Spectr. Related Phenom.* **129**, 293 (2003), doi:10.1016/S0368-2048(03)00080-X.

[220] L. Henrard and P. Lambin, "Calculation of the energy loss for an electron passing near giant fullerenes", *J. Phys. B: At. Mol. Opt. Phys.* **29**(21), 5127 (Nov. 1996), doi:10.1088/0953-4075/29/21/024.

[221] A. S. Berdinsky, P. S. Alegaonkar, J. B. Yoo, H. C. Lee, J. S. Jung, J. H. Han, D. Fink, and L. T. Chadderton, "Carbon nanotube growth in SiO_2 etched ion tracks" (2006), (unpublished).

[222] Z. Zhu, D. Zhu, R. Lu, Z. Xu, W. Zhang, and H. Xia, "The experimental progress of channeling of charged particles along nanostructure", *Proc. SPIE* **5974**, 597413 (Dec. 2006), doi:10.1117/12.640101.

[223] P. Hohenberg and W. Kohn, "Inhomogeneous electron gas", *Phys. Rev.* **136**(3B), B864 (Nov. 1964), doi:10.1103/PhysRev.136.B864.

[224] D. Pines, *Elementary Excitations in Solids* (Benjamin, New York, 1964).

[225] C. T. Chantler, K. Olsen, R. A. Dragoset, A. R. Kishore, S. A. Kotochigova, and D. S. Zucker, *X-Ray Form Factor, Attenuation and Scattering Tables* (National Institute of Standards and Technology, Gaithersburg, MD, 2005).

[226] M. Dingfelder, D. Hantke, M. Iokuti, and H. G. Partzke, "Electron inelastic-scattering cross sections in liquid water", *Radiation Phys. Chem.* **53**(1), 1 (Jan. 1999), doi:10.1016/S0969-806X(97)00317-4.

[227] M. R. Spiegel, *Mathematical Handbook of Formulas and Tables*, 35th ed. (McGraw-Hill, New York, 1996).

[228] M. L. Glasser, "Integration methods" (2004), (private communication).

Nomenclature

2D	two dimensional
3D	three dimensional
a_0	Bohr radius $\hbar^2/(m_e e_p^2)$ atomic units in length $\approx 5.29177249 \times 10^{-11}$ metres
AFM	atomic force microscopy
A_i	oscillator strength *see Tables C.1, C.2, C.4*
A_i'	oscillator strength *see Table C.3*
a_j	$\approx \{3.222, 5.270, 2.012, 0.5499\} \times 10^{-4}$ nm^2
α	Thomas-Fermi coefficient πn_0 atomic units
α-CNT	carbon nanotube surrounded by amorphous carbon
α_j	Thomas-Fermi coefficient for jth electron fluid πn_j^0 atomic units
α_ℓ	$\approx \{0.1, 0.55, 0.35\}$ atomic units
a_m	screening length $(9\pi^2/128 Z_{\mathrm{C}})^{1/3}$ $\approx 0.8853 Z_{\mathrm{C}}^{-1/3}$ atomic units
Å	1 ångström ≈ 1.778726 atomic units of length 10^{-10} metres

$\mathbf{B}(\mathbf{r},\omega)$	magnetic field
β	von Weiszäcker coefficient $\approx 1/4$ atomic units
β_ℓ	$\approx \{6.0, 1.2, 0.3\}$ atomic units
b_j	$\approx \{10.330, 18.694, 37.456, 106.88\}$ nm^{-1}
c	speed of light ≈ 137.03599 atomic units of speed
$\chi(m,\kappa,\omega)$	susceptibility $\widetilde{\Phi}/\widetilde{n}$
$\chi_j(m,\kappa_j,\omega)$	susceptibility of jth fluid with induced density n_j $\widetilde{\Phi}/\widetilde{n}_j$
CNT	carbon nanotube
C_{TF}	3D Thomas-Fermi coefficient $\frac{3}{10}(3\pi^2)^{2/3}$
C_x	3D Dirac exchange coefficient $\frac{3}{4}\left(\frac{3}{\pi}\right)^{1/3}$
D	$-\frac{1}{\zeta}\frac{d}{d\zeta}$
$\mathbf{D}(\mathbf{r},\omega)$	electric displacement field
Δ	cutoff parameter for $H(\omega - E_C, \Delta)$
$\Delta(m,\kappa)$	electrostatic interaction between π and σ electron fluids $\Omega_\pi\Omega_\sigma(\kappa^2+m^2)I_m(\lvert\kappa\rvert)K_m(\lvert\kappa\rvert)$
$\frac{\delta F[f]}{\delta f}$	functional derivative of the functional $F[f]$ with respect to the function f
$\delta(x-x_0)$	Dirac delta function ∞ if $x = x_0$

	0 if $x \neq x_0$ $\int_{-\infty}^{\infty} dx\ f(x)\delta(x - x_0) = f(x_0)$
ΔE_{loss}	energy loss $-\int \mathbf{F}_{\text{ind}}(\mathbf{r}_0(t), t) \cdot \mathbf{v}_0 dt$
ΔE_{self}	increments of level curves for self energy *see Fig. 4.24*
$\dfrac{\delta F[n]}{\delta n}$	functional derivative of the density functional $F[n]$ with respect to density n
$\left[\dfrac{\delta F[n]}{\delta n}\right]_0$	functional derivative of the density functional $F[n]$ with respect to equilibrium density n_0
$\left[\dfrac{\delta F[n]}{\delta n}\right]_1$	linear order coefficient of the functional derivative of the density functional $F[n]$ with respect to density n
$\left[\dfrac{\delta F[n]}{\delta n}\right]_N$	$\mathcal{O}(\lambda^N)$ coefficient of the functional derivative of the density functional $F[n]$ with respect to density n
δ_{ij}	Kronecker delta 1 if $i = j$ 0 if $i \neq j$
$\Delta\varphi$	$\varphi - \varphi'$
$\Delta\varphi_p^q$	$\varphi_q - \varphi_p$
$\Delta\varpi_p^q$	$\varpi_q - \varpi_p$
$\Delta\mathbf{p}_\perp$	ion momentum change perpendicular to trajectory $\int F_{\text{ind}}^{\perp}(\mathbf{r}_0(t), t)dt$
Δp_x	change of ion's momentum for ion trajectory perpendicular to nanotube axis
Δr	$r - r'$
Δr_b	boundary separation $\lvert r_{\text{out}} - R\rvert$

$\Delta\varrho$	$\Delta r/R$
Δr_s	radial step size
$\Delta\mathbf{r}$	separation in 2D cylindrical coordinates $\mathbf{r}_R - \mathbf{r}'_R$
$\Delta\mathbf{r}_R$	separation in 3D cylindrical coordinates $\mathbf{r} - \mathbf{r}'$
$\Delta\theta$	$\theta - \theta'$
$\Delta\boldsymbol{\theta}$	angle of ion's deflection by nanotube $\approx \dfrac{\Delta\mathbf{p}_\perp}{p_0}$ for small deflections
$\Delta\theta_x$	angle of deflection by nanotube for ion trajectory perpendicular to nanotube axis $\approx \dfrac{\Delta p_x}{p_0}$ for small deflections
Δz	$z - z'$
Δz_p^q	$z_q - z_p$
DFT	density-functional theory
$\dot{f}$	partial derivative with respect to time t of the function f, $\dfrac{\partial}{\partial t} f$
DWNT	double-walled carbon nanotube
E	energy
$\mathbf{E}(\mathbf{r}, \omega)$	electric field
E_0	ground state energy
E_C	ionization energy threshold for the imaginary part of the dielectric function of water ≈ 7 eV
EELS	electron energy loss spectroscopy
E_F	Fermi energy maximum energy of an electron in the ground state system

$E_{\mathrm{HF}}[\rho]$	Hartree-Fock ground state energy as functional of spinless density matrix ρ
E_j	transition energy *see Table C.4*
E_p	free-electron plasma energy of liquid water ≈ 21.46 eV
$E_\ell[k]$	energy at angular wave number ℓ and longitudinal wave number k $\frac{1}{2}\left(\frac{\ell^2}{R^2}+k^2\right)$
EMA	effective mass approximation
e_p	proton charge 1 atomic units of charge ≈ 14.4 eV Å $\approx 1.6021773\times 10^{-19}$ Coulombs
$\epsilon(\omega)$	optical dielectric function ($k=0$)
ϵ_0	permittivity of free space $\frac{1}{4\pi}$ atomic units $\approx 8.85\times 10^{-12}$ C^2/Nm^2
$\varepsilon_1(\omega)$	real part of optical dielectric function for nickel Re$[\epsilon_{\mathrm{Ni}}(\omega)]$ $\epsilon_{\mathrm{B}}-\sum_i \frac{A_i'(\omega^2-\omega_i^2)}{(\omega^2-\omega_i^2)^2+\omega^2\gamma_i^2}$
$\varepsilon_2(\omega)$	imaginary part of optical dielectric function for nickel Im$[\epsilon_{\mathrm{Ni}}(\omega)]$ $\sum_i \frac{A_i'\gamma_i\omega}{(\omega^2-\omega_i^2)^2+\omega^2\gamma_i^2}$
$\epsilon_{\mathrm{Al}}(\omega)$	optical dielectric function for aluminum *see Table C.2*
ϵ_{B}	background dielectric function in solid *see Table C.3*

$\epsilon_{\rm C}(\omega)$	optical dielectric function for amorphous carbon *see Table C.1*
$\epsilon_{\rm H_2O}(\omega)$	optical dielectric function for water *see Table C.4*
$\epsilon_{\rm in}(\omega)$	optical dielectric function of inner region for $r < r_{\rm in}$
$\varepsilon^{\ell}_{\rm in}(m,\kappa,\omega)$	$\dfrac{\epsilon_{\rm nt}[\mathcal{R}_{\rm in}^{-1}\mathcal{R}_{\rm out}^{-1} - r_{\rm out}g'(r_{\rm in},r_{\rm out})r_{\rm in}g'(r_{\rm out},r_{\rm in})]}{\mathcal{R}_{\rm out}^{-1}R_\ell g'(r_{\rm in},R_\ell) + r_{\rm out}g'(r_{\rm in},r_{\rm out})R_\ell g'(r_{\rm out},R_\ell)}$
$\epsilon_{\rm out}(\omega)$	optical dielectric function of outer region for $r > r_{\rm out}$
$\epsilon_{\rm Ni}(\omega)$	optical dielectric function for nickel *see Table C.3*
	$\varepsilon_1(\omega) + i\varepsilon_2(\omega)$
$\epsilon_{\rm nt}(\omega)$	background optical dielectric function for nanotube
$\varepsilon^{\ell}_{\rm out}(m,\kappa,\omega)$	$\dfrac{\epsilon_{\rm nt}[\mathcal{R}_{\rm in}^{-1}\mathcal{R}_{\rm out}^{-1} - r_{\rm out}g'(r_{\rm in},r_{\rm out})r_{\rm in}g'(r_{\rm out},r_{\rm in})]}{\mathcal{R}_{\rm in}^{-1}R_\ell g'(r_{\rm out},R_\ell) + r_{\rm in}g'(r_{\rm out},r_{\rm in})R_\ell g'(r_{\rm in},R_\ell)}$
$\varepsilon^{n}_{\rm plane}$	relative error between the cylindrical and planar densities
	$\left\| \dfrac{n(\mathbf{r}_R) - n_{\rm plane}(\mathbf{r}_\infty)}{n_{\rm plane}(\mathbf{r}_\infty)} \right\|_\infty$
	$\approx 0.302\ell_F^{-3/2}$ atomic units
$\varepsilon^{\nabla^2\rho}_{\rm plane}$	relative error between $\nabla^2\rho$ for cylindrical and planar geometries
	$\left\| \dfrac{\nabla^2_{\Delta\mathbf{r}_R}\rho(\overline{\mathbf{r}}_R,\Delta\mathbf{r}_R) + \pi n^2_{\rm plane}(\mathbf{r}_\infty)}{\pi n^2_{\rm plane}(\mathbf{r}_\infty)} \right\|_\infty$
	$\approx 0.3303\ell_F^{-3/2}$ atomic units
$\varepsilon_{\rm RPA}(\mathbf{k},\omega)$	Lindhard dielectric function from random phase approximation (RPA)
$E_{\rm self}$	self energy or image potential
	$\frac{1}{2}Q\Phi_{\rm ind}(\mathbf{r}_0(t))$
eV	1 electron volt

	≈ 27.211396 atomic units of energy
$\mathbf{e}_\varphi$	angular unit vector $\sin\varphi\,\mathbf{e}_x - \cos\varphi\,\mathbf{e}_y$
$\mathbf{e}_r$	radial unit vector $\cos\varphi\,\mathbf{e}_x + \sin\varphi\,\mathbf{e}_y$
$\mathbf{e}_x$	unit vector perpendicular to nanotube axis and ion's trajectory, in direction of ion's closest approach to nanotube axis
$\mathbf{e}_y$	unit vector parallel to component of ion's trajectory perpendicular to nanotube axis
$\mathbf{e}_z$	unit vector parallel to nanotube axis
$\mathbf{F}_{\mathrm{ind}}$	force induced by ion
$F_{\mathrm{ind}}^{\perp}$	component of induced force perpendicular to ion trajectory $\|(\mathbf{v}_0 \times \mathbf{F}_{\mathrm{ind}}) \times \mathbf{v}_0\|/v_0^2$
$\mathbf{F}_{\mathrm{ind}}^{\perp}$	component of force induced by ion perpendicular to ion's trajectory
f_j	oscillator strength *see Table C.4*
$F[n]$	energy density functional *see Eqns.* (2.39) *and* (5.7) $\iint d^2\mathbf{r}_R \left[\frac{\pi}{2}n^2(\mathbf{r}_R) + \frac{1}{8}\frac{\|\vec{\nabla}n\|^2}{n} + \frac{1}{2}\iint d^2\mathbf{r}'_R\,\frac{n(\mathbf{r}_R)n(\mathbf{r}'_R)}{\|\mathbf{r}_R - \mathbf{r}'_R\|}\right]$
$g(\varrho,\varrho';m,\kappa)$	radial Green's function in cylindrical coordinates $4\pi I_m(\varrho_<\kappa)K_m(\varrho_>\kappa)$, where $\varrho_< = \min(\varrho,\varrho')$ and $\varrho_> = \max(\varrho,\varrho')$
γ	friction coefficient
γ_0	Euler's constant $\approx 0.577215664901532$

	$\lim_{n\to\infty}\left(1+\frac{1}{2}+\frac{1}{3}+\cdots+\frac{1}{n}-\ln n\right)$
γ_i	damping constant *see Tables C.1, C.2, C.3*
γ_j	damping energy *see Table C.4*
$\gamma(\mathbf{r}, s)$	diagonal elements of spin density matrix, that is $\gamma(\mathbf{r}, s; \mathbf{r}, s)$
$\gamma(\mathbf{r}, s; \mathbf{r}', s')$	spin density matrix $\sum_{i=1}^{N} \psi_i^*(\mathbf{r}', s')\psi_i(\mathbf{r}, s)$
$G[n]$	reduced energy density functional $F[n] - \iiint d^3\mathbf{r} \iiint d^3\mathbf{r}' \frac{n(\mathbf{r}')n(\mathbf{r})}{\|\mathbf{r}-\mathbf{r}'\|}$
$\vec{\nabla}$	gradient operator in cylindrical coordinates $\frac{\partial}{\partial r}\mathbf{e}_r + \frac{1}{r}\frac{\partial}{\partial \varphi}\mathbf{e}_\varphi + \frac{\partial}{\partial z}\mathbf{e}_z$
$H(\omega - E_C, \Delta)$	cutoff function *see Eqns.* (C.5) *and* (C.6)
$H[n, \phi]$	Hamiltonian $F[n] + \iiint d^3\mathbf{r} \frac{1}{2} n(\mathbf{r}, t)\|\mathbf{v}[\phi(\mathbf{r}, t)]\|^2 + \iiint d^3\mathbf{r}\, n(\mathbf{r}, t)V_{\text{ext}}(\mathbf{r}, t)$
h	Planck's constant 2π atomic units of action
$\hbar$	reduced Planck's constant $\frac{h}{2\pi} = 1$ atomic units of action
$\mathscr{H}$	integrand of the Hamiltonian H Hamiltonian density
$\widehat{\mathcal{H}}$	Hamiltonian operator $\sum_i -\frac{1}{2}\nabla_{\mathbf{r}_i}^2 + V_{\text{ext}}(\mathbf{r}_i) + \sum_{j<i} \frac{1}{\|\mathbf{r}_i - \mathbf{r}_j\|}$

$\mathrm{Im}[-\epsilon^{-1}(\omega)]$	energy-loss function
$\iint d^2\mathbf{r}_R$	integration over 2D spatial coordinate $\mathbf{r}_R$ $\int R d\varphi \int dz$
$\iiint d^3\mathbf{r}$	integration over 3D spatial coordinate $\mathbf{r}$ $\int dr \int r d\varphi \int dz$
$I_\nu(z)$	modified Bessel function of the first kind of order ν
$J_E(m,k,\omega)$	integral over time t in $\mathcal{P}(\omega)$ $\frac{\pi r_{\min}}{v_\perp}\frac{e^{-\zeta}}{\zeta}\left(\frac{\xi+\zeta}{u}\right)^m$
$J_\theta(m,k,\omega)$	integral over time t in $\Delta\theta_x$ *see Eqn.* (7.31)
$J_\nu(z)$	Bessel function of the first kind of order ν
k	longitudinal wave number Fourier transform of z $\frac{2\pi}{L}n_z$
κ	kR dimensionless longitudinal wave number
κ_j	kR_j dimensionless longitudinal wave number
k_C	cutoff wave number for $m=0$
$k_F(\ell)$	maximum occupied reciprocal wave vector $\sqrt{2E_F - \frac{\ell^2}{R^2}}$
$K[n]$	Dirac exchange energy $\frac{4\hbar^2}{3m_e}\sqrt{\frac{2}{\pi}}\iint d^2\mathbf{r}_R\, n^{3/2}(\mathbf{r}_R)$
$K_\nu(z)$	modified Bessel function of the second kind of order ν, MacDonald function
KS	Kohn-Sham
$\mathbf{k}$	3D wave vector

	Fourier transform of $\mathbf{r}$
L	length of electron's longitudinal confinement
$L[n,\phi]$	Lagrangian $\iiint d^3\mathbf{r}\; n(\mathbf{r},t)\dfrac{\partial\phi}{\partial t} - H[n,\phi]$
ℓ	angular wave number n_φ
λ	bookkeeping parameter used to denote terms of the same "order" as the external perturbing potential Φ_{ext}
λ_e	de Broglie wavelength of an electron $\dfrac{\hbar}{m_e v}$
λ_W	von Weizsäcker coefficient taken to be one $\hbar^2/m_e$ throughout $\approx {}^1\!/_9$ atomic units in 3D, 0 in 2D, $\approx -{}^1\!/_3$ atomic units in 1D
∇^2	Laplacian operator in cylindrical coordinates $\dfrac{\partial^2}{\partial r^2} + \dfrac{1}{r}\dfrac{\partial}{\partial r} + \dfrac{1}{r^2}\dfrac{\partial^2}{\partial\varphi^2} + \dfrac{\partial^2}{\partial z^2}$
$\nabla^2_{\mathbf{r}_R}$	Laplacian operator in 2D cylindrical coordinates $\dfrac{1}{R^2}\dfrac{\partial^2}{\partial\varphi^2} + \dfrac{\partial^2}{\partial z^2}$
ℓ_{C}	atomic spacing in nanotube ≈ 0.144 nm
LDA	local density approximation
ℓ_F	maximum occupied ℓ value for Fermi energy E_F $R\sqrt{2E_F}$
$\lfloor \ell_F \rfloor$	largest integer less than ℓ_F
$\mathscr{L}$	integrand of the Lagrangian L Lagrangian density

	$n(\mathbf{r},t)\dfrac{\partial\phi}{\partial t} - \mathscr{H}[n,\phi]$
$\ell(t)$	$\sqrt{1+w^2}$
M	ion mass
$\mathfrak{M}$	matrix form for the density response function $\mathfrak{M}\widetilde{\mathbf{n}} = \widetilde{\mathbf{\Phi}}$ *see Eqn.* (3.30)
m	angular wave number
	Fourier transform of φ
MD	molecular dynamics
m_e	electron mass
	1 atomic units of mass
	$\approx 9.1093897 \times 10^{-31}$ kilograms
$\boldsymbol{\mu}$	dipole vector
$\mu_{\mathrm{H_2O}}$	dipole moment of water
	≈ 0.73 atomic units of charge length
	$\approx 6.2 \times 10^{-30}$ Coulomb metres
μ	magnitude of the dipole moment $\|\boldsymbol{\mu}\|$
	1 atomic units = $e_p a_0$
	$\approx 8.4783578 \times 10^{-30}$ Coulomb metres
μ_0	chemical potential
μ_φ	angular dipole $Q\sqrt{4x_0^2 - \Delta r^2}\sin(\Delta\varphi/2)$
μ_r	radial dipole $Q\Delta r$
μ_z	longitudinal dipole $Q\Delta z$
MWNT	multiwalled carbon nanotube
n_0	equilibrium electron number density
	≈ 0.428 atomic units of surface density
$n_0(r)$	radially dependent equilibrium electron number density per unit volume
$n_0(\mathbf{r}_R)$	equilibrium electron number density per unit area

$n_1(\mathbf{r}_R, t)$	linearized induced electron number density per unit area
n_i	principal atomic number of the ith atomic orbital
$\widetilde{n}_j(m, \kappa, \omega)$	Fourier transform of induced charge density on jth cylinder, n_j
$n_N(\mathbf{r}_R, t)$	$\mathcal{O}(\lambda^N)$ coefficient of electron number density per unit area
$n_{\rm one}(\mathbf{r}_R, t)$	single-fluid induced electron density per unit area on a cylinder of radius R *see Eqn.* (4.17)
$\|f(x)\|$	norm of the function $f(x)$ $\int_0^\infty dx\|f(x)\|$
$\|f(\mathbf{x})\|_\infty$	infinity norm of the function $f(\mathbf{x})$ $\max_{\mathbf{x}} \|f(\mathbf{x})\|$
$\|\Phi_{\rm at}(\mathbf{r}_R)\|_\infty$	infinity norm of the time-independent confining potential $\max_{\mathbf{r}_R} \|\Phi_{\rm at}(\mathbf{r}_R, t)\|$
$\|\Phi_{\rm ext}(\mathbf{r}_R, t)\|_\infty$	infinity norm of the time-dependent perturbing potential $\max_{\mathbf{r}_R, t} \|\Phi_{\rm ext}(\mathbf{r}_R, t)\|$
n_φ	angular orbital occupation number
n_π^0	equilibrium density of π electron fluid $\approx \frac{1}{4} n_0 \approx 0.107$ atomic units of surface density
$n_{\rm plane}$	planar density $\frac{E_F}{\pi} = \frac{\ell_F^2}{2\pi R^2}$
$n(\mathbf{r})$	electron number density per unit volume at position $\mathbf{r}$ diagonal elements of spinless density matrix, that is $\rho(\mathbf{r}, \mathbf{r})$
n_σ^0	equilibrium density of σ electron fluid

	$\frac{3}{4}n_0 \approx 0.321$ atomic units of surface density
$n_{\rm two}(\mathbf{r}_R, t)$	two-fluid induced electron density per unit area on a cylinder of radius R *see Eqn.* (4.18)
$\widetilde{\mathbf{n}}$	vector form of the induced electron surface density of a MWNT with elements $\widetilde{n}_j$ *see Eqn.* (3.29)
n_z	longitudinal orbital occupation number
Ω^2	combined frequency
	$\omega(\omega + i\gamma)$
$\Omega^2(m,\kappa)$	$\frac{\Omega_\pi^2\Omega_\sigma^2}{2R\Omega_{\rm p}^2}(\kappa^2+m^2) + \frac{\beta}{R^4}(\kappa^2+m^2)^4$
ω	plasma frequency
	Fourier transform of t
$\omega_+^2(m,\kappa)$	plasma frequencies of $\sigma+\pi$ nanotube branches
	$\frac{\omega_\pi^2+\omega_\sigma^2}{2} + \sqrt{\left(\frac{\omega_\pi^2-\omega_\sigma^2}{2}\right)^2 + \Delta^2}$
$\omega_-^2(m,\kappa)$	plasma frequencies of π nanotube branches
	$\frac{\omega_\pi^2+\omega_\sigma^2}{2} - \sqrt{\left(\frac{\omega_\pi^2-\omega_\sigma^2}{2}\right)^2 + \Delta^2}$
$\Omega_{\rm c}(m,\kappa)$	plasma frequencies for metal channel
	$\omega_p\sqrt{\kappa\varrho_{\rm out}I_m(\lvert\kappa\rvert\varrho_{\rm out})\lvert K_m'(\lvert\kappa\rvert\varrho_{\rm out})\rvert}$
$\omega_{\rm D+}^a(m,\kappa)$	antisymmetrically coupled (antibonding) metal-$(\sigma+\pi)$ plasma frequency
$\omega_{\rm D\pm}^a(m,\kappa)$	antisymmetrically coupled (antibonding) π-metal-$(\sigma+\pi)$ plasma frequency
$\omega_{\rm D\pm}^s(m,\kappa)$	symmetrically coupled (bonding) π-metal-$(\sigma+\pi)$ plasma frequency
$\omega_{\rm D+}^s(m,\kappa)$	symmetrically coupled (bonding) metal-$(\sigma+\pi)$ plasma frequency
ω_i	critical-point energy *see Tables C.1, C.2, C.3*
$\Omega_{\rm p}$	$\sqrt{4\pi n_0/R}$ atomic units of frequency

ω_p	plasma frequency $\sqrt{4\pi n}$ atomic units of frequency
Ω_π	$\sqrt{4\pi n_\pi^0/R}$
$\omega_\pi(m,\kappa)$	plasma frequencies of π electron fluid $\Omega_\pi^2(\kappa^2+m^2)\left[\frac{1}{4R}+\beta\frac{\kappa^2+m^2}{\Omega_\pi^2R^4}+I_m(\lvert\kappa\rvert)K_m(\lvert\kappa\rvert)\right]$
Ω_σ	$\sqrt{4\pi n_\sigma^0/R}$
$\omega_\sigma(m,\kappa)$	plasma frequencies of σ electron fluid $\Omega_\sigma^2(\kappa^2+m^2)\left[\frac{1}{4R}+\beta\frac{\kappa^2+m^2}{\Omega_\sigma^2R^4}+I_m(\lvert\kappa\rvert)K_m(\lvert\kappa\rvert)\right]$
$\Omega_{\mathrm{w}}(m,\kappa)$	plasma frequencies for metal wire $\omega_p\sqrt{\kappa\varrho_{\mathrm{in}}I'_m(\lvert\kappa\rvert\varrho_{\mathrm{in}})K_m(\lvert\kappa\rvert\varrho_{\mathrm{in}})}$
p_0	ion momentum Mv_0
$\Phi(\mathbf{r},t)$	total electric potential
ϕ	spherical polar angle *see Fig. 6.8*
φ	angular coordinate
$\varphi_0(t)$	angular coordinate of ion $\arctan\left(\frac{v_\perp t}{r_{\min}}\right)$
$\Phi_{\mathrm{at}}(\mathbf{r})$	time-independent confining potential arising from the positive charge background
$\Phi_{\mathrm{C}}(\mathbf{r})$	Molière approximation for total electrostatic potential for a single carbon atom $\frac{Z_{\mathrm{C}}}{r}\varphi(r/a_m)$
$\Phi_{\mathrm{ext}}(\mathbf{r},t)$	time-dependent perturbing potential external to the system
$\Phi_{\mathrm{in}}(\mathbf{r},t)$	potential due to polarization charge on inner dielectric boundary
$\Phi_{\mathrm{ind}}(\mathbf{r},t)$	induced electric potential *see Eqn. 6.1*

$\widetilde{\Phi}_{\rm ind}(r, m, \kappa, \omega)$	Fourier transform of induced electric potential $\Phi_{\rm ind}$
$\widehat{\Phi}_{\rm ind}(\mathbf{r}, \omega)$	Fourier transform of the induced electric potential with respect to time t
$\Phi_{\rm nt}(\mathbf{r}, t)$	induced potential from nanotube
$\widetilde{\Phi}_{\rm nt}(\mathbf{r}, t)$	Fourier transform of induced potential from nanotube $-\epsilon_{\rm nt}^{-1}(\omega) \sum_j R_j g(\varrho, \varrho_j; m, \kappa) \widetilde{n}_j(m, \kappa, \omega)$
$\Phi_{\rm out}(\mathbf{r}, t)$	potential due to polarization charge on outer dielectric boundary
$\phi_i(\mathbf{r})$	single electron spatial wave function
$\sigma_i(s)$	single electron spin function
$\varphi(r/a_m)$	screening function $\sum_{\ell=1}^{3} \alpha_\ell e^{-\beta_\ell r/a_m}$
$\phi_i(\Vert\mathbf{r} - \mathbf{r}'\Vert)$	doubly occupied normalized non-orthogonal orbitals $\sqrt{\frac{2^{2n_i+1}\zeta_i^{2n_i+1}}{4\pi(2n_i)!}} \Vert\mathbf{r} - \mathbf{r}'\Vert^{n_i-1} e^{-\zeta_i \Vert\mathbf{r}-\mathbf{r}'\Vert}$
$\phi(\mathbf{r}, t)$	scalar conjugate variable satisfying Legendre transformation with $n(\mathbf{r}, t)$ scalar potential of transverse part of the fluid velocity $\mathbf{v}(\mathbf{r}, t)$
$\Phi_{\rm sc}(\mathbf{r}, t)$	screened external perturbing potential
$\widetilde{\mathbf{\Phi}}$	vector form of the external potential, with elements $\widetilde{\Phi}_{\rm ext}(R_j; m, k, \omega)$ *see Eqn.* (3.31)
ϖ	v/R atomic units of frequency
ϖ_p	v_p/R atomic units of frequency
$\mathcal{P}(\omega)$	plasmon excitation probability function of ω

$\Psi_{\rm HF}(\mathbf{r}^N, s^N)$	Hartree-Fock approximation to N-electron anti-symmetric wave function $\Psi(\mathbf{r}^N, s^N)$ given by $\frac{1}{\sqrt{N!}}\det[\psi_1\psi_2\cdots\psi_N]$ where ψ_i are single electron wave functions
$\psi_i(\mathbf{r}, s)$	single electron orthonormal wave functions
$\Psi(\mathbf{r}_1, s_1, \ldots, \mathbf{r}_N, s_N)$	N-electron wave function (also denoted by $\Psi(\mathbf{r}^N, s^N)$)
$\Psi(\mathbf{r}^N, s^N)$	N-electron wave function (also denoted by $\Psi(\mathbf{r}_1, s_1, \ldots, \mathbf{r}_N, s_N)$)
$\mathrm{P.V.}\int_a^b dx$	principal value of the integral *see Eqn.* (G.2)
Q	ion charge
$Q_{\rm C}$	atomic charge of carbon $Z_{\rm C}e_p$
Q_p	charge of the pth ion
R	nanotube radius
$\mathbf{r}$	$\{r, \varphi, z\}$ cylindrical coordinates aligned with nanotube axis
$\mathbf{r}_R$	$\{r = R; \varphi, z\}$ cylindrical coordinates on cylinder of radius R aligned with nanotube axis
r	radial coordinate
R_j	radius of jth wall of multiwalled nanotube
$\mathbf{r}_0$	ion position $\{r_0, \varphi_0, z_0\}$
$r_0(t)$	radial coordinate of ion in laboratory frame of reference $\sqrt{r_{\rm min}^2 + v_\perp^2 t^2}$
$\overline{\mathbf{r}}$	average position in 3D cylindrical coordinates

	$\frac{1}{2}(\mathbf{r}+\mathbf{r}')$
$\overline{\mathbf{r}}_R$	average position in 2D cylindrical coordinates $\frac{1}{2}(\mathbf{r}_R+\mathbf{r}'_R)$
$r_>$	$\max(r,r')$
$\rho(\mathbf{r},\omega)$	total charge density
$\rho_0(\mathbf{r})$	equilibrium charge density per unit volume of an electron fluid confined to a cylinder of radius R $-n_0\delta(r-R)$
$\rho_1(\mathbf{r},t)$	linear order correction to equilibrium charge density per unit volume of an electron fluid confined to a cylinder of radius R $-n_1(\mathbf{r}_R,t)\delta(r-R)$
$\rho_{\mathrm{at}}(\lVert\mathbf{r}-\mathbf{r}'\rVert)$	electron density for a free carbon atom *see Eqn.* (5.35)
$\rho_{\mathrm{ext}}(\mathbf{r},\omega)$	external charge density
$\rho_f(\mathbf{r},\omega)$	total free charge density
$\rho_N(\mathbf{r}_R,t)$	$\mathcal{O}(\lambda^N)$ coefficient of equilibrium charge density per unit volume of an electron fluid confined to a cylinder of radius R $-n_N(\mathbf{r}_R,t)\delta(r-R)$
$\rho(\mathbf{r}',\mathbf{r})$	spinless density matrix $\sum_s \gamma(\mathbf{r}',s;\mathbf{r},s) = 2\sum_1^{N/2}\phi_i^*(\mathbf{r}')\phi_i(\mathbf{r})$
ϱ	r/R dimensionless radial coordinate
ϱ_0	r_0/R dimensionless radial position of ion
$\varrho_{0>}$	$\max(1,r_0/R)$
$\varrho_{0<}$	$\min(1,r_0/R)$
ϱ_{in}	r_{in}/R dimensionless radial position of inner dielectric boundary

$\varrho_{\rm out}$	$r_{\rm out}/R$ dimensionless radial position of outer dielectric boundary
ϱ_j	r/R_j dimensionless radial coordinate
$\mathcal{R}_{\rm in}(m,\kappa,\omega)$	response function of polarization charge due to external electric field in radial direction on inner boundary $r_{\rm in}$ $\dfrac{\epsilon_{\rm out}-\epsilon_{\rm nt}}{4\pi[\epsilon_{\rm nt}+(\epsilon_{\rm nt}-\epsilon_{\rm out})\kappa\varrho_{\rm out}I_m(\lvert\kappa\rvert\varrho_{\rm out})K'_m(\lvert\kappa\rvert\varrho_{\rm out})]}$
$r_{\rm in}$	radius of inner dielectric boundary (wire)
$\mathbf{r}_\infty$	2D planar coordinate $\lim_{R\to\infty}\{r=R;\varphi,z\}$
$r_<$	$\min(r,r')$
$r_{\rm min}$	distance of ion's closest approach to nanotube axis $\min_t r_0(t)$
$d^3\mathbf{r}^N$	$d^3\mathbf{r}_1\ \cdots d^3\mathbf{r}_N$
$\mathbf{r}^N$	$\mathbf{r}_1,\ldots,\mathbf{r}_N$
s^N	$s_1,\ldots,s_N$
$\mathcal{R}_{\rm out}(m,\kappa,\omega)$	response function of polarization charge due to external electric field in radial direction on outer boundary $r_{\rm out}$ $\dfrac{\epsilon_{\rm nt}-\epsilon_{\rm in}}{4\pi[\epsilon_{\rm nt}-(\epsilon_{\rm nt}-\epsilon_{\rm in})\kappa\varrho_{\rm in}I'_m(\lvert\kappa\rvert\varrho_{\rm in})K_m(\lvert\kappa\rvert\varrho_{\rm in})]}$
$r_{\rm out}$	radius of outer dielectric boundary (channel)
RPA	random phase approximation
$\mathbf{r}_{R_j}$	position on the cylinder of radius R_j $\{r=R_j;\varphi,z\}$
s	dimensionless separation $k_F\lVert\Delta\mathbf{r}\rVert$
SCF	self-consistent field

σ_a surface atomic density
≈ 0.107 atomic units of surface density

$\sigma_{\rm in}$ surface polarization charge density on inner dielectric boundary

$\widetilde{\sigma}_{\rm in}$ Fourier-Bessel transform of surface polarization charge density on inner dielectric boundary
$$\mathcal{R}_{\rm in}\frac{\partial}{\partial r}\left[\widetilde{\Phi}_{\rm sc}+\widetilde{\Phi}_{\rm nt}+\widetilde{\Phi}_{\rm out}\right]_{r_{\rm in}}=\widetilde{\sigma}^{\rm sc}_{\rm in}-\sum_{\ell}\frac{\widetilde{n}_\ell}{\varepsilon^\ell_{\rm in}}$$

$\widetilde{\sigma}^{\rm sc}_{\rm in}(m,\kappa,\omega)$ polarization charge on inner boundary due to external charge
$$\frac{\mathcal{R}_{\rm in}\frac{\partial\widetilde{\Phi}_{\rm sc}}{\partial r}\|_{r_{\rm in}}+\mathcal{R}_{\rm in}\mathcal{R}_{\rm out}r_{\rm out}g'(r_{\rm in},r_{\rm out})\frac{\partial\widetilde{\Phi}_{\rm sc}}{\partial r}\|_{r_{\rm out}}}{1-r_{\rm out}g'(r_{\rm in},r_{\rm out})r_{\rm in}g'(r_{\rm out},r_{\rm in})\mathcal{R}_{\rm in}\mathcal{R}_{\rm out}}$$

$\widetilde{\sigma}^{\rm sc}_{\rm in}(m,\kappa,\omega)$ polarization charge on inner boundary due to external charge
$$\frac{\mathcal{R}_{\rm out}\frac{\partial\widetilde{\Phi}_{\rm sc}}{\partial r}\|_{r_{\rm out}}+\mathcal{R}_{\rm in}\mathcal{R}_{\rm out}r_{\rm in}g'(r_{\rm out},r_{\rm in})\frac{\partial\widetilde{\Phi}_{\rm sc}}{\partial r}\|_{r_{\rm in}}}{1-r_{\rm out}g'(r_{\rm in},r_{\rm out})r_{\rm in}g'(r_{\rm out},r_{\rm in})\mathcal{R}_{\rm in}\mathcal{R}_{\rm out}}$$

$\sigma_{\rm out}$ surface polarization charge density on outer dielectric boundary

$\widetilde{\sigma}_{\rm out}$ Fourier-Bessel transform of surface polarization charge density on outer dielectric boundary
$$\mathcal{R}_{\rm out}\frac{\partial}{\partial r}\left[\widetilde{\Phi}_{\rm sc}+\widetilde{\Phi}_{\rm nt}+\widetilde{\Phi}_{\rm in}\right]_{r_{\rm out}}=\widetilde{\sigma}^{\rm sc}_{\rm out}-\sum_{\ell}\frac{\widetilde{n}_\ell}{\varepsilon^\ell_{\rm out}}$$

$S_{\rm one}$ single-fluid stopping force *see Eqn.* (4.21)

sp^2 hybridization of an atom's $2s$, $2p_x$, and $2p_y$ orbitals producing three planar σ orbitals separated by 120°

S stopping force
$Q\ \frac{\partial}{\partial z}\Phi_{\rm ind}\big\|_{\mathbf{r}_0(t)}$

S_l local stopping force contribution

S_n non-local stopping force contribution

$S_{\rm two}$ two-fluid stopping force *see Eqn.* (4.22)

SWNT	single-walled carbon nanotube
t	time
TD-DFT	time-dependent density-functional theory
Θ	screening factor due to dielectric media surrounding nanotube $1+\frac{(\epsilon-1)x_{\rm out}I_m(x_{\rm out})K'_m(x_{\rm out})}{1-(\epsilon-1)x_{\rm out}I_m(x_{\rm out})K'_m(x_{\rm out})}\frac{I_m(\lvert\kappa\rvert)K_m(\lvert\kappa_{\rm out}\rvert)}{I_m(\lvert\kappa_{\rm out}\rvert)K_m(\lvert\kappa\rvert)}$
θ	azimuthal angle *see Fig. 6.8*
$\Theta(x)$	Heaviside step function 1 if $x>0$ $\frac{1}{2}$ if $x=0$ 0 if $x<0$ $\int_{-\infty}^{x} dx\delta(x)$
$T_{\rm TF}[n]$	Thomas-Fermi kinetic energy $\frac{\pi}{2}\iint d^2\mathbf{r}_R\, n^2(\mathbf{r}_R)$ atomic units of energy $\frac{\pi\hbar^2 a_0}{2m_e}\iint d^2\mathbf{r}_R\, n^2(\mathbf{r}_R)$
$T_{\rm TFvW}[n]$	kinetic energy functional for Thomas-Fermi model with von Weizsäcker gradient correction $T_{\rm TF}[n]+\lambda_W T_W[n]$
$T_W[n]$	von Weizsäcker gradient correction $\frac{1}{8}\iiint d^3\mathbf{r}\,\frac{\lVert\vec{\nabla}n(\mathbf{r})\rVert}{n(\mathbf{r})}$ $\frac{\hbar^2}{8m_e}\iiint d^3\mathbf{r}\,\frac{\lVert\vec{\nabla}n(\mathbf{r})\rVert}{n(\mathbf{r})}$
$U_{\rm at}$	repulsive atomic potential
$U_{\rm DT}(r)$	Doyle-Turner atomic potential $\sum_{p=1}^{N}\frac{32\pi Q_p Z_{\rm C} R}{3^{3/2}\ell^2}\sum_{j=1}^{4} a_j b_j^2 e^{-b_j^2(r^2+R^2)} I_0(2b_j^2 rR)$

$u(k)$	$kr_{\min}$
$U_{\mathrm{M}}(r)$	Molière atomic potential $4\pi \sum_{p=1}^{N} Q_p \sigma_a Z_{\mathrm{C}} \sum_{\ell=1}^{3} \alpha_\ell g(r, R; 0, \beta_\ell / a_m)$
U_T	total potential energy
UV	ultra-violet energy spectrum
V	volume of electron's confinement
v	ion speed parallel to nanotube axis
$\mathbf{v}_0$	velocity of an ion with trajectory at an oblique angle to nanotube axis
$\mathbf{v}_1(\mathbf{r}_R, t)$	linearized induced velocity of the electron fluid on cylinder of radius R
V_{C}	Coulomb potential $\dfrac{Q}{\|\mathbf{r} - \mathbf{r}'\|}$
V_{ee}	electron-electron interaction potential
$v_{\mathrm{eff}}(\mathbf{r})$	effective potential from KS equations $V_{\mathrm{ext}}(\mathbf{r}) + \iiint d^3\mathbf{r}' \, \dfrac{n(\mathbf{r}')}{\|\mathbf{r} - \mathbf{r}'\|} + v_{xc}(\mathbf{r})$
$V_{\mathrm{ext}}(\mathbf{r})$	external potential
v_F	Fermi velocity $\sqrt{2\pi n_0}$ atomic units of speed
$\mathbf{v}_j(\mathbf{r}_{R_j}, t)$	velocity of jth electron fluid on cylinder of radius R_j
$\mathbf{v}_N(\mathbf{r}_R, t)$	$\mathcal{O}(\lambda^N)$ coefficient of electron fluid velocity tangential to a cylinder of radius R
$v_\parallel \mathbf{e}_z$	ion speed parallel to nanotube axis
$v_\perp \mathbf{e}_y$	ion speed perpendicular to nanotube axis

V^{pseudo}	pseudopotential which models the effective potential felt by electrons from the screened ion cores
$\mathbf{v}_{\mathrm{rot}}(\mathbf{r},t)$	rotational part of fluid velocity $\mathbf{v}(\mathbf{r},t)$
$v_{xc}(\mathbf{r})$	exchange and correlation potential from KS equations
$v_{xc}^{\mathrm{LDA}}(\mathbf{r})$	LDA approximation of exchange and correlation potential from KS equations
$w(t)$	$-\dfrac{v_{\perp}t}{r_{\min}}$
x_0	radial distance from the nanotube axis
$\xi(k,\omega)$	$\dfrac{r_{\min}}{v_{\perp}}(\omega - kv_{\parallel})$
Z	number of valence electrons per atom in electron fluid
z	longitudinal coordinate
z_0	longitudinal coordinate of ion in moving frame of reference
$z_0(t)$	longitudinal coordinate of ion in laboratory frame of reference
	$v_{\parallel}t$
Z_{C}	number of valence electrons per carbon atom
$\zeta(k,\omega)$	$\sqrt{\xi^2+u^2}$
$\zeta_{1\mathrm{s}}$	variational parameter for 1s orbital of free carbon atom
	≈ 5.57071 atomic units of inverse length
$\zeta_{2\mathrm{p}}$	variational parameter for 2p orbital of free carbon atom
	≈ 1.23526 atomic units of inverse length

ζ_{2s}	variational parameter for 2s orbital of free carbon atom ≈ 2.70341 atomic units of inverse length
ζ_i	variational parameter for Cruz free atom electron density model